Polymers and Plastrons: Active and Passive Drag Reduction in Wall-Bounded Turbulent Flows

by

Anoop Rajappan

B. Tech., Indian Institute of Technology Madras (2015)
S. M., Massachusetts Institute of Technology (2017)

Submitted to the Department of Mechanical Engineering
in partial fulfillment of the requirements for the degree of

Doctor of Science in Mechanical Engineering

at the

Massachusetts Institute of Technology

September 2020

© 2020 Massachusetts Institute of Technology. All rights reserved.

Signature of Author .....
Department of Mechanical Engineering
August 7, 2020

Certified by .....
Gareth H. McKinley
SoE Professor of Teaching Innovation
Thesis Supervisor

Accepted by .....
Nicolas Hadjiconstantinou
Professor of Mechanical Engineering
Graduate Officer

The space below is intentionally left blank.

Polymers and Plastrons: Active and Passive Drag Reduction in Wall-Bounded Turbulent Flows

by

Anoop Rajappan

Submitted to the Department of Mechanical Engineering
on August 7, 2020, in partial fulfillment of the
requirements for the degree of Doctor of Science in
Mechanical Engineering

Abstract

Frictional energy dissipation in wall-bounded turbulence is ubiquitous in modern engineering systems, ranging from the flow of liquids through pipelines, to the drag-inducing boundary layer around ships and submarines. The effective mitigation of this frictional drag is therefore of great practical interest, and offers substantial economic and environmental benefits. This thesis focuses on two complementary techniques for turbulent drag reduction—the active injection of polymers into the flow, and the passive aerophilic texturing of the wall—and aims to address practical challenges that prevent their widespread adoption in real-life systems, with an emphasis on marine applications.

The prohibitive cost of synthetic polymers remains a key impediment to their large-scale deployment in commercial marine operations. This thesis hence focuses on affordable and readily accessible sources of high molecular weight biopolymers: specifically, the water-soluble fiber, or mucilage, extracted from seeds such as flax, chia and psyllium. By means of frictional drag measurements inside a bespoke Taylor-Couette apparatus, seed mucilage is shown herein to display drag reduction efficacy and flow longevity comparable to common synthetic polymers, while offering significant advantages in terms of raw material cost and biodegradability. Preliminary investigations confirm that oil-soluble natural polymers, such as rubber latex, can analogously be employed as eco-friendly drag reducers for the transport of hydrocarbon feedstocks.

Superhydrophobic texturing of submerged flow boundaries has emerged recently as another viable method of drag reduction in aqueous flows. Despite sustained research interest in both polymers and superhydrophobic walls as standalone methods for drag mitigation, attempts to employ them jointly has remained unsuccessful. In this thesis, cooperative drag reduction effects are explored for two common drag-reducing polymers, paired with regularly patterned as well as randomly textured superhydrophobic walls. Dissolved flexible macromolecules are shown to act in concert with the slip-inducing air layer, or plastron, trapped atop the superhydrophobic texture, yielding enhanced reductions in turbulent drag greater than that achievable from either method employed independently. An additive law in Prandtl-von Kármán coordinates is derived that accurately predicts this combined effect at dilute polymer concentrations, and the adverse influence of the surface activity of polymers on wall slip is also elucidated.

Thesis Supervisor: Gareth H. McKinley
Title: School of Engineering Professor of Teaching Innovation

The space below is intentionally left blank.

I dedicate this thesis to my parents.

And both that morning equally lay
In leaves, no step had trodden black.
Oh, I kept the first for another day!
Yet knowing how way leads on to way,
I doubted if I should ever come back.

—Robert Frost, The Road Not Taken,
Mountain Interval (1916).

The space below is intentionally left blank.

Acknowledgments

I am deeply indebted to Prof. Gareth McKinley, my doctoral advisor, for his support, guidance and mentorship during my graduate studies here at MIT. I have greatly admired his enthusiasm for science, his passion for teaching, his objective approach to research, and his rigorous attention to detail. I am grateful to have had an opportunity to work with him these past five years. I also express my immense gratitude to Prof. Irmgard Bischofberger and Prof. Patrick Doyle, for agreeing to be part of my doctoral thesis committee, and for their helpful suggestions and feedback on my work at every stage, from the initial proposal to the final defense.

I thank the many sponsors and funding sources that provided financial support for my research and graduate studies at MIT: the Office of Naval Research (ONR) through the MURI program, the National Science Foundation (NSF) through the MRSEC program, the Procter and Gamble Company, Chevron Corporation, and the MIT School of Engineering through the Nicholas Hobson Wheless, Jr. fellowship.

I thank all my friends, collaborators and colleagues, and all members of the NNF group—Ahmed, Alex, Amir, Bavand, Caroline, Crystal, Dayong, Divya, Gibum, Igor, Jake, Jarvis, Joshua, Justin, Louis, Michela, Pablo, Philippe, Sami, Setareh, Shabnam, Shourav, Teja, Thibaut, and Yonatan—for making my time here more memorable and enjoyable than I could have hoped for, both inside and outside the lab. Thank you for your kindness, generosity and friendship, and for making me feel welcome and at home right from my first day at HML. I will always cherish the fond memories and conversations I have had in your company during the last five years; they have helped me grow both as a person and as a researcher during my time at MIT.

I am profoundly grateful to Ms. Leslie Regan, MechE graduate administrator, for her extraordinary kindness and support, especially during my initial few months at MIT as I struggled to adjust to the challenging research and academic environment here; to Mr. Pierce Hayward, for teaching me everything I know about machining today, and for permitting me to use the machines at the Graduate Student Shop, which I relied on extensively to build my experimental fixtures; and to Mr. Sean Buhrmester, for his

patient assistance with countless purchases, chemical procurement, and myriad other administrative matters over the past five years.

Above all, I am forever indebted to my parents for their unconditional love, their unwavering support in times of crisis, their unending patience and understanding, and their prayers and blessings at every stage of my life; I owe everything to them. I can only hope to give back a fraction of all they have done and sacrificed for my well being.

Just five years ago, I would not have dreamt of having the opportunity to attend MIT for my graduate studies. I can only attribute all that has happened since to the grace of Providence, for which I am eternally thankful.

August 7, 2020
Cambridge, Massachusetts

Contents

1. Introduction · 25

I Background and Motivation 25

II Research Goals and Expected Outcomes 27

III Organization of Thesis Contents 30

2. Drag Reduction in Wall-Bounded Turbulent Flows: A Review · 33

I Drag Reduction Using Polymer Additives 33

A A Brief Introduction to Polymer Drag Reduction 33

B The Phenomenology of Drag Reduction 37

C Mechanistic Descriptions of Drag Reduction 47

D Biopolymers as Drag-Reducing Agents 52

II Drag Reduction Using Superhydrophobic Walls 54

A Fundamentals of Wetting and Superhydrophobicity 54

B Plastron-Mediated Wall Slip and Frictional Drag Reduction 59

C Designing Scalable Surfaces for Large-Scale Drag Reduction 63

D Surface Resilience Through Active Plastron Management 66

III Closing Remarks 68

3. Overview of Experimental Techniques · 71

I Frictional Drag Measurements in Turbulent Flow 71

A The Turbulent Taylor-Couette Flow Apparatus 71

B Taylor-Couette Flow of Newtonian Fluids 77

II Characterization of Drag-Reducing Polymer Solutions 88

A Polymer Dissolution, Gravimetry & Lyophilization 88

B Dilute Solution Viscometry 89

C Capillary Breakup Extensional Rheometry 100

4. Seed Mucilage: An Eco-Friendly Drag Reducer for Aqueous Flows · 107

I Introduction 107

II Experimental Characterization of Mucilage 109

A Polysaccharide Extraction and Macromolecular Analysis 109

B Rheology of Mucilage Polysaccharides 114

III Drag Reduction by Mucilage Polysaccharides 123

A Drag Reduction Measurements in Turbulent TC Flow 123

B Practical Considerations in Engineering Systems 127

IV Closing Remarks 132

A Exploring Alternate Sources of Mucilage 132

B A Brief Note on Biodegradability 133

5. Combining Polymers & Plastrons for Enhanced Drag Reduction · 135

I Introduction 135

II Preparation of Polymers and Superhydrophobic Surfaces 138

A Fabrication of drag-reducing superhydrophobic textures 138

B Preparation of aqueous drag-reducing polymer solutions 139

III Experimental Results and Discussion 141

A Turbulent Flow Experiments in the Bespoke TC Apparatus 141

B Individual and Combined Drag Reduction Measurements 142

C Surface-Active Polymers and Interfacial Effects 152

IV Closing Remarks 156

6. Conclusion · 159

I A Brief Summary of Results 159

II Potential Avenues for Future Research 165

Appendices

A. Plant-Based Drag Reducers for Hydrocarbon Flows · 169

I Introduction 169

A Background and Motivation 169

B Oil-Soluble Plant Biopolymers 171
II Frictional Drag Measurements in Liquid Alkanes 173
A The High Temperature Taylor-Couette Apparatus 174
B Calibration of Baseline Friction 176
C Preliminary Studies on Drag-Reducing Polymers 182

Image credits and attribution 185

References 187

The space below is intentionally left blank.

List of Tables

2.1 Examples of natural polymers that have been successfully employed for aqueous drag reduction in the literature; also listed are the maximum percentage drag reduction observed, the corresponding polymer concentration, and the flow configuration used for experimental friction measurements. 52

2.2 List of selected drag-reducing biopolysaccharides, along with the plant or bacterial source of each polymer, the typical range of molar masses, and the monosaccharide residues of the principal constituent polysaccharide. 53

2.3 Examples of past studies reporting frictional drag measurements in the turbulent flow regime on scalable superhydrophobic surfaces with random textural roughness. The flow configuration utilized for turbulent drag measurements, the range of shear Reynolds numbers investigated, and the percentage drag reduction achieved are listed. 64

3.1 A comparison of dimensions, geometry ratios and key flow parameters between the TC apparatus used in this study, and the original wide-gap TC device described by Srinivasan et al. (2015). 74

3.2 Technical specifications for the AR-G2 rheometer. 76

3.3 Density and viscosity data for Newtonian fluids used in the baseline calibration of the bespoke TC apparatus. 81

4.1 The concentration c and the characteristic relaxation time λ of aqueous PEO and flax mucilage solutions used in drag reduction experiments. . 119

5.1 Concentration and relative viscosity of dilute PAM and PEO solutions used in combined drag reduction measurements. 141

A.1 Thermophysical data for dodecane at a pressure of $P = 1\,\text{atm}$, and for temperatures in the range $20\,°\text{C} \leqslant T \leqslant 60\,°\text{C}$. 174

A.2 A comparison of dimensions, geometry ratios and key flow parameters between the bespoke TC apparatus used for aqueous flow measurements, and the HTTC apparatus used for frictional drag measurements in liquid alkanes. 177

List of Figures

1.1 Active and passive methods for drag reduction in the turbulent boundary layer around ships, submarines and underwater projectiles. 27

2.1 High molar mass drag reducing agent (DRA) used for drag reduction in crude oil pipelines. DRA injection ports along the Trans-Alaska Pipeline System (TAPS). 34

2.2 New York Fire Department demonstration of the use of "slippery water" in fire engines, May 1969. 35

2.3 Full-scale polymer drag reduction trials on the *HMS Highburton* in 1971. The Pacific barracuda, *Sphyraena argentea*, which produces a drag-reducing epidermal mucus (slime). 36

2.4 Empirical friction curves for the flow of pure water and an aqueous PEO solution through a circular pipe. Data from Virk (1975). 42

2.5 Schematic representation of viscoelastic flow regimes in the Wi–Re plane, as well as in Prandtl-von Kármán coordinates. 44

2.6 Raindrops on the leaves of lotus and taro plants, displaying plastron-mediated non-wettability. Scanning electron micrographs of leaf dorsa. 55

2.7 Schematic representations of Wenzel and Cassie-Baxter wetting regimes on a two-dimensional array of superhydrophobic microposts. Water droplets on a superhydrophobic texture comprising regularly patterned posts, illustrating the two wetting regimes. 57

2.8 Liquid flowing over a submerged superhydrophobic wall in the Cassie-Baxter state, and the flow boundary conditions prevailing atop the composite interface. 60

2.9 Depth-composition micrograph of a scalable, randomly textured, etched aluminum superhydrophobic surface, and the corresponding surface profilogram measured using a confocal laser profilometer. 66

3.1 The bespoke TC apparatus utilized for frictional drag measurements in turbulent flow. 73

3.2 Representative photographs of flow patterns inside the bespoke TC apparatus at increasing Reynolds numbers, as observed during flow visualization experiments. 80

3.3 Experimental baseline torque $G = \mathscr{T}/\rho\nu^2 L$ for the TC apparatus as a function of the Reynolds number Re. 82

3.4 The local torque exponent α as a function of the Reynolds number Re, derived from the baseline curve for the TC apparatus. A change in slope is observed near $\mathrm{Re}_{\mathrm{crit}} \simeq 1.1 \times 10^4$, indicating the point of transition to the featureless turbulent flow regime. 83

3.5 The baseline friction curve for the bespoke TC apparatus in Prandtl-von Kármán coordinates. The torque exponent α as a function of the Reynolds number Re, compared with the corresponding theoretically predicted value. 85

3.6 The experimental friction curve for the bespoke TC apparatus in featureless turbulent flow, compared with the semi-empirical models of Cheng et al. (2020) and Berghout et al. (2020), both evaluated for a radius ratio of $\zeta = 0.75$. 87

3.7 Lyophilization of seed mucilage extracts: frozen mucilage inside a vacuum flask connected to a laboratory freeze dryer; spongy plugs of dried mucilage recovered at the end of lyophilization; and the manual grinding of the freeze-dried mucilage pellets by mortar and pestle, in preparation for reconstitution with water. 90

3.8 Photograph of the experimental setup used for viscosity measurements on dilute drag-reducing polymer solutions. 92

3.9 Schematic sectional view of the experimental setup used for viscosity measurements on dilute drag-reducing polymer solutions, identifying key internal components. A labeled photograph of an Ubbelöhde glass capillary viscometer. 93

3.10 Huggins-Kraemer extrapolation of the viscosity data for a sample of aqueous polyethylene oxide, measured by successive dilution at 21 °C. 96

3.11 A representative sequence of frames drawn from the high-speed (5 kfps) recording of a capillary breakup experiment on the CaBER device. The sample being tested is a semi-dilute extract ($c = 11\,\mathrm{g\,L^{-1}}$) of flaxseed mucilage in water. 101

3.12 A composite image showing the inception and development of the beads-on-a-string instability in the terminal stages of self-thinning of an elastic liquid filament. The viscoelastic liquid depicted is a solution of $0.56\,\mathrm{g\,L^{-1}}$ of PEO (nominal molar mass 5 MDa) and $0.56\,\mathrm{g\,L^{-1}}$ of SDS in a mixture comprising equal parts by volume of glycerol and water. 103

3.13 Evolution of the non-dimensional filament diameter $d(t)/d_0$ with time t, for the capillary thinning and breakup of a semi-dilute extract ($c = 11\,\mathrm{g\,L^{-1}}$) of flaxseed mucilage in water. 104

4.1 Brown flaxseed (*Linum usitatissimum*) employed in the extraction of mucilage. 'Open siphoning' of the as-extracted mucilage, possible on account of the viscoelasticity imparted by dissolved long-chain polysaccharides; the solution used in this demonstration was extracted at a seed-to-water ratio of 1:8. 110

4.2 Image sequence showing a 60 mm rheometer plate dipped in and withdrawn from concentrated flax mucilage, showing the viscous consistency of the solution and the elasticity of the liquid filament as it drains under gravity. 111

4.3 Molar mass distribution of purified flaxseed mucilage, determined using triple-detection size exclusion chromatography (SEC). 112

4.4 The intrinsic viscosity $[\eta]$ of mucilage fractions as a function of the molar mass M. 113

4.5 Reduced viscosity η_{red} of purified and desalted flax mucilage, displaying polyelectrolyte-like behavior. Fuoss plot for desalted flax mucilage, showing linear dependence of the inverse reduced viscosity $1/\eta_{\mathrm{red}}$ on the square root of the concentration $\sqrt{c}$. 115

4.6 Huggins-Kraemer plots constructed from experimental viscometry data, used to determine the intrinsic viscosity of desalted flax mucilage, flax mucilage in 0.5 M aqueous NaCl, flax mucilage at the as-extracted ionic strength, and the aqueous solution of 2 MDa PEO used in comparative studies with mucilage. 116

4.7 Intrinsic viscosity $[\eta]$ of aqueous flax mucilage measured at different ionic strengths of the solvent, corresponding to varying concentrations of dissolved salts. 118

4.8 Image sequence showing the elasto-capillary thinning of 2 MDa PEO ($c = 1460$ ppm) dissolved in 0.7 g mL^{-1} aqueous sucrose during a CaBER experiment. Also shown are magnified images of the filament midpoint recorded using the high speed camera, and used to measure the filament diameter $d(t)$ as a function of time t. 120

4.9 Evolution of the filament diameter $d(t)$ with time t for 2 MDa PEO ($c = 1460$ ppm) in 0.7 g mL^{-1} aqueous sucrose, as measured during a CaBER experiment. The relaxation time λ of aqueous PEO and flax mucilage solutions, as a function the normalized polymer concentration $c[\eta]$. 121

4.10 Experimental skin friction curves for flax mucilage and aqueous PEO solutions at identical values of $c[\eta]$, shown in Prandtl-von Kármán coordinates. 124

4.11 Shear viscosity $\eta(\dot{\gamma})$ of flax mucilage solutions as a function of the shear rate $\dot{\gamma}$, measured using a double-gap concentric cylinder geometry on the AR-G2 rheometer (temperature $T = 25$ °C). 125

4.12 The slope increment δ for aqueous PEO and mucilage solutions, as a function of the normalized polymer concentration $c[\eta]$. 126

4.13 The percentage drag reduction $\mathscr{D}$ as a function of the Reynolds number Re_s for a 285 ppm aqueous solution of PEO, and a 1:400 extract ($c = 460$ ppm) of flax mucilage. The two solutions show near identical performance in the drag-reducing regime, $\mathrm{Re}_s \geqslant 26\,000$. 128

4.14 Diminution in the percentage drag reduction $\mathscr{D}(t)$ with time t for a 285 ppm aqueous solution of 2 MDa PEO, and a 1:400 ($c = 460$ ppm) mucilage extract, under sustained shearing at $\mathrm{Re}_s = 62\,000$; and for a 10 ppm solution of 5 MDa PEO, and a 1:800 ($c = 260$ ppm) mucilage extract, under sustained shearing at $\mathrm{Re}_s = 59\,400$. 130

4.15 The percentage drag reduction $\mathscr{D}$, as a function of the Reynolds number Re_s, for PEO and flax mucilage solutions in deionized water and synthetic seawater. 131

4.16 The percentage drag reduction $\mathscr{D}$ as a function of the Reynolds number Re_s for a 1:400 aqueous extract derived from flax seeds, a 1:800 extract from chia seeds, and a 1:1600 extract from psyllium husk. 132

5.1 Water droplets deposited on the grooved and the randomly textured superhydrophobic surfaces. Scanning electron micrographs of the two surface textures. 137

5.2 Huggins-Kraemer extrapolation plots for aqueous PAM and aqueous PEO samples employed in combined frictional drag measurements. . . 140

5.3 Experimental friction curves for the smooth no-slip rotor in aqueous solutions of PAM and PEO at different polymer concentrations, showing turbulent drag reduction induced by the dissolved polymer chains. 143

5.4 The slope M_P of the polymeric friction curves in Prandtl-von Kármán coordinates, as a function of the normalized concentration c/c^* 144

5.5 Experimental friction curves for the grooved (S_G) and the randomly textured (S_R) rotors in air-saturated water, showing drag reduction induced by wall slip. The slip length b^+ for the two rotors, as a function of the shear Reynolds number Re_τ. 145

5.6 Combined drag reduction curves for the superhydrophobic grooved rotor in a 50 ppm solution of aqueous PAM. The percentage drag reduction $\mathscr{D}$ is also shown as a function of the Reynolds number Re_s. . . 147

5.7 Schematic depiction of the additive two-layer model for combined drag reduction in wall-bounded turbulence. The inset shows a magnified view of the near-wall viscous sublayer within which the composite flow boundary conditions are assumed to homogenize, yielding a uniform effective slip velocity V^+_{SLIP} perceived by the outer layers. 149

5.8 Percentage drag reduction $\mathscr{D}_C$ for the grooved rotor in aqueous PAM and PEO solutions of various concentrations, and the ratio $\mathscr{D}_C/\mathscr{D}_C^\circ$ of the actual drag reduction achieved to the ideal estimate predicted by the two-layer model. 151

5.9 Combined drag reduction data for the randomly textured rotor in 50 ppm solutions of PAM and PEO; the corresponding percentage drag reduction $\mathscr{D}$ is also shown as a function of the Reynolds number Re_s. . 153

5.10 Surface tension σ of aqueous PAM and PEO solutions as a function of the polymer concentration c. Surface tension of a binary solution of 2-butanol in water, versus the percentage volume of 2-butanol. 154

5.11 Experimentally determined slip lengths b^+ on the grooved as well as the randomly textured rotors, in a 0.5 % solution of 2-butanol. 155

5.12 Combined drag reduction estimates for the randomly textured rotor in 50 ppm aqueous PEO, re-computed based on the diminished slip length measured in the 0.5 % butanol solution. 157

A.1 Examples of oil-soluble plant biopolymers: mastic resin, dammar resin, and natural rubber latex. 170

A.2 Histogram depicting the molar mass distribution of the oil-soluble polymers in natural rubber latex. 172

A.3 Schematic sectional view of the HTTC apparatus, used for frictional drag measurements in alkanes. 175

A.4 Photograph of the HTTC apparatus, fully assembled and mounted on the AR-G2 rheometer during a flow measurement. 178

A.5 The baseline friction curve for the HTTC apparatus, obtained for a smooth no-slip rotor in dodecane at a temperature of (40.0 ± 0.5) °C; the data is represented as the non-dimensional rotor torque $G = \mathscr{T}/\rho v^2 L$ versus the Reynolds number Re. 179

A.6 The local torque exponent α as a function of the Reynolds number Re, derived from the baseline curve for the HTTC apparatus. A change in slope is observed near $\mathrm{Re}_{\mathrm{crit}} \simeq 9.9 \times 10^3$, indicating the point of transition to the featureless turbulent flow regime. 180

A.7 The baseline friction curve for the HTTC apparatus in Prandtl-von Kármán coordinates. The torque exponent α as a function of the Reynolds number Re, compared with the corresponding theoretically predicted value. 181

A.8 The baseline friction curve for the HTTC apparatus in the featureless turbulent regime, compared with the semi-empirical models of Cheng et al. (2020) and Berghout et al. (2020), evaluated for a radius ratio of $\zeta = 0.653$. 182

A.9 Experimental friction data for a $50\,\mathrm{mg\,L^{-1}}$ solution of PIB (molar mass 4.7 MDa) in dodecane, measured at $T = (40.0 \pm 0.5)\,°\mathrm{C}$. 183

A.10 Experimental friction data for a $50\,\mathrm{mg\,L^{-1}}$ solution of natural rubber in dodecane, measured at $T = (40.0 \pm 0.5)\,°\mathrm{C}$. 184

The photograph on the facing page shows the New York Fire Department's public demonstration of the use of 'slippery water' (an extremely dilute solution of a polymeric drag-reducing agent mixed into regular firefighting water) in fire engines in May 1969. The addition of the polymer yielded a 50 % increase in flow rate, and a 40–50 % enhancement in the reach of the water jet, as compared to a similar fire hose issuing plain water at the same pump operating pressure (seen in the foreground).

New York Fire Department photo, reproduced from Ref. [1], "Slippery water cuts friction loss," *Fire Eng.* **122**:48–49 (Sep 1969). Also see Fig. 2.2 on p. 35, and the discussion therein for details.

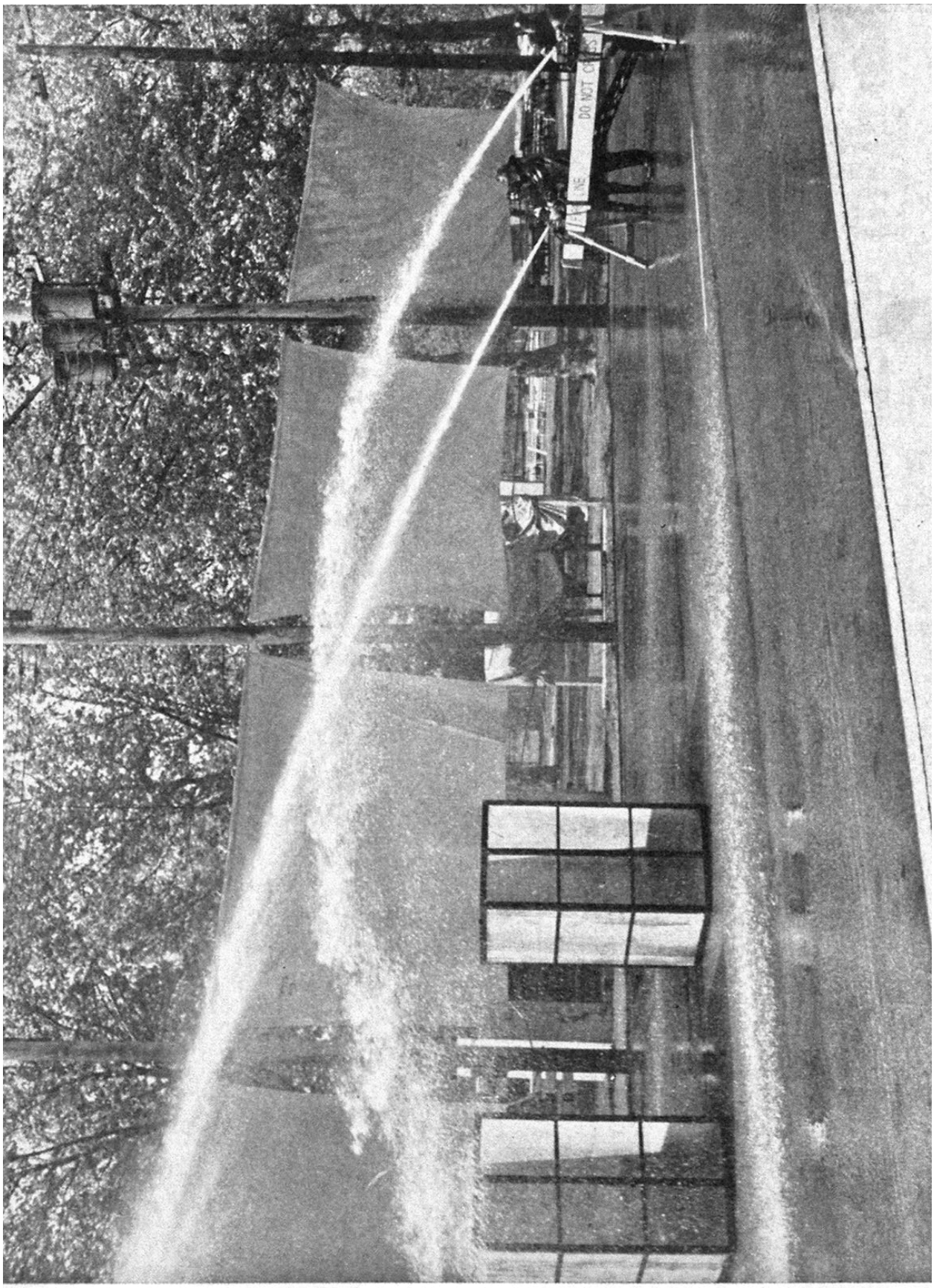
DO NOT CROSS

The space below is intentionally left blank.

1 *Introduction*

I. Background and Motivation

Wall-bounded turbulent flows constitute an essential feature of numerous real-life flow systems:[2,3] common examples include the flow of water in pipes, sewers, district heating networks and fire hoses, the transportation of crude oil via long-distance pipelines, the drag-inducing boundary layer over the hulls of ships and submarines, and even the flow of blood in the large arteries of the human body. Given its ubiquitous importance in wide-ranging engineering and industrial applications, the effective mitigation of frictional losses in turbulent flows is of considerable engineering and practical interest, with the potential to confer significant economic and environmental benefits. For example, turbulent skin friction accounts for a significant fraction of the total hydrodynamic resistance on surface and sub-surface watercraft; under routine operating conditions, about 50 % of the total drag on ships, and about 60 % of the drag on submarines, arises from frictional drag on the hull.[4] Because modern ships have carefully designed hull forms to mitigate form and wave drag, the net hydrodynamic resistance at design speed is largely due to viscous skin friction, and an estimated 60 % of the propulsive power of a typical ship is expended solely in overcoming this viscous drag.[5] Techniques to mitigate boundary layer drag, even moderately, can thus impart considerable savings in fuel consumption and operating costs, with attendant improvements in propulsive efficiency and reductions in exhaust emissions into the atmosphere. To put the latter into context, the international shipping industry is estimated to have released approximately 796 Mt of carbon dioxide in 2012, accounting for about 2.2 % of the total anthropogenic emissions for that year.[6] Furthermore, carbon emissions from shipping are projected to increase between 50 % and 250 % by 2050, concomitant with the anticipated growth in global maritime trade.[6] The development of practical drag reduction strategies is thus of contemporary relevance in the context of the global effort towards the adoption of sustainable and energy-efficient technologies.

From an academic and research perspective, sustained theoretical, experimental, and

numerical investigations into turbulent drag reduction techniques over several decades have yielded considerable insight into the physics of wall-bounded turbulence, and the mechanisms underlying its production and self-sustenance. The systematic modification of turbulence dynamics through the introduction of either dissolved polymer chains[7–15] or boundary slip,[16–21] leading to drag reduction, remains an active area of research and has witnessed resurgent interest in recent years.[22–24] This renewed focus has been driven largely by the development of novel and powerful computational tools enabling the direct numerical simulation and dynamical analysis of near-wall turbulence in unprecedented detail,[24] and in the case of superhydrophobic surfaces, by the rapid advances in microfabrication techniques and scalable surface texturing processes over the last two decades.[25] A successful mechanistic framework for the quantitative prediction of the polymeric and superhydrophobic drag reduction effects is, however, yet to be realized; this is perhaps unsurprising, given the formidable complexity of the phenomenon of turbulence itself, a challenge further exacerbated by the non-linear and often two-way interaction between polymer molecules, wall slip, and near-wall turbulent flow structures.

Active and Passive Techniques for Turbulent Drag Reduction

A number of passive and active flow interventions have been attempted in the past, with varying levels of success, as prospective techniques for drag mitigation in turbulent liquid flows;[4,22] Fig. 1.1 lists some of the more common techniques explored in the literature, particularly in the context of marine and naval applications. *Active* methods for frictional drag reduction include the injection of air bubbles[26] or high molecular weight polymers[27] into the turbulent boundary layer, and incorporating submerged air-filled recesses, or 'partial air cavities', under the hull.[28] These methods require some form of continuous input to sustain drag reduction, and become economically viable in long-haul operations only if the expense incurred in active flow modification is offset by the savings gained in fuel and operating costs;[4] they may also be suitable for naval applications that require increased vessel speed over relatively short distances, or when the need for enhanced performance takes precedence over cost. *Passive* drag reduction methods, on the other hand, do not require any form of continuous energy input, but usually produce a smaller percentage reduction in drag than active methods. For example, shark-skin inspired riblet surfaces have been extensively investigated in the literature, and are reported to reduce wall shear stress in turbulent boundary layer flows by modifying the near-wall vortex dynamics.[29] As mentioned above, superhydrophobic coatings on the hull have gained interest as a potential passive technique for skin friction reduction on ships and undersea vehicles.[4,22] However, scalable aerophilic textures that can successfully operate at the high Reynolds numbers ($\mathrm{Re} \sim 10^8$–10^9) typically encountered in marine applications are yet to

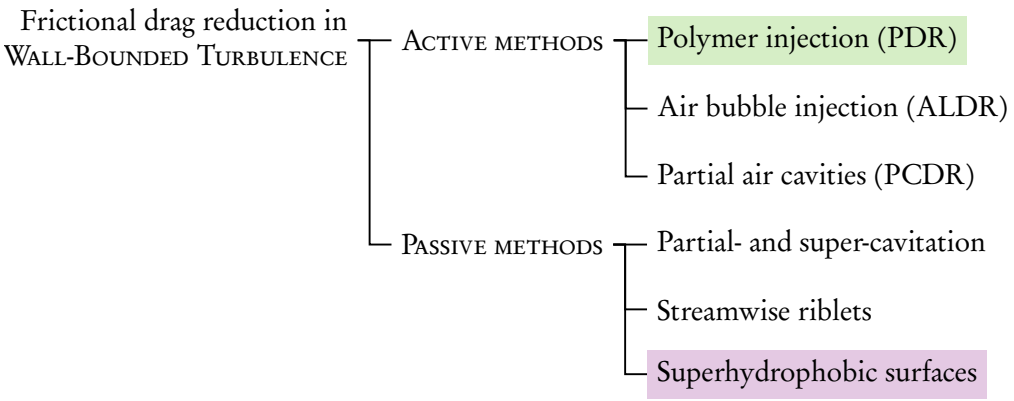

Figure 1.1. Active and passive methods for frictional drag reduction in the turbulent boundary layer around the hulls of ships, submarines and underwater projectiles. This thesis focuses on the two techniques highlighted above: polymer injection into the boundary later, and active method; and the superhydrophobic texturing of wetted solid boundaries, a passive method. Abbreviations: PDR, polymer drag reduction; ALDR, air layer drag reduction; and PCDR, partial cavity drag reduction.

be developed,[25] although encouraging developments on this front have been reported in recent years.[30] This thesis specifically focuses on two well-known methods that are yet to see practical deployment in large-scale aqueous systems, especially in marine applications: the ejection of long-chain polymers into the boundary layer, a proven and highly effective method for active drag reduction; and the superhydrophobic texturing of flow boundaries, an emerging passive technique that has shown considerable promise for the near future.

II. Research Goals and Expected Outcomes

The central focus of the author's Master's thesis was on the experimental characterization of superhydrophobic surfaces, intended for turbulent drag reduction in naval and marine applications. Specifically, this earlier study was part of a multi-institutional collaborative effort, funded by the Office of Naval Research (ONR), to develop drag-reducing textures capable of robust operation in high Reynolds number turbulent flows, and which can be feasibly scaled-up to cover large hull areas typical of real-life service requirements. To this end, a number of prototype surfaces were manufactured in collaboration with other research groups, and a bespoke Taylor-Couette (TC) apparatus was devised to enable the experimental evaluation of the drag reduction performance of these test surfaces under turbulent flow conditions.[31]

The aim of this thesis is to build on the results of the foregoing study, and further

enlarge its scope to cover a second, well-known strategy for marine drag reduction, namely, the injection of long-chain polymers into the near-wall boundary layer. Inasmuch as the fundamental principles of this canonical technique are by now well-established, the emphasis of the current study, as in the one before, is on addressing practical hurdles delaying its large-scale deployment in real-life flow systems: these include issues of cost, scalability, efficacy, biodegradability, and sustainability. The principal objectives of the research presented in this thesis can be broadly summarized as follows:

- ▷ *Investigate the drag-reducing properties of the water-soluble mucilage extracted from common seeds such as flax, chia, and psyllium*. Despite the considerable volume of scientific evidence—assembled over seven decades of sustained research effort—affirming the efficacy of polymer drag reduction techniques, its adoption in real-life seafaring vessels has been impeded by the prohibitive cost of current synthetic polymers, which has rendered their deployment on a commercial scale presently unfeasible.[4] There is thus a pressing incentive to develop cost-effective sources of drag-reducing polymers, if the full potential of this well-proven technique is to be realized. This circumstance provides the perfect opportunity where inexpensive plant-sourced biopolymers can play an impactful role, by providing a low-cost, yet equally efficacious, alternative to synthetic drag reducing polymers. Mucilage from the bran of seeds such as flax, chia and psyllium, despite being excellent sources of long chain polysaccharides,[32–36] has not been explored in any great detail in the context of turbulent drag reduction, a deficiency that has motivated a substantial part of the research focus of this thesis.

- ▷ *Quantify the effect of flow-induced degradation and salinity* on the drag reduction efficacy of mucilage biopolymers. Chain scission and the attendant diminution in drag reduction are important considerations in internal and closed-loop flow systems in which dissolved polymers are subject to sustained turbulent shear for prolonged periods. The effect of water salinity is clearly of significant concern in ocean environments, and also in enhanced oil recovery operations where the produced water is often mostly brine. Dissolved salt content has been reported to cause loss of drag reduction efficiency as well as delay the onset of drag reduction in common water-soluble polymers such as polyethylene oxide (PEO); in xanthan gum, a widely used biopolymer additive, the presence of salts induces a helix-coil transition, causing a drastic loss of drag reduction capacity.[37] A careful evaluation of the effects of solvent ionic strength on mucilage polysaccharides is thus an essential prerequisite for its successful deployment in saline environments, given that the mucilage content of many common seeds are known to comprise varying fractions of charged, polyelectrolyte-like chains.[32,34–36]

- ▷ *Explore the use of oil-soluble biopolymers as candidate drag reducing agents in hydrocarbon flows,* as a supplement to the study of seed mucilage. The extant literature on drag-reducing biopolymers has focused almost exclusively on water-soluble polysaccharides from plant, animal or bacterial sources, which are typically insoluble in oils and are hence limited to use in aqueous environments. However, turbulent drag reduction in the pipeline transport of crude oil and petroleum products is a vital area of application with vast potential for cost and energy savings; indeed, synthetic drag reducing agents (DRAs) have seen routine deployment in the oil industry in the past several decades.[38] Certain resins, latices, and plant exudates, such as natural rubber, are known to contain polymeric fractions of moderate to large molar mass,[39] and consequently merit attention as candidate sources of eco-friendly, drag-reducing chains that can complement (or potentially replace) the expensive, highly engineered synthetic agents currently used for hydrocarbon flows and biphasic water/oil systems.

- ▷ *Investigate the parallel deployment of superhydrophobic textures in conjunction with polymer additives* to enable enhanced reductions in frictional drag. As mentioned above, superhydrophobic texturing of submerged walls has emerged in recent years as a promising technique for drag reduction in turbulent aqueous flows. A thin layer of air trapped atop the roughness asperities of the superhydrophobic texture, called the *plastron*, permits the flowing liquid to partially slip over the surface, thus reducing drag.[40] The progressive development of robust and highly scalable surfaces has opened the possibility of economically modifying large surface areas, and may, in the near future, enable texturing the entire submerged hull surface of a marine vessel.[25,30] Whereas polymer additives reduce frictional drag by altering the bulk dynamics of near-wall turbulence, aerophilic surfaces reduce drag primarily by inducing an effective slip at the boundary. Inasmuch as the two drag-reducing mechanisms are fundamentally different, it is plausible that they can be employed synergistically, a question that has not been explored in the literature to date.

The anticipated outcomes of the study are therefore: (*a*) a detailed characterization of the macromolecular and rheological properties of seed mucilage, and experimental results demonstrating its viability as a drag reducing additive in turbulent flows of practical interest; (*b*) a quantitative assessment of the flow longevity of mucilage and its efficacy in saline environments, in comparison with common synthetic polymers; (*c*) the proof of concept use of natural oil-soluble polymers, specifically rubber latex, as a drag reducer in turbulent hydrocarbon flows; (*d*) the successful realization of enhanced drag reduction through joint deployment of polymer additives and superhydrophobic textures, and an empirical model to predict this combined effect; and finally, (*e*) an elucidation of the

adverse impact of the surface activity of dissolved polymers on the slip over randomly textured superhydrophobic walls. Hopefully, these ideas will help address some of the current challenges facing the widespread adoption of drag reduction strategies in real-life flow systems, and contribute meaningfully to the ongoing scientific effort to gain deeper insight into the physics of polymeric and slip-mediated drag reduction phenomena.

III. Organization of Thesis Contents

Chapter 1 provides a contextual overview of the background and motivation for this study, and outlines the key goals and expected research outcomes of the thesis.

Chapter 2 reviews extant literature on the two well-known drag reduction methods that form the central focus of this thesis—polymer additives and plastron-stabilizing superhydrophobic textures. The chapter begins with a brief historical perspective of polymer drag reduction, followed by a summary of experimental phenomenology and classical mechanistic descriptions of the drag reduction mechanism. Recent developments in the field, including key physical insights gained from numerical investigations, are mentioned where appropriate. Fundamental concepts in surface wetting, superhydrophobicity, and plastron-mediated slip are then reviewed, and a quick survey of the superhydrophobic drag reduction literature is presented. Basic terminology and flow variables related to turbulent flows and experimental drag reduction measurements are defined at relevant locations in the text, and referred to in the remainder of the thesis.

Chapter 3 describes experimental techniques and procedure employed for frictional drag measurements in turbulent flow, and for the rheological characterization of dilute polymer solutions. The design, operation, and baseline characterization of the bespoke TC apparatus, utilized for the evaluation of drag-reducing polymers and superhydrophobic textures, are discussed. Afterwards, the preparation of aqueous polymer solutions, the determination of the intrinsic viscosity by means of capillary viscometry, and the inference of polymer relaxation time using capillary breakup extensional rheometry (CaBER), are detailed.

Chapter 4 explores the use of epidermal polysaccharides, or *mucilage*, extracted from flax seeds as a cost-effective and eco-friendly substitute for synthetic polymers in large-scale drag reduction applications. The extraction of mucilage polysaccharides and the experimental characterization of its molecular and rheological properties are described. Results from turbulent drag measurements in the TC apparatus are presented which show that the as-extracted mucilage offers drag reduction efficacy

comparable to common synthetic polymers while incurring a significantly lower raw material cost. Practical considerations relating to polymer longevity and use in saline environments are discussed.

Chapter 5 demonstrates the concurrent use of polymers and superhydrophobic walls to achieve enhanced drag reduction in turbulent aqueous flows. The combined drag reduction effect is successfully demonstrated in the TC apparatus for common drag-reducing polymers paired with regular as well as irregularly textured superhydrophobic walls. An empirical two-layer model is proposed which leads to an additive friction law that accurately predicts the overall drag reduction efficacy of polymer-surface pairs with known individual frictional properties. The influence of surface activity of polymer chains on plastron-induced wall slip is investigated.

Chapter 6 concludes the thesis with a summary of the overall study, its outcomes and anticipated impact, and ends with a brief outlook on potential avenues for future exploration and research.

Appendix A reports exploratory investigations into the utility of oil-soluble natural polymers for drag reduction in turbulent hydrocarbon flows. The construction and baseline flow characterization of a redesigned TC apparatus, capable of turbulent drag measurements in alkanes at elevated temperatures, are discussed. Preliminary experimental results are presented that validate the use of polyisoprene in natural rubber latex as a drag-reducing polymer for oil-based applications.

Image Credits and Attribution are provided for all externally sourced photographs reproduced in this thesis.

References are numbered sequentially in the order of their first appearance and are listed at the end of the text.

The space below is intentionally left blank.

2 *Drag Reduction in Wall-Bounded Turbulent Flows: A Review*

I. Drag Reduction Using Polymer Additives

A. *A Brief Introduction to Polymer Drag Reduction*

In 1948, B. A. Toms observed that the addition of small quantities of high molar mass polymers can yield significant reductions in the frictional pressure drop arising from turbulent flows through pipes.[41] In his experiments, a dilute solution (0.25 % by weight) of polymethyl methacrylate in monochlorobenzene yielded friction factors that were smaller by as much as 50 % in comparison to that of the pure, unmodified Newtonian solvent in the turbulent flow regime. Similar observations were made by K. J. Mysels, who reported in 1949 that gasoline thickened with various aluminum soaps—an incendiary agent more commonly known as Napalm—showed a much smaller frictional loss in turbulent pipe flow than pure gasoline,[42,43] contrary to what one would intuitively expect. The reduction in frictional drag in wall-bounded turbulent flows caused by dissolved polymer additives is referred to as polymer drag reduction (PDR), or the "Toms' effect" in the literature, and has been extensively studied by researchers since its discovery in the late 1940s. Even after seventy years of experimental, theoretical and (more recently) computational investigations, polymer drag reduction continues to remain an active area of research, and has garnered renewed interest in recent times.

The most striking aspect of polymer-mediated drag reduction is, perhaps, its efficacy; small concentrations of high polymers, as low as 5–10 ppm, are often sufficient to cause significant alterations in the near-wall turbulence dynamics, yielding appreciable drag reductions of the order of 20–40 % that seem incommensurate with the sparse quantity of additives used.[44,45] These solutions are so dilute that the polymer contribution to the zero shear rate viscosity is often too small to measure using all but the most sensitive rotational rheometers. In more concentrated polymer solutions, asymptotic drag reduction levels as large as 70–80 % have been observed in experimental studies.[27,44]

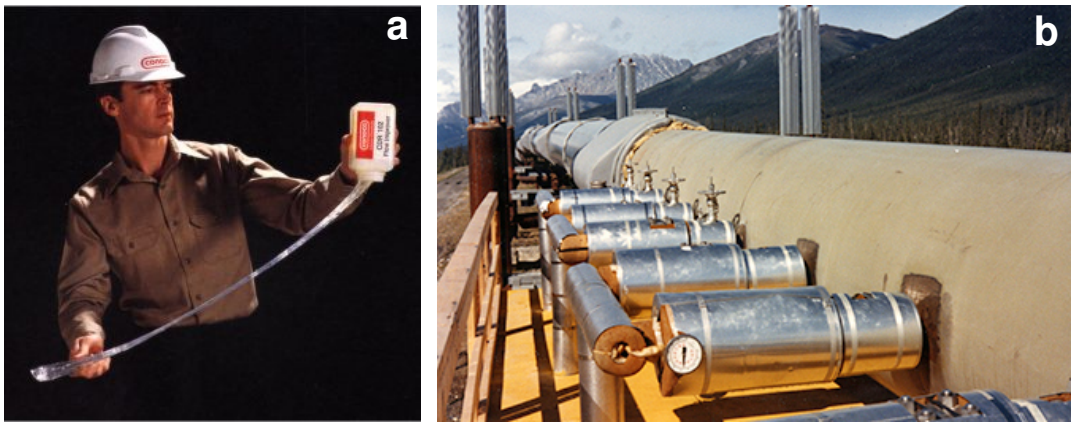

FIGURE 2.1. (a) A high molar mass gel-type DRA (CDR 102, Conoco) used for drag reduction in crude oil pipelines. (b) DRA injection ports along the Trans-Alaska Pipeline System (TAPS). The injected polymer forms an elongated strand that stretches downstream of the ports, dissolving gradually into the crude oil inside the pipe. For image sources and attribution, see p. 185.

The small concentration of polymer additives required to achieve practicable levels of drag reduction immediately suggests a number of potential cost- and energy-saving applications in real-life flow systems, ranging from the internal flow of liquids through transport and process pipelines, to the external boundary layer flow around the hulls of ships and submarines—in short, wherever a reduction in wall shear stress in turbulent flows is desired. Indeed, the utility of polymeric drag-reducing agents has, over the years, been explored or demonstrated in a diverse array of turbulent flow applications, including their use as flow enhancers in pipelines, sewers, district heating networks, field irrigation systems, and hydraulic fracturing fluids,[46,47] as frictional drag reducers for ships and submarines,[4,44,48] and even as intravenous hemorheological modifiers that inhibit atherosclerosis or aid in resuscitation from hemorrhagic shock.[49–52] For instance, drag reducing polymers have been utilized for mitigating head losses in several long distance pipeline networks around the world, primarily in the transport of crude oil. A successful case in point is the Trans-Alaska Pipeline System (TAPS), where the injection of high molecular weight polymeric drag-reducing agents (or DRAs) has been used since 1979 to increase the flow rate of crude oil, without the need for additional pumping stations[38] (see Fig. 2.1). Careful engineering and optimization of the injected polymer solution has enabled increases in crude oil flow rates of up to 33 %, using dissolved polymer concentrations as low as 1 ppm.[38] Water-soluble polymers such as polyethylene oxide (PEO) have similarly been tested for firefighting applications, to mitigate pressure losses in the fire hose and thereby enhance the reach and discharge of the ejected water stream.[1,53] The

FIGURE 2.2. NYFD demonstrates the use of "slippery water" in fire engines, May 1969. The polymer solution produced a more coherent jet, and reached 40–50 % farther than the plain water jet seen prematurely fragmenting in the foreground. For image source and attribution, see p. 185.

New York Fire Department held a public demonstration of the use of "slippery water" (an extremely dilute solution obtained by mixing high molar mass PEO into regular firefighting water) in fire engines in May 1969; the addition of the polymer resulted in a 50 % increase in flow rate and a 40–50 % improvement in the reach of the water jet, in comparison to a similar fire hose issuing plain water at the same pump operating pressure[1] (see Fig. 2.2).

Besides their use in pipe flows, polymer additives have also been investigated as a potential strategy for reducing skin reduction drag on marine and underwater vessels. As early as 1965, dilute polymer solutions were being used in towing tanks to lower the viscous resistance and obtain a simultaneous matching of both the (effective) Reynolds and Froude numbers during ship model tests.[54] Experiments conducted in towing tanks as well as water tunnel facilities have demonstrated that the injection of a concentrated polymer stock solution into the near-wall region of a turbulent boundary layer can reduce frictional resistance by up to 75 %, which can potentially translate into substantial savings in propulsive power requirements and fuel costs.[27] Ablative polymer coatings that dissolve gradually into the flow, applied to the nose of submerged bodies, have also been studied and demonstrated experimentally to reduce drag.[55] In 1971, full scale trials were performed on a 140 feet long coastal minesweeper, the *HMS Highburton* [Fig. 2.3(a)],

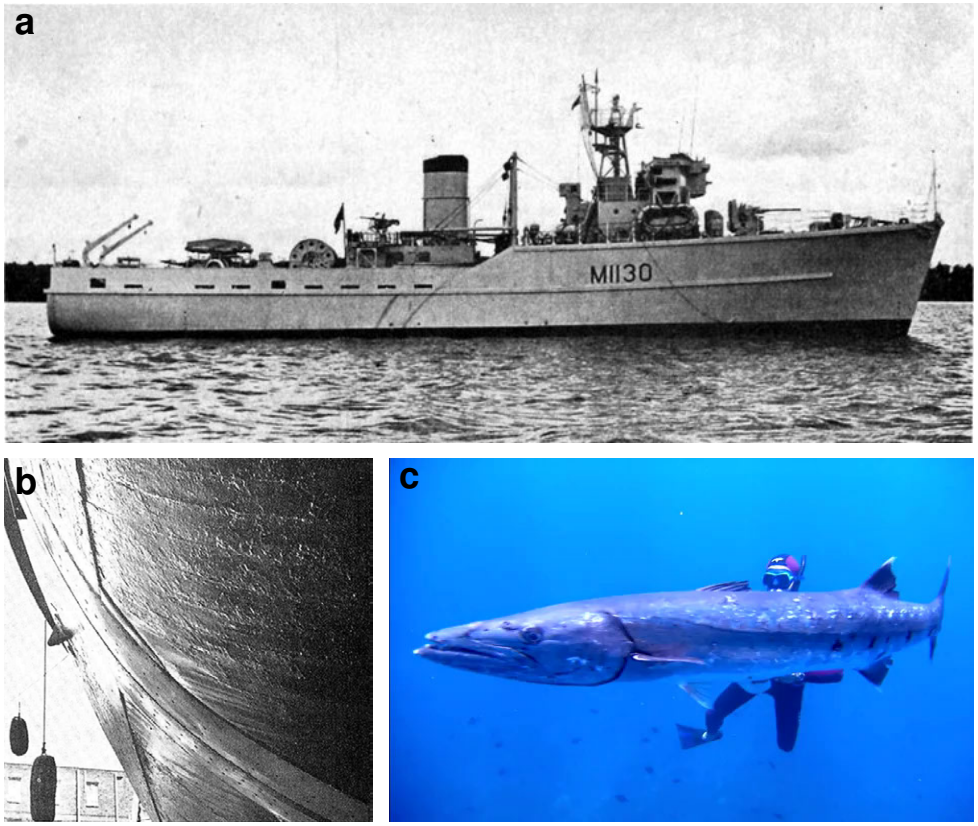

FIGURE 2.3. (a) The *HMS Highburton*, a Royal Navy Ton-class minesweeper, as photographed in 1956. (b) Polymer ejection slot on the hull of the *HMS Highburton*, 0.07 inches wide and located 35 feet aft of the bow. A second slot was located further forward, 5 feet aft of the bow. (c) The Pacific barracuda, *Sphyraena argentea*. Note the diver in the background for scale. Image sources and attribution can be found on p. 185.

during which a concentrated stock solution of 4 MDa PEO was ejected through slots in the hull to produce a nominal polymer concentration of 10 ppm in the boundary layer [see Fig. 2.3(b)]. Even with the less than ideal weather conditions during the test and the uneven mixing of the polymer in the boundary layer, a net reduction of 12.7 % in total drag, and 17 % in diesel fuel consumption, were realized.[48] In the same vein, successful examples of boundary layer drag reduction also can be found in nature, promoted by the epidermal mucus (slime) of several species of fast-swimming fish.[56,57] The slime of the Pacific barracuda [*Sphyraena argentea*, see Fig. 2.3(c)], for instance, has been shown to comprise a high molar mass biopolymer that yields drag reductions of up to 63 % at fast swimming speeds, for concentrations as low as 12 ppm.[56]

From a research perspective, experimental and computational investigations into polymer drag reduction have yielded considerable insight into the physics of viscoelastic and elastoinertial turbulence, and of its self-sustaining mechanisms. Attempts at a simple theoretical explanation of polymer drag reduction have so far been thwarted by the formidable complexity of the phenomenon of turbulence itself, which is further exacerbated by the complex two-way interaction between polymer molecules and turbulent flow structures. With the rapid growth of computing power and computational resources in modern times, we have begun to rely on powerful tools like direct numerical simulations (DNS) to obtain increasingly detailed insights into the influence of dissolved polymer chains on the structure and dynamics of near-wall coherent structures. Beginning in 1997 with the pioneering work of Sureshkumar, Beris and Handler,[58] researchers have performed direct numerical simulations of wall-bounded turbulent flow of dilute polymer solutions, using relatively simple constitutive equations (such as the 'finitely extensible non-linear elastic' model with Peterlin closure, or FENE-P for short) to model polymer conformation and viscoelastic behavior. However, the use of more fine-grained models such as the freely jointed bead-rod chain (FJC), which possess a greater number of internal degrees of freedom, continues to remain computationally prohibitive.

B. *The Phenomenology of Drag Reduction*

In the years immediately following the first published accounts of polymer drag reduction in 1949,[41,42] several research groups embarked on careful experimental measurements of the gross flow behavior of dilute polymer solutions in the turbulent regime, primarily in circular pipes; by the 1970s, a large corpus of empirical data had been assembled for a variety of polymer-solvent combinations at different concentrations, and the basic phenomenology of the polymer-mediated drag reduction effect was well-established. An extensive survey of the drag reduction literature and the experimental data available at the time may be found in two comprehensive review articles written on the topic, first by Hoyt (1972),[44] and later by Virk (1975).[59] The various polymeric species investigated in these early drag reduction studies include solutions of polyethylene oxide (PEO), polyacrylamide (PAM), carboxymethylcellulose (CMC), xanthan gum (XG) and guar gum (GG) dissolved in water, solutions of polydimethylsiloxane (PDMS) and polymethyl methacrylate (PMMA) in toluene, polyisobutylene (PIB) dissolved in cyclohexane, and cis-polyisoprene (PIP) dissolved in acetonitrile.[44,59] These early studies showed that the basic phenomenology of drag reduction remains quite similar across different polymer additives, regardless of their individual chemical structure; the drag reduction effect results purely from the dynamics of the dissolved macromolecules, which, in turn, is dictated by the size, conformation, and rigidity of the individual polymer chains in solution. The

remainder of this section aims to provide a brief outline of the typical flow phenomena observed in experimental studies involving drag-reducing polymer solutions.

Flow Geometry

The flow configuration employed most frequently in the drag reduction literature is the fully-developed, pressure-driven flow through circular pipes and channels; pipe flows are commonly used in experimental studies, whereas rectangular channels, often with periodic boundary conditions enforced in the streamwise and spanwise directions, usually serve as the computational domain in most DNS investigations.[24,59] The flow may be set up to maintain either a constant flow rate, or a constant average pressure drop per unit length. Besides pipes and channels, other flow setups have also been used in drag reduction studies, albeit less frequently: examples include plane Couette[7,8,60–63] and Taylor-Couette flows[64–67] (which refer, respectively, to the wall-driven flow inside a channel with a moving wall, and that in the annulus between concentric rotating cylinders), zero pressure gradient boundary layers[27,68,69] (which form adjacent to a stationary wall in contact with a uniform outer flow), and rotating disk apparatuses[70–76] (in which the flow is generated by a circular disk rotating inside a fluid-filled enclosure).

Flow Variables and Turbulent Inner Scales

The primary non-dimensional group characterizing fluid flows that are governed by inertia and viscous stresses is the *Reynolds number* Re, defined as

$$\mathrm{Re} = \frac{\rho V l}{\eta}. \tag{2.1}$$

Here V is a characteristic velocity scale indicative of the overall speed of the flow, l is a characteristic length scale representing spatial gradients in the velocity field, and ρ and η respectively denote the density of the fluid and its (dynamic) viscosity. The choice of the specific velocity and length scales used in defining the Reynolds number, for the various flow configurations mentioned above, is largely dictated by convention. The velocity scale V is usually set equal to the bulk average velocity $\overline{V}$ for pressure-driven flows (such as pipe, channel and duct flows), the freestream speed V_∞ for boundary layers, or the wall speed V_w in the case of Couette, Taylor-Couette, and rotating disk flows that are driven by a moving boundary. Similarly, the length scale l is typically chosen to be the diameter D for circular pipes, the half-height H for channels, the inter-wall gap d for Couette and Taylor-Couette geometries, the disk radius R for rotating disks, and the downstream distance x for near-wall boundary layers. For Newtonian liquids, the

viscosity η is a material property which, at constant temperature, remains independent of the flow conditions. However, solutions of most polymers are non-Newtonian, and except at very dilute concentrations, typically exhibit *shear thinning* whereby their steady shear viscosity $\eta(\dot{\gamma})$ decreases with increasing shear rate $\dot{\gamma}$. This variation in the solution viscosity with shear rate is often modeled using empirical fits, such as to the 5-parameter Carreau-Yasuda equation[77]

$$\eta(\dot{\gamma}) = \eta_\infty + (\eta_0 - \eta_\infty)[1 + (\lambda\dot{\gamma})^a]^{(n-1)/a} \tag{2.2}$$

where the constants λ, n, a, η_0, and η_∞ for a given polymer solution are obtained by regression to the experimental viscometric data. Inasmuch as dissolved polymer molecules may undergo both shear-induced thinning as well as significant extensional thickening in the turbulent near-wall region, there is some degree of incertitude on the appropriate choice of the viscosity η to be used in defining the Reynolds number; different authors have, in the past, variously set it equal to the viscosity η_0 at zero shear rate,[66,78] the limiting viscosity η_∞ at infinite shear rate,[66] or the shear-rate-dependent viscosity $\eta(\dot{\gamma}_w)$ corresponding to the nominal shear rate $\dot{\gamma}_w$ at the wall.[79–81] Lumley (1969)[82] recommended the stricter criterion of using the viscosity η_s of the pure Newtonian solvent, and this convention will be adopted in the remainder of this thesis. Furthermore, this definition enables a straightforward evaluation of the drag reduction efficacy of polymer solutions in comparison to the unmodified solvent at the same flow rate or wall speed, which is often the most practically relevant baseline case from the perspective of engineering applications.

In experiments and numerical studies alike, the flow-induced frictional drag at the wall is usually expressed as a non-dimensional *friction factor* C_f, given by the ratio of the time- or ensemble-averaged wall shear stress τ_w to the inertial scale $(1/2)\rho V^2$ of the bulk flow:

$$C_f = \frac{\tau_w}{\frac{1}{2}\rho V^2}. \tag{2.3}$$

In the case of fully developed flow through circular pipes, experimental friction data are sometimes reported in terms of the *Darcy friction factor* f, which appears in the empirical Darcy-Weisbach equation[83]

$$\frac{\Delta P}{L} = \frac{f}{D} \cdot \frac{1}{2}\rho \overline{V}^2 \tag{2.4}$$

that relates the pipe diameter D, the bulk flow velocity $\overline{V}$, and the average frictional pressure drop per unit length $\Delta P/L$. A steady-state momentum balance of the form $\Delta P\left(\pi D^2/4\right) = \tau_w(\pi D L)$ shows that the two friction factors as defined above simply differ by a constant factor of 4:

$$f = 4\,C_f. \tag{2.5}$$

The percentage drag reduction $\mathscr{D}$ is given by

$$\mathscr{D} = \frac{\tau_{w,N} - \tau_w}{\tau_{w,N}} \cdot 100\,\% \tag{2.6}$$

where τ_w and $\tau_{w,N}$ denote, respectively, the frictional wall shear stress exerted by the polymer solution and the corresponding pure solvent at the same Reynolds number Re. (The subscript 'N' here refers to the 'Newtonian' solvent used as the baseline.) Using Eq. 2.3, $\mathscr{D}$ may also be expressed as

$$\mathscr{D} = \frac{C_{f,N} - C_f}{C_{f,N}} \cdot 100\,\% \tag{2.7}$$

A key feature of wall-bounded turbulence is the attendant separation of scales between the *outer* bulk flow and the *inner* near-wall region; whereas the 'global' length and velocity scales, V and l, characterize the gross outer flow, the dynamics in the near-wall region are governed by *inner scales* derived solely from local flow quantities: namely, the shear rate $\dot{\gamma}_w$, and the corresponding frictional shear stress $\tau_w = \eta\,\dot{\gamma}_w$, at the wall.[2,3] Combining the wall shear stress τ_w with fluid properties ρ and η yields a unique inner velocity scale, known as the *friction velocity*

$$u_\tau = \sqrt{\frac{\tau_w}{\rho}}\,, \tag{2.8}$$

and an inner length scale, also called the *viscous length scale* or simply the 'wall unit,'

$$\delta_\nu = \frac{\eta}{\rho\,u_\tau} = \frac{\eta}{\sqrt{\rho\tau_w}}\,. \tag{2.9}$$

Analogous to the Reynolds number Re defined using the outer velocity V, we define the *shear Reynolds number* Re_τ based on the friction velocity u_τ:

$$\mathrm{Re}_\tau = \frac{\rho u_\tau l}{\eta} \tag{2.10}$$

Note that the outer length scale l still appears in the above definition, since using the viscous length scale δ_ν gives the trivial result $\mathrm{Re}_\tau = 1$. Equations 2.8, 2.9, and 2.10 together yield

$$\mathrm{Re}_\tau = \frac{l}{\delta_\nu} = \frac{l\sqrt{\rho\tau_w}}{\eta}\,. \tag{2.11}$$

The first equality shows that the shear Reynolds number Re_τ is equivalent to the size l of the flow geometry (i.e., the pipe diameter, channel half-height, or Taylor-Couette

cell gap) expressed in units of the viscous length scale δ_ν characterizing the near-wall flow. From the second equality, it follows that for a given fluid and flow geometry, Re_τ is a function only of the wall shear stress τ_w, in the same way as Re depends only on the flow velocity V. As is the case with the Reynolds number, differing conventions exist regarding the choice of the viscosity η used to define the shear Reynolds number in polymeric flows. For reasons to be explained in Chapter 4, the zero shear rate viscosity η_0 has been used to compute Re_τ for all experimental data involving polymer solutions presented in this thesis.

In turbulent flow experiments, it is customary to present skin friction measurements in the form of *Prandtl-von Kármán plots*, in which the non-dimensional velocity $V^+ = V/u_\tau$ is shown against the shear Reynolds number Re_τ in semi-logarithmic axes. Figure 2.4 shows three different representations of the same frictional data, obtained from turbulent pipe flow experiments using water and an aqueous solution of PEO. In panel (c), the friction curves can be seen graphed in Prandtl-von Kármán coordinates; the quantities along the two axes are equivalent to V^+ and Re_τ, since Eqs. 2.1, 2.3, and 2.11 together yield,

$$\sqrt{2}\,\mathrm{Re}_\tau = \mathrm{Re}\sqrt{C_f}\,, \quad \text{and} \quad \frac{V^+}{\sqrt{2}} = \frac{1}{\sqrt{C_f}}\,. \tag{2.12}$$

Empirical Observations and Flow Regimes

The fundamental interaction underlying polymer-mediated drag reduction is the repeated elongation and relaxation of dissolved macromolecules in the near-wall turbulent flow structures. In a good solvent, flexible linear polymers at equilibrium adopt a random coil conformation,[84] from which they are perturbed by externally imposed velocity gradients. If the external forcing is removed, these stretched chains revert to their equilibrium coiled configurations via intramolecular conformational changes driven by thermal fluctuations. The overall rate of this process is determined by the slowest internal mode of the polymer chain, involving the entropic rearrangement of the greatest number of 'chain links' (or more accurately, Kuhn steps). The time scale of this longest relaxation mode is often referred to simply as the *relaxation time* λ of the dissolved polymer, and depends both on the entropic potential driving the relaxation ($\propto k_B T$, where k_B is the Boltzmann constant and T the solution temperature), as well as the molecular friction resisting it (which, in turn, is proportional to the solvent viscosity η_s).[84]

Viscoelastic flows are thus governed by the interplay between the intrinsic relaxation time of the dissolved polymer chains, and the time scale of deformation of these chains by the flow; the ratio of the two time scales is given by the non-dimensional *Weissenberg*

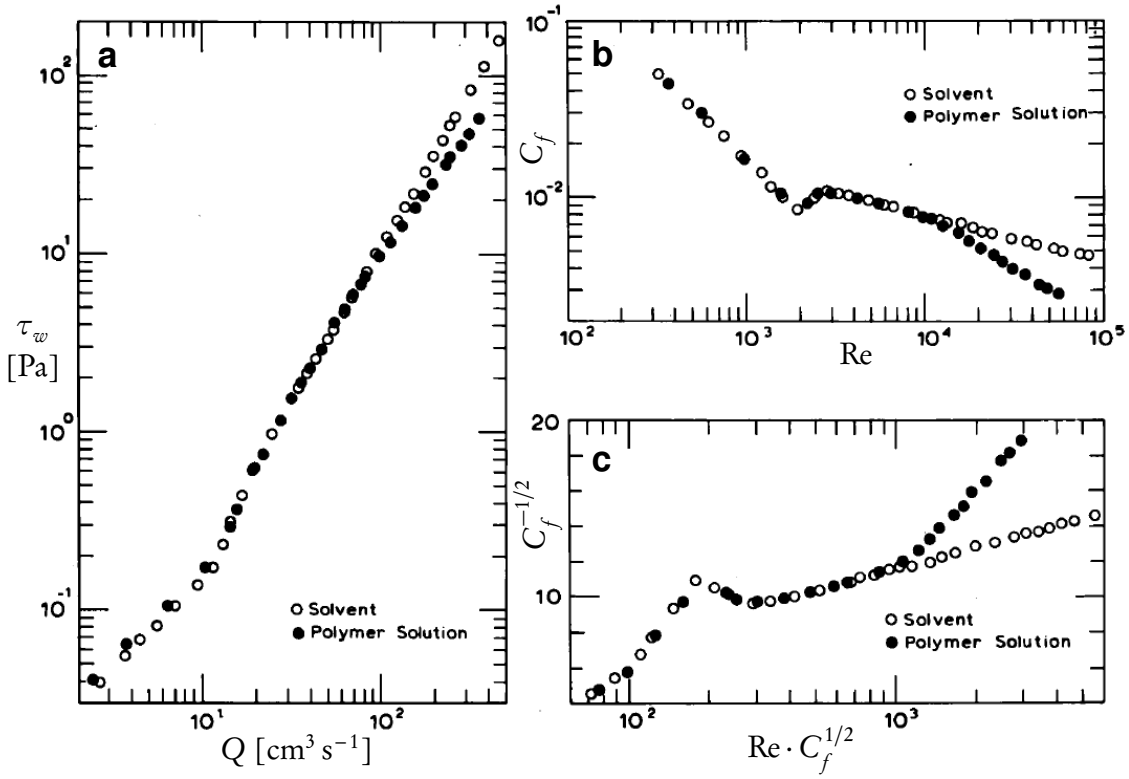

FIGURE 2.4. Empirical friction curves for the flow of pure water and an aqueous PEO solution through a circular pipe. The data corresponds to pipe diameter $D = 8.46\,\mathrm{mm}$, PEO molar mass $M_w = 570\,\mathrm{kDa}$, and concentration $c = 296\,\mathrm{ppm}$. The same data is represented variously as plots of (a) the wall shear stress τ_w versus the volumetric flow rate Q, (b) the friction factor C_f versus the Reynolds number Re, and (c) in Prandtl-von Kármán coordinates. Reproduced from Ref. [59].

number, defined as

$$\mathrm{Wi} = \lambda \dot{\gamma}, \tag{2.13}$$

where λ is the relaxation time of the polymer, and $\dot{\gamma}$ represents a characteristic shear rate indicative of the strength of the flow field. For Wi << 1, relaxation outpaces flow-induced deformation; polymer chains, passively advected by the flow, remain close to their equilibrium conformations, and viscoelastic effects are largely indiscernible. The limit $\mathrm{Wi} = 0$ corresponds to purely viscous Newtonian flow. Conversely, flows with Wi >> 1 typically exhibit significant elastic effects or even flow instabilities arising from strong elongation of polymer chains.[85]

The Wi–Re plane, shown schematically in Fig. 2.5, provides a convenient visualization of the various flow regimes encountered in turbulent flow experiments using polymer solutions. In numerical studies, a systematic exploration of this parameter space is usually possible since Wi and Re may be varied independent of each other. Experimental measurements, on the other hand, typically involve varying either the wall speed or the flow rate, entailing concurrent changes in both Wi and Re. Indeed, setting $\dot{\gamma} = V/l$ in the definition of the Weissenberg number, Eq. 2.13, we see that the ratio

$$\frac{\mathrm{Wi}}{\mathrm{Re}} = \frac{\lambda V}{l} \frac{\eta}{\rho V l} = \frac{\lambda \eta}{\rho l^2} \tag{2.14}$$

remains constant for a given polymer solution and flow geometry, independent of the imposed flow velocity V; an 'experimental path' on the Wi–Re plane thus corresponds to a straight line trajectory passing through the origin.[9,11,23,24] The quantity on the right-hand side of Eq. 2.14 is often termed the *elasticity number*,[23]

$$\mathrm{El} = \frac{\lambda \eta}{\rho l^2}\,. \tag{2.15}$$

Alternatively, if the wall shear rate $\dot{\gamma}_w = \tau_w/\eta$ is used instead to define the shear Weissenberg number $\mathrm{Wi}_\tau = \lambda \dot{\gamma}_w$,[45] it follows from Eq. 2.11 that the ratio

$$\frac{\mathrm{Wi}_\tau}{\mathrm{Re}_\tau^2} = \frac{\lambda \tau_w}{\eta} \frac{\eta^2}{\rho \tau_w l^2} = \frac{\lambda \eta}{\rho l^2} = \mathrm{El} \tag{2.16}$$

is now independent of the flow conditions, and therefore represents the invariant quantity along a given experimental path.

Consider a typical flow experiment using polymer solutions, represented by the path labeled ABC in Fig. 2.5(a); the corresponding friction curve is sketched schematically in Fig. 2.5(b) in Prandtl-von Kármán coordinates. For simplicity, the example of pressure-driven flow through pipes has been used in the discussion below to illustrate key aspects

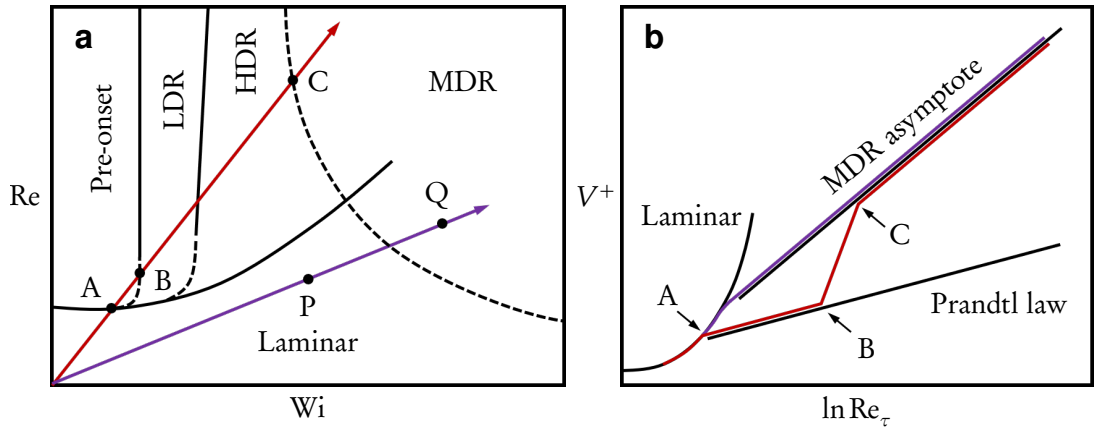

FIGURE 2.5. Schematic representation of viscoelastic flow regimes in (a) the Wi–Re plane, and (b) in Prandtl-von Kármán coordinates. The red and purple curves denote two distinct experimental paths—labeled ABC and PQ, respectively—corresponding to different elasticity numbers El. Figure adapted from Refs. [24] and [9].

of the drag reduction effect; the results remain qualitatively similar for experiments performed in other flow configurations. As the path ABC is traversed experimentally by increasing the solution flow rate, the following regimes are sequentially observed:

— *Laminar flow and the transition to turbulence.* The addition of polymers has no appreciable effect on the flow behavior in the laminar regime, and the friction curve follows the usual Hagen-Poiseuille relation for Newtonian fluids, given by

$$C_f = \frac{16}{\mathrm{Re}} \,. \tag{2.17}$$

As the flow rate is increased, a transition to turbulent flow occurs when a critical value of the Reynolds number is reached, marked by the point A in Fig. 2.5. For solutions of low molar mass polymers or in flows through large diameter pipes [i.e. for small elasticity numbers $\mathrm{El} = \lambda\eta/\rho D^2$, corresponding to steep experimental trajectories in Fig. 2.5(a)], the polymer additive has no apparent influence on the laminar-to-turbulent transition;[9,59] turbulent flow commences more or less at the same value of the critical Reynolds number as the Newtonian flow, namely $\mathrm{Re}_{\mathrm{crit}} \sim 2100$. At larger elasticity numbers (for example, in experiments involving small diameter pipes, high molar mass polymers, or concentrated solutions), transition to turbulence is delayed or may even be bypassed altogether[9] (see the discussion at the end of this section).

— *Onset of drag reduction.* Drag reduction does not appear immediately on transition of the flow to the turbulent regime. In fact, the dissolved polymer has no discernible effect on the flow dynamics until a threshold value of the Weissenberg number is reached, corresponding to the point of *onset* marked B in Fig. 2.5. In the 'pre-onset' regime AB, flow statistics are indistinguishable from that of Newtonian turbulence,[24] and the frictional curve is well described by the Prandtl friction law for turbulent (Newtonian) flow through pipes:[59]

$$\frac{1}{\sqrt{C_f}} = 4.0 \log_{10}\left(\mathrm{Re}\sqrt{C_f}\right) - 0.4\,. \tag{2.18}$$

The onset of polymeric effects at point B is marked by a well-defined departure of the viscoelastic friction curve away from the Newtonian baseline; notice that an upward deviation on the Prandtl-von Kármán plot indicates a decrease in the friction factor (cf. Eq. 2.12), signifying drag reduction. The onset boundary roughly coincides with the point where the time scale of flow-induced deformations in the near-wall region becomes comparable to the intrinsic relaxation time of the dissolved polymer. Indeed, an abrupt elongation of coiled polymer chains can occur in regions of strong extensional flow, where the local Weissenberg number $\mathrm{Wi}_\varepsilon = \lambda\varepsilon \geqslant 1$; here ε is the principal Lyapunov exponent of the velocity field, equal to the mean logarithmic rate of separation of infinitesimally close Lagrangian trajectories.[86–88] The above *coil-stretch transition* of polymer chains usually entails drastic rheological consequences including a substantial increase in the extensional viscosity, and is expected to produce perceptible alterations in turbulence dynamics and the near-wall coherent flow structures. Insofar as $\varepsilon \sim \dot{\gamma}_w$, the characteristic shear rate of the near-wall flow, we anticipate the criterion for drag reduction onset to be[24]

$$(\mathrm{Wi}_\tau)_{\mathrm{ons}} = \lambda\left(\dot{\gamma}_w\right)_{\mathrm{ons}} \sim 1. \tag{2.19}$$

In practice, a slightly larger value of $(\mathrm{Wi}_\tau)_{\mathrm{ons}} \simeq 5\text{–}10$ has been inferred from DNS investigations.[24]

— *Intermediate drag reduction regime.* As the Reynolds number is increased beyond the onset point, the friction curve steadily diverges from the Newtonian baseline along the path BC, and the percentage drag reduction $\mathscr{D}$ increases. The segment BC on the Prandtl-von Kármán plot becomes steeper as the elasticity number El is increased (i.e., when higher molar mass polymers or greater concentrations are employed). Although no conspicuous changes are observed in either the gross flow behavior or the friction curve with increasing Re, a close examination of the velocity profile and flow statistics reveals the existence of two distinct drag reduction

regimes along the path BC; these are designated the LDR and HDR regimes (short for *low* and *high drag reduction*, respectively) on the Wi–Re plane in Fig. 2.5(a). The LDR regime is characterized by an enlarged buffer layer to which drag reduction effects are confined; the overlying inertial layer is consequently displaced farther from the wall, but is otherwise unchanged and conforms to the von Kármán (Newtonian) logarithmic profile. By contrast, viscoelastic effects in the HDR regime operate across the full width of the boundary layer, altering most regions of the flow except the viscous sublayer; a von Kármán type log-law region, as seen in LDR, is thus no longer detectable. The differentiation of LDR and HDR states was first proposed by Warholic, Massah and Hanratty (1999),[80] and has been subsequently confirmed by numerous computational and experimental studies in the literature.[24] The transition between the two regimes is marked by distinctive changes in the flow statistics, and usually occurs at drag reduction levels near $\mathscr{D} \simeq 30$–$40\,\%$. It has been suggested that the LDR-HDR boundary signals a fundamental shift in the underlying drag reduction mechanism, arising from qualitative changes in the dynamics of near-wall coherent structures.[89] This hypothesis is further borne out by supporting evidence emerging from very recent numerical investigations.[90,91]

— *Maximum drag reduction* (*MDR*). At even higher Reynolds numbers, a second change in slope of the friction curve is observed [at point C in Fig. 2.5(b)] where it finally joins the *maximum drag reduction asymptote* (or *Virk's asymptote*), discovered by Virk et al. (1970)[78] and described by the empirical correlation

$$\frac{1}{\sqrt{C_f}} = 19.0 \log_{10} \mathrm{Re} \sqrt{C_f} - 32.4 \,. \tag{2.20}$$

Intriguingly, this asymptotic behavior is seen to be a universal feature, independent of the specific choice of the polymer used, its molar mass, or its concentration in the solution;[59] the frictional drag C_f in the MDR regime is a function only of the Reynolds number Re (or Re_τ), and is intermediate between that of laminar flow (L) and Newtonian turbulence (NT): $C_f^{\mathrm{L}}(\mathrm{Re}_\tau) < C_f^{\mathrm{MDR}}(\mathrm{Re}_\tau) < C_f^{\mathrm{NT}}(\mathrm{Re}_\tau)$. Although the flow is not fully relaminarized, it has been proposed that the MDR regime is dominated by a weak form of turbulence displaying a prolonged "hibernation" state that is insensitive to changes in viscoelastic parameters.[13,15] The physics underlying such universal behavior is not yet completely understood, and there is at present no definitive theory that can consistently (or quantitatively) explain all features of the MDR phenomenon, such as its existence and universality. Recent experimental and numerical studies seem to support the inference that the flow state underlying the MDR regime is a self-sustaining instability likely of inertio-elastic origin, which

has since been termed *elastoinertial turbulence* (EIT) and is fundamentally different from the conventional inertia-driven turbulence (IDT) observed in the Newtonian and LDR flow regimes.[92–94]

On a final note, an experiment in which the elasticity number is sufficiently large may completely bypass the intermediate drag reduction regime, transitioning directly from laminar flow to the MDR state as the flow rate is increased;[9] this is illustrated by the path PQ in Fig. 2.5(a). Presumably, a similar path has been followed in the pipe flow experiment shown in Fig. 2.4.

C. *Mechanistic Descriptions of Drag Reduction*

Classical Theories

Classical descriptions of the drag reduction mechanism were formulated well before the advent of direct numerical simulations of viscoelastic turbulence in the late 1990s. At the time of their development, the distinction between LDR and HDR regimes had not yet been recognized, nor was detailed information available on the spatial and temporal evolution of viscoelastic coherent structures, as provided by the DNS techniques of today. These early theoretical efforts were therefore largely aimed at understanding the criterion for onset, drag reduction in the vicinity of the onset point (now known to be the LDR regime), and—albeit with limited success—the maximum drag reduction phenomenon.

Most theoretical explanations of the drag reduction mechanism are premised upon an early disruption of the turbulent energy cascade by dissolved polymers, causing a decrease in the total dissipation. These explanations may be broadly classified into *viscous* and *elastic* theories, based on whether the proposed suppression of turbulent eddies results primarily from the viscosity or the elasticity of polymer chains deformed by the flow.

Drag reduction as a viscous effect. In the viscous mechanism of drag reduction proposed by Lumley (1973),[95] polymer molecules are stretched by the fluctuating velocity gradients outside the viscous sublayer, causing a local enhancement in the effective viscosity that leads to the suppression of turbulent eddies near the wall. Under steady shear conditions, extensional strain is always accompanied by vorticity; polymer molecules "tumble" with the flow, and consequently do not remain aligned with the principal axes of strain rate long enough to undergo any significant elongation. In the turbulent regime, on the other hand, Lumley argued that vorticity and strain rate are in general uncorrelated; there is thus a greater probability of finding regions of strong extensional flow, with little vorticity. If the local onset criterion $\mathrm{Wi}_\varepsilon > 1$ is now met, molecules in these locations are stretched by the flow faster than they can relax, and undergo rapid expansion that causes a large

increase in extensional viscosity. Indeed, for solutions of flexible long-chain polymers, the ratio of the extensional viscosity η_e to the shear viscosity η, called the *Trouton ratio*,[96]

$$\mathrm{Tr} = \frac{\eta_e}{\eta}\,, \tag{2.21}$$

can quickly reach values as large as 10^3–10^4 in the vicinity of the coil-stretch transition,[97,98] representing a substantial increase of several orders of magnitude over the Newtonian value of $\mathrm{Tr} = 3$.

In the region outside the thin viscous sublayer, turbulent eddies in the energy cascade exist over a range of length scales: the size of the largest energy-containing eddies is comparable to the distance y from the wall, whereas the size of the smallest dissipative eddies is given by the *Kolmogorov scale*,[3]

$$l_\nu \sim \left(\frac{\nu^3}{\epsilon}\right)^{1/4}, \tag{2.22}$$

where ϵ is the rate of viscous dissipation per unit mass of the fluid, and $\nu = \eta/\rho$ is the kinematic viscosity. Suppose now that a long-chain polymer solute is present in small quantities in the flow. Inside the viscous sublayer, the fluid is in simple shear, and polymer molecules do not experience any appreciable elongation as explained above. However, in the turbulent flow field beyond the viscous sublayer, velocity fluctuations rapidly stretch the polymer molecules, causing a large increase in effective viscosity. The dissipation ϵ remains unchanged, since it is set by the energy-containing eddies and is not dependent on the dissipative eddies. From Eq. 2.22, therefore, the net result of the enhanced viscosity is an increase in the dissipative scale l_ν. Consequently, small eddies are suppressed and the viscous sublayer (where the viscosity remains unchanged) expands outwards from the wall. The thickening of the sublayer entails a forward displacement of the mean velocity profile, which manifests as drag reduction. In the framework of the viscous theory, maximum drag reduction is assumed to occur when the growing viscous sublayer reaches the core of the pipe, and no further expansion is possible; the mechanism sustaining turbulence in this terminal regime is, however, not explicitly specified.

Drag reduction as an elastic effect. Lumley's theory of drag reduction, as outlined above, relies on a large increase in effective viscosity due to the elongation of polymer molecules in the turbulent boundary layer. Tabor and de Gennes (1986)[99] proposed an alternative scheme in which the drag reduction effect is predicated not on the viscosity, but on the *elasticity* of coiled polymer chains subject to high frequency flow-induced strains. They argued that within the energy cascade, there exist length scales at which polymer chains

deform affinely with the fluid; although strain rates in the turbulent boundary layer may be large, as seen by the molecule they fluctuate rapidly in time, and therefore can cause only partial expansion of polymer coils. Since large changes in viscosity occur only when molecules are close to full extension, they concluded that any change in fluid viscosity that actually occurs in a turbulent flow would be quite small, and has no significant consequences for the drag reduction effect. By contrast, polymer molecules, even in dilute solutions, can display elastic behavior at the high frequency of deformation encountered in turbulence.

The elastic theory was originally formulated by Tabor and de Gennes in the context of homogeneous turbulence of polymer solutions; it was later adapted by Sreenivasan and White (2000)[100] to the case of wall-bounded turbulence in pipes. The key ideas of the theory can be summarized as follows: Turbulent eddies of length scale r in the inertial range are associated with a time scale $\tau(r)$, given by

$$\tau(r) \simeq \left(\frac{r^2}{\epsilon}\right)^{1/3}. \tag{2.23}$$

Here ϵ is the mean rate of dissipation of kinetic energy, which remains constant across all length scales in the cascade. The time scale $\tau(r)$ decreases at smaller scales r, and the temporal frequency of velocity fluctuations increases. A length scale r_0 can thus be found where the eddy time scale becomes comparable to the relaxation time λ of the dissolved polymer chains:

$$\tau(r_0) = \left(\frac{r_0^2}{\epsilon}\right)^{1/3} = \lambda. \tag{2.24}$$

At scales $r < r_0$, the frequency of hydrodynamic forcing experienced by the polymer chain is larger than its characteristic relaxation rate; it therefore becomes "embedded" in the flow, and deforms affinely with the local fluid element in which it lies.

Consider now a polymer chain that is stretched in size by a factor ξ. de Gennes argued that the elastic free energy stored by deformed polymer chains per unit volume of the solution, which is also equivalent to the polymer stress σ_p, is given by

$$\sigma_p = G\xi^{5/2}, \tag{2.25}$$

where G is an elastic modulus proportional to the polymer concentration c, and the exponent of $5/2$ on ξ (instead of the nominal power of 2) has been used to account for the non-linear restoring force and excluded volume effects at strong chain elongations.[101] To relate the chain extension ξ to the flow length scale r, de Gennes and Tabor postulated a simple power law dependence, of the form

$$\xi(r) \simeq \left(\frac{r_0}{r}\right)^n \tag{2.26}$$

where the exponent n varies with the "dimensionality" of chain stretching ($n = 1$ for stretching in two dimensions, and $n = 2$ in three dimensions). A second length scale r_E can now be defined where the elastic energy σ_P becomes comparable to the turbulent kinetic energy E per unit volume:

$$\sigma_P(r_E) = G[\xi(r_E)]^{5/2} = E(r_E). \tag{2.27}$$

At length scales $r_E < r < r_0$, the elastic energy stored in the stretched polymer chains is smaller than the turbulent kinetic energy; polymer molecules, although stretched by the flow, are assumed to exert no influence on the turbulent motion at these scales. On the other hand, elastic effects become significant in eddies with $r < r_E$; it is presumed that the turbulent energy cascade, which usually extends down to the viscous scale l_ν, is then prematurely truncated at the larger length scale r_E. As in the viscous theory, the result of this suppression of small scale eddies is a thickening of the buffer layer which, in turn, manifests as drag reduction.

Referring to Eq. 2.27, the length scale r_E depends explicitly on the the polymer concentration c, via the elastic modulus G which is proportional to c. Consequently, at a given Wi_τ, the elastic scale r_E for a sufficiently dilute solution may lie outside the inertial range (i.e. $r_E < l_\nu$, the Kolmogorov scale), in which case the energy cascade remains unaltered. Thus, unlike the viscous mechanism (wherein drag reduction is permitted at arbitrarily small concentrations), we obtain a finite threshold concentration $c_0(\mathrm{Wi}_\tau)$ of the polymer below which no drag reduction effect is observed. This prediction of a concentration-dependent onset criterion is a distinctive feature of the elastic mechanism.

Insights from Computational Studies

The two theoretical schemes discussed in the previous section rely on quite general scaling arguments; they do not delve into the details of how the presence of polymer molecules alter the turbulent flow structures to produce drag reduction. The viscous versus elastic debate remains an important unsettled question in the field of polymeric turbulence, with experimental and numerical evidence in support of both theories being presented over the years.[24] As such, neither model is sufficiently detailed to make quantitative predictions about the extent of drag reduction itself, nor provide a satisfactory account of the MDR phenomenon and the self-sustaining mechanisms of turbulence in this regime. They yield only a simple, qualitative picture of what happens within the flow, and offer plausible explanations for how dissolved polymers suppress turbulence at the smallest scales of the energy cascade. For practical engineering purposes, therefore, one is forced to rely on more phenomenological models and fits to experimental data.

Much of what we know today about the details of interaction between polymer chains and turbulent flow comes from numerical experiments. Beginning with the work

of Sureshkumar et al. (1997),[58] researchers have performed direct numerical simulations of wall-bounded turbulent flows of dilute, homogeneous polymer solutions in a variety of flow configurations. Most studies describe the polymer using a coarse-grained model, very often the FENE-P; in this case, the equations to be solved numerically are the continuity and momentum conservation equations,

$$\nabla \cdot \mathbf{v} = 0 \tag{2.28}$$

$$\rho \frac{\mathrm{D}\mathbf{v}}{\mathrm{D}t} = -\nabla p + \eta_s \nabla^2 \mathbf{v} + \nabla \cdot \tau_p \tag{2.29}$$

where $\mathbf{v}$ is the velocity field, p denotes the pressure, η_s is the solvent viscosity, and τ_p is the polymer contribution to the stress; the latter is obtained from the polymer conformation tensor $\mathbf{C}$, which evolves according to[102, 103]

$$\tau_p = -\eta_p \overset{\nabla}{\mathbf{C}} = \frac{\eta_p}{\lambda} \left[\left(\frac{L^2}{L^2 - \mathrm{tr}\,\mathbf{C}} \right) \mathbf{C} - \left(\frac{L^2}{L^2 - 3} \right) \mathbf{I} \right]. \tag{2.30}$$

Here, $\overset{\nabla}{\mathbf{C}}$ denotes the upper-convected derivative of $\mathbf{C}$, η_p is the polymer contribution to the zero shear rate viscosity η_0 (and is proportional to the concentration c), λ is the polymer relaxation time, and L^2 represents the maximal value of $\mathrm{tr}\,\mathbf{C}$ corresponding to full extension of the polymer chains. Often, a small artificial diffusion (AD) term is also added to Eq. 2.30 to suppress numerical instabilities that otherwise occur even at moderately large Weissenberg numbers.[104]

DNS findings in the LDR regime are in qualitative agreement with the picture of a thickened buffer layer in the presence of polymers, with the "inertial plug" displaced outwards, away from the wall and into the core. Viscoelastic effects tend to suppress the near-wall coherent structures, vortex stretching and hairpin vortex formation, as well as shear layer and wake instabilities, all of which are important routes for turbulence production in the boundary layer. Polymer chains are stretched in the near-wall velocity streaks, and they subsequently relax within the quasi-streamwise vortices, suppressing them.[45] Quasi-streamwise vortices are therefore weakened and reduced in number, and the streamwise velocity streaks are consequently widened and stabilized. Since these streamwise vortices form the primary means of convective momentum transport within the buffer layer, their suppression leads to a reduction in the frictional wall shear stress.[45]

However, at larger Wi, the mechanisms operating in the HDR and MDR regimes are qualitatively different, and yet to be fully elucidated. Recent advances such as vortex conformation analysis and the discovery of elasticity-driven flow instabilities seem to have finally begun to shed light on these historically challenging aspects of polymeric turbulence; a comprehensive account of these modern developments can be found in the extensive and insightful review of the topic by Xi (2019).[24]

TABLE 2.1. Examples of natural polymers that have been successfully employed for aqueous drag reduction in the literature. Also listed are the maximum percentage drag reduction observed in each study, the corresponding polymer concentration, and the flow configuration used for experimental friction measurements. Table adapted in part from Ref. [105].

Biopolymer additive	Conc. c [ppm]	Max. DR $\mathscr{D}$ [%]	Flow configuration
Amylopectin-PAM[74]	30	27	Rotating disk
Carboxymethyl cellulose[106]	1000	42	Circular pipe
Carrageenan[107]	1000	60	Circular pipe
Guar gum[75]	200	32	Rotating disk
Guar gum[107]	300	70	Circular pipe
Hydroxyethyl cellulose[108]	300	42	Circular pipe
Locust bean gum[107]	700	65	Circular pipe
Okra mucilage[109]	1600	74	Circular pipe
Scleroglucan[68]	500	12	Boundary layer
Xanthan gum[66]	100	22	Double-gap cylinders
Xanthan gum[76]	200	36	Rotating disk

D. *Biopolymers as Drag-Reducing Agents*

Among synthetic polymers that are often employed as model drag-reducing additives in experimental studies, polyethylene oxide (PEO) seems to be by far the most popular choice; other water-soluble polymers such as polyacrylamide (PAM) and polyacrylic acid (PAA) have also been investigated, albeit to a lesser extent.[114] Concurrently, a diverse array of naturally sourced polymers have also been explored as potential drag reducers in aqueous turbulent flows; examples include water-soluble derivatives of cellulose, various food gums, starch (amylopectin), alginate, carrageenan, chitosan, deoxyribonucleic acid (DNA) and even the pectinous sap of plants such as okra.[68,105,109] The most frequently studied among natural polymers seem to be two (relatively expensive) members of the gum family, namely xanthan gum (XG) and guar gum (GG), probably on account of their widespread use as viscosifiers in drilling muds, and as proppant suspenders in hydraulic fracturing fluids.[47,111] Bewersdorff and Singh (1988)[115] studied turbulent drag reduction by aqueous solutions of purified and commercial-grade samples of xanthan gum using a pressurized capillary flow setup, at different concentrations of gum and added salt. The rheology and drag reduction behavior of XG solutions changed from that typical of rigid molecules at high concentrations, to that of semi-flexible or flexible molecules at lower concentrations, as well as in the presence of dissolved salt. Kim et al. (2002)[73] used a rotating disk apparatus to characterize the drag reducing properties of aqueous

TABLE 2.2. Molecular properties of selected drag-reducing biopolysaccharides. The plant or bacterial source of each polymer, the typical range of molar masses, and the monosaccharide residues of the principal constituent polysaccharide are listed.

Biopolymer additive (plant/bacterial source)	Molar mass M_w [MDa]	Principal polysaccharide (residues in parenthesis)
FOOD GUMS:		
Guar gum[110] (*Cyamopsis tetragonoloba*)	1–2	Guaran (galactose, mannose)
Locust bean gum[110] (*Ceratonia siliqua*)	0.3–0.4	Galactomannan (galactose, mannose)
Xanthan gum[111] (*Xanthomonas campestris*)	2–20	(Glucose, mannose, glucuronic acid)
SEED MUCILAGE:		
Flax mucilage[32,112] (*Linum usitatissimum*)	1.2	Arabinoxylan (arabinose, xylose)
Chia mucilage[34] (*Salvia hispanica*)	0.8–2	(Xylose, mannose, glucose, arabinose, galacturonic acid)
OTHER:		
Okra mucilage[113] (*Abelmoschus esculentus*)	1.4	(Galactose, rhamnose, galacturonic acid)

guar gum solutions of different concentrations and molecular weight fractions; guar gum was observed to be more resistant to mechanical degradation than PEO under identical flow conditions. The same experimental system had been used previously by Sohn et al. (2001)[72] for a similar characterization of the drag-reducing properties of xanthan gum solutions.

Besides food gums, drag reduction has also been attempted using other classes of plant-sourced polysaccharides, including cellulose, starch, alginate, and carrageenan.[105] Being insoluble in water in its native form, cellulose has to be chemically modified before use in aqueous drag reduction applications; the two cellulose derivatives commonly employed in experimental studies are hydroxyethyl cellulose (HEC) and carboxymethyl cellulose (CMC), both of which have excellent solubility in water. Another potential source of high molecular weight polysaccharides for drag reduction is the viscous sap of various plants. Coelho et al. (2016)[109] showed that a fiber-mucilage mixture derived from okra pods (*Abelmoschus esculentus*) can act as an effective drag reducer in turbulent pipe flows, with longevity comparable to that of rigid polymer additives such as xanthan and guar. For several of the above mentioned polysaccharides, graft-copolymerization

with a flexible chain, such as polyacrylamide (PAM), has been shown to enhance the drag reduction performance and the shear stability of the original polymer; the graft copolymer synergizes the drag reducing ability of the flexible PAM chains with the mechanical strength of the rigid polysaccharide backbone, yielding an efficacious drag reducing agent that is also resistant to shear degradation.[106,116,117] Table 2.1 lists a few examples of water-soluble biopolymers that have been successfully employed for turbulent drag reduction in previous experimental studies; the plant or bacterial source from which some of these biopolysaccharides are extracted, along with their representative molar masses and constituent monosaccharide residues, are listed in Table. 2.2. A comprehensive survey of various biopolymer additives that have been investigated for turbulent drag reduction applications in the literature may be found in the review articles by Han and Choi (2017),[105] and Han et al. (2017).[114]

II. Drag Reduction Using Superhydrophobic Walls

A. *Fundamentals of Wetting and Superhydrophobicity*

When raindrops fall on the leaves of the lotus plant *Nelumbo nucifera*, or of the taro plant *Colocasia esculenta*, they bead up and roll off quickly without wetting the leaf surface[118,119] (see Fig. 2.6). A closer inspection of the adaxial surface of these leaves under a scanning electron microscope reveals the presence of a complex hierarchical roughness, consisting of microscopic bumps or papillae a few tens of micrometers in size, overlaid further by a finer texture of epicuticular wax crystalloids on the scale of about 1 μm and smaller.[118] The extraordinary water-repellency of the leaves—and their resulting self-cleaning ability—is enabled by a thin layer of air that remains trapped within these textural features underneath the water drop, shielding most of the leaf surface from direct contact with the liquid phase.[120] This layer of entrapped air, called the *plastron*, can be observed as the silvery sheen visible at the base of the water drops in Figs. 2.6a and 2.6c; the luster is a result of the total internal reflection of ambient light at the composite air-water interface bridging the texture asperities.[121] Surfaces such as the lotus and taro leaves, that display extreme water repellency and minimal drop stiction, are termed *superhydrophobic* surfaces.[120] Numerous examples of superhydrophobic surfaces can be found in nature; the leaves of several plants, including the lotus, taro, and kohlrabi,[118,122] the wings of insects such as butterflies and cicadas,[123,124] the compound eyes of the common mosquito,[125] and the feathers of birds such as ducks, geese, pigeons and penguins,[126–128] all exhibit varying degrees of water repellency. A careful examination of these natural surfaces reveals two primary factors that contribute to their superhydrophobic properties—low surface energy, usually facilitated by a coating of epicuticular wax, and a microscale surface roughness, often possessing

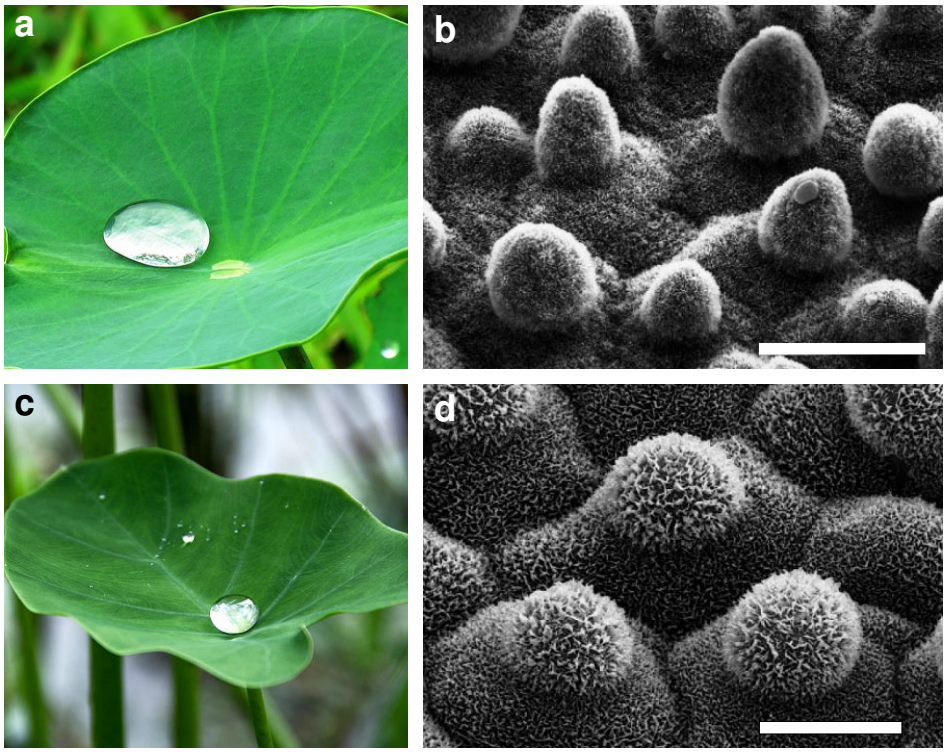

FIGURE 2.6. Raindrops do not wet the leaves of (a) the lotus plant *Nelumbo nucifera*, or (c) the taro plant *Colocasia esculenta*. The silver sheen visible under the drops arises from total internal reflection of light at interface of the trapped air layer, or *plastron*. (b) and (d) Scanning electron micrographs of the dorsal surfaces of the lotus and taro leaves, respectively. The scale bars denote 20 μm. For image sources and attribution, see p. 185.

hierarchical features at multiple length scales.

When liquid is deposited on a solid surface, it may either spread spontaneously or coalesce into droplets; the wetting behavior on an smooth, chemically homogeneous surface is dictated by the sign of the spreading coefficient S, defined as[120]

$$S = \gamma_{SA} - (\gamma_{SL} + \gamma_{LA}), \tag{2.31}$$

where γ_{SA}, γ_{SL} and γ_{LA} respectively denote the interfacial tensions at the solid-air, solid-liquid and liquid-air interfaces. The interfacial tension γ represents the excess (Gibbs) free energy per unit area of the two-phase boundary, and therefore has the physical dimensions of an energy per unit area (or a force per unit length). When the solid-liquid pair is such that $S > 0$, the liquid spreads spontaneously into a thin film and fully wets the solid. If $S < 0$, on the other hand, the liquid beads up into lens-shaped droplets, subtending a finite

angle θ_Y at the line of contact with the solid. For an ideal solid surface that is smooth, chemically homogeneous, and free of adsorbed impurities, the equilibrium angle θ_Y at the three-phase contact line is given by the Young equation,[129]

$$\cos\theta_Y = \frac{\gamma_{SA} - \gamma_{SL}}{\gamma_{LA}} = 1 + \frac{S}{\gamma_{LA}} \tag{2.32}$$

The angle θ_Y is called the *Young contact angle*, and may be regarded as a thermodynamic property of the three intersecting phases.[130] When the liquid phase is water, θ_Y varies typically from 0° on high-energy solids, such as clean glass and metal surfaces, to a maximum of about 120°, on self-assembled monolayers of highly fluorinated alkanoic acids.[131] A solid substrate is termed *hydrophilic* if $\theta_Y < 90°$, and *hydrophobic* if $\theta_Y > 90°$.

Substrates in real-life are, however, seldom smooth, and the inclusion of surface roughness can induce significant changes in the wetting behavior of liquids on solid surfaces.[120] Wenzel (1936)[132] quantified the effect of roughness on the apparent contact angle θ_W, the average macroscopic angle measurable at the contact line. In the Wenzel mode of wetting, the liquid fully inundates the surface texture, thereby completely displacing the gas phase [see Fig. 2.7(a)]; the apparent contact angle, modeled based on an 'effective' change in surface free energy, is then given by

$$\cos\theta_W = r_W \cos\theta_Y, \tag{2.33}$$

where the parameter r_W, known as the Wenzel roughness, is the ratio of the actual (or developed) area of the rough substrate to its apparent (or projected) area. Because $r_W > 1$ by definition, Eq. 2.33 predicts a roughness-induced enhancement of the inherent wettability of the solid—a hydrophilic solid, when roughened, becomes more hydrophilic ($\theta_W < \theta_Y$), and a hydrophobic surface becomes more hydrophobic ($\theta_W > \theta_Y$). Although these trends are qualitatively observed, a unique value of the apparent angle is rarely obtained in practice. Instead, the free energy landscape for a liquid wetting a rough solid surface is typically rugged with several local minima,[130] leading to a range of possible metastable configurations and attendant contact angles arising from the pinning of the contact line on roughness asperities and surface defects.[120] The largest value of the apparent contact angle, observed when the contact line advances on the dry substrate, is called the *advancing contact angle* θ_A.[133] Analogously, the smallest value of the apparent contact angle, measured as the contact line recedes from the previously wetted substrate, is called the *receding contact angle* θ_R. The difference between the two angles is termed the *contact angle hysteresis*, $\Delta\theta = (\theta_A - \theta_R)$; a small value of the hysteresis $\Delta\theta$ indicates low friction and high mobility of sessile liquid drops. Unsurprisingly, the Wenzel regime—wherein the roughness elements are in full contact with the wetting liquid phase—is characterized

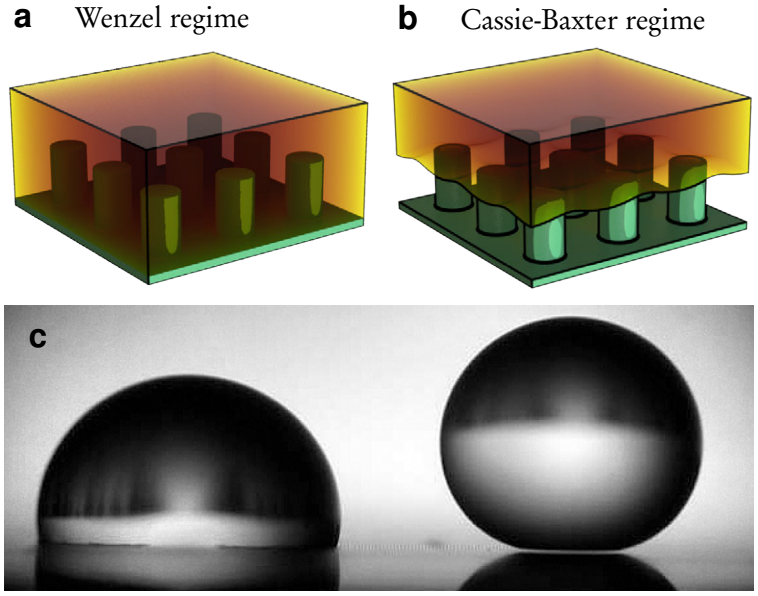

FIGURE 2.7. Schematic representations of (a) Wenzel and (b) Cassie-Baxter wetting regimes on a two-dimensional array of superhydrophobic microposts. (c) Millimeter-size water droplets resting on a superhydrophobic texture consisting of regularly patterned posts (solid fraction $\phi = 0.01$). The droplet on the right is in a metastable Cassie-Baxter state, as evidenced by the light transmitted through the thin plastron trapped underneath its base. The droplet on the left was gently pressed after deposition, which triggered a transition to the more stable Wenzel state. Droplet images in panel (c) reproduced from Ref. [134].

by strong contact line pinning and large contact angle hysteresis, preventing the facile movement and roll-off of incident water droplets.

On the other hand, if a hydrophobic substrate possesses sufficient surface roughness, an alternate regime called the Cassie-Baxter state can be observed.[120] In this mode of wetting, the liquid simply bridges across textural peaks and asperities, leaving pockets of air trapped between the liquid-air interface and the underlying solid substrate [Fig. 2.7(b)]. Provided the liquid meniscus remains largely flat compared to the length scale of the roughness features, the apparent contact angle in this composite wetting state may be estimated as[135]

$$\cos\theta_{CB} = \phi r_\phi \cos\theta_Y + (1-\phi)\cos\pi = \phi r_\phi \cos\theta_Y + \phi - 1, \tag{2.34}$$

where ϕ represents the areal fraction of the solid surface in direct contact with the liquid, and r_ϕ denotes the average Wenzel roughness of these wet contact patches. Notice that Eq. 2.34, in effect, represents an areal average of $\cos\pi$, weighted by the gas fraction $1-\phi$,

and the local Wenzel angle $\cos\theta_W = r_\phi \cos\theta_Y$ at the contact spots, weighted by the wetted solid fraction ϕ. The presence of an extensive plastron layer facilitates vastly diminished contact between the solid and liquid phases, and the degree of contact line pinning is substantially reduced. As a result, the Cassie-Baxter regime is typically associated with large apparent contact angles, low contact angle hysteresis, and minimal liquid adhesion, and therefore corresponds to the true superhydrophobic state.[120]

On hydrophobic substrates with moderate levels of roughness, the Cassie-Baxter regime tends to be more commonly observed in practice, even though the Wenzel state possesses a smaller interfacial free energy and thereby represents the stable thermodynamic configuration of the system.[120] These metastable Cassie-Baxter states typically result when the intrusion of the liquid into the surface texture is impeded by an energy barrier, arising from contact line pinning, large aspect ratio asperities, or re-entrant overhangs.[136–139] In such cases, the plastron layer is retained within the texture until an irreversible transition to the Wenzel regime is precipitated by an increase in liquid pressure (or droplet curvature), mechanical vibration of the substrate, or the diffusive loss of gas into the bulk liquid phase.[140–142] Once plastron collapse occurs and the liquid invades the surface texture, the resulting Wenzel state is energetically more stable, and an irrevocable loss of superhydrophobic properties usually ensues in the absence of external intervention to replenish the displaced gas and reinflate the plastron. In Fig. 2.7(c), water droplets of equal volume can be seen coexisting in two distinct wetting regimes on the same superhydrophobic substrate; the drop on the left was undisturbed after deposition and remained in a metastable Cassie-Baxter state, whereas the drop on the right was mechanically perturbed, triggering an irreversible transition to the thermodynamically stable Wenzel state.

Rapid advances in microfabrication techniques in the last two decades have enabled the development of a diverse and impressive array of synthetic superhydrophobic surfaces, which emulate the water-repellent and self-cleaning properties of their natural, biological counterparts. Such artificial surfaces developed over the years include regular patterns of ridges or posts created through photolithographic processing, fiber bundles made by electrospinning, carbon nanotube forests grown using chemical vapor deposition, and randomly textured surfaces produced through a variety of surface texturing methods such as spray-coating, chemical etching, sandblasting, thermal deposition and boehmitization.[143–150] A number of anti-rain, water-repellent, and self-cleaning surface treatment products are today commercially available for industrial as well as household use. For the vast majority of artificial surfaces reported in the literature, the crucial step of chemical functionalization—which imparts the requisite low surface energy and hydrophobicity to the substrate—has been heavily reliant on the use of fluorinated organic compounds, such as perfluoroalkanoic acids, organosilanes, and fluoropolymers; these substances have

recently come under increasing scrutiny over concerns regarding their toxicity and environmental persistence. Encouragingly, novel superhydrophobic textures that employ naturally occurring, plant-derived fatty acids for surface functionalization have been successfully developed in recent years,[151] paving the way towards the future development of eco-friendly and biodegradable surfaces for safe deployment in real-life applications.

B. *Plastron-Mediated Wall Slip and Frictional Drag Reduction*

In addition to conferring liquid-repellency and self-cleaning properties, superhydrophobic texturing of wetted solid boundaries can also serve to mitigate frictional drag reduction in wall-bounded aqueous flows. When a suitably aerophilic surface is immersed in water, a thin layer of air remains trapped between its textural features in the Cassie-Baxter state; this entrapped plastron layer, in turn, enables slip at the wall and reduces the overall frictional shear stress exerted by the flowing liquid.[40] Examples of such drag reduction strategies can be found in nature; emperor penguins, for instance, are known to utilize the air trapped in their water-repellent feathers to reduce drag as they resurface from underwater dives.[128]

As a simple illustration of plastron-induced wall slip, consider the external flow of liquid over a superhydrophobic surface, depicted schematically in Fig. 2.8. Provided the submerged plastron remains intact underwater in the Cassie-Baxter state, the flow near the wall experiences only intermittent contact with the underlying solid substrate; the usual no-slip boundary condition holds locally atop these wetted contact patches. A substantial fraction of the flow boundary, on the other hand, remains entirely shielded from the wall by the extensive plastron layer overlying the surface texture. The liquid-air interface bridging the texture asperities effectively presents a shear-free boundary to the near-wall flow, inasmuch as the viscosity of air is considerably smaller than that of water (by a factor of ~ 55 at 20 °C). Consequently, the liquid partially slips over the composite boundary, and the frictional shear stress at the wall is reduced because of the significant diminution in contact between the solid substrate and the flowing liquid.[40] The heterogeneous boundary condition over a superhydrophobic texture is often modeled by prescribing an equivalent slip velocity $\mathbf{v}_S = (U_S, V_S)$ at the wall, given by the Navier slip condition[152]

$$U_S = b_x \frac{\tau_{zx}}{\eta}, \quad \text{and} \quad V_S = b_y \frac{\tau_{zy}}{\eta}. \tag{2.35}$$

Here x, y and z respectively denote the streamwise, spanwise, and wall-normal coordinates, τ_{zx} and τ_{zy} represent (components of) the frictional shear stress at the wall, η is the dynamic viscosity of the liquid phase, and b_x and b_y are the effective slip lengths in the streamwise and spanwise directions. On a randomly textured surface with no salient

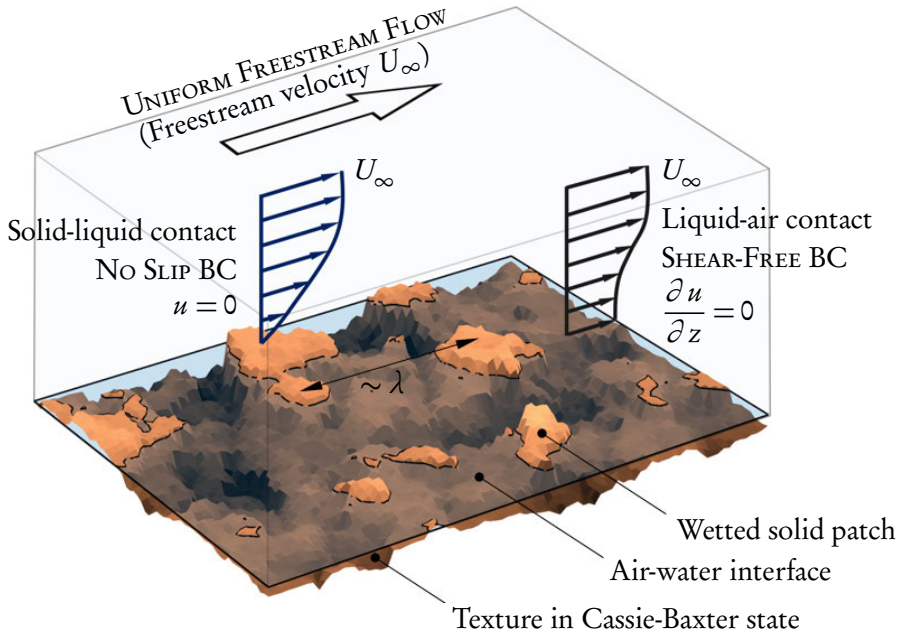

Figure 2.8. Liquid flowing over a submerged superhydrophobic wall in the Cassie-Baxter state. The wetted solid asperities act as no-slip boundaries, whereas the air-water interfaces effectively act as shear-free boundaries. The flow far from the wall can be modeled by replacing the composite boundary with an effective slip length b at the wall. The flat interface depicted here is only for illustration; in practice, the air-water interface may be curved and may not lie at a uniform height above the mean textural plane.

in-plane directions, we expect the wall slip to be isotropic, yielding a single value of the slip length ($b_x = b_y = b$) characterizing the slip-inducing properties of the texture.

Slip Length and Drag Reduction in Laminar Flows

Analytical expressions for the effective slip length in Stokes flow over periodic arrays of longitudinal and transverse shear-free slots were first obtained by Philip (1972);[153,154] similar results for other flow configurations were subsequently derived by Lauga and Stone (2003),[155] Cottin-Bizonne et al. (2004),[156] and Schönecker et al. (2014).[157] These theoretical results indicate that in the limit of creeping flows, the effective slip length b over a periodic array of stripes is a function of the spatial periodicity L of the stripe pattern, the areal fraction ϕ of the no-slip boundary, and—in the case of fluid-filled grooves—the ratio of viscosities of the bulk liquid and the lubricant filling the groove troughs. Furthermore, the effective slip length for spanwise slots was shown to be one-

half the value for slots aligned in the flow direction. Generic scaling laws for the slip length over two-dimensional periodic patterns in the Stokes flow limit were derived by Ybert et al. (2007);[158] they showed that in the limit of vanishing solid contact ($\phi \to 0$), the slip length b for a periodic array of microposts scales as $b \sim L/\phi^{1/2}$, which was then verified against numerical results.

Plastron-mediated drag reduction was first reported experimentally by Watanabe and coworkers (1996),[159] who measured the frictional pressure drop for the flow of water and glycerol-water mixtures through square and rectangular ducts treated with a water-repellent coating. A maximum drag reduction of 22 % was obtained in the laminar regime, whereas no drag reduction was observed under turbulent flow conditions, presumably due to the collapse of the entrapped plastron layer on their superhydrophobic texture. These results were soon replicated in other flow configurations, namely in circular pipe, rotating disk, and Taylor-Couette flows.[160–163] Ou et al. (2004)[164] demonstrated laminar drag reduction in a microchannel with one wall textured with regular arrays of microridges or microposts. Ou and Rothstein (2005)[165] employed μ-PIV techniques to measure the velocity profiles in laminar flow over a regular array of streamwise ridges in a microchannel; they obtained slip lengths of the same order as the size of the textural features, and verified that drag reduction increases with decreasing solid fraction ϕ. Lee and Kim (2009)[166] used deep reactive ion etching (DRIE) combined with Au-assisted porous silicon etching to fabricate post and ridge arrays with remarkably low solid fractions ($\phi = 0.03$ % and 2 % respectively); a dual-scale texture incorporating smooth tops and nanotextured sidewalls was employed to enhance the local contact angle and thereby stabilize the air-water meniscus spanning widely separated contact regions. Large slip lengths of approximately 140 μm on the post array, and 400 μm on the ridges, were inferred from flow measurements using a cone-and-plate rheometer.

Superhydrophobic Drag Reduction in Turbulent Flows

The use of superhydrophobic textures for turbulent drag reduction entails additional challenges not present in the laminar regime.[25] The intense velocity and pressure fluctuations that characterize turbulent flow can easily induce plastron collapse and an irreversible transition to the Wenzel regime,[20] after which the surface texture merely serves to amplify hydrodynamic roughness, further enhancing, rather than reducing, frictional drag. Even if the plastron interface is only partially impaled by the texture, the viscous sublayer and near-wall coherent structures can nevertheless interact strongly with the protruding surface asperities, potentially offsetting any drag reduction arising from wall slip effects. Min and Kim (2004)[167] performed DNS studies of turbulent channel flow with prescribed steamwise or spanwise slip boundary conditions at the wall; they showed that

even as streamwise slip resulted in drag reduction, spanwise slip led to strengthening of near-wall vortex structures, enhancing turbulent momentum transport and increasing the frictional shear stress on the wall. This mechanism of drag enhancement is unique to turbulent flows, and is wholly absent in laminar flows. On random textures which have equal slip lengths in both streamwise and spanwise directions, drag reduction generated by streamwise slip is therefore partly offset by the drag increase due to spanwise slip. Martell et al. (2009)[16] arrived at similar conclusions regarding the effect of streamwise and spanwise slip, and in a separate study showed that the extent of drag reduction in turbulent flow increases with Reynolds number, unlike in the case of laminar flow.[17] More recently, Seo and Mani (2016)[21] derived a scaling law for the evolution of the slip length in the high Reynolds number limit, and validated it using DNS results. In their analysis, a laminar boundary layer is assumed to develop over each solid-liquid contact spot, and the resulting scaling law for slip length is given by $b^+ \sim (L^+)^{1/3}\phi^{-1/2}$, where $L^+ = L/\delta_\nu$ and $b^+ = b/\delta_\nu$ are, respectively, the surface periodicity and the slip length scaled by the wall unit $\delta_\nu = (\rho\nu^2/\tau_w)^{1/2}$, ρ and ν denote the density and kinematic viscosity of the liquid phase, and τ_w is the average frictional shear stress at the wall. Unlike the result for low Reynolds numbers, the dimensional slip length $b \sim L^{1/3}\delta_\nu^{2/3}\phi^{-1/2}$ now also becomes a function of the wall shear stress τ_w, which determines the characteristic viscous length scale δ_ν in the inner boundary layer.

Daniello et al. (2009)[168] measured turbulent drag reduction for water flowing through a rectangular microchannel with one wall patterned with superhydrophobic streamwise ridges made of polydimethylsiloxane. Drag reduction levels approaching the theoretical maximum of $(1-\phi)$ were obtained, and slip lengths over 100 µm were reported at the largest Reynolds numbers. Park et al. (2014)[169] made careful, direct measurements of frictional drag reduction in the turbulent boundary layer flow over a superhydrophobic pattern of streamwise micrograte; close visual monitoring of the plastron within the groove troughs was maintained to prevent inadvertent collapse or overinflation events from vitiating the experimental data. The influence of texture geometry on drag reduction levels was further evaluated by varying the pitch L and the solid fraction ϕ of the groove array. Rosenberg et al. (2016)[170] obtained reductions in frictional torque of approximately 10 % in turbulent Taylor-Couette flow, using an inner cylinder textured with a periodic array of circumferential (i.e. streamwise) superhydrophobic grooves; the relatively small value of drag reduction was attributed to localized plastron collapse and wetting of some of the grooves in the turbulent regime, which could be mitigated by infusing the grooves with a low-viscosity alkane lubricant, such as heptane, in place of air. Utilizing the same Taylor-Couette setup but with a modified groove geometry on the inner cylinder, Van Buren and Smits (2017)[171] subsequently reported plastron-mediated drag reduction levels approaching 45 % in the turbulent regime. Alongside these experi-

mental efforts, numerical investigations into the mechanism of turbulence modification and drag reduction in the presence of periodic shear-free patterns at the boundary have also been concurrently pursued by several research groups; see, for example, the computational flow studies by Martell and coworkers (2009, 2010),[16,17] Park et al. (2013),[18] and Rastegari and Akhavan (2015).[19]

C. *Designing Scalable Surfaces for Large-Scale Drag Reduction*

Although regularly patterned superhydrophobic textures—exemplified by the periodic post or grooves arrays fabricated by means of micromachining or photolithography—serve as valuable 'canonical' surfaces in drag reduction studies owing to their carefully tunable slip properties, their high manufacturing cost and limited scalability render them impracticable in almost all large-scale turbulent flow systems. Practical drag reduction applications require superhydrophobic textures that can be easily produced and economically scaled to cover large areas of the solid boundary in contact with the flowing liquid.[4,25] As an illustration of the typical scales involved in real-life applications, the wet hull area of ships and submarines is often in the range of 100–1000 m^2, far exceeding the capabilities of most microfabrication techniques available today.

Consequently, there exists a practical need to develop drag-reducing surfaces with irregular or random textural roughness, which can be produced by means of relatively inexpensive and easily scalable techniques—such as spray-coating, sandblasting, and chemical or electrochemical etching—that are already in widespread use in industrial-scale surface treatment processes. Indeed, over the past ten years, several such prototype surfaces have been developed and successfully demonstrated to reduce frictional drag. For example, Samaha et al. (2012)[172] prepared randomly rough SH surfaces by depositing hydrophobic aerogel silica beads on a metal substrate, and measured the slip length and percentage drag reduction in laminar flow using a parallel-plate rheometer. Moaven et al. (2013)[173] produced scalable SH textures by spray-coating a sandblasted aluminum substrate with titania nanoparticles, and performed flow measurements using a rotating disk apparatus; drag reduction of up to 15 % was reported under turbulent flow conditions, corresponding to wall speeds of 8–12 $m\,s^{-1}$ and Reynolds numbers in the range of $5 \times 10^5 \leqslant \mathrm{Re} \leqslant 8 \times 10^5$ at the disk rim. Table 2.3 lists a selection of past experimental reports of drag reduction by randomly textured superhydrophobic surfaces in a variety of turbulent flow configurations.

In contrast to regularly patterned surfaces, the topography of irregular textures is less straightforward to characterize, inasmuch as quantitative descriptions of randomly rough surfaces are essentially limited to specifying one or more statistical averages or distributions of profile heights. Given these difficulties, it is perhaps not surprising that

TABLE 2.3. Examples of past experimental studies reporting frictional drag measurements in the turbulent flow regime on scalable superhydrophobic surfaces with random textural roughness. Also listed are the flow configuration utilized for turbulent drag measurements, the range of shear Reynolds numbers Re_τ investigated, and the percentage drag reduction $\mathscr{D}$ observed. A negative value of $\mathscr{D}$ indicates drag enhancement in the presence of the superhydrophobic texture.

Reference	Flow configuration	Re_τ range [−]	$\mathscr{D}$ [%]
Gogte et al. (2005)[174]	Joukovsky hydrofoil placed in water tunnel	40 to 290	+3 to +18
Zhao et al. (2007)[175]	Plate and cylindrical models placed in water tunnel	1700 to 3300	−5 to +9
Peguero and Breuer (2009)[176]	Channel flow with particle image velocimetry	200	−50 to +40
Aljallis et al. (2013)[177]	Plate model drawn through towing tank	520 to 5170	−30 to +30
Bidkar et al. (2014)[150]	Surface mounted on water tunnel wall, with strain gauge sensors for wall shear stress	1000 to 5000	−13 to +30
Srinivasan et al. (2015)[178]	Taylor-Couette cell coupled to rotational rheometer	480 to 3810	0 to +22
Zhang et al. (2015)[179]	Flat plate boundary layer with particle image velocimetry	330 to 470	+10 to +24
Ling et al. (2016)[180]	Surface mounted flush on water tunnel wall, with PIV and holographic microscopy	700 to 4500	−10 to +36
Gose et al. (2018)[30]	Surface mounted flush on channel wall, with streamwise pressure taps	215 to 950	−90 to +90
Rajappan et al. (2019)[31]	Taylor-Couette cell coupled to rotational rheometer	800 to 3000	0 to +26

generic scaling laws for wall slip on irregular superhydrophobic textures—in terms of their roughness statistics—are yet to be derived. Although superhydrophobic textures with random roughness have shown extraordinary success as liquid-repellent and self-cleaning surfaces,[119,145,181] many of them do not perform adequately in drag reduction applications; in fact, many highly water-repellent surfaces, even as they remain perfectly aerophilic underwater, either produce no drag reduction in turbulent flows, or otherwise enhance the overall frictional drag.[25] This, in turn, underlines the necessity to investigate the specific textural characteristics which confer drag-reducing ability under turbulent flow conditions. Indeed, a number of recent studies have focused on addressing the gap in understanding the relationship between the textural features of randomly rough surfaces, and their drag reduction efficacy in turbulent flows. For example, Bidkar et al. (2014)[150] conducted experimental measurements of the frictional wall shear stress on various randomly textured surfaces inside a water tunnel, and concluded that in addition to retaining an intact plastron when submerged, the texture must also possess low surface roughness to produce a net reduction in drag; specifically, the roughness amplitude has to be smaller than the viscous length scale of the turbulent boundary layer. This requirement of low textural roughness has been further supported by subsequent experimental observations of Hokmabad and Ghaemi (2016).[182] Gose et al. (2018)[30] performed skin friction measurements on four randomly rough superhydrophobic textures inside a channel flow facility at Reynolds numbers in the range $1 \times 10^4 \leqslant \mathrm{Re} \leqslant 3 \times 10^4$, reaching wall shear stresses of up to 65 Pa. They reported that a net positive drag reduction was observed only when the product $k^+\Delta\theta_{HP}$ is below a threshold value of about 9, where $k^+ = k/\delta_\nu$ is the root mean square roughness k expressed in wall units, and $\Delta\theta_{HP}$ denotes the contact angle hysteresis of sessile drops on the texture measured at small drop volumes (and hence corresponding to high internal Laplace pressures).

Rajappan et al. (2019)[31] evaluated the drag reduction efficacy of four randomly rough superhydrophobic surfaces in turbulent Taylor-Couette flow, and used confocal profilometry to investigate the influence of various statistical measures of textural roughness on the experimentally inferred slip length. Each of the four prototype surfaces in their study was fabricated using readily scalable mechanical or chemical texturing processes—namely sand blasting, chemical etching, boehmitization, and spray coating—that generate a random, self-affine height profile on the base substrate; an example is shown in Fig. 2.9(a), of a surface prepared by the acid etching and subsequent boehmitization of aluminum. The frictional drag on all four surfaces was measured when fully submerged in featureless turbulent flow inside a bespoke Taylor-Couette apparatus, at Reynolds numbers in the range $1 \times 10^4 \leqslant \mathrm{Re} \leqslant 1 \times 10^5$. An effective slip length quantifying the overall drag-reducing ability of each surface was determined from the resulting Prandtl-von Kármán friction curves. Plastron-mediated reduction in frictional drag of up to 26 % was observed, with one of

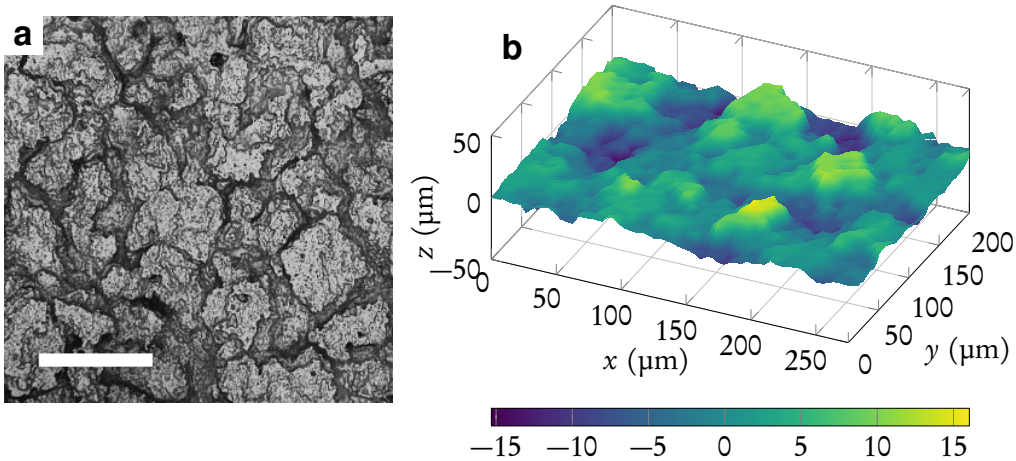

FIGURE 2.9. (a) Depth-composition optical micrograph of a scalable, randomly textured, etched aluminum superhydrophobic surface. The scale bar denotes 50 μm. (b) Two-dimensional profilogram of the surface shown in (a), measured using a confocal laser profilometer.

the hierarchically textured surfaces sustaining a wall shear stress of 26 Pa (corresponding to $\mathrm{Re} \sim 7 \times 10^4$) before the onset of pressure-induced wetting and plastron collapse. The surface topography of each random texture was characterized using a non-contact optical profilometer [see Fig. 2.9(b)], and the influence of various statistical measures of roughness on the effective slip length was explored. For robust textures capable of retaining an intact plastron under turbulent flow conditions, the lateral autocorrelation length λ of the two-dimensional height profile was identified to be an important determinant of slip length, playing a role analogous to the spatial periodicity L for regularly patterned surfaces. Three key requirements were proposed to ensure the optimal design of scalable random textures intended for turbulent drag reduction applications: (*a*) the texturing process should be tailored to generate a large mean autocorrelation length ($\lambda >> \delta_\nu$) for the primary roughness profile, (*b*) the final texture should possess a small roughness amplitude ($k^+ < 1$) to prevent asperity-induced enhancement of frictional drag, and (*c*) the texture should ideally incorporate secondary (and possibly higher order) hierarchical roughness features to stabilize the plastron interface against collapse under large turbulent pressure fluctuations.

D. *Surface Resilience Through Active Plastron Management*

A critical consideration in the practical deployment of superhydrophobic surfaces in real-life applications is the longevity of the entrapped plastron atop the submerged aerophilic

texture. Indeed, this would of a primary concern in instances where sustained drag reduction is desired over long periods of time, such as in pipelines, or on seafaring vessels. Even the best designed drag-reducing surface will fail due to plastron collapse if the gas trapped between textural asperities is depleted; this can occur either as a result of shear-induced drainage,[177] or by diffusion and the forced convective mass transfer of dissolved gas in the turbulent boundary layer.[172]

Several strategies have been explored in the literature to prolong plastron lifetime through active replenishment of the lost gas, for instance, by supplying pressurized air to the texture through a porous backing plate,[180] generating vapor by heating the wall above its Leidenfrost point to initiate film boiling,[183–185] or by employing electrochemical[186, 187] or catalyst-mediated reactions that evolve gaseous products within the texture.[188] Lee and Kim (2011)[186] used thin-film gold electrodes integrated into a regular array of superhydrophobic posts to enable gas generation through the electrolysis of water in the Wenzel regime. Once dewetting is complete and the texture reverts to the Cassie-Baxter state, the reaction is automatically halted by the cessation of contact between the liquid and the electrode, yielding a self-regulating mechanism for plastron management. Vakarelski et al. (2012)[183] showed that nucleate boiling is completely suppressed on a heated superhydrophobic texture, allowing a continuous vapor film to be sustained in the Leidenfrost regime even at small values of the wall superheat. Taking advantage of this phenomenon, Saranadhi et al. (2016)[185] utilized active Joule heating of the textured rotor surface in a bespoke Taylor-Couette apparatus to obtain substantial reductions in turbulent drag of the order of 80–90 %; this method was, however, noted to be highly energy-intensive, with the requisite input of thermal power far outweighing the energy savings gained by mitigating frictional dissipation.

Du et al. (2017)[189] achieved plastron reinflation on a superhydrophobic random texture in turbulent flow conditions inside a water tunnel, by the direct injection of air into the near-wall region through an orifice in the wall. The successful retention and spreading of the injected air into a stable drag-reducing plastron was found to be contingent on ensuring adequate aerophilicity of the superhydrophobic texture, failing which the supplied air is quickly swept away by the high speed flow. Panchanathan et al. (2018)[188] employed a catalyst-mediated, gas generating chemical reaction to effectuate a partial recovery of the collapsed plastron layer atop the superhydrophobic rotor wall in turbulent Taylor-Couette flow. In their study, a porous layer of catalytic manganese dioxide (MnO_2) was incorporated into the texture using a scalable, solution-based anodic electrodeposition process. The original plastron layer on the submerged rotor remained stable for over 4 h under turbulent flow conditions, and a wetting transition was artificially induced by flushing the flow cell with deaerated water. After the plastron had collapsed, a dilute solution of hydrogen peroxide was injected into the bulk flow to initiate the recovery

process. The catalytic MnO_2 layer accelerates the spontaneous decomposition of the dissolved hydrogen peroxide, producing gaseous oxygen at the wall that displaces the liquid from within the texture. As in the case above, adequate aerophilicity of the texture is again a necessary prerequisite to ensure that lateral spreading of the generated gas along the surface is energetically favored over the formation of sessile gas bubbles that may enhance drag. After steady state conditions were reached, which was about 20 min after the injection of the reactant, the freshly formed plastron layer had an areal coverage of approximately 58 % of the rotor surface, with an attendant recovery of ~ 51 % of the original drag reduction efficacy prior to plastron collapse. Very recently, Xu et al. (2020)[187] demonstrated a 'semi-active' superhydrophobic surface capable of plastron regeneration when submerged in seawater, enabled by cathodic gas generation on metal electrodes inlaid into the textured polymer substrate. A sacrificial galvanic anode was kept immersed in the bulk liquid phase, so that the occurrence of a wetting transition creates a local electrochemical cell involving the two dissimilar metals which powers the gas-generating reaction, wherein the infiltrated seawater itself acts as the conductive electrolyte.

III. Closing Remarks

This chapter surveyed the extant literature on two well-known drag reduction methods that form the principal focus of this thesis: polymer additives injected into the turbulent boundary layer, and superhydrophobic surfaces that induce an effective slip velocity at the wall. A brief historical perspective of polymer drag reduction was presented in §2.I, covering theoretical, numerical and experimental advances made in seventy years since the discovery of the Toms' phenomenon. In §2.II, the literature on drag-reducing superhydrophobic surfaces was reviewed, including recent developments enabling the fabrication of scalable and durable randomly rough textures capable of frictional drag reduction in large Reynolds number turbulent flows. Active methods for sustaining and replenishing the gaseous plastron atop these textures, during prolonged service under turbulent flow conditions, were also briefly discussed.

As mentioned in Chapter 1, despite numerous instances of successful experimental trials affirming the efficacy of polymer drag reduction techniques, the prohibitive cost of synthetic drag-reducing polymers has largely precluded their deployment in large-scale turbulent flow systems, except within the oil industry. To address these consumable cost constraints, inexpensive plant mucilage extracted from commonly available seeds is investigated in Chapter 4 as a potential cost-effective substitute for synthetic drag-reducing agents, particularly in marine applications. In Chapter 5, we further explore the possibility of combining drag-reducing polymers with superhydrophobic wall textures to enhance the overall levels of drag reduction achievable in turbulent flows of practical

and commercial relevance.

Experimental characterization of the drag reduction efficacy of polymer additives and superhydrophobic textures, both individually and in parallel, requires the use of a simple and reliable experimental setup, capable of accurate measurements of skin friction drag and wall slip under carefully controlled and repeatable turbulent flow conditions. In this study, frictional drag measurements were performed by means of a custom-built Taylor-Couette fixture operating in the featureless turbulent flow regime, and coupled to a commercial rotational rheometer to enable accurate determination of the rotor speed and torque. The design and baseline flow characterization of this bespoke experimental device forms the subject matter of the next chapter, along with detailed descriptions of various experimental techniques employed for the preparation and macromolecular characterization of synthetic as well as plant-based drag-reducing polymer solutions.

Notes

Parts of the material reviewed in §III of this chapter—specifically, those pertaining to drag reduction using scalable, randomly rough superhydrophobic textures, and plastron regeneration via catalyst-mediated gas generation—are based on the following published works by the author.

A. Rajappan. Skin friction drag reduction in turbulent flows using superhydrophobic surfaces. *Master's thesis.* Massachusetts Institute of Technology, Cambridge, MA (2017).

D. Panchanathan, A. Rajappan, K. K. Varanasi, and G. H. McKinley. Plastron regeneration on submerged superhydrophobic surfaces using in situ gas generation by chemical reaction. *ACS Appl. Mater. Interfaces* **10**:33684–33692 (2018).

A. Rajappan, K. Golovin, B. Tobelmann, V. Pillutla, Abhijeet, W. Choi, A. Tuteja, and G. H. McKinley. Influence of textural statistics on drag reduction by scalable, randomly rough superhydrophobic surfaces in turbulent flow. *Phys. Fluids* **31**:042107 (2019).

The space below is intentionally left blank.

3 *Overview of Experimental Techniques*

I. Frictional Drag Measurements in Turbulent Flow

A. *The Turbulent Taylor-Couette Flow Apparatus*

Skin friction data for drag-reducing polymer solutions and superhydrophobic surfaces were measured experimentally using a bespoke *Taylor-Couette* (*TC*) *apparatus*, operated at rotational speeds sufficiently large to generate featureless turbulent shear flow inside the cell gap. Figure 3.1(a) shows a schematic sectional view of the apparatus and its key components. The device, in essence, consists of a rotating inner cylinder (hereafter called the *rotor*) housed concentrically within a stationary outer cylinder (or the *stator*), creating a cylindrical annular gap inside which the working fluid is contained. For this particular configuration in which the inner rather than the outer cylinder rotates, the primary azimuthal shear flow within the annulus is unstable above a critical rate of rotation, and a sequence of secondary vortex flow patterns develop as the rotor speed is increased.[190–194] At even higher speeds, these secondary vortex flows themselves become unstable and eventually dissipate, and featureless turbulence is attained in the cell gap.[193–196] The Taylor-Couette system thus provides a simple means of generating and studying turbulent shear flows inside a compact and convenient experimental setup.

The TC geometry can be characterized by its three principal dimensions: the inner (or rotor) radius R_i, the outer (or stator) radius R_o, and the height of the flow cell L; the radial width of the annular flow gap is then $d = R_o - R_i$. The following non-dimensional geometric ratios are immediately obtained:

$$\text{Radius ratio} \quad \zeta = \frac{R_i}{R_o}, \quad \text{and} \tag{3.1}$$

$$\text{Aspect ratio} \quad \xi = \frac{L}{d}. \tag{3.2}$$

The azimuthal speed of the rotor wall is given by $V = R_i\Omega$, where Ω is the angular speed of rotation. Let $\nu = \eta/\rho$ denote the kinematic viscosity of the working fluid inside the gap. The Reynolds number Re for the TC flow is defined, per usual convention, using the wall speed V and the gap width d as the velocity and length scales:

$$\mathrm{Re} = \frac{V\,d}{\nu} = \frac{\Omega R_i\,d}{\nu} \tag{3.3}$$

A second dimensionless group relevant to TC flows is the *Taylor number*, given by

$$\mathrm{Ta} = \Lambda\left(\frac{R_i + R_o}{2}\right)^2 \frac{d^2\Omega^2}{\nu^2}\,, \tag{3.4}$$

where the prefactor Λ is a function of the radius ratio ζ of the Taylor-Couette geometry:

$$\Lambda = \frac{(1+\zeta)^4}{16\,\zeta^2}\,. \tag{3.5}$$

The above definition of the Taylor number was suggested by Eckhardt, Grossmann and Lohse (2007)[197] based on an exact analogy between the equations of motion governing Taylor-Couette flow and Rayleigh-Bénard (RB) convection. The Taylor number Ta in TC flow is analogous to the Rayleigh number Ra in RB convection, and the factor Λ is a geometric counterpart of the Prandtl number Pr.[197] Rearranging equation 3.4 shows that the Reynolds and Taylor numbers are related, with $\mathrm{Ta} \propto \mathrm{Re}^2$ for fixed rotor and stator radii:

$$\mathrm{Ta} = \frac{(1+\zeta)^6}{64\,\zeta^4}\,\mathrm{Re}^2 \tag{3.6}$$

Rationale for Choosing Taylor-Couette Flow

In the present study, a Taylor-Couette system was chosen over other experimental flow configurations on account of the simplicity of the flow geometry, its compact design, the relative ease of fabricating and operating the device, and the small volume of working fluid required per flow test. The cylindrical symmetry of the flow permits a simple and straightforward determination of wall friction by measuring the steady-state torque on the rotor. Furthermore, the flow is homogeneous in the streamwise direction, unlike pressure-driven flows through pipes or channels, or the developing boundary layer over flat plates. The uniformity of mean pressure and wall shear stress along the flow direction is of great advantage in characterizing randomly textured superhydrophobic surfaces, since the degree of impalement of the air-water interface into the texture—and consequently the

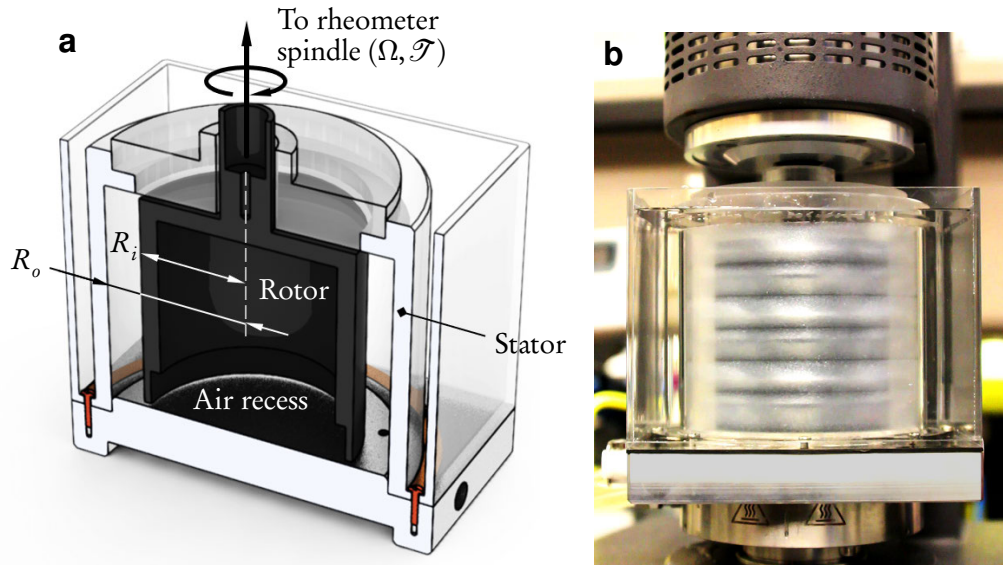

FIGURE 3.1. The bespoke Taylor-Couette (TC) apparatus used for frictional drag measurements in turbulent flow. (a) Schematic diagram, showing the transparent stator and the end-recessed rotor. (b) The TC fixture mounted on the AR-G2 rheometer. Three pairs of counter-rotating Taylor vortices are observed in the cell gap at Re = 156, made visible by a rheoscopic fluid comprising synthetic mica flakes dispersed in a glycerol-water mixture.

wetted solid fraction and the slip length—all depend critically on local flow conditions, which would otherwise vary from one location to another on the test surface.

In building a stand-alone Taylor-Couette test facility, the rotor end bearings and hydraulic seals are often among the most exacting components in the overall design; these must operate with minimal friction, add no noise to the rotor torque measurement, and also maintain a leak-proof liquid seal at large rotational speeds. Additionally, the accurate calibration of angular speed and torque transducers is vital to obtaining reliable experimental data. In the present study, an easier recourse was simply to repurpose the speed and torque control capabilities of a commercial rotational rheometer that was readily available in the lab. The rotor is coupled to, and driven by, the spindle of the rheometer, which is internally supported on a frictionless magnetic bearing that enables the rotational speed and frictional torque to be measured with great precision. Within the TC apparatus itself, extraneous friction was minimized by adopting a design that involves no direct contact between rotating and stationary surfaces. Further details on the construction and operational features of the TC apparatus are provided in the following section.

Table 3.1. A comparison of the dimensions, geometry ratios and key flow parameters between the TC apparatus used in this study, and the original wide-gap TC device described by Srinivasan et al. (2015).[178] The listed values pertain to a smooth no-slip rotor, with pure water at 25 °C as the working fluid. Asterisks denote flow quantities estimated approximately.

Parameter		Unit	Wide-gap device Srinivasan et al.	TC apparatus (this work)
Dimensions				
Rotor radius	R_i	mm	14.0	38.1
Stator radius	R_o	mm	34.3	50.8
Rotor length	L	mm	42.0	76.2
Cell gap	d	mm	20.3	12.7
Bottom end gap		mm	2.50	0.10
Geometry ratios				
Radius ratio	ζ	—	0.41	0.75
Aspect ratio	ξ	—	2.07	6.00
Flow parameters				
Transition Reynolds number	$\mathrm{Re}_{\mathrm{crit}}$	—	10 000	11 000
Max. Reynolds number	Re_{∞}	—	79 600	86 800
Max. angular speed	Ω_{∞}	$\mathrm{rad\,s^{-1}}$	250	160
Max. wall speed	V_{∞}	$\mathrm{m\,s^{-1}}$	3.50	6.10
Max. shear Reynolds number*	$\mathrm{Re}_{\tau,\infty}$	—	3800	3000
Max. wall shear stress*	$\tau_{w,\infty}$	Pa	25	50
Transition viscous length scale*	$\delta_{\nu,\mathrm{crit}}$	µm	27	18
Min. viscous length scale	$\delta_{\nu,\infty}$	µm	5	4

The TC Apparatus: Design and Fabrication

The TC apparatus built for this study is a revamped version based on the wide-gap design introduced by Srinivasan et al. (2015).[178] The dimensions of their original device were substantially reworked to improve the geometry of the flow cell, minimize end effects, and extend the range of operation to greater wall shear stresses and turbulence intensities without exceeding the operating limits of the rheometer (see Table 3.1). The device had to fit within the limited clearance available between the rheometer head and bottom plate, restricting the overall dimensions to about 6 × 6 × 6 inches. The total weight of the apparatus, inclusive of the working fluid, was kept below the 50 N measurement range of the normal force transducer on the bottom plate.

The key dimensions and operational specifications of the TC apparatus are listed in

Table 3.1. The rotors were machined out of aluminum 6061-T6 alloy, with a radial runout less than 0.50 mm (4 % of the cell gap) when mounted on the rheometer spindle. The hollow interior of the rotor body remains air-filled during experiments, providing a shear-free interface which effectively eliminates the extraneous torque from fluid friction acting on the bottom face. The rotors, as machined, were positively buoyant, each weighing approximately 170 g in air but displacing over 350 g of water when submerged to its normal operating depth. To prevent excessive upthrust on the rheometer spindle due to buoyancy, the rotor cavity was partly filled with a thermosetting elastomer—either polydimethylsiloxane (Sylgard 184, Dow) or a silicone RTV casting rubber (R-2374, Silpak Inc.)—adding roughly 130 g to the overall pendant mass. The elastomeric plug also helped detune a rotor resonance mode that inadvertently matched the frequency of the magnetic bearing gap controller; this was discovered only at the time of initial trial runs, when it resulted in undesirable vertical oscillations of the spindle before corrective measures were adopted.

For baseline friction measurements requiring smooth no-slip walls, the machined surface of the rotor was further polished to ensure minimal hydrodynamic roughness even at the largest Reynolds numbers achieved experimentally. To this end, the rotor wall was smoothened with progressively finer grades of sandpaper (600, 1200, 1500 and 2000 grit), and finally buffed to a mirror finish using a fine (10 μm) abrasive paste. The resulting surface finish was inspected using a portable surface roughness tester (Surftest SJ-210, Mitutoyo), and found to have an average roughness of $R_a = 0.05\,\mu\text{m}$ and a root mean square roughness of $R_q = 0.07\,\mu\text{m}$, well below the minimum viscous length scale of $\delta_{\nu,\infty} \simeq 4\,\mu\text{m}$ anticipated at the highest operating speeds.

The stator and the surrounding rectangular box form an integral unit made of optically clear cast acrylic, with all joints bonded permanently though solvent welding. When the rotor was to be photographed in situ during an experiment, the space between the outer box and the stator was first filled with glycerol, which has an index of refraction that closely matches that of the acrylic stator wall. The flat faces of the box, along with the glycerol, reduce the severe optical distortion otherwise produced by the curved stator, significantly improving the quality of images obtained. The base of the stator unit was made of aluminum and has a circular recess that mates with the bottom plate, locating the stator concentrically with the rotational axis of the spindle and the rotor. Two fluidic inlets drilled through the base plate enable filling and draining of the cell gap, and each inlet port was equipped with a self-closing quick-disconnect socket to prevent leaks.

A typical flow experiment using the TC apparatus proceeded as follows: The rotor was attached to the spindle and lowered into the stator, leaving a 100 μm clearance at the bottom to prevent contact with the base plate during rotation. The stator was then sealed at the top with an acrylic lid, the latter held firmly in place by a neutral cure RTV

TABLE 3.2. Technical specifications for the AR-G2 rotational rheometer, as reported by the manufacturer. The listed values are for steady shear operation; specifications differ in the case of oscillatory tests. The notation 'CR' denotes 'controlled-rate' mode of operation.

Specification	Value	Unit
Maximum torque	2.0×10^{-1}	N m
Minimum torque (CR)	1.0×10^{-8}	N m
Maximum speed	3.0×10^{2}	rad s^{-1}
Minimum speed (CR)	1.4×10^{-9}	rad s^{-1}
Angular displacement resolution	2.5×10^{-8}	rad

silicone sealant (Dow Corning 737) applied to the joint. With the lid affixed, the working fluid was introduced into the cell gap through one of the two fluid inlets, until the rotor wall was fully submerged and the liquid reached a predefined level about halfway up the stem. Flow measurements were then performed by varying the rotor speed Ω in discrete steps, and recording the steady state frictional torque $\mathcal{T}$; the fluid-filled space above the rotor functions as an effective hydraulic seal that prevents air ingress into the flow cell even at high rotor speeds. Post completion of the experiment, the liquid was drained out through the fluid ports, and the lid was dismantled to allow the rotor to be raised along with the rheometer head. The spent, hardened sealant was scraped off, and fresh sealant was reapplied to the lid seat before the next experimental run. Figure 3.1(b) shows the TC apparatus, fully assembled and mounted on the rheometer during a flow test.

The AR-G2 Rheometer

As mentioned previously, a key challenge in the design of an experimental Taylor-Couette facility is ensuring the accurate measurement and control of rotor speed and torque. To circumvent the complex task of installing and calibrating stand-alone transducers and data acquisition equipment, the TC apparatus was designed as a removable fixture that couples directly to an AR-G2 rheometer, capable of precise speed and torque measurements. A brief description of the rheometer and its key features is provided below, and a few relevant specifications, as reported by the manufacturer, are listed in Table 3.2.

The AR-G2 is a commercial rotational rheometer of the CMT type (short for 'combined motor and transducer'), manufactured by TA Instruments. It has a fixed bottom plate equipped with a normal force sensor and thermoelectric temperature control, and a rotating spindle to which standard cone or plate geometries can be attached. The spindle is driven by a low-inertia drag cup induction motor with accurately calibrated torque versus current characteristics; the AR-G2 thus operates as a controlled-stress instrument

in its native mode, and uses feedback control to impose prescribed strains or shear rates. The angular displacement of the spindle is monitored continuously by a rotary optical encoder, enabling precise determination of its rotational speed and acceleration. The spindle, along with the motor assembly, bearings and the optical encoder, is mounted on a vertically traversing head which can be positioned accurately at the desired working height by means of a linear ball screw drive. The spindle is suspended from the head unit entirely using magnetic and pneumatic bearings, and the absence of direct mechanical contact permits near-zero friction on the spindle during rotation. Axial support for the spindle is provided by a magnetic bearing, comprising an iron thrust plate held suspended between two electromagnetic actuators; the vertical position of the thrust plate is detected and rigidly maintained by a closed-loop controller. Radial stiffness is provided by porous carbon air bearings located near the top and bottom ends of the spindle, and supplied from a compressed air line at 30 psi working pressure.

At large sustained torques, motor temperature rises and active cooling is enabled to counter thermal expansion of the drag cup. Automatic motor cooling with compressed air commences when the torque exceeds a preset value of approximately 35 mN m. When operating at large angular speeds above this threshold, the measured torque as reported by the instrument was found to have a large systematic (positive) error, presumably arising from extraneous friction imparted by the cooling airflow. To ensure the veracity of experimental data, measurements using the TC apparatus were therefore restricted to torques below 35 mN m (corresponding to wall shear stresses $\tau_w \leqslant 50\,\mathrm{Pa}$), and data points obtained after the onset of motor cooling were discarded. This limitation restricts the maximum rotor speed attainable with the TC fixture to about $160\,\mathrm{rad\,s^{-1}}$ in water and most aqueous drag-reducing solutions, even though the stated speed limit of the rheometer is nearly twice this value, at $300\,\mathrm{rad\,s^{-1}}$.

B. *Taylor-Couette Flow of Newtonian Fluids*

Centrifugal Instability and Secondary Flow Regimes

Consider the steady laminar shear flow of a viscous fluid between two concentric cylinders of radii R_i and R_o, rotating with angular speeds Ω_i and Ω_o respectively. The simplified momentum equation in the azimuthal direction reads[83]

$$\frac{1}{r}\frac{\mathrm{d}}{\mathrm{d}r}\left(r\frac{\mathrm{d}V_\theta}{\mathrm{d}r}\right)-\frac{V_\theta}{r^2}=0\,, \tag{3.7}$$

where r is the radial distance in cylindrical coordinates aligned with the common axis of rotation, and $V_\theta(r)$ is the azimuthal velocity of the fluid in the annular gap. Along with

the no-slip boundary conditions at the two cylindrical walls,

$$V_\theta(R_i) = R_i\,\Omega_i \quad \text{and} \quad V_\theta(R_o) = R_o\,\Omega_o\,, \tag{3.8}$$

Eq. 3.7 yields the velocity profile

$$V_\theta(r) = r\,\Omega_i + R_i\,\frac{\Omega_o - \Omega_i}{1-\zeta^2}\left(\frac{r}{R_i} - \frac{R_i}{r}\right) \tag{3.9}$$

for the primary flow, where $\zeta = R_i/R_o < 1$ is the radius ratio of the TC geometry.

The stability of the velocity profile described by Eq. 3.9 can be examined in the context of the *Rayleigh criterion*: the two-dimensional swirling flow of an inviscid fluid is stable to axisymmetric disturbances if the square of the circulation $r\,V_\theta$ increases monotonically with radius, i.e.,[190,198]

$$\frac{\mathrm{d}}{\mathrm{d}r}(r\,V_\theta)^2 > 0 \quad \text{for all} \quad R_i \leqslant r \leqslant R_o\,. \tag{3.10}$$

If the fluid has non-zero viscosity, the above condition is still sufficient, though not necessary, to ensure stability of the flow to infinitesimal axisymmetric perturbations.[199] Substituting Eq. 3.9 into 3.10 yields the inequality

$$\left(\Omega_o - \Omega_i\zeta^2\right)\,V_\theta(r) > 0 \quad \text{for all} \quad R_i \leqslant r \leqslant R_o\,. \tag{3.11}$$

The above criterion is satisfied only if the two cylinders rotate in the same direction, *and* the circulation at the outer cylinder is larger than that at the inner cylinder; if both conditions are met, the azimuthal shear flow inside the annulus remains stable. In particular, the Rayleigh criterion is always satisfied for a TC device in which the inner cylinder is stationary, and the outer cylinder rotates; no secondary flows are observed in this case, and the primary laminar Couette flow transitions directly to turbulent shear flow as the speed of rotation Ω_o is increased.

By contrast, in a Taylor-Couette configuration comprising a rotating inner cylinder and a fixed outer cylinder—as in the case of the bespoke apparatus used in this study—the primary velocity profile is Rayleigh unstable, and secondary flow patterns are expected to develop as the speed of rotation is increased. The critical angular speed of the rotor at which the viscid primary flow becomes unstable to radial perturbations was first derived analytically by Taylor (1923).[191] Above this critical speed, linear stability theory predicts the onset of a steady and axisymmetric secondary flow, consisting of axially periodic pairs of counter-rotating toroidal vortices known as *Taylor vortices*.[191] When the rotor speed Ω exceeds a second critical threshold, the Taylor vortex flow (TVF) itself develops

a traveling wave instability, leading to an unsteady flow pattern called wavy vortex flow (WVF).[192] At even larger speeds, the waves disappear and turbulent Taylor vortices (TTV) are observed.[193] Further increase in rotor speed causes the vortex pattern to gradually dissipate, and the flow eventually transitions to featureless wall-driven turbulence (TUR) with no discernible large-scale structure.[193,196]

The secondary flow regimes and transitions within the bespoke TC apparatus, occurring en route to turbulence, were visualized with the aid of a rheoscopic suspension made by dispersing $4\,\mathrm{g\,L^{-1}}$ of finely powdered synthetic mica in a glycerol-water mixture of suitable viscosity; a viscous 80 % glycerol solution was used for low Reynolds numbers $\mathrm{Re} \leqslant 500$, a 50 % solution was used for intermediate Reynolds numbers $500 < \mathrm{Re} \leqslant 10\,000$, and pure deionized water with no glycerol was used to observe the flow at Reynolds numbers $\mathrm{Re} > 10\,000$. Representative photographs of the flow patterns observed at different Reynolds numbers are shown in Fig. 3.2. Beyond the transition to fully turbulent flow, the initial 3-pair vortex structure is no longer detectable; however, circulation arising from boundary layers at the top and bottom ends, as well as vortex-like coherent structures in the flow, continue to persist even at the highest Reynolds numbers, an observation which is consistent with past experimental reports in the literature.[200]

Transition to Featureless Turbulence

To locate the point of transition to featureless turbulent flow inside the TC apparatus, the baseline friction on a smooth, no-slip rotor was measured experimentally in various Newtonian liquids of known viscosities. Deionized water and two different glycerol-water mixtures were used to obtain high resolution friction data spanning five decades of the Reynolds number, in the range $4.0 \times 10^{-1} \leqslant \mathrm{Re} \leqslant 8.6 \times 10^{4}$. The density and viscosity of the Newtonian test fluids are listed in Table 3.3; property data were obtained from the literature[201,202] in the case of water, and determined experimentally for the two glycerol solutions. Viscosities of the glycerol-water mixtures were measured on the AR-G2 rheometer using a 60 mm 2° cone and plate geometry, and found to be constant within limits of experimental error for shear rates in the range $100\,\mathrm{s^{-1}} \leqslant \dot{\gamma} \leqslant 600\,\mathrm{s^{-1}}$. All fluid property measurements and flow experiments were performed at an ambient temperature of 25 °C.

With each of the above liquids filling the cell gap, the steady state torque $\mathscr{T}$ on the smooth rotor was varied in discrete steps, and the resulting angular speed Ω was recorded. To compare friction curves obtained using liquids of different viscosities, it is convenient to define a non-dimensional torque G, given by[196]

$$G = \frac{\mathscr{T}}{\rho\, \nu^2 L}, \tag{3.12}$$

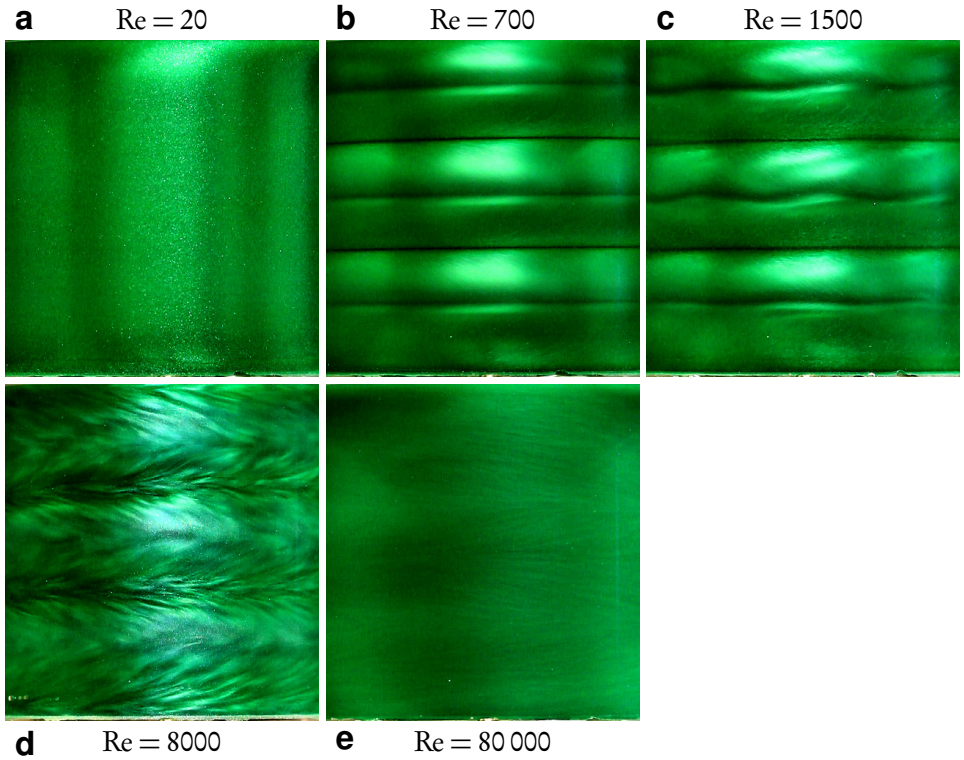

FIGURE 3.2. Representative photographs of flow patterns observed inside the bespoke TC apparatus at increasing Reynolds numbers during flow visualization experiments. (a) Laminar azimuthal Couette flow (AZI) at Re = 20. (b) Taylor vortex flow (TVF) with three vortex pairs at Re = 700. (c) Vortex flow with wavy outflow boundaries (WOB) at Re = 1500. (d) Turbulent Taylor vortices (TTV) at Re = 8000. (e) Featureless turbulence (TUR) at Re = 80 000.

where ρ and ν are respectively the density and the kinematic viscosity of the working fluid, and L is the rotor height. Figure 3.3 shows the non-dimensional torque G as a function of the Reynolds number Re; in these variables, the three data sets collapse onto a single Newtonian baseline characterizing the TC apparatus, and the individual friction curves for different liquids agree quite well in their regions of overlap. To determine the critical transition Reynolds number $\mathrm{Re}_{\mathrm{crit}}$ from this curve, we adopt the method proposed by Lathrop, Fineberg, and Swinney (1992),[196] and assume a power law scaling for the frictional torque of the form $G \sim \mathrm{Re}^{\alpha}$, valid in the limit of large Reynolds numbers; a torque exponent α can then be derived using the relation

$$\alpha = \frac{\mathrm{d}\log G}{\mathrm{d}\log \mathrm{Re}} \,. \tag{3.13}$$

TABLE 3.3. Density and viscosity data for Newtonian fluids used in the baseline calibration of the bespoke TC apparatus. The properties of water were obtained from reference tables,[201,202] and of the two glycerol solutions were determined experimentally. All values correspond to a temperature of 25 °C.

Working fluid	Density ρ [kg m^{-3}]	Dynamic viscosity η [Pa s]	Kinematic viscosity ν [m^2 s^{-1}]
Deionized water	997	8.90×10^{-4}	8.93×10^{-7}
57 % glycerol in water	1107	1.30×10^{-2}	1.17×10^{-5}
84 % glycerol in water	1218	1.18×10^{-1}	9.70×10^{-5}

The dataset for the largest Reynolds numbers, obtained using water as the working fluid, comprises discrete torque measurements spaced at uniform log intervals of $\Delta(\log_{10} G) = 0.05$, spanning the range of Reynolds numbers $2.1 \times 10^3 \leqslant \mathrm{Re} \leqslant 8.6 \times 10^4$. Since direct numerical differentiation accentuates noise in the data, the exponent α was estimated using a sliding linear least squares regression over 15 adjacent data points (equivalent to a log interval of $\Delta(\log_{10} G) = 0.70$). The resulting value of α is shown as a function of the Reynolds number in Fig. 3.4. As evident from the plot, α increases monotonically with Re, suggesting the absence of a unique power law scaling for the the frictional torque that applies uniformly throughout this range of Reynolds numbers. However, a marked discontinuity in the slope of the curve is observed at $\mathrm{Re} \simeq 1.1 \times 10^4$, indicating a change in the dependence of α on Re (and by extension, a change in the scaling of G with Re). Following Lathrop et al.,[196] we identify $\mathrm{Re}_{\mathrm{crit}} = 1.1 \times 10^4$ as the critical Reynolds number at which the (Newtonian) shear flow within the TC apparatus transitions to featureless wall-driven turbulence.

An empirical equation for α may be derived via piecewise fits to the experimental data in the vicinity of the transition point:

$$\alpha = \begin{cases} 1.59 + 0.469 \log_{10}(\mathrm{Re}/\mathrm{Re}_{\mathrm{crit}}) & \mathrm{Re} \leqslant \mathrm{Re}_{\mathrm{crit}} \\ 1.59 + 0.172 \log_{10}(\mathrm{Re}/\mathrm{Re}_{\mathrm{crit}}) & \mathrm{Re} > \mathrm{Re}_{\mathrm{crit}} \end{cases} \tag{3.14}$$

The critical exponent α at the transition point is approximately 1.59, which is close (but not exactly equal) to the marginal stability exponent[196] of 5/3. The value of $\mathrm{Re}_{\mathrm{crit}} = 1.1 \times 10^4$ obtained above for the TC apparatus (which has a radius ratio of $\zeta = 0.75$), compares well to the value of $\mathrm{Re}_{\mathrm{crit}} = 1.3 \times 10^4$ obtained by Lathrop et al. for their TC flow geometry, which had a similar radius ratio of $\eta = 0.72$.[196] Subsequent measurements using drag-reducing superhydrophobic surfaces or polymer solutions, reported hereafter in this thesis, were performed at Reynolds numbers $\mathrm{Re} > 15\,000$, well above the value of $\mathrm{Re}_{\mathrm{crit}}$

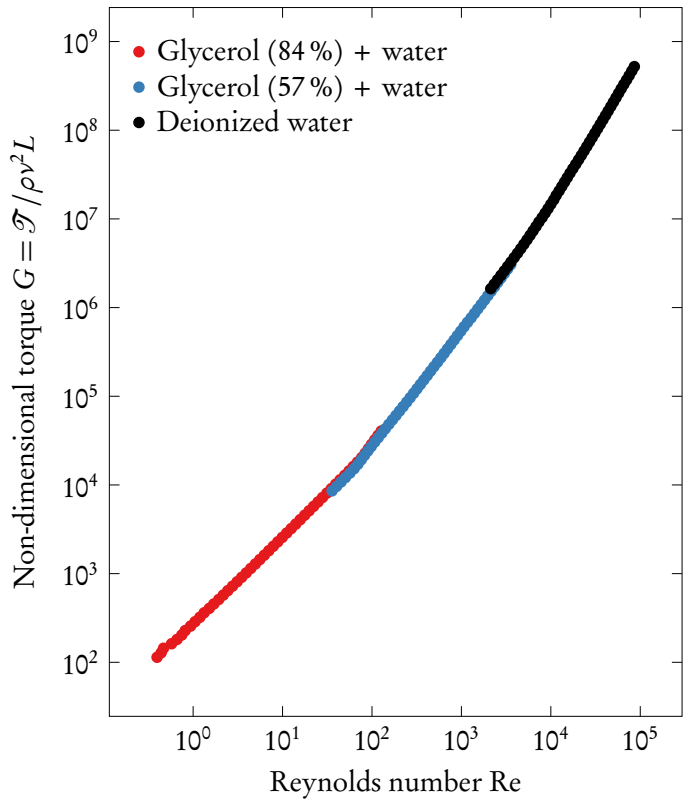

FIGURE 3.3. Experimental baseline torque $G = \mathcal{T}/\rho\nu^2 L$ for the TC apparatus as a function of the Reynolds number Re. Friction data spanning successive ranges of the Reynolds number were obtained using deionized water and two different glycerol-water mixtures, the properties of which are listed in Table 3.3.

determined for the Newtonian case; this extra allowance was intended as a precaution against possible effects of delayed transition or wall slip caused by the drag-reducing polymer or superhydrophobic surface under evaluation.

TORQUE SCALING IN THE TURBULENT REGIME

In the fully-developed turbulent flow regime, a scaling law for the frictional shear stress on the rotor wall can be derived through asymptotic matching of either the fluid velocity or the angular momentum in the region of overlap of the core flow with the inner and outer boundary layers.[196,203] The shear stress on the rotor wall at steady state is given by

$$\tau_w = \langle \tau_{r\theta} \rangle|_{r=R_i} = \eta R_i \frac{\mathrm{d}}{\mathrm{d}r} \frac{\langle V_\theta \rangle}{r}\bigg|_{r=R_i} \tag{3.15}$$

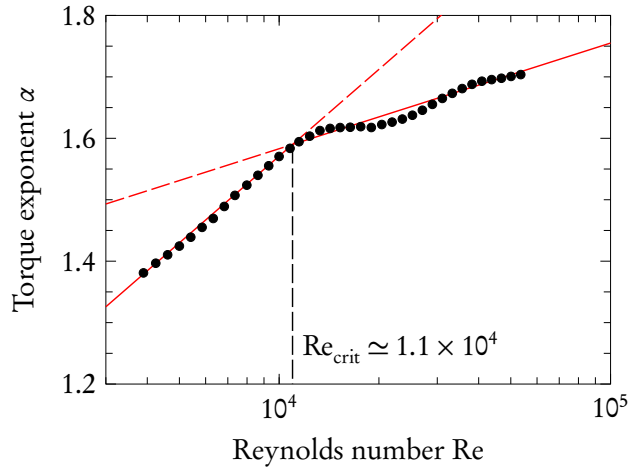

FIGURE 3.4. The local torque exponent α as a function of the Reynolds number Re, derived from the baseline curve for the TC apparatus shown in Fig. 3.3. A change in slope is observed near $\mathrm{Re}_{\mathrm{crit}} \simeq 1.1 \times 10^4$, indicating the point of transition to the featureless turbulent flow regime. The red lines denote piecewise log-linear fits to $\alpha(\mathrm{Re})$ in the vicinity of the transition point, given by Eq. 3.14.

where $\langle \cdots \rangle$ denotes the time average of fluctuating flow quantities. Provided the aspect ratio $\xi = L/d$ is sufficiently large, end effects can be neglected, and the shear stress τ_w is largely uniform across the rotor surface; the steady state frictional torque $\mathscr{T}$ is then given by

$$\mathscr{T} = \tau_w (2\pi R_i L) R_i \,. \tag{3.16}$$

Rearranging, this gives

$$\tau_w = \frac{\mathscr{T}}{2\pi R_i^2 L} \,, \tag{3.17}$$

which allows the frictional wall shear stress τ_w to be inferred directly from experimental measurements of the rotor torque.

Panton (1992)[203] used matched asymptotic expansions for the angular momentum $r\langle V_\theta \rangle$ of the fluid to derive a logarithmic scaling for the frictional shear stress in turbulent Taylor-Couette flow, valid in the limit of large Reynolds numbers. The flow is assumed to comprise an inviscid core region of nearly constant angular momentum, flanked by thin wall layers near the inner and outer cylindrical walls; this structure is consistent with the observations of Smith and Townsend (1982),[195] who used hot-wire anemometry to obtain velocity profiles of turbulent flow inside an experimental Taylor-Couette apparatus. Starting from the Reynolds-averaged Navier-Stokes equations and using general scaling

arguments, Panton obtained a skin friction law of the form[203]

$$V^+ = M \log \mathrm{Re}_\tau + N \,, \tag{3.18}$$

where $V^+ = V/u_\tau = R_i\Omega/u_\tau$ is the rotor speed normalized by the friction velocity $u_\tau = \sqrt{\tau_w/\rho}$ at the inner boundary layer (cf. Eq. 2.8), $\mathrm{Re}_\tau = \rho u_\tau d/\eta$ is the shear Reynolds number at the inner wall (cf. Eq. 2.10), and M and N are constants that depend on the radius ratio ζ of the TC geometry. In limit of zero curvature (i.e. $\zeta \to \infty$), the value of M is expected to approach $2/\kappa \simeq 4.88$, where $\kappa \simeq 0.41$ is the empirical value of the von Kármán constant.[203]

Figure 3.5(a) shows the baseline friction curve for the TC apparatus in Prandtl-von Kármán coordinates, corresponding to the experimentally measured frictional torque on a smooth, no-slip rotor in deionized water in the featureless turbulent flow regime. Baseline tests were performed at an ambient temperature of (23.0 ± 0.5) °C, and replicate measurements were obtained and averaged. As evident from the plot, the data shows good conformance to the logarithmic functional form predicted by Eq. 3.18, and a linear least-squares regression was used to extract the constants

$$M = 4.76 \quad \text{and} \quad N = -10.0 \tag{3.19}$$

quantifying the frictional characteristics of the bespoke TC geometry in the turbulent regime.

Incidentally, the logarithmic form of the friction law given by Eq. 3.18 admits an explicit analytic expression for the torque exponent α. From Eqs. 2.1 and 2.10, we have

$$\frac{\mathrm{Re}}{\mathrm{Re}_\tau} = \frac{\rho V d}{\eta} \frac{\eta}{\rho u_\tau d} = \frac{V}{u_\tau} = V^+ \,. \tag{3.20}$$

Substituting Eq. 3.20 in Eq. 3.18 gives

$$\mathrm{Re} = \mathrm{Re}_\tau \left(M \log \mathrm{Re}_\tau + N \right) \,, \tag{3.21}$$

which, in turn, can be inverted to yield Re_τ as a function of Re:

$$\mathrm{Re}_\tau = \frac{\mathrm{Re}'}{\mathrm{W}\left(e^{N/M}\mathrm{Re}'\right)} \,. \tag{3.22}$$

Here $\mathrm{Re}' = \mathrm{Re}/M$, and $\mathrm{W}(x)$ denotes (the principal branch of) the product logarithm function, also known as the Lambert W function, defined as the functional inverse of $f(x) = xe^x$ satisfying the functional equation

$$x = \mathrm{W}(xe^x) \,. \tag{3.23}$$

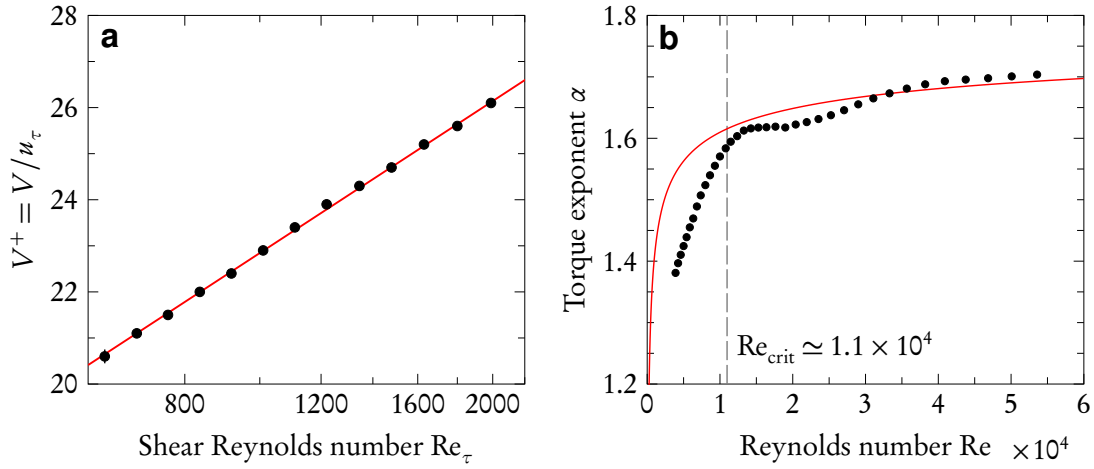

FIGURE 3.5. (a) The baseline friction curve for the bespoke TC apparatus in Prandtl-von Kármán coordinates. The red line denotes the linear least-squares fit used to extract the empirical constants M and N appearing in Eq. 3.18. (b) The torque exponent α as a function of the Reynolds number Re, reproduced from Fig. 3.4. The solid red curve indicates the theoretical prediction for α, Eq. 3.25, using the values of M and N (see Eq. 3.19) inferred from the fit in panel (a).

The principal branch of $\mathrm{W}(x)$ is identified by $\mathrm{W}(0) = 0$; for real $x \geqslant 0$, $\mathrm{W}(x)$ is single-valued, non-negative, and increases monotonically with x. Combining Eqs. 3.12, 3.16, and 2.11 with Eq. 3.22 above, we get

$$G = \frac{2\pi R_i^2}{d^2}\mathrm{Re}_\tau^2 = \frac{2\pi R_i^2}{d^2}\left[\frac{\mathrm{Re}'}{\mathrm{W}\left(e^{N/M}\mathrm{Re}'\right)}\right]^2. \tag{3.24}$$

Logarithmic differentiation of the above equation directly yields a closed-form expression for the torque exponent α (cf. Eq. 3.13):

$$\alpha = \frac{\mathrm{d}\log G}{\mathrm{d}\log \mathrm{Re}} = 2\left[1 - \frac{1}{1+\mathrm{W}\left(e^{N/M}\mathrm{Re}'\right)}\right]. \tag{3.25}$$

As $\mathrm{Re} \to \infty$, the expression on the right hand side of Eq. 3.25 asymptotically approaches the value 2. This is consistent with the theoretical requirement that $\alpha \leqslant 2$, a strict upper bound which can be rigorously derived from the Navier-Stokes equations.[204] Figure 3.5(b) compares Eq. 3.25 with the value of α computed directly by regression to experimental data; an excellent fit is observed for Reynolds numbers beyond the critical point $\mathrm{Re}_{\mathrm{crit}}$.

Very recently, semi-empirical models have been developed that describe the mean velocity profile and frictional shear stress in highly turbulent Taylor-Couette flow, at

Reynolds numbers sufficiently large for the boundary layers near the two cylinders to have also transitioned to turbulence—a terminal flow state often called the 'ultimate' regime in the literature.[194,205] Cheng et al. (2020)[206] proposed a three-layer model comprising log-law velocity profiles near the two walls, matched to a central region of constant angular momentum equal to the average of the fluid angular momenta at the inner and outer cylinders. The wall shear stress at the (hydrodynamically smooth) inner cylinder then obeys the friction law

$$V^+ = \frac{4}{\kappa}\,\mathrm{W}\left[a Z(\zeta)\sqrt{\mathrm{Re}}\right], \tag{3.26}$$

where

$$Z(\zeta) = \frac{\sqrt{\zeta}}{\sqrt{1-\zeta}} \tag{3.27}$$

is a function of the radius ratio ζ, and the constant a is given by

$$a = \frac{\kappa}{8}\exp\left[\frac{\kappa}{8}(4A-1)\right] \simeq 0.117, \tag{3.28}$$

with the canonical values $\kappa = 0.4$ and $A = 4.5$ used for the von Kármán constant κ and the boundary layer offset parameter A, respectively. The skin friction predicted by Eq. 3.26 was validated against previous numerical and experimental results from the literature as well as the authors' own wall-resolved large-eddy simulations (LES), for large Reynolds numbers $\mathrm{Re} \sim 10^5$–10^6 and radius ratios between 0.50 and 0.91.[206]

Berghout et al. (2020)[207] extended the three-layer model by introducing the curvature length scale $L_c = u_\tau/\kappa\Omega$, which separates regions near the wall where the production of turbulent kinetic energy is dominated by shear, and regions farther from the wall where it is influenced significantly by streamline curvature; the curvature length L_c is thus analogous to the Obukhov length in the Monin-Obukhov similarity theory for stratified shear flows. The resulting scale separation generates a new curvature boundary layer, overlying the usual Prandtl-von Kármán log-law layer, within which turbulent flow quantities scale with the curvature length L_c instead of the viscous length δ_ν. Asymptotic matching of the fluid angular velocity then yields a modified friction law for the inner wall, similar in form to Eq. 3.26:[207]

$$V^+ = \frac{4}{\kappa}\,\mathrm{W}\left[b Z(\zeta)\sqrt{\mathrm{Re}}\right]. \tag{3.29}$$

The new empirical constant b is given by

$$b = \frac{\sqrt{\kappa}}{4}\exp\left[\frac{\kappa}{2}\left(C + \frac{\log\psi}{\lambda}\right)\right] \simeq 0.166, \tag{3.30}$$

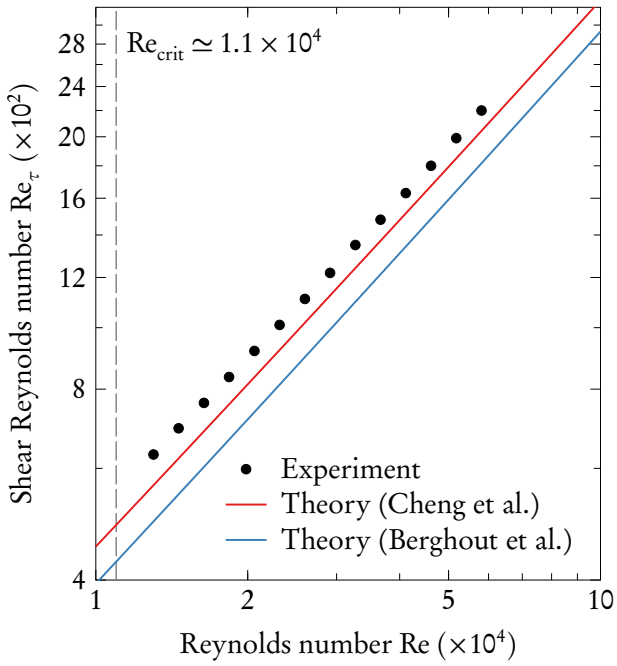

FIGURE 3.6. The experimental friction curve for the bespoke TC apparatus in featureless turbulent flow, compared with the semi-empirical models of Cheng et al. (Eq. 3.26) and Berghout et al. (Eq. 3.29), both evaluated for a radius ratio of $\zeta = 0.75$. For a given Newtonian fluid, notice that the abscissa Re is a function only of the rotor speed Ω (or equivalently, the wall speed V), whereas the ordinate Re_τ depends solely on the frictional torque $\mathscr{T}$ (or the wall shear stress τ_w). The above plot can thus be regarded as a non-dimensional representation of the "torque versus speed" characteristics of the TC apparatus in the turbulent regime.

where the model parameters $C = 1.0$, $\psi = 0.65$, and $\lambda = 0.64$ were inferred from fits to available experimental (PIV) and numerical (DNS) velocity profiles, at large rotation rates $10^8 \leqslant \mathrm{Ta} \leqslant 10^{12}$ and for radius ratios $0.50 \leqslant \zeta \leqslant 0.91$.[207]

Figure 3.6 compares the experimentally measured baseline for the TC apparatus [$\zeta = 0.75$, $Z(\zeta) = 1.732$] with the friction curves predicted by Eqs. 3.26 and 3.29; notice that with ζ fixed, there are no further adjustable parameters in either model. The baseline data shows good agreement with the three-layer model of Cheng et al. (Eq. 3.26); small deviations from the theoretical prediction can be attributed to end effects in rotor torque measurements, and perhaps more importantly, the relatively moderate range of operating Reynolds numbers achieved in the TC apparatus, and the attendant lack of strong scale separation or curvature effects as envisioned in the above models.

II. Characterization of Drag-Reducing Polymer Solutions

A. *Polymer Dissolution, Gravimetry & Lyophilization*

Preparation of Stock Solutions and Dilutions

Synthetic polymers employed in drag reduction tests were procured either in solid or powder form, and used as is without further purification or processing. Typically, a concentrated stock solution ($c \geqslant 0.2\,\%$) of the polymer was first prepared, from which small aliquots were drawn when required and diluted with pure solvent to obtain solutions of the desired concentration for use in flow experiments. To prepare stock solutions of polyethylene oxide (PEO) and polyacrylamide (PAM), the requisite amount of dry powder was gently dispersed over deionized water in a wide-mouth container, and allowed to hydrate slowly in quiescent solvent for a few hours. Afterwards, the container was sealed and transferred to a laboratory benchtop roller (Wheaton W348923-A, DWK Life Sciences) to permit gradual dissolution of the polymer by slow rolling over a period of 48–96 h. Meticulous care was taken to ensure uniform laminar mixing, and to avoid any vigorous agitation or turbulent stirring that could induce mechanical degradation of the dissolved high molar mass chains.[208] After complete and homogeneous dissolution was achieved, the stock solution was refrigerated ($T \simeq 5\,°\mathrm{C}$) in an airtight vessel to mitigate chemical degradation and hydrolysis during storage.

All stock solutions and dilutions of aqueous polymers were prepared using distilled water (VWR Chemicals BDH), conforming to ASTM Type II specifications for reagent water (see ASTM standard D1193).[209] Large volumes were measured out using a volumetric flask (250 mL at 20 °C, precision class A, tolerance ±0.12 mL), and smaller volumes were dispensed using calibrated micropipettes. Refrigerated stock solutions were allowed to warm to room temperature, 20 °C, before commencing volumetric measurements. Dry polymer powder was weighed using a digital analytical microbalance (XS64, Mettler Toledo) with a least count of 0.1 mg. Mucilage solutions were usually extracted from raw seeds directly at the desired strength, and used within the same day in flow measurements; the long-term storage of preprepared mucilage concentrates was infeasible because of its high susceptibility to bacterial degradation. When the preservation of extracted mucilage for periods longer than 24 h was unavoidable—say, for dispatch to a size exclusion chromatography facility—approximately 0.02 % of sodium azide was added as a bacteriostatic agent, after which the solution was promptly refrigerated to deter microbial growth.

Lyophilization and Gravimetry

The unknown polysaccharide content in mucilage extracts was determined by freeze drying (or lyophilizing) the filtered aqueous solution to remove water, and weighing the

remnant dry solid yield. First, a known volume of the solution, usually in the range of 5–25 mL, was accurately measured out into a clean glass vial or centrifuge tube by means of a calibrated micropipette; the dry weight of the vessel, as well as its weight inclusive of the sample, were carefully recorded using a precision microbalance (XS64, Mettler Toledo) of least count 0.1 mg. The solution was then frozen overnight in a refrigerator ($T \simeq -18\,°\mathrm{C}$), with the containers resting in an inclined position to maximize the free surface area of the resulting solid plug. Once completely frozen below the eutectic point, the samples were transferred to a vacuum flask, and left attached to a laboratory freeze dryer (77540 FreeZone 12 L, Labconco) for 48–72 h [see Fig. 3.7(a)].

The lyophilizer evacuates the sample flask and maintains a partial vacuum of approximately 13.3 Pa absolute pressure, which is well below the triple point pressure of water ($P_{TP} \simeq 612\,\mathrm{Pa}$). As the frozen mass gradually thaws at room temperature, absorbing latent heat from the environment, the solidified water content in the sample sublimates directly into vapor, and is drawn into the lyophilizer collector (kept at $T = -40\,°\mathrm{C}$) where it is deposited as ice. After all of the ice has vaporized, the non-volatile dissolved constituents in the original solution remain as a solid plug with a characteristic spongy texture [Fig. 3.7(b)]. After drying is complete, the tubes containing the dry residue were retrieved and carefully weighed to ascertain the dissolved polysaccharide content in the original extract. Typically, two or three samples were drawn from each solution and processed separately to give replicate measurements, which were then averaged to minimize experimental error. If reconstitution of the dried polymer was desired, the spongy plug was pulverized by pestle and mortar [Fig. 3.7(c)], and allowed to dissolve gradually in water on a laboratory roller mixer.

B. *Dilute Solution Viscometry*

At the typical concentrations employed in drag reduction tests, aqueous solutions of polymers are often too dilute to permit accurate determination of shear viscosity using conventional cone and plate geometries or double-gap concentric cylinders on the AR-G2 rheometer. Although the solution viscosities, per se, are within the stated measurement range of the instrument, practical limitations (such as environmental noise, temperature fluctuations, and minor errors in calibration or alignment) preclude the high sensitivity required for resolving small changes in viscosity corresponding to systematic variations in polymer concentration in the dilute regime (the latter usually in the parts per million range). Furthermore, the acquisition of noise-free torque data necessitates the use of moderate to large shear rates during measurements, thus making the accurate estimation of zero shear rate viscosity challenging.

For the above reasons, the viscosity of dilute drag-reducing solutions was measured

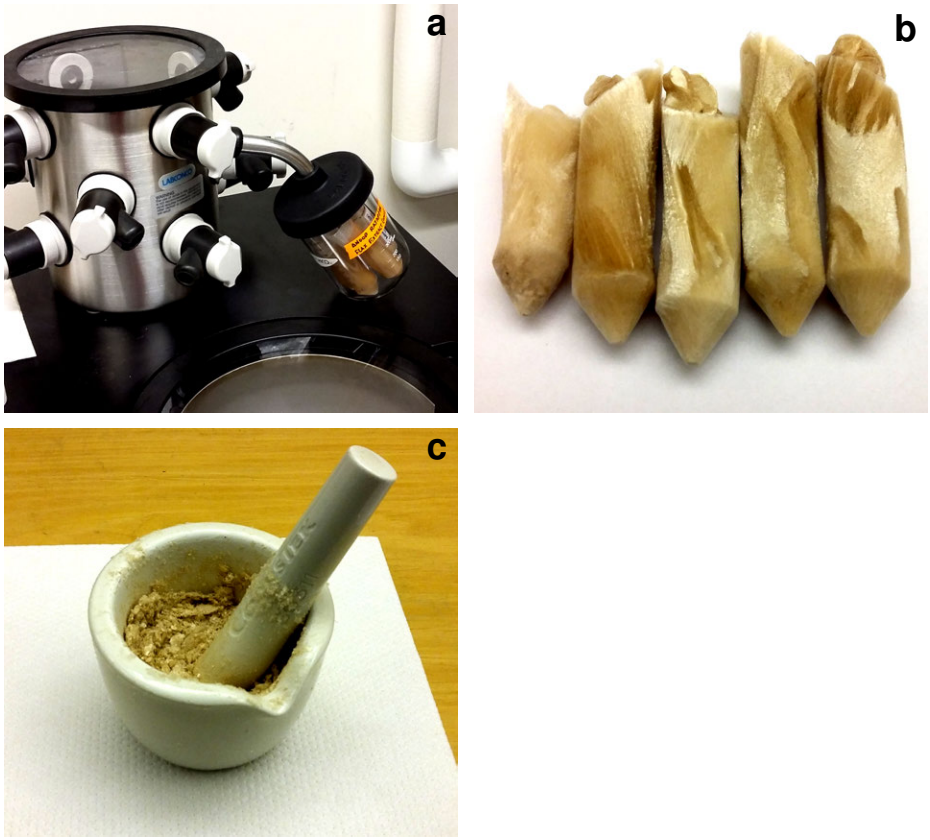

FIGURE 3.7. Lyophilization of aqueous seed mucilage extracts. (a) Frozen mucilage samples placed inside a vacuum flask and connected to one of multiple ports on a laboratory freeze dryer. (b) Spongy plugs of dried mucilage recovered at the end of lyophilization. The pellets have a characteristic porous structure, and the conical points replicate the shape of the centrifuge tubes in which the original samples were frozen. (c) Manual grinding of the freeze-dried mucilage pellets by mortar and pestle, in preparation for reconstitution with water.

by recording the rate of efflux through a glass capillary viscometer, suspended vertically inside a bespoke water bath at a constant, well-controlled temperature. The dimensions of the capillary tube and the efflux volume of the viscometer are designed such that solutions within a narrow range of viscosities, $1\,\text{cSt} \leqslant \nu \leqslant 5\,\text{cSt}$, are resolved into a wide spectrum of efflux times, namely $200\,\text{s} \leqslant \Delta t \leqslant 1000\,\text{s}$; this yields a measurement resolution of 5×10^{-3} cSt for kinematic viscosity, assuming a 1 s accuracy in measuring efflux times (which could be easily achieved using a handheld stopwatch). The capillary viscometer thus offers the requisite sensitivity for differentiating small changes in viscosity at dilute concentrations, and in turn enables the accurate measurement of the intrinsic viscosity of polymers through the use of successive dilution techniques. The experimental setup and test protocols employed in the viscometric characterization of dilute polymer solutions are briefly summarized in this section.

Capillary Viscometry of Dilute Polymer Solutions

The glass capillary viscometer used in this study is a manually operated, suspended level instrument of the Ubbelöhde type (Size 0B, Cannon Instrument Company), with a temperature-independent calibration constant of $\Theta = 5.21 \times 10^{-3}\,\text{mm}^2\,\text{s}^{-2}$ as certified by the manufacturer; the latter corresponds to a baseline efflux time of approximately $\Delta t = 193\,\text{s}$ for pure water at 20 °C. Figure 3.8 shows the bespoke experimental setup constructed to facilitate accurate and reproducible measurements using the capillary viscometer; a schematic sectional view of its main components is shown in Fig. 3.9. The viscometer is clamped in a vertical position by means of a detachable brass holder, and is kept immersed to its full height inside a transparent water bath to ensure isothermal conditions during measurements. The vessel surrounding the viscometer has thin glass walls to minimize thermal resistance, and is equipped with a total immersion thermometer for accurate monitoring of the bath temperature. A thermal jacket encloses the inner bath and is connected via rubber tubes to a laboratory thermal circulator (F12, Julabo), which pumps water around the inner vessel at the desired stable temperature. The outer jacket is fabricated from thick transparent acrylic panels to provide thermal insulation while maintaining visual access to the viscometer bulb; furthermore, its flat rectangular faces reduce optical distortion and affords a clear view of the liquid meniscus during observations. The entire fixture is rigidly mounted on a pneumatically isolated optical table, which provides a stable platform free of mechanical vibrations.

Viscosity measurements were performed largely in accordance with the recommended procedure outlined in ASTM standards D445 and D446.[210,211] A typical experiment generally proceeded as follows: A small quantity of the test solution, $\sim$ 10–15 mL, was introduced into the bulb R of the (cleaned and dried) viscometer through the large tube A.

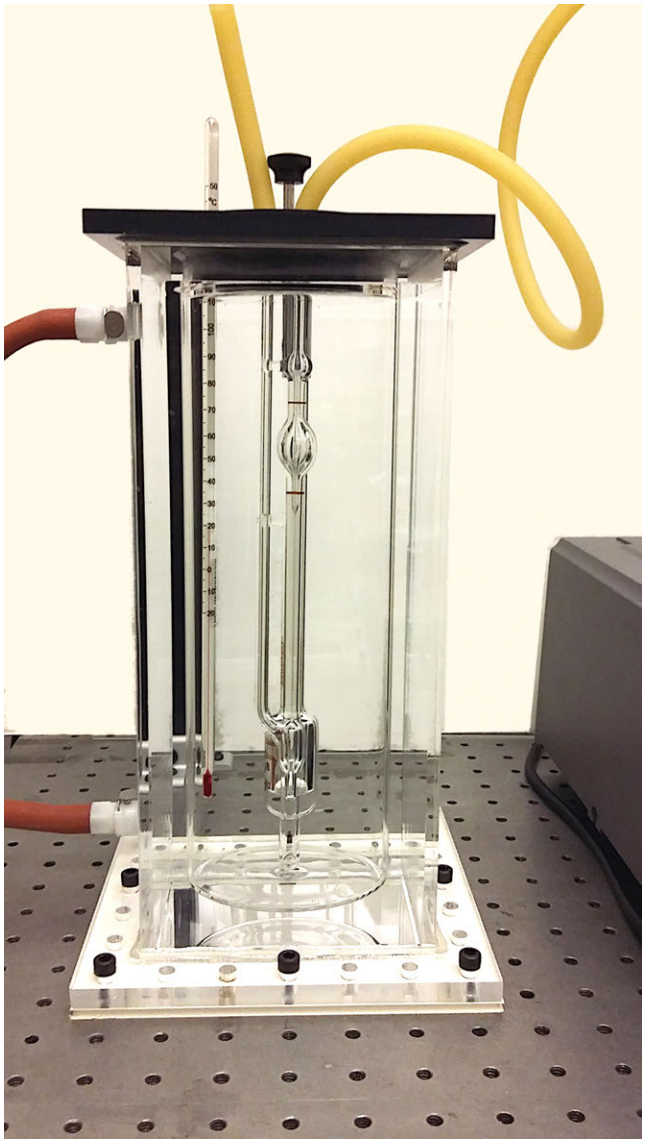

FIGURE 3.8. The bespoke experimental setup used for viscosity measurements on dilute drag-reducing polymer solutions. Visible in the photograph are the Ubbelöhde capillary viscometer, the open glass vessel forming the water bath, the total immersion thermometer monitoring the bath temperature, and the acrylic thermal jacket surrounding the inner vessel. The red tubes are connected to a thermal circulator (not in the picture) and convey water to and from the outer jacket at the desired temperature. The yellow tubes emerging from the top are removable suction and vent lines attached to the corresponding tubes of the viscometer. Also see Fig. 3.9(a).

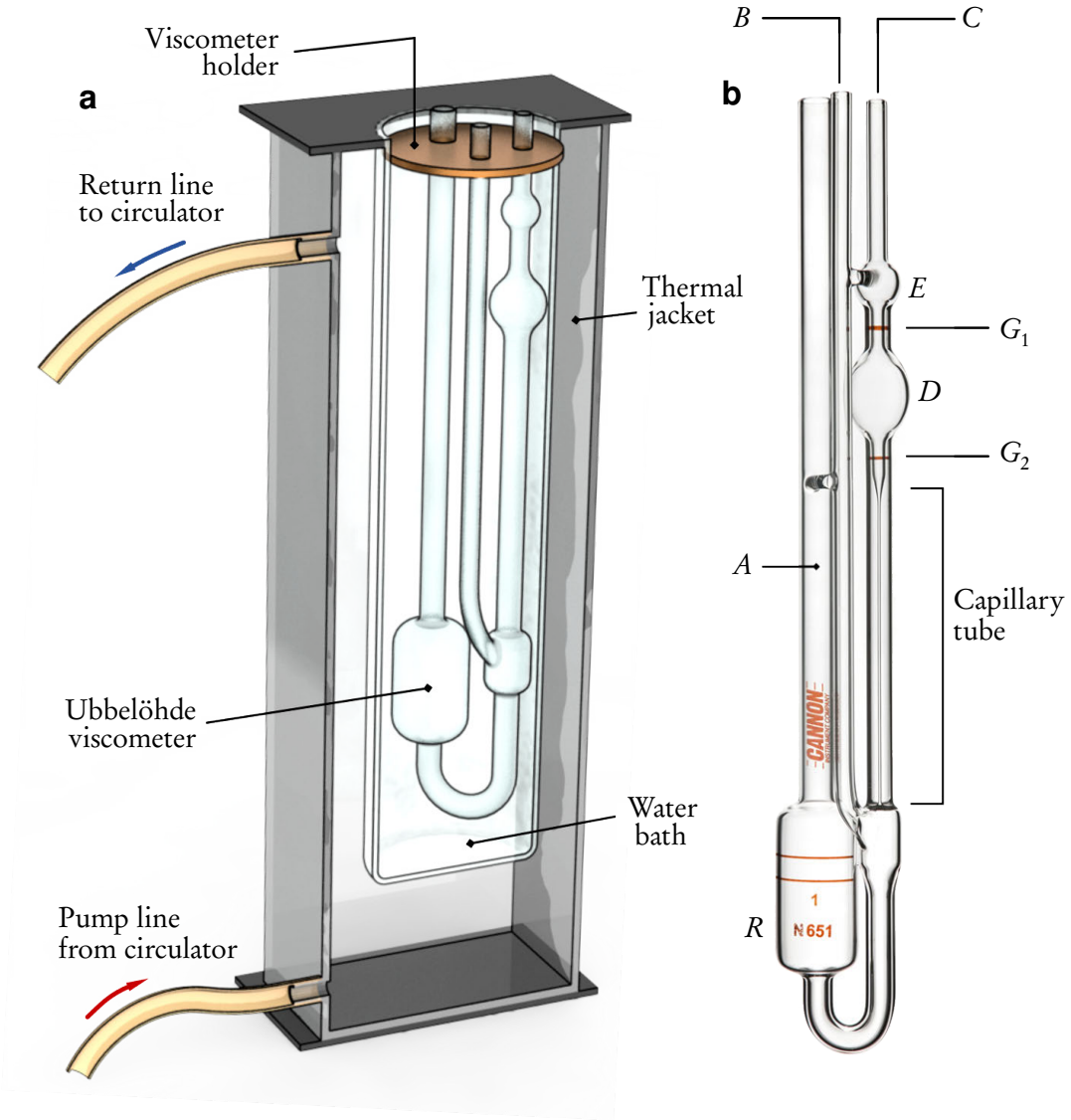

FIGURE 3.9. (a) Schematic sectional view of the experimental setup shown in Fig. 3.8, identifying key internal components. The bath thermometer has been omitted from the diagram for clarity. (b) An Ubbelöhde glass capillary viscometer of the type used for viscosity measurements. A Size 1 viscometer is shown here for illustration, whereas a Size 0B instrument was used in actual experiments. The main parts have been labeled in accordance with the discussion in the text. For image source and attribution, see p. 185.

The solution was then allowed to stand for approximately 15–20 min to attain thermal equilibrium with the water bath, the latter having been pre-heated to the required temperature by running the thermal circulator for about an hour in advance of the test. After sufficient time had elapsed for the solution to reach test temperature, a finger was used to firmly occlude the vent *B*, and moderate suction ($\simeq -100$ mbar gauge) was applied to the tube *C* using a vacuum blotting pump (VacuGene, Amersham Biosciences) to draw the sample up through the capillary tube into the bulbs *D* and *E*. Suctioning was continued until the upper bulb *E* was approximately half-filled with liquid. The suction was then released and the finger was removed to unplug the tube *B*; this breaks the liquid column just beneath the capillary tube, allowing the updrawn sample to begin draining into ambient pressure under gravity. The time of travel of the liquid meniscus between the graduation marks G_1 and G_2 was recorded manually using a calibrated, NIST-traceable laboratory digital timer, with a least count of 1 s. After the liquid had drained completely into the lower reservoir *R*, the experiment was repeated (without recharging the viscometer) until a minimum of three concordant readings for the efflux time were obtained.

Throughout each experiment, great care was exercised to prevent entrainment of air bubbles into the capillary tube or bulbs that could interfere with the free draining of the liquid under gravity; if spurious air bubbles were detected at any stage during the test, the experiment was aborted and the entire process was restarted from the beginning using a fresh aliquot of the solution. At the conclusion of tests on a given sample, the viscometer was promptly emptied of its contents, and vigorously cleaned by flushing deionized water through the tubes, followed by anhydrous ethanol. Any residual traces of ethanol was thoroughly dried off by purging with a stream of compressed nitrogen gas, before the viscometer was returned to the bath for use in subsequent experiments.

The viscosity η of the polymer solution at the test temperature can be derived by multiplying the efflux time Δt with the density ρ (assumed equal to the solvent density for dilute solutions), and the viscometer constant Θ:

$$\eta = \rho \Theta \Delta t \ . \tag{3.31}$$

In routine practice, however, the *relative viscosity* η_r of the solution was directly estimated by computing the ratio of efflux times

$$\eta_r = \frac{\eta}{\eta_s} = \frac{\Delta t}{\Delta t_s} \ , \tag{3.32}$$

where η_s and Δt_s denote, respectively, the viscosity and the efflux time of the pure solvent (water) at the test temperature, the latter determined at least once during each set of experimental measurements. This approach inherently compensates for small drifts in viscometer calibration, arising from, say, contaminant adsorption on the capillary walls, or the gradual wear of the capillary tube under repeated cycles of cleaning and reuse.

Determination of Intrinsic Viscosity

In addition to routine measurements of the viscosity η of dilute solutions used in flow tests, capillary viscometry was also utilized to estimate the intrinsic viscosity $[\eta]$ of various drag-reducing polymer species in solution. This was accomplished via the conventional method of successive dilution, which involves determining the *reduced viscosity*,

$$\eta_{\text{red}} = \frac{\eta - \eta_s}{\eta_s c}, \tag{3.33}$$

and the *inherent viscosity*,

$$\eta_{\text{inh}} = \frac{1}{c} \ln\left(\frac{\eta}{\eta_s}\right), \tag{3.34}$$

for a series of solutions of progressively smaller concentration c, and extrapolating both quantities simultaneously to the limit of infinite dilution, $c \to 0$.[212] The Ubbelöhde viscometer features an integral dilution bulb R which enabled the dilution of samples in situ, eliminating the need for repeated emptying and recharging of the bulb at each dilution step, a process susceptible to cross-contamination and concentration errors. The viscometer bulb was charged initially with $\sim$ 7–8 mL of the most concentrated solution in the series; subsequent dilutions were achieved simply by adding fresh solvent, usually in increments of 1–2 mL, until the total sample volume reached the maximum capacity of the bulb, $\simeq$ 15–16 mL. The diluent was dispensed using a calibrated micropipette or syringe pump, the accuracy of which was verified beforehand by repeatedly measuring out a set volume of liquid and weighing it on a precision microbalance. Furthermore, to prevent the added liquid from sticking to the walls of tube A and not reaching the bulb, the requisite quantity of diluent was introduced directly into the sample volume through a long needle, carefully avoiding all contact with the glass walls. Afterwards, the solution was mixed gently for a few seconds by sparging clean air through the open vent tube B. The stirred solution was then let to stand for 15–20 min in the controlled-temperature bath to reach diffusive and thermal equilibrium, after which viscosity measurements were performed as usual according to the standard procedure described previously. For a given polymer species, several iterations of the experiment were typically required before a suitable range of concentrations, amenable to linear extrapolation, could be correctly identified through trial and error analysis of the viscosity data.

Figure 3.10 shows an example of the typical viscosity data for flexible, neutral polymer chains in solution, which in this case was an aqueous PEO sample (Sigma-Aldrich Inc) of nominal molar mass 5 MDa. Successive dilution tests were performed at a temperature of $T = 21\,°\text{C}$, and the results have been presented in the form of a *Huggins-Kraemer plot*, which shows both the reduced and inherent viscosities as a function of the polymer

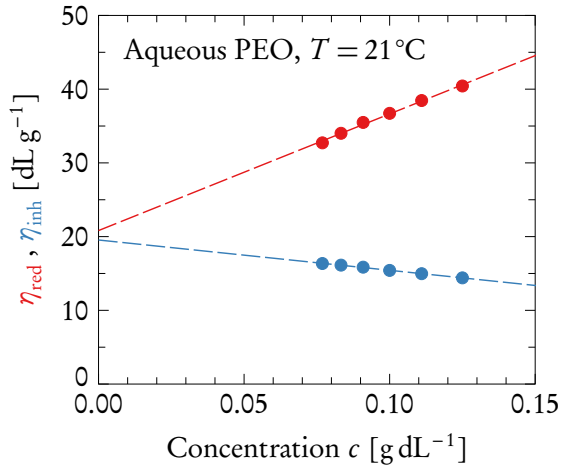

FIGURE 3.10. Huggins-Kraemer extrapolation of experimental viscosity data for a sample of aqueous polyethylene oxide, measured by successive dilution at $T = 21\,°C$. The red and blue lines denote, respectively, least-squares fits to the Huggins relation, Eq. 3.35, and the Kraemer relation, Eq. 3.36; their common intercept at zero concentration provides the intrinsic viscosity $[\eta] = (20.2 \pm 0.5)\,\mathrm{dL\,g^{-1}}$ of the PEO chains in solution.

concentration c. At the start of the experiment, the viscometer was charged with 8 mL of sample at a initial concentration of $c_0 = 1.25 \times 10^{-1}\,\mathrm{dL\,g^{-1}}$. After five dilutions steps, each performed by adding 1 mL of the solvent (water) to the bulb, the final sample volume reached 13 mL, with a resulting concentration of $c_5 = (8/13)\,c_0 = 7.69 \times 10^{-2}\,\mathrm{dL\,g^{-1}}$. As evident from the plot, both η_{red} and η_{inh} exhibit a linear dependence on the concentration c within this range, in accordance with the Huggins equation,

$$\eta_{red} = [\eta] + k_H [\eta]^2 c + O(c^2)\,, \tag{3.35}$$

and the Kraemer equation,

$$\eta_{inh} = [\eta] - k_K [\eta]^2 c + O(c^2)\,, \tag{3.36}$$

respectively;[212] the common intercept of the two lines, when extended to $c = 0$, gives the intrinsic viscosity $[\eta]$ of the polymer molecules in solution. In the example above, the Huggins and Kraemer relations respectively yielded the intercepts $[\eta] = (20.8 \pm 0.5)\,\mathrm{dL\,g^{-1}}$ and $[\eta] = (19.5 \pm 0.1)\,\mathrm{dL\,g^{-1}}$ at zero concentration; the two values are concordant within the limits of experimental error, and their arithmetic average, $[\eta] = (20.2 \pm 0.5)\,\mathrm{dL\,g^{-1}}$, can be regarded as an estimate of the intrinsic viscosity of this particular sample of PEO in water. (Uncertainties reported here represent standard errors.)

A direct consequence of the definitions of η_{red} and η_{inh} (given by Eqs. 3.33 and 3.34) is that the slope k_{H} appearing in Eq. 3.35, called the *Huggins constant*, is mathematically related to the slope k_{K} in the Kramer relation, Eq. 3.35.[212] Indeed, for dilute concentrations such that $x = \eta/\eta_s$ is close to unity, the natural logarithm in the definition of the inherent viscosity, Eq. 3.34, can be expanded in a Taylor series about $x = 1$:

$$\ln x = (x-1) - \frac{1}{2}(x-1)^2 + \frac{1}{3}(x-1)^3 \cdots, \quad 0 < x \leqslant 2 \tag{3.37}$$

Combined with Eq. 3.34, this gives

$$\eta_{\text{inh}} = \frac{1}{c}\ln\left(\frac{\eta}{\eta_s}\right) = \frac{1}{c}\left[\left(\frac{\eta}{\eta_s}-1\right) - \frac{1}{2}\left(\frac{\eta}{\eta_s}-1\right)^2 + \frac{1}{3}\left(\frac{\eta}{\eta_s}-1\right)^3 \cdots\right] \tag{3.38}$$

$$= \left(\frac{\eta-\eta_s}{\eta_s c}\right) - \frac{c}{2}\left(\frac{\eta-\eta_s}{\eta_s c}\right)^2 + \cdots \tag{3.39}$$

Recognizing the quantity in parenthesis to be the reduced viscosity η_{red} (cf. Eq. 3.33), and substituting the Huggins relation, Eq. 3.35, we get

$$\eta_{\text{inh}} = \left([\eta] + k_{\text{H}}[\eta]^2 c\right) - \frac{c}{2}\left([\eta] + k_{\text{H}}[\eta]^2 c\right)^2 + \cdots \tag{3.40}$$

$$= [\eta] + k_{\text{H}}[\eta]^2 c - \frac{c}{2}[\eta]^2 + O(c^2) \tag{3.41}$$

$$= [\eta] + \left(k_{\text{H}} - \frac{1}{2}\right)[\eta]^2 c + O(c^2)\,. \tag{3.42}$$

Comparing this result with the Kraemer expansion, Eq. 3.36, and equating like terms of order c immediately yields

$$k_{\text{H}} + k_{\text{K}} = \frac{1}{2}\,. \tag{3.43}$$

The above constraint serves as an independent check for verifying the accuracy of linear extrapolations used to infer the intrinsic viscosity from experimental data;[212] in actual practice, linear fits with concordant intercepts and slopes satisfying $k_{\text{H}} + k_{\text{K}} = 0.50 \pm 0.03$ (i.e. a deviation of 6 %) were deemed acceptable. For example, the two lines in Fig. 3.10 respectively correspond to slopes of $k_{\text{H}} = 0.39$ and $k_{\text{K}} = 0.10$; this yields $k_{\text{H}} + k_{\text{K}} = 0.49$ which satisfies the above criterion, confirming extrapolation in the linear regime.

Inference of Macromolecular Properties

Knowledge of the intrinsic viscosity permits the straightforward estimation of a number of other elementary macromolecular properties, such as the average molar mass of the

polymer molecules and the size of their random coils in solution. For example, the intrinsic viscosity $[\eta]$ can be used to infer a viscosity-averaged molar mass M_v for the polymer sample, by means of the empirical *Mark-Houwink-Sakurada* equation[84,213]

$$[\eta] = K \cdot M_v^a \,. \tag{3.44}$$

The Mark-Houwink parameters K and a for common polymers can be found in the scientific literature, and are routinely tabulated in polymer reference handbooks. The Mark-Houwink exponent a is, in turn, related to the *Flory exponent* ν by[84,213]

$$a = 3\nu - 1 \,. \tag{3.45}$$

The characteristic exponent ν yields information about the quality of the solvent and the conformation adopted by polymer chains in solution; its value varies from $\nu = 1/3$ for collapsed chains (or dense globules) in poor solvents, to $\nu = 1/2$ for unperturbed random coils in theta solvents, $\nu = 3/5$ for expanded coils in good solvents, and $\nu = 1$ for rigid rod-like molecules.[84,213]

For polydisperse samples, the viscosity-averaged molar mass in Eq. 3.44 is given by

$$M_v = \left[\int_0^\infty x(M)\, M^{1+a}\, \mathrm{d}M \Big/ \int_0^\infty x(M)\, M\, \mathrm{d}M \right]^{1/a}, \tag{3.46}$$

where $x(M)\,\mathrm{d}M$ is the mole fraction of polymer chains having molar masses between M and $M + \mathrm{d}M$.[213] Notice that for $a = 1$, the above equation gives $M_v = M_w$, the weight-averaged molar mass of the sample; for values of a close to one, therefore, M_w may be reasonably approximated by M_v for polymer samples of relatively low polydispersity.[213] The mean radius of gyration R_g of dissolved polymer coils can then be related to the weight-averaged molar mass by a power law of the form

$$R_g = K_R \cdot M_w^\nu \,, \tag{3.47}$$

where K_R is an empirical prefactor and ν the Flory exponent, both typically determined using static light scattering experiments.[213]

As an illustration, consider the PEO sample analyzed in Fig. 3.10; its intrinsic viscosity, as determined from Huggins-Kraemer extrapolation, was $[\eta] = 20.2\,\mathrm{dL\,g^{-1}}$ at $T = 21\,°\mathrm{C}$. The Mark-Houwink-Sakurada relation for aqueous PEO, as reported in the literature, reads (cf. Eq. 3.44):[214]

$$[\eta] = \left\{ 1.25 \times 10^{-4}\,\mathrm{dL/g(g/mol)^{-0.78}} \right\} \cdot M_v^{0.78} \,, \quad (T = 30\,°\mathrm{C}). \tag{3.48}$$

Similarly, the radius of gyration for PEO chains in water is given by (cf. Eq. 3.47)[215]

$$R_g = \left\{2.15 \times 10^{-2}\,\mathrm{nm}\,(\mathrm{g/mol})^{-0.58}\right\} \cdot M_w^{0.58}\,, \quad (T = 30\,^\circ\mathrm{C}). \tag{3.49}$$

Neglecting the disparity in solution temperatures, Eq. 3.48 yields a viscosity-averaged molar mass of $M_v = 4.76 \times 10^6\,\mathrm{g\,mol^{-1}}$ for the PEO sample, which is consistent with the value of $5 \times 10^6\,\mathrm{g\,mol^{-1}}$ reported by the manufacturer. Setting $M_w \approx M_v$, Eq. 3.49 then provides an estimate for the mean radius of gyration, $R_g = 160\,\mathrm{nm}$, of the flexible PEO coils in solution. Note that Eq. 3.49 indicates a Flory exponent of $\nu = 0.58$, which is quite close to the theoretical value of 0.60 for expanded coils, confirming that water is indeed a good solvent for PEO. Furthermore, Eq. 3.45 gives $a = 3(0.58) - 1 = 0.74$, which is in excellent agreement with the exponent in Eq. 3.48, the slight difference in values quite explicable considering the disparate sources and experiments from which Eqs. 3.48 and 3.49 were derived.

Finally, the experimentally measured intrinsic viscosity can also be used to estimate the *critical overlap concentration* c^* of the dissolved polymer, which characterizes the onset of interchain steric and hydrodynamic interactions between adjacent polymer coils in solution. At $c = c^*$, the polymer concentration within the pervaded volume of a single random coil becomes comparable to the gross concentration of the polymer species in the solution, and the equilibrium conformation of dissolved coils begins to depart from their ideal random configuration.[216] Although an exact value for the overlap concentration is difficult to prescribe unambiguously, the simple definition proposed by Graessley (1980)[217] sets c^* to be the concentration at which the average chain spacing is $2R_g$, namely twice the radius of gyration of individual coils at infinite dilution:

$$c^* = \frac{M}{N_A (2R_g)^3}\,. \tag{3.50}$$

Here, M is the molar mass of the polymer chain, and N_A is the Avogadro constant. For *flexible random coils*, the radius of gyration is given by[84,213]

$$R_g^2 = \frac{1}{6}\left\langle R^2 \right\rangle_\theta \tag{3.51}$$

where $\langle R^2 \rangle_\theta$, the mean square end-to-end distance of an unperturbed chain, is related to the intrinsic viscosity $[\eta]$ by the Flory-Fox equation,[213]

$$[\eta] = \phi \frac{\langle R^2 \rangle_\theta^{3/2}}{M}\,. \tag{3.52}$$

Here $\phi \simeq 2.5 \times 10^{23}\,\mathrm{mol}^{-1}$ is the Flory coefficient for an isolated Gaussian coil in the non-draining limit.[217] Combining Eqs. 3.50, 3.51, and 3.52 yields the classical result for flexible polymers, first derived by Graessley:[217]

$$c^* = \left(\frac{6^{3/2}\phi}{8N_A}\right)\frac{1}{[\eta]} \simeq \frac{0.77}{[\eta]}\,. \tag{3.53}$$

For the particular PEO sample in Fig. 3.10, the above equation therefore predicts a critical overlap concentration of $c^* = 3.81 \times 10^{-1}\,\mathrm{g\,L}^{-1}$, or approximately 380 ppm.

Notice that Eqs. 3.51 and 3.52 are strictly valid only for flexible random coils in theta solvents. It follows, consequently, that the prefactor 0.77 in Eq. 3.53 will differ for other molecular conformations, such as semiflexible chains or rigid rods. Indeed, a more involved analysis is required in these cases to derive the appropriate analog of Eq. 3.52 relating the intrinsic viscosity to chain dimensions; see, for instance, the theory for worm-like chains by Yamakawa and Fujii (1974).[218] Nonetheless, the scaling relation $c^* \sim M \sim 1/[\eta]$ still holds, with the result that $c^* \simeq 1/[\eta]$ may be employed as a generic approximation for the overlap concentration regardless of the actual chain conformation, accurate to within a multiplicative constant of order one.

C. *Capillary Breakup Extensional Rheometry*

The characteristic relaxation time for dissolved polymer chains in dilute solutions can be inferred theoretically from the intrinsic viscosity $[\eta]$, and is given by[84,213]

$$\lambda_Z \simeq \frac{[\eta]M_w\eta_s}{RT}\,, \tag{3.54}$$

where M_w is the (weight-averaged) molar mass of the polymer, η_s is the solvent viscosity, T is the solution temperature, and $R = N_A k_B$ is the universal gas constant. However, in flows that entail significant deformation of dissolved chains, such as extensional flows or turbulence, the effective relaxation time λ of the stretched and 'unraveled' polymer coils is often larger than the theoretical estimate λ_Z above, even as the solution remains 'canonically' dilute in weak flows such as steady shear.[216] When the rate of elongation is sufficiently large, the pervaded volume of the chains increase substantially as they undergo coil-stretch transition, resulting in intermolecular interactions which, in effect, render the solution no longer dilute.[216,219] This, in turn, manifests as a concentration dependence of the effective relaxation time λ which persists down to concentrations much below c^*, the usual threshold for single chain dynamics in weak laminar shear flows.

To probe the dynamics of polymer chains at concentrations and deformation modes relevant to drag reduction, the longest relaxation time λ in uniaxial extensional flow was

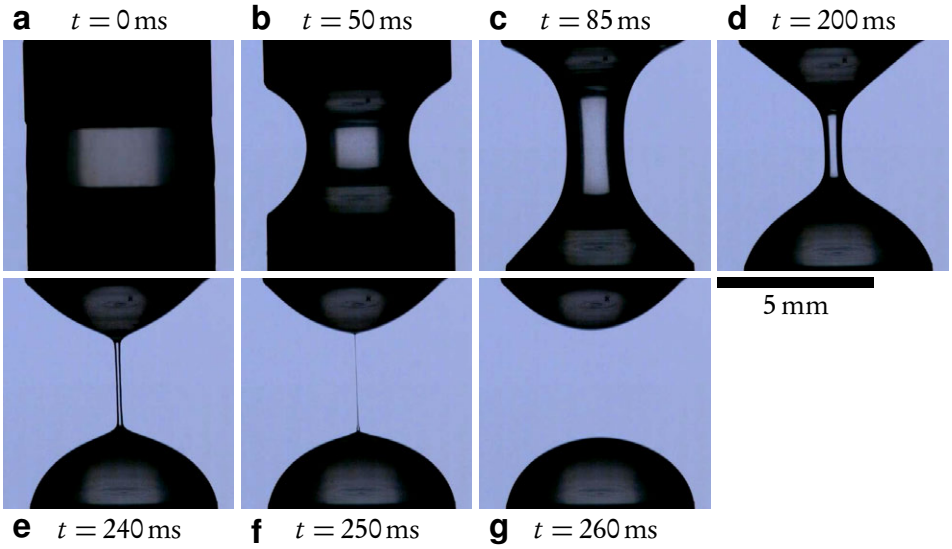

FIGURE 3.11. A representative sequence of frames drawn from the high-speed (5 kfps) recording of a capillary breakup experiment on the CaBER device. The sample being tested is a semi-dilute extract ($c = 11\,\mathrm{g\,L^{-1}}$) of flaxseed mucilage in water. The images show (a) the cylindrical bridge of liquid sample at the start of the test; (b) the plates approximately halfway through retraction (the 'strike'); (c) the stretched liquid bridge immediately after the plates have come to rest; (d) and (e) capillary-driven self-thinning of the unstable liquid filament; (f) the liquid thread seen just before breakup; and (g) the fully separated liquid lenses on the top and bottom plates post filament breakup. The annotations indicate the elapsed time t since the beginning of the experiment.

inferred directly by observing the self-thinning of liquid filaments on a *capillary breakup extensional rheometer* (*CaBER*), at dilute concentrations similar to those employed in flow measurements.[220] Filament thinning experiments were performed using a bespoke CaBER device built by Du (2018), of which a full description can be found in Ref. [221]. Briefly, the setup comprises a pair of coaxial cylindrical pins with flat parallel faces called 'plates,' each of diameter $d_0 = 6\,\mathrm{mm}$, and driven independently by two vertically mounted, high-speed linear servomotors. At the start of each experiment, a small quantity of test fluid was deposited in the millimetric gap between the plates, to create a cylindrical liquid bridge of the same diameter as the plate faces and held in place by capillarity [see Fig. 3.11(a)]. The initial gap was set at $l_0 = 2.0\,\mathrm{mm}$ for all tests reported in this study, and the exact volume of sample required, $V = \pi d_0^2 l_0/4 \simeq 57\,\mu\mathrm{L}$, was dispensed using a calibrated micropipette to prevent underfilling or overfilling of the gap. The plates were then rapidly separated to a final gap of $l = 7.0\,\mathrm{mm}$ within a short 'strike' time of $\sim 50\,\mathrm{ms}$ [Fig. 3.11(b)], imposing an axial step strain of $\epsilon = \ln(l/l_0) \simeq 1.25$ on the sample. To

mitigate inertial effects during the 'strike' (i.e. the gap opening step), the linear motors were programmed to withdraw the two pins synchronously and symmetrically away from the sample midplane, thereby keeping the midpoint of the fluid column stationary. The sudden change in aspect ratio induces a capillary instability in the stretched liquid bridge, which results in the formation and subsequent self-thinning of a slender filament connecting the liquid lenses attached to the top and bottom plates [see Fig. 3.11, panels (c–g)]. The evolution of the filament diameter was tracked as a function of time using a CCD laser micrometer (IG-028, Keyence Corp.), which had a measurement resolution of 5 µm, a minimum detection threshold of 100 µm, and a sampling frequency of 1 kHz. Concurrently, the thinning liquid thread was imaged using a high-speed camera (Phantom Miro 320S, Vision Research Inc.) at frame rates of 1–4 kfps, occasionally attached to a high magnification lens (12X Zoom Lens System, Navitar Inc.) for resolving the thin filament diameters obtained in the case of dilute, weakly elastic solutions.

Depending on the relative dominance of forces that govern the thinning dynamics, different types of self-thinning behavior can be observed, marked by distinctive trends in the temporal evolution of the filament diameter. In Newtonian fluids, the capillary force that drives the thinning flow is resisted mostly by viscous stresses in the filament, yielding a midpoint diameter $d(t)$ that decreases linearly with time t:[220]

$$\frac{d(t)}{d_0} = 0.1418\,\frac{\sigma}{\eta_s d_0}\,(t_c - t)\ . \tag{3.55}$$

Here d_0 is the diameter of the initial liquid plug (which, in the present case, is set by the diameter of the rheometer plates), σ is the interfacial tension at the liquid-air boundary, η_s is dynamic viscosity of the liquid, and t_c denotes the time of breakup of the filament neck. In the case of viscoelastic fluids, on the other hand, a slender cylindrical thread forms in which the uniaxial extensional draining flow causes the progressive elongation and unraveling of dissolved polymer chains, resulting in a concomitant rise in the transient extensional viscosity.[220,222] In this *elasto-capillary thinning* regime wherein the capillary force is balanced the by non-linear growth in polymer elastic stresses, the filament diameter $d(t)$ decreases exponentially with time t according to[220,222]

$$\frac{d(t)}{d_0} = \left(\frac{G d_0}{4\sigma}\right)^{1/3} \exp\left(-\frac{t}{3\lambda}\right)\,, \tag{3.56}$$

where G and λ denote, respectively, the elastic modulus and the longest relaxation time of the polymer chains in solution. A least-squares regression of the experimental thinning profile $d(t)$ to the exponential form predicted by Eq. 3.56 directly yields the relaxation time λ of the polymer chains in solution.[219,220,222,223]

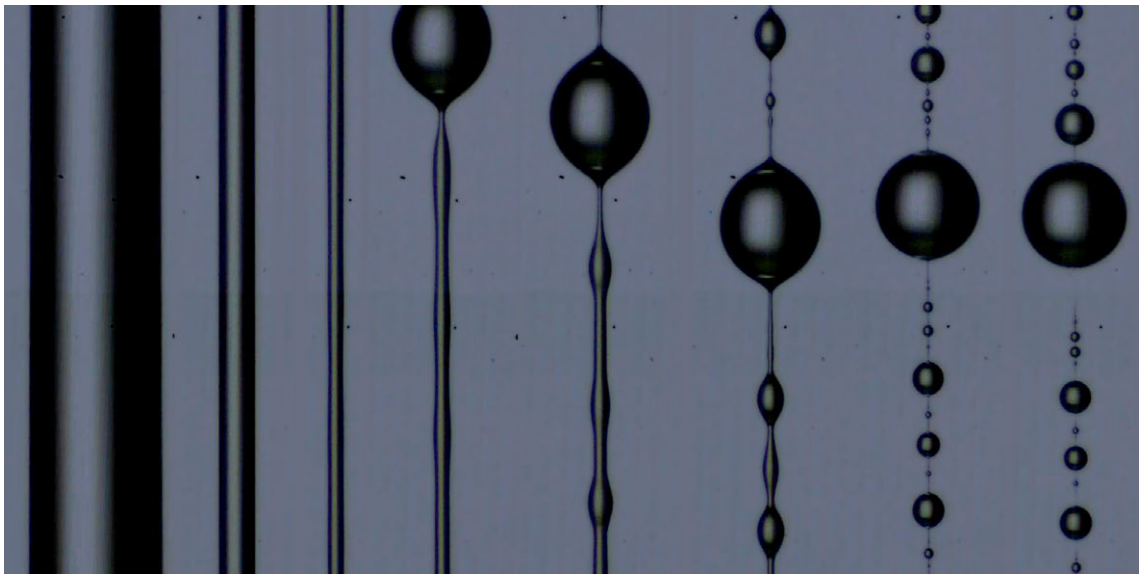

FIGURE 3.12. A composite image showing the inception and development of the beads-on-a-string (BoaS) instability in the terminal stages of self-thinning of an elastic liquid filament; time in this montage progresses from left to right. The frames were captured at 1 kfps using a high-speed camera (Phantom Miro 320S) with an attached high-magnification lens (Navitar 12X Zoom Lens System). The viscoelastic liquid depicted here is a solution of $0.56\,\mathrm{g\,L^{-1}}$ of polyethylene oxide (nominal molar mass 5 MDa) and $0.56\,\mathrm{g\,L^{-1}}$ of sodium dodecyl sulfate (SDS) in a mixture comprising equal parts by volume of glycerol and water.

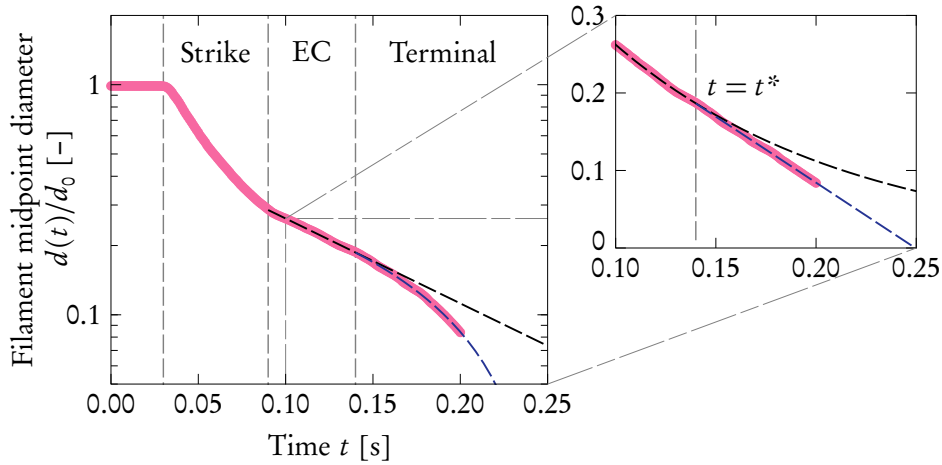

FIGURE 3.13. Evolution of the non-dimensional filament diameter $d(t)/d_0$ with time t, for the CaBER experiment shown in Fig. 3.11. The strike period, the elasto-capillary (EC) region, and the terminal regime are demarcated based on the high-speed recording of the experiment and the observed thinning profile. The black and blue dashed curves denote least-squares fits to Eqs. 3.56 and 3.57, respectively, in the elasto-capillary and terminal regimes. The inset replots the data from the final stages of filament thinning on linear axes, showing a clear departure from the exponential thinning law, Eq. 3.56, towards linear thinning at terminal viscosity, given by Eq. 3.57, beyond the crossover time $t \geqslant t^* \simeq 0.14\,\mathrm{s}$.

The steady increase in the extensional viscosity of the filament in the elasto-capillary regime is ultimately bounded by the finite extensibility of real polymer chains.[220] As the stretched chains eventually reach their maximal (though not necessarily full) extension, the apparent extensional viscosity saturates at a constant value $\eta_{E,\infty}$ (called the *terminal elongational viscosity*), and the subsequent thinning of the filament is linear in time similar to a Newtonian thread of constant, albeit highly anisotropic, viscosity:[220,224,225]

$$\frac{d(t)}{d_0} = \frac{\sigma}{d_0 \eta_{E,\infty}} (t_c - t) \,. \tag{3.57}$$

The terminal extensional viscosity $\eta_{E,\infty}$ can be shown to be related to the diameter $d^* = d(t^*)$ of the filament at the time of crossover, $t = t^*$, from elasto-capillary thinning to the terminal regime:[224,225]

$$\eta_{E,\infty} = \frac{3\sigma\lambda}{d^*} \,. \tag{3.58}$$

The terminal regime may not be observable in solutions of highly extensible polymers, if the filament diameter becomes too small to be discernible on the laser micrometer or the

high speed imaging system. Occasionally, diameter measurements are vitiated in the later stages of the thinning process by the development of an 'iterated stretching' instability, leading to a characteristic *beads-on-a-string* (*BoaS*) morphology (see Fig. 3.12) comprising multiple generations of spherical droplets (the 'beads') connected by thin fluid ligaments (the 'string').[226]

Figure 3.13 shows the experimentally observed evolution of the filament diameter for a semi-dilute solution ($c = 11\,\mathrm{g\,L^{-1}}$, $c\,[\eta] \simeq 11$) of aqueous mucilage extracted from flax seeds. Soon after the plates come to rest after separation, elasto-capillary thinning commences at around $t \simeq 90\,\mathrm{ms}$, and the filament diameter decreases exponentially with time; a least-squares regression of the measured filament diameter $d(t)$ to Eq. 3.56 in this region yields a relaxation time of $\lambda = 39\,\mathrm{ms}$. A crossover to terminal behavior is observed at $t^* \simeq 140\,\mathrm{ms}$, corresponding to a filament diamater of $d^* = 1.12\,\mathrm{mm}$; the inset panel shows a replot of the terminal regime in linear axes, confirming that the diameter indeed decreases linearly in time. A least-squares fit of Eq. 3.57 then yields a terminal extensional viscosity of $\eta_{E,\infty} = 7.1\,\mathrm{Pa\,s}$, and a predicted breakup time of $t_c = 250\,\mathrm{ms}$; these values are in good agreement, respectively, with the terminal viscosity $\eta_{E,\infty} = 7.6\,\mathrm{Pa\,s}$ anticipated from Eq. 3.58 (for $\sigma = 72.6\,\mathrm{mN\,m^{-1}}$, the surface tension of water at 21 °C), and the experimentally observed filament breakup time of $t_c = 245\,\mathrm{ms}$.

The space below is intentionally left blank.

4 *Seed Mucilage: An Eco-Friendly Drag Reducer for Aqueous Flows*

The high cost of synthetic long chain polymers has been a key impediment limiting the widespread adoption of polymer drag reduction techniques in large-scale engineering systems, including marine drag reduction. Despite showing considerable promise as an effective strategy for hydrodynamic drag mitigation on ships and underwater vessels, the prohibitive cost of synthetic polymers has largely precluded their deployment in commercial marine operations. By means of experimental friction measurements in turbulent Taylor-Couette flow, we show in this chapter that the inexpensive, high molar mass polysaccharides exuded in flaxseed mucilage display drag reduction efficacy and flow longevity comparable to PEO, a widely used synthetic drag-reducing polymer. This suggests the possibility of utilizing aqueous mucilage extracted from seed bran as a low-cost, eco-friendly, and biodegradable alternative to synthetic polymers for cost-effective drag reduction in marine and naval applications.

I. Introduction

As reviewed in §2.I, the addition of small quantities of soluble, high molar mass polymer chains has long been known to yield large reductions in the frictional pressure drop and skin friction drag in turbulent pipe and boundary layer flows.[44,59] Given the efficacy of this technique, it is perhaps unsurprising that the ejection of drag-reducing polymers into the boundary layer has been explored over the years as a prospective technique for the mitigation of hydrodynamic drag on marine and naval vessels.[4,44] Skin friction on the hull accounts for about 50 % of the total drag on ships, and 60 % of the drag on submarines;[4] an estimated 60 % of the propulsive power of a typical ship is expended in overcoming this frictional resistance.[5] Methods of reducing skin friction, even moderately, thus offer the potential to generate substantial savings in fuel and operating costs, improve speed and propulsive efficiency, and reduce exhaust emissions into the atmosphere. To put the latter into context, the international shipping industry is estimated to have released 796 million

tonnes of carbon dioxide in 2012, accounting for about 2.2 % of the total anthropogenic emissions for that year; furthermore, carbon emissions from international shipping are projected to increase between 50 % and 250 % by 2050, concomitant with the anticipated growth in global maritime trade.[6]

Experimental friction measurements performed in towing tanks and water tunnels have consistently shown that injecting a concentrated polymer stock solution into the near-wall region of a turbulent boundary layer can produce appreciable reductions in skin friction, approaching levels as high as 75 %.[27] In 1971, full scale drag reduction trials were performed on a 140-feet long coastal minesweeper, the HMS Highburton, during which a concentrated solution of 4 MDa polyethylene oxide (PEO) was ejected through slots in the hull to achieve a nominal polymer concentration of 10 ppm in the boundary layer.[48] Notwithstanding adverse weather conditions and the uneven mixing of the polymer in the boundary layer, a net reduction of 12.7 % in the total drag, and a 17 % decline in diesel consumption, were realized. Despite the considerable body of favorable experimental evidence, the deployment of polymers in real-life marine applications has been largely impeded by practical difficulties, primarily the high material cost of synthetic polymer additives; water-soluble polymers such as PEO are, at present, too expensive to be viable in commercial marine operations.[4,44,227] This, however, provides an opportunity where inexpensive plant-sourced biopolymers can play an impactful role, serving as equally efficacious yet cost-effective alternatives to synthetic drag-reducing agents.

A number of natural polymers have been explored in the literature as potential drag reducers, including water-soluble derivatives of cellulose, various food gums, starch (amylopectin), alginate, carrageenan, chitosan, DNA and even the pectinous sap of plants such as okra.[68,105,109] In particular, past investigations have focused extensively on two relatively expensive food gums, namely xanthan and guar, on account of their widespread use in drilling muds and as proppant suspenders in hydraulic fracturing fluids.[47,111] By contrast, the aqueous mucilage derived from the seeds of plants such as flax, chia or psyllium, despite being inexpensive sources of high molar mass polysaccharides,[32,34,228] has remained largely unexplored as potential drag reducing agents in turbulent flows. The rheology of these seed extracts as liquid food modifiers were studied recently, and flax mucilage, in particular, was shown to dramatically enhance the viscoelasticity of aqueous solutions.[229] Besides their low cost, the use of seed mucilage entails several practical advantages over synthetic drag reducing polymers: It is biodegradable and non-toxic to aquatic life,[109,230–232] these being essential requirements for any drag-reducing additive intended for large-scale release into oceans and navigable water bodies. Furthermore, mucilage can be easily eluted from raw, unprocessed seeds using simple hot water extraction techniques (for example, using low-grade waste heat from the engine or steam boilers), and requires no chemical synthesis or solvents in its production.

With the goal of addressing consumable cost constraints hindering the deployment of polymers in large-scale aqueous flow systems, this chapter explores the use of mucilage extracted from seeds of the flax plant, *Linum usitatissimum*, as an inexpensive source of water-soluble, high molar mass biopolysaccharides that can employed as drag reducers in turbulent flows. The macromolecular and rheological properties of flaxseed mucilage—characterized by means of size exclusion chromatography, dilute solution viscometry, and capillary breakup extensional rheometry—are consistent with the presence of high molar mass polysaccharides, comprising a significant acidic fraction of semiflexible, negatively charged chains. Frictional drag measurements, performed using the bespoke TC apparatus, confirm that the as-extracted mucilage has comparable drag reduction performance under turbulent flow conditions as aqueous PEO solutions, while concurrently offering advantages in terms of raw material cost, availability, and bio-compatibility. Finally, the effects of mechanical degradation and water salinity on the drag reduction efficacy of mucilage are investigated, thereby addressing two exigent concerns pertinent to the use of polymer additives in turbulent internal flows and marine environments.

II. Experimental Characterization of Mucilage

A. *Polysaccharide Extraction and Macromolecular Analysis*

Preparation of Flaxseed Extracts

The water-soluble polysaccharide content, or *mucilage*, was extracted from the mucous epidermis (seed coat) of the brown variety of flax seeds [*Linum usitatissimum*, see Fig. 4.1(a)], by soaking unprocessed, whole seeds in deionized water at 80 °C for 30 min; this protocol has been previously reported in the literature as optimal for the aqueous extraction of mucilage with minimal protein contamination.[112] Solutions of various concentrations were prepared by combining the raw unbroken seeds with warm water at the desired weight ratio, and gently stirring the mixture at 80 °C for 30 min in a covered glass beaker over a laboratory hot plate. To ensure repeatability of the extraction process, the requisite quantity of dry seeds was weighed accurately using a microbalance and added directly to the preheated water inside the beaker, and the temperature of the mixture was carefully monitored throughout the extraction process using a partial immersion thermometer. Afterwards, the clear mucilage solution was promptly separated from the seeds by filtering once through a coarse (grade 90) cotton mesh cloth, allowed to gradually cool to room temperature in a closed container over a laboratory bench roller, and subsequently employed in flow measurements on the same day without any further dilution or processing.

The principal component of the mucilage from flax seeds, constituting approximately

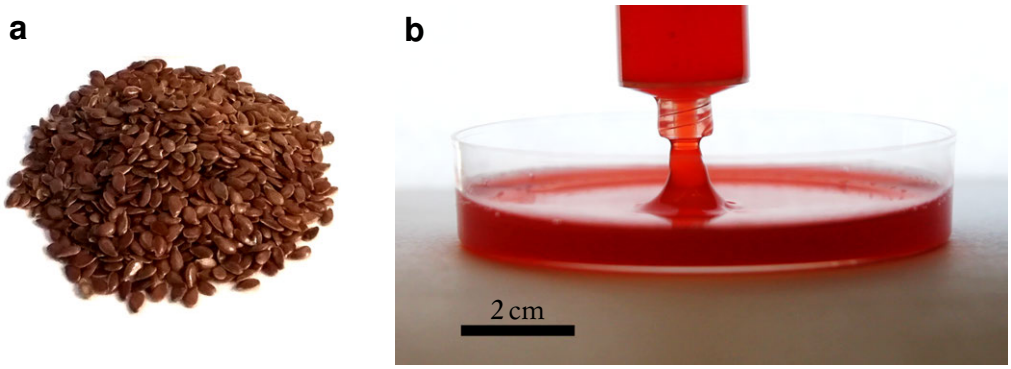

FIGURE 4.1. (a) Brown flaxseed (*Linum usitatissimum*) employed in the extraction of mucilage. (b) 'Open siphoning' of the as-extracted mucilage solution, possible on account of the viscoelasticity imparted by dissolved long-chain polysaccharides. The mucilage extract in the lower reservoir is being drawn upwards into a syringe that is raised and held above the free surface, via a "tubeless" liquid thread supported by non-linear elastic stresses arising from the elongation of dissolved polymer chains. The solution used in this demonstration was extracted at a seed-to-water ratio of 1:8, and red food coloring was added to aid visualization. Also see Fig. 4.2.

75 % by weight, is known to be a high molar mass ($\geqslant 10^6\,\mathrm{g\,mol^{-1}}$) neutral arabinoxylan, and the remainder mostly an acidic fraction consisting of various negatively charged rhamnogalacturonans of lower molar mass.[32] The as-extracted aqueous mucilage solution is moderately viscoelastic on account of these dissolved long-chain polysaccharides, and at sufficiently large concentrations, can be drawn up in a 'tubeless siphon'[96] due to the large increase in extensional viscosity imparted by stretched polymer chains. Figure 4.1(b) shows a demonstration this 'open siphoning' effect for a concentrated mucilage extract prepared at a 1:8 ratio of flax seeds to water; see Fig. 4.2 for a further illustration of the elasticity and consistency of this solution.

Gravimetry of Mucilage Constituents

Gravimetric estimates of various mucilage components were obtained by lyophilizing the filtered extract and carefully weighing the dry solid yield (details of this process are provided in §3.II.A). A seed to water weight ratio of 1:25 was employed during the initial extraction stage, as per the optimal conditions reported by Ziolkovska (2012).[112] The aqueous mucilage concentrate so obtained, after coarse filtration, was found to contain dissolved constituents amounting to roughly 9.8 % of the original dry weight of seeds used. Of this, about 4 % was a gel-like fraction separable by centrifugation, and approximately 40 % consisted of low molar mass solutes below 100 kDa. The gel-like fraction was

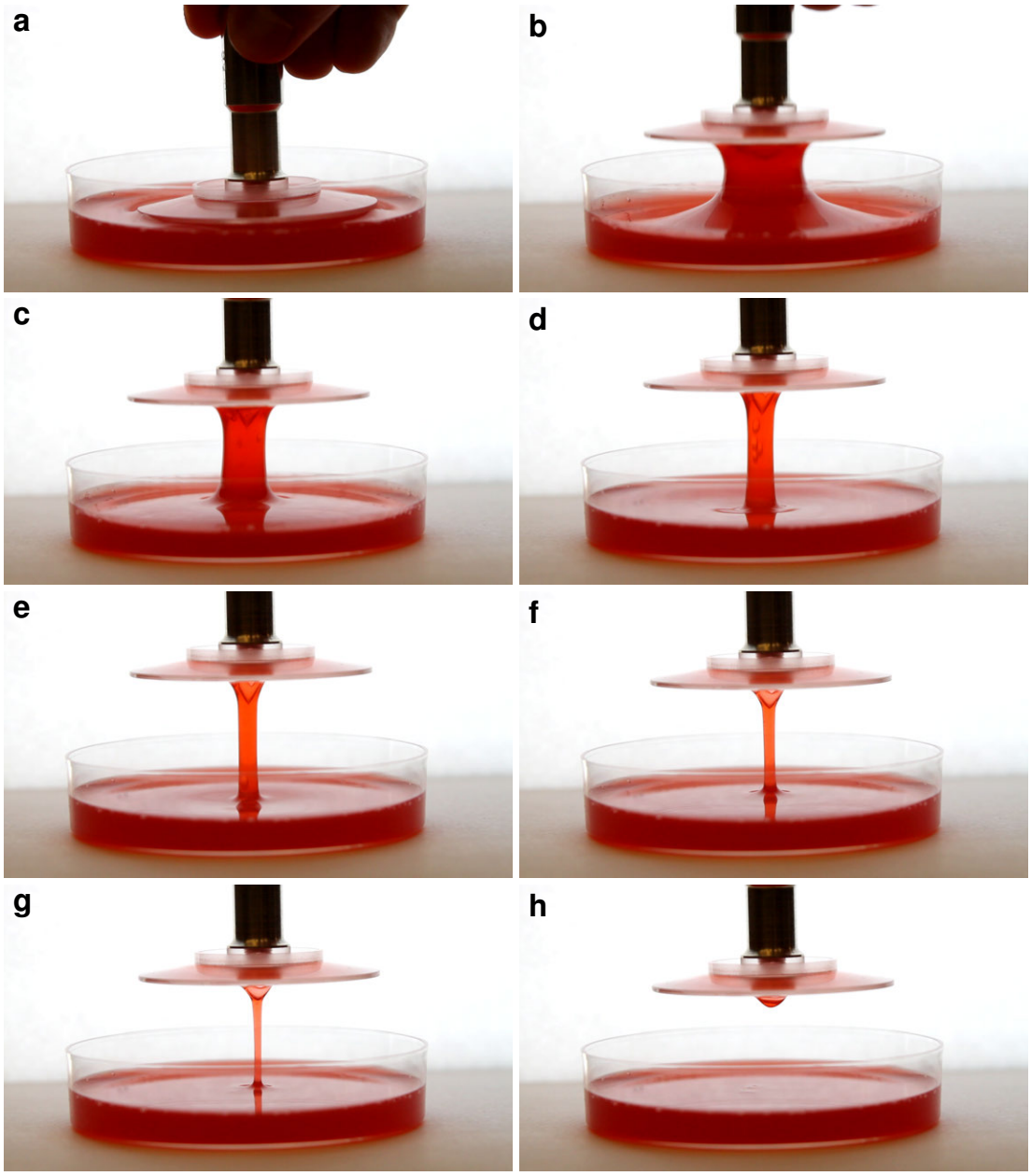

FIGURE 4.2. A 60 mm rheometer plate dipped and then withdrawn from the concentrated mucilage solution shown in Fig. 4.1(b). The viscous consistency of the solution, and the elasticity of the liquid filament as it drains under gravity, are readily apparent.

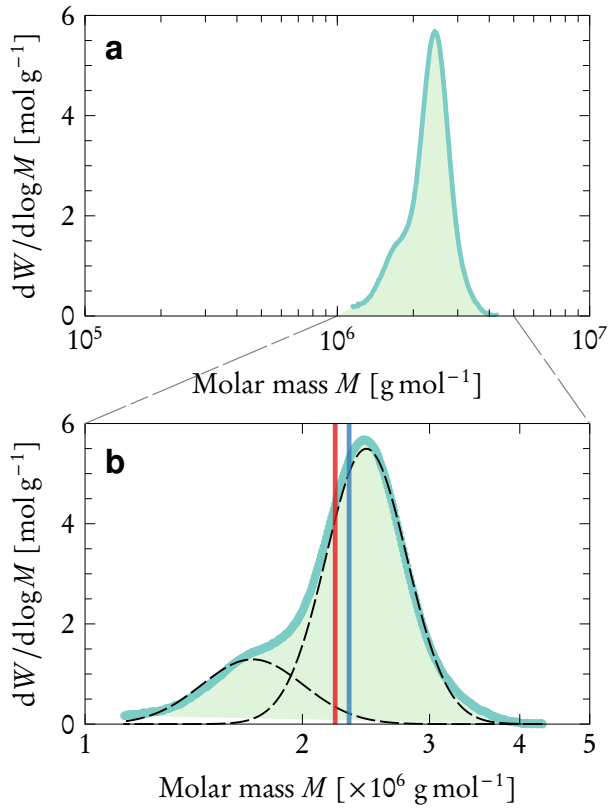

FIGURE 4.3. (a) Molar mass distribution of purified flaxseed mucilage, determined using triple-detection size exclusion chromatography (SEC). W here is the cumulative mass fraction of the eluted polymer. (b) An enlarged view of the chromatogram shows that the narrow peak seen in panel (a) is bimodal, and can be resolved into two distinct log-normal distributions represented by the black dashed curves. The red and blue vertical lines denote, respectively, the the number-averaged molar mass $M_n = 2.22 \times 10^6\,\mathrm{g\,mol^{-1}}$ and the weight-averaged molar mass $M_w = 2.32 \times 10^6\,\mathrm{g\,mol^{-1}}$ of the aggregate distribution.

removed by centrifuging the aqueous mucilage extract at RCF $= 10\,000 \times g$ for 30 min. The high molar mass polysaccharide fraction was isolated from the resulting supernatant using a 100 kDa molecular weight cutoff (or MWCO) filter (Macrosep, Pall Corporation) and was separately analyzed by size exclusion chromatography (see below).

Size Exclusion Chromatography

The high molar mass polysaccharide fraction isolated from flax mucilage was analyzed by triple detection size exclusion chromatography (SEC), using an Agilent PL-GPC 220

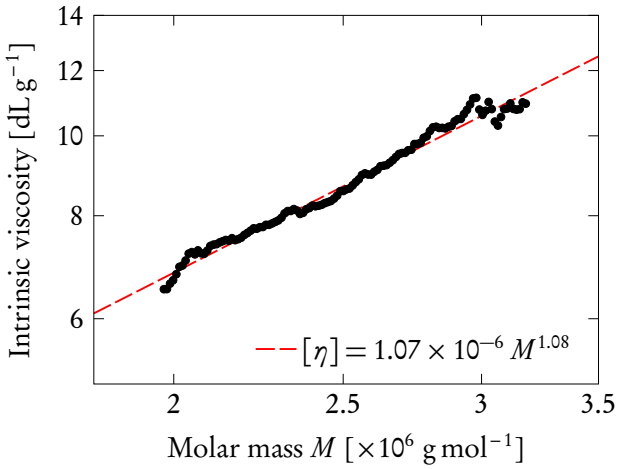

FIGURE 4.4. The intrinsic viscosity $[\eta]$ of mucilage fractions as a function of the molar mass M. The red dashed line is a linear least-squares fit used to estimate the Mark-Houwink parameters K and a from the experimental data.

triple detection system equipped with a refractive index concentration detector, an inline viscometer, and a 650 nm wavelength dual-angle light scattering detector for absolute determination of molar mass. A 0.1 M aqueous solution of $NaNO_3$ was used as the column eluent, with 0.02 % sodium azide added as a bacteriostatic agent. The refractive index increment dn/dc of mucilage polysaccharides was measured independently using a differential refractometer, and was determined to be $dn/dc = 0.145\,\mathrm{mL\,g^{-1}}$ at 40 °C and for a laser wavelength of 650 nm. The molar mass distribution of polysaccharides inferred from the SEC analysis is shown in Fig. 4.3(a). Although the molar mass of the sample is narrowly distributed and relatively monodisperse, on closer inspection the distribution is discernibly bimodal [as seen in Fig. 4.3(b)], and is well described by a superposition of two log normal peaks, centered at $M_1 = 1.71 \times 10^6\,\mathrm{g\,mol^{-1}}$ and $M_2 = 2.45 \times 10^6\,\mathrm{g\,mol^{-1}}$ respectively. Overall, this yields a weight-averaged molar mass of $M_w = 2.32 \times 10^6\,\mathrm{g\,mol^{-1}}$ for the aggregate sample, and a polydispersity index $\mathrm{PDI} = M_w/M_n = 1.05$.

Fig. 4.4 shows the intrinsic viscosity $[\eta]$, obtained from the SEC inline differential viscosity detector, as a function of the chain molar mass M, determined using dual-angle light scattering. By performing a linear least-squares fit of the Mark-Houwink-Sakurada equation[84,213] $[\eta] = K M^a$ to the data (see §3.II.B and Eq. 3.44), we estimated the Mark-Houwink parameters for the flax polysaccharides to be $a = 1.08 \pm 0.02$ and $K = (1.07 \pm 0.27) \times 10^{-6}\,\mathrm{dL/g\,(g/mol)^{-a}}$. These estimates, however, may have large associated uncertainties arising from the limited range of molar masses available for fitting, on account of the narrow polydispersity of the original sample. Furthermore, the values

of K and a obtained above correspond to a solvent ionic strength of 0.1 M, equivalent to the molarity of the aqueous $NaNO_3$ solution employed as the eluent during SEC analysis. A value of $a = 1.08$ for the Mark-Houwink exponent yields a Flory exponent of $\nu = (a+1)/3 = 0.69$ (cf. Eq. 3.45), larger than the value of $\nu = 0.6$ expected for flexible chains in good solvents.[84,213] This in turn suggests an expanded conformation for the charged polysaccharide constituents in the mucilage, which is further evidenced by the results of the viscometric study to be discussed in the next section.

B. *Rheology of Mucilage Polysaccharides*

Determination of Intrinsic Viscosity

In addition to the aforementioned viscometric characterization performed as part of SEC analysis, the intrinsic viscosity $[\eta]$ of aqueous flax mucilage was measured independently by successive dilution inside an Ubbelöhde glass capillary viscometer, in accordance with the procedure detailed in §3.II.B. To determine $[\eta]$ at zero ionic strength, the extracted mucilage was first desalted and rinsed via multiple solvent exchange passes in a 100 kDa MWCO centrifugal filter (Macrosep, Pall Corporation). The reduced viscosity η_{red} of this desalted mucilage was found to initially increase with dilution in deionized water, in conformance with the empirical *Fuoss equation*[233,234]

$$\eta_{\text{red}} = \frac{A}{B + \sqrt{c}}, \tag{4.1}$$

which is depicted by the dashed blue curve in Fig. 4.5(a); the constants A and B above are fit parameters obtained from a least-squares regression of Eq. 4.1 to the experimental viscosity data. Alternatively, Eq. 4.1 can be rearranged to yield a linear dependence of $1/\eta_{\text{red}}$ on $\sqrt{c}$, as evident from the *Fuoss plot*, Fig. 4.5(b), which replicates the viscosity data for desalted mucilage shown in Fig. 4.5(a).

The atypical increase in reduced viscosity with dilution is, in fact, a well-known attribute of polyelectrolytes in solution, and is ascribed primarily to chain expansion caused by the increased dissociation of ionizable groups, and the concomitant increase in electrostatic intramolecular repulsion.[235] The reduced viscosity increases as the molecules progressively adopt a stretched conformation, and eventually attains a local maximum when the dissolved chains reach maximal expansion at very low concentrations. Further dilution beyond this limit results in a decrease in reduced viscosity, as in the usual case of flexible neutral polymer chains.[235] In the case of flax mucilage, this transition was observed at a concentration of approximately $c = 46\,\text{mg}\,\text{L}^{-1}$; beyond this point, the conventional Huggins-Kraemer extrapolation in the linear region [see Fig. 4.6(a)] was

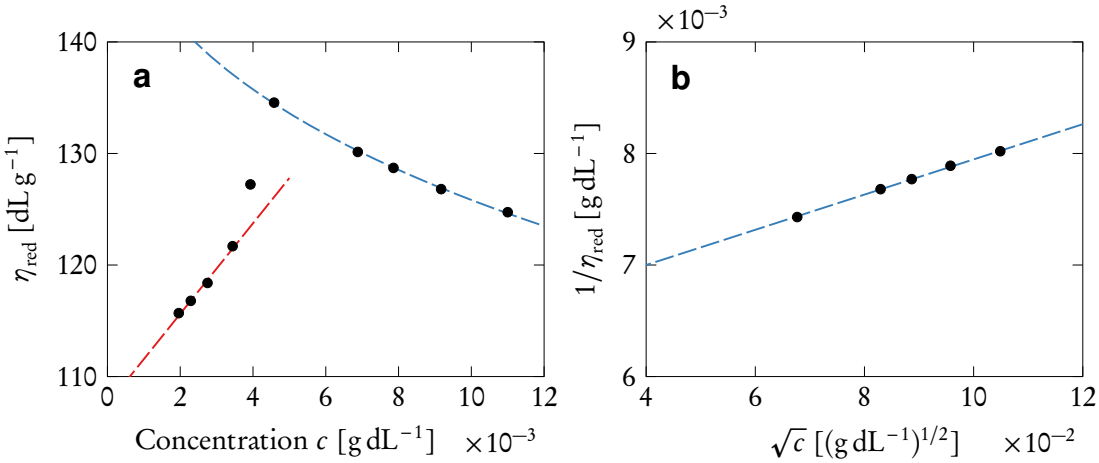

FIGURE 4.5. (a) Reduced viscosity η_{red} of purified and desalted aqueous flax mucilage, displaying polyelectrolyte-like behavior. With progressive dilution, the reduced viscosity initially increases in accordance with the Fuoss equation (Eq. 4.1, dashed blue curve), reaches a maximum, and subsequently decreases along the Huggins line (cf. Eq. 3.35, red line) at very low concentrations. (b) Fuoss plot of desalted flax mucilage, showing linear dependence of the inverse reduced viscosity $1/\eta_{red}$ on the square root of the concentration $\sqrt{c}$, for concentrations $c \geqslant 4.6 \times 10^{-3}\,\mathrm{g\,dL^{-1}}$. The data points and the blue dashed line are identical to those shown in panel (a).

used to infer an intrinsic viscosity of $[\eta] = 108\,\mathrm{dL\,g^{-1}}$ at 25 °C, which is in reasonable agreement with the estimate of $[\eta] = A/B = 157\,\mathrm{dL\,g^{-1}}$ obtained by directly extrapolating the Fuoss equation, Eq. 4.1, to zero concentration [see Fig. 4.5(b)]. Furthermore, this value is an order of magnitude larger than the intrinsic viscosity of neutral, flexible coils of similar molar mass (for comparison, PEO with a molar mass of $2 \times 10^6\,\mathrm{g\,mol^{-1}}$ has an intrinsic viscosity of $[\eta]_{PEO} = 9.13\,\mathrm{dL\,g^{-1}}$ in water), again suggesting the presence of extended rod-like chains in the desalted mucilage. The polyelectrolyte-like behavior of mucilage is consistent with the presence of an acidic fraction comprising negatively charged, semiflexible rhamnogalacturonan chains, as has been reported in previous studies in the literature.[32]

The intrinsic viscosity of mucilage was further observed to be highly sensitive to the ionic strength of the solution,[236,237] falling by more than an order of magnitude from $[\eta] = 108\,\mathrm{dL\,g^{-1}}$ at zero salt concentration, to $[\eta] = 8.57\,\mathrm{dL\,g^{-1}}$ in a 0.5 M aqueous NaCl solution [see Fig. 4.6(b)]. This can be explained as a consequence of the effective charge screening by the added ions, permitting the expanded chains to revert to a random coil configuration.[238] Insofar as the crude seed extract was intended to be used directly for drag reduction without the need for any additional purification or desalting, it was pertinent

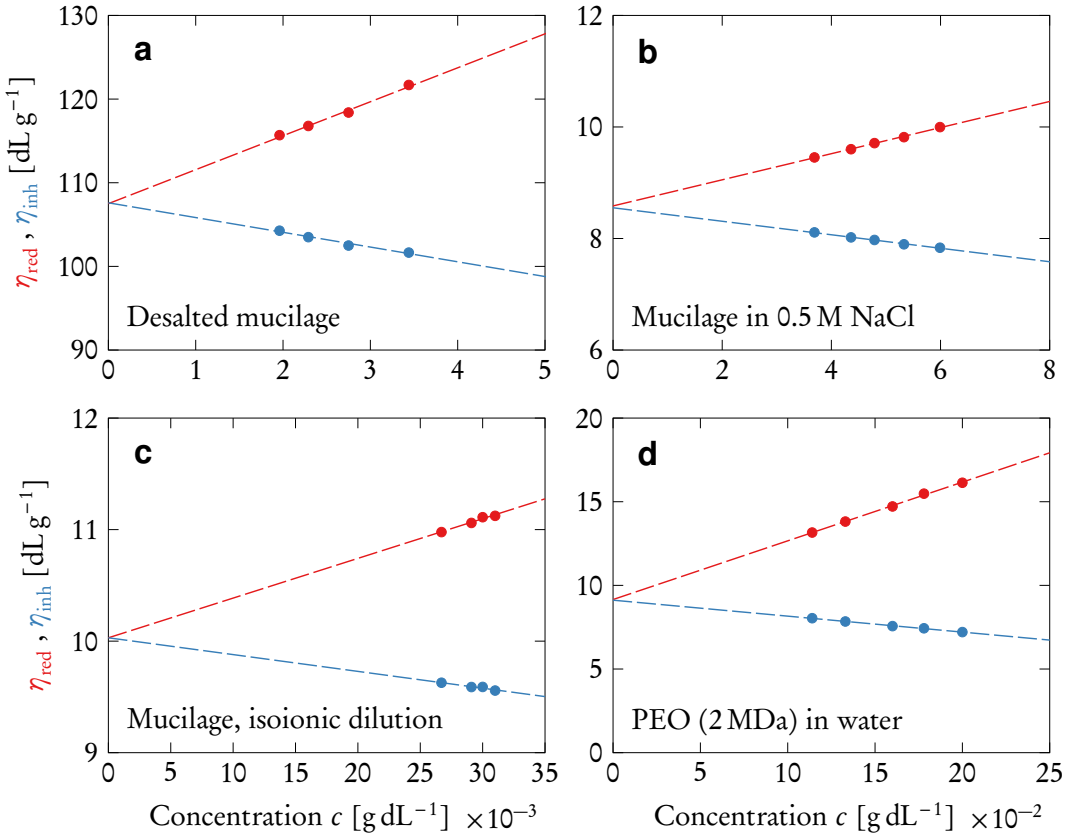

FIGURE 4.6. Huggins-Kraemer plots (see §3.II.B) constructed from experimental viscometry data, used to determine the intrinsic viscosity $[\eta]$ of (a) desalted flax mucilage; (b) flax mucilage in 0.5 M aqueous NaCl; (c) flax mucilage at the as-extracted ionic strength, measured by isoionic dilution; and (d) aqueous solution of 2 MDa PEO, used in comparative studies with mucilage.

to characterize the properties of the mucilage at ionic strengths similar to that of the original, as-extracted solution. To this end, the intrinsic viscosity measurements were repeated under isoionic conditions [Fig. 4.6(c)], for which the low molar mass fraction isolated from the as-extracted mucilage solution (recovered as the filtrate during the first pass through the MWCO filter) was collected and employed as the diluent in place of water. No discernible polyelectrolyte-like effect was observed during experiments at this ionic strength,[236] and an isoionic intrinsic viscosity of $[\eta]_{FM} = 10.03\,\mathrm{dL\,g^{-1}}$ at 25 °C was inferred, which is quite close to the value of $[\eta]_{PEO} = 9.13\,\mathrm{dL\,g^{-1}}$ obtained for aqueous PEO of comparable molar mass, as seen in Fig. 4.6(d). On account of this close correspondence in terms of the molar mass and intrinsic viscosity (and thereby,

the chain size in solution), 2 MDa PEO was adopted as the benchmark against which the drag reduction efficacy of flax mucilage was evaluated as a bio-sourced alternative. Furthermore, PEO is among the synthetic polymers most commonly employed for drag reduction in aqueous flows, and 2 MDa PEO has indeed been successfully utilized as a drag-reducing agent in past experimental studies in the literature.[27,70]

As mentioned above, the polyelectrolyte-like behavior of mucilage disappeared in the presence of dissolved salts, and the Fuoss regime was observed neither in the 0.5 M NaCl solution nor during isoionic dilution at the as-extracted ionic strength.[236,238] In both cases, the Huggins regime was attained at larger concentrations than in the case of desalted mucilage, and the usual linear extrapolation was directly employed to estimate the intrinsic viscosity $[\eta]$ of the dissolved polymer chains. The Huggins-Kraemer fits for flax mucilage at various salt concentrations are shown as a single composite plot in Fig. 4.7. For each experiment, extrapolation in the linear regime was confirmed by verifying that $k_H + k_K = 0.50 \pm 0.03$, as required mathematically by the definitions of η_{red} and η_{inh} (see the discussion preceding Eq. 3.43 in §3.II.B for a derivation of this relation).[212]

For turbulent drag reduction measurements using the TC apparatus (to be described below), dilute mucilage extracts were prepared by varying the ratio by weight of seeds to water between 1:100 and 1:800, with the resulting solutions having polysaccharide concentrations in the range $260\,\text{ppm} \leqslant c \leqslant 1310\,\text{ppm}$. The critical overlap concentration c^* for dissolved polymer chains may be estimated approximately as $c^* \simeq 1/[\eta]$ (see discussion underneath Eq. 3.53),[84] yielding the values $(c^*)_{FM} = 1.00\,\text{g}\,\text{L}^{-1}$ for flax mucilage (at the as-extracted ionic strength), and $(c^*)_{PEO} = 1.10\,\text{g}\,\text{L}^{-1}$ for aqueous 2 MDa PEO. The mucilage extracts used in flow measurements therefore correspond to $0.26 \leqslant c/c^* \leqslant 1.3$, thus being largely in the dilute (or the weakly semi-dilute) regime; to ensure a fair comparison at the same "effective" polymer concentration, benchmark flow tests using aqueous PEO were performed at identical values of the normalized concentration c/c^* as the mucilage extracts, as listed in Table 4.1.

Extensional Rheology of Dilute Mucilage

Finally, as a direct characterization of the extensional rheology of mucilage, the relaxation time λ of the dissolved polymer chains was measured by means of a capillary breakup extensional rheometer (CaBER), at the low concentrations relevant to drag reduction applications. A full description of the experimental apparatus and procedure employed for CaBER measurements is provided in §3.II.C. Briefly, a small volume of the test solution is confined between two coaxial end plates, and subjected to an axial step strain via a rapid separation of the plates to a fixed final gap. The resulting capillary instability leads to the formation, and subsequent self-thinning, of a cylindrical liquid thread (see Fig. 4.8),

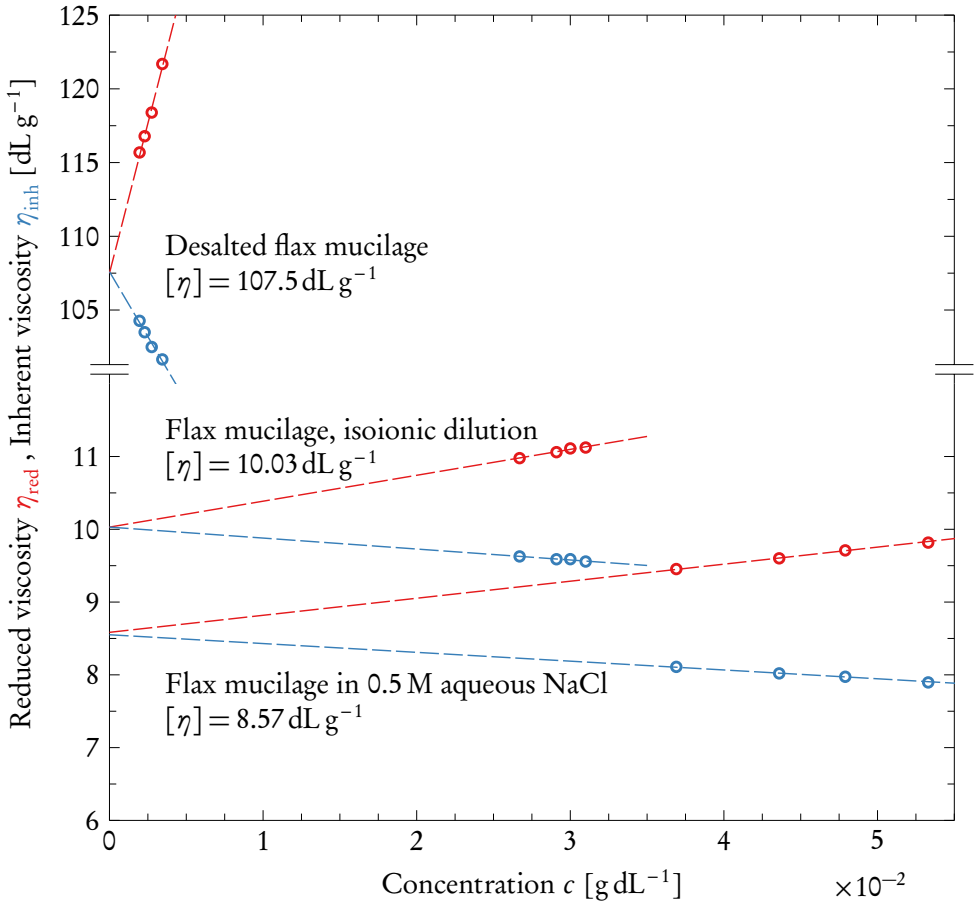

FIGURE 4.7. Intrinsic viscosity $[\eta]$ of aqueous flax mucilage measured at different ionic strengths of the solvent, corresponding to varying concentrations of dissolved salts. The data from Fig. 4.6, panels (a–c) are reproduced here as a composite plot to aid comparison.

TABLE 4.1. The concentration c and the characteristic relaxation time λ of aqueous PEO and flax mucilage solutions used in drag reduction experiments; in the case of mucilage extracts, the ratio by mass of flax seeds to water employed during hot water extraction is also reported. For the 5 MDa PEO solution, λ corresponds to the Zimm relaxation time estimated using Eq. 4.3, and the intrinsic viscosity $[\eta]$ was inferred from the data in Fig. 3.10. For mucilage solutions, the listed value of $[\eta]$ is the one obtained by isoionic dilution [see Fig. 4.6(c)], and the relaxation time λ was estimated from the power law fit shown in Fig. 4.9(b).

Polymer		Concentration c [ppm]	$c\,[\eta]$	Relaxation time λ [ms]
Flax mucilage $[\eta] = 10.03\,\mathrm{dL\,g^{-1}}$	1:800	260	0.26	0.03
	1:400	460	0.46	0.05
	1:200	780	0.78	0.10
	1:100	1310	1.31	0.18
PEO 2 MDa $[\eta] = 9.13\,\mathrm{dL\,g^{-1}}$		285	0.26	2.74
		504	0.46	3.74
		865	0.79	4.49
		1460	1.33	5.67
PEO 5 MDa $[\eta] = 20.2\,\mathrm{dL\,g^{-1}}$		10	0.02	3.65

whose diameter $d(t)$ decreases exponentially with time t in accordance with Eq. 3.56, reproduced here for convenience:

$$d(t) \sim d(0)\exp\left(-\frac{t}{3\lambda}\right). \tag{4.2}$$

The evolution of the diameter $d(t)$ was tracked concurrently using a laser micrometer as well as a high speed camera, and a least-squares fit of the data to Eq. 4.2 in the elasto-capillary regime, as shown in Fig. 4.9(a), was used to infer the relaxation time λ of the polymer chains in solution.[219,220,222,223] Experiments were conducted at room temperature, $T = (23 \pm 2)\,°\mathrm{C}$, and at least three replicate measurements were performed for each polymer solution and then averaged.

A simple theoretical estimate of the longest relaxation time of polymer chains in dilute solution is given by (cf. Eq. 3.54)

$$\lambda_Z \simeq \frac{[\eta] M_w \eta_s}{RT} \tag{4.3}$$

which, excepting a numerical prefactor of order unity that depends on the solvent quality, is equivalent to the *Zimm relaxation time* of dilute Gaussian coils in the 'non-draining'

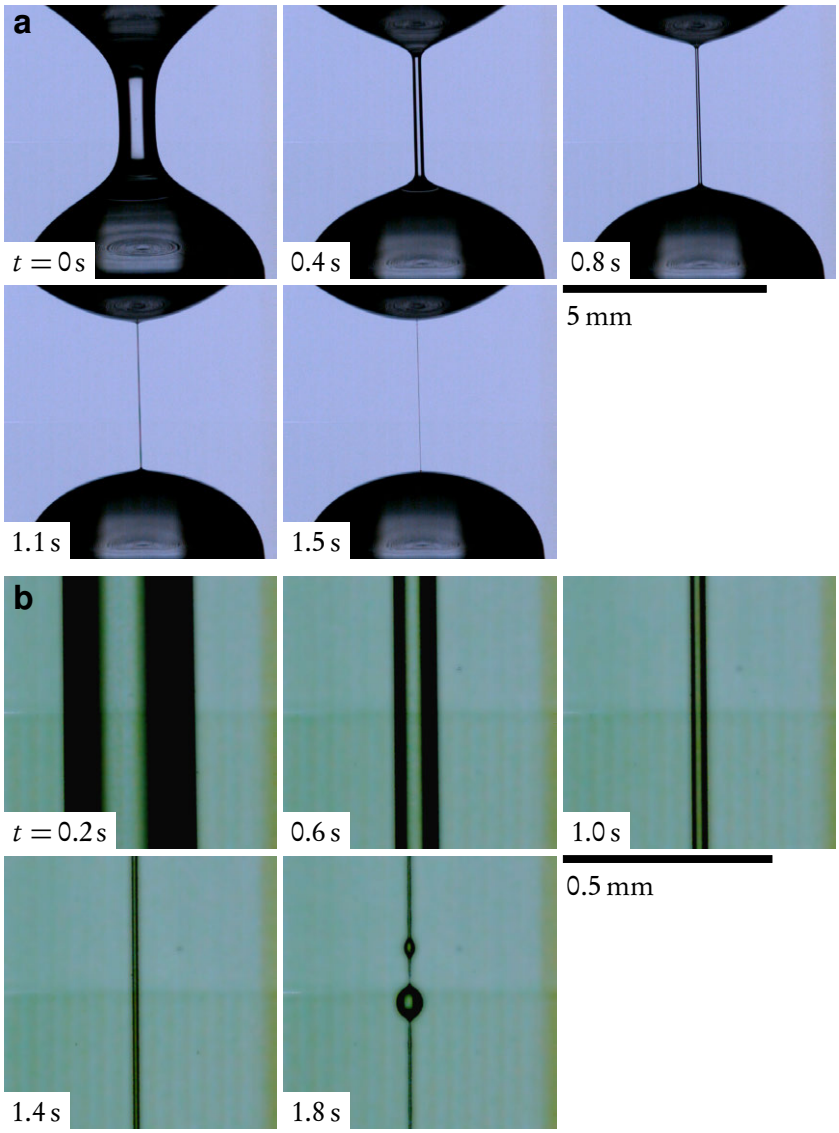

FIGURE 4.8. (a) Image sequence showing the elasto-capillary thinning of 2 MDa PEO (c = 1460 ppm) dissolved in 0.7 g mL^{-1} aqueous sucrose (solvent viscosity η_s = 0.019 Pa s) during a CaBER experiment. The annotations indicate the elapsed time t measured from the instant when the plates come to rest after separation. (b) Images of the filament midpoint recorded using the high speed camera, and used to measure the filament diameter $d(t)$ as a function of time t. The final image shows the inception of the beads-on-a-string (BoaS) instability. Faint striations visible in the background are an artifact produced by the camera's CCD sensor.

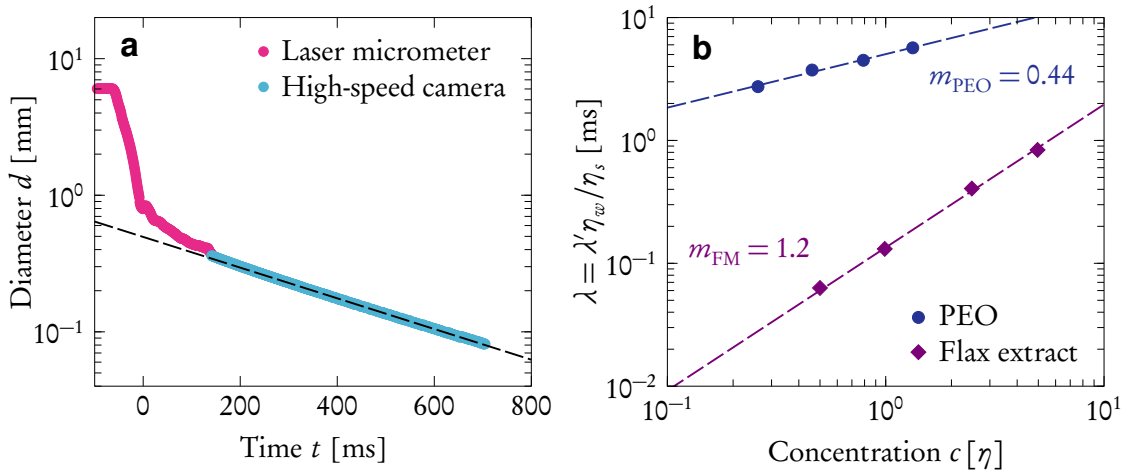

FIGURE 4.9. (a) Evolution of the filament diameter $d(t)$ with time t, for the CaBER experiment shown in Fig. 4.8. The diameter at initial times was measured using a laser micrometer, and at later times was inferred from the high speed recording shown in Fig. 4.8(b). The dashed line denotes a least-squares fit of the form $d(t) \sim \exp\left(-t/3\lambda'\right)$ to the data in the exponential thinning region. (b) The relaxation time λ of aqueous PEO and flax mucilage solutions, as a function the normalized polymer concentration $c[\eta]$. The relaxation time λ in water was estimated by rescaling the experimentally measured relaxation time λ' in aqueous sucrose with the ratio of solvent viscosities: $\lambda = \lambda'(\eta_w/\eta_s)$. Error bars are smaller than or comparable to the size of the data markers, and are omitted for clarity.

limit of dominant intrachain hydrodynamic interactions;[84] here, η_s denotes the solvent viscosity, T the solution temperature, and R the universal gas constant. Utilizing the empirical values of the intrinsic viscosity $[\eta]$ determined previously by means of capillary viscometry, Eq. 4.3 yields estimated relaxation times of $(\lambda_Z)_{PEO} = 0.66\,\text{ms}$ and $(\lambda_Z)_{FM} = 0.84\,\text{ms}$ for PEO and mucilage polysaccharides respectively, at a temperature of $T = 25\,°\text{C}$ and with pure water as the solvent. Accurate measurements of the chain relaxation time using CaBER becomes increasingly challenging for small relaxation times λ approaching 1 ms, at which point the filament lifetime becomes so short as to render the elasto-capillary regime, described by Eq. 4.3, experimentally inaccessible.[239] Additionally, at the dilute concentrations employed in drag reduction tests, the viscosity of aqueous polymer solutions are so small ($\eta_0 \leqslant 3\,\text{mPa s}$) that inertial oscillations of the upper and lower liquid bulbs, triggered by the moving plates, persist throughout the observation window, vitiating diameter measurements and often forcing a premature breakup of the filament.[239] To surmount these practical difficulties, the solvent viscosity η_s was enhanced by adding sucrose to the test solutions prior to CaBER measurements, which mitigates

inertial effects and delays filament rupture sufficiently to permit reliable measurements of the diameter $d(t)$ in the elasto-capillary regime. Sucrose was chosen on account of its excellent solubility in water, and was preferred over high molar mass viscosifiers such as dextran to preclude any extraneous viscoelastic effects introduced artificially by the additive. An aqueous solution of $0.67\,\mathrm{g\,mL^{-1}}$ sucrose (viscosity $\eta_s = 0.0188\,\mathrm{Pa\,s}$) was used as the solvent in the case of PEO, and a more viscous solution of $0.83\,\mathrm{g\,mL^{-1}}$ sucrose in water (viscosity $\eta_s = 0.102\,\mathrm{Pa\,s}$) was employed for measurements using flax mucilage. From Eq. 4.3, the relaxation time increases linearly with solvent viscosity as $\lambda \propto \eta_s$, a general result of bead-spring models that is true of flexible coils, semiflexible chains, and extended rigid rods in solution.[84] By simply rescaling the relaxation time λ' (measured in the sucrose solution) to account for the increase in solvent viscosity, one therefore obtains better-resolved estimates of the actual relaxation time $\lambda = \lambda'(\eta_w/\eta_s)$ of polymer chains in the original aqueous solution, η_w here being the viscosity of pure water, and η_s that of the sucrose solution of higher viscosity used as the solvent during CaBER measurements.

Fig. 4.9(b) shows the relaxation time λ of PEO and mucilage polysaccharides in water, as a function of the normalized concentration $c[\eta]$ of the solution. The experimental relaxation time λ exceeds the theoretical estimate λ_Z predicted from Eq. 4.3 by nearly an order of magnitude in the case of PEO, whereas they are comparable or smaller than λ_Z in the case of flax mucilage. An enhanced relaxation time for flexible chains such as PEO in uniaxial extensional flows has been consistently observed in past studies in the literature.[216,223] Equation 4.3, which is strictly valid only in the limit of infinite dilution, predicts a relaxation time λ_Z that is independent of the concentration of chains in solution. However, in strong extensional flows, the pervaded volume of the chain increases substantially as it undergoes a coil-stretch transition, resulting in interchain hydrodynamic interactions which render the solution, in effect, semi-dilute.[216,219] This, in turn, manifests as a concentration dependence of the extensional relaxation time λ which persists down to concentrations far below c^*, the usual threshold for single chain dynamics in weak shear flows. On the other hand, the addition of sucrose is known to lower the dielectric constant of aqueous solutions much like ionic electrolytes,[240] and the resulting charge screening can cause expanded polyelectrolyte chains to partially revert to a random coil configuration; indeed, a decrease in solvent quality and radius of gyration in the presence of sucrose has been reported for a number of polysaccharides in aqueous solution.[241–243] A similar decrease in the intrinsic viscosity of mucilage, effected by the dissolved sucrose, would explain the smaller value of the experimental relaxation time λ, in comparison to the theoretical value λ_Z estimated from Eq. 4.3 for isoionic conditions.

From Fig. 4.9(b), we see that the relaxation time λ for both PEO and flax mucilage solutions exhibit a power-law behavior of the form $\lambda \sim (c[\eta])^m$, with exponents $m_{\mathrm{PEO}} = 0.44$ and $m_{\mathrm{FM}} = 1.2$ respectively. For unentangled, semi-dilute solutions of flexible chains,

"blob" theories predict a scaling exponent $m = (2-3\nu)/(3\nu-1)$;[216,223] substituting $m_{\mathrm{PEO}} = 0.44$ in this expression yields a Flory exponent of $\nu = 0.56$ for aqueous PEO, which is close to, but slightly smaller than, the value of $\nu = 0.59$ reported in the literature for dilute solutions of PEO in water;[214] the slight discrepancy may be attributed to a decrease in solvent quality in the presence of sucrose. For flax mucilage, $m_{\mathrm{FM}} = 1.2$ yields $\nu = 0.48$, again indicative of the strong charge screening and poor solvent quality effected by the dissolved sucrose in the solution. The estimated relaxation times for aqueous PEO and flax mucilage solutions employed in drag reduction experiments are listed in Table 4.1.

III. Drag Reduction by Mucilage Polysaccharides

A. *Drag Reduction Measurements in Turbulent TC Flow*

The drag reduction efficacy of aqueous PEO and flax mucilage solutions was characterized by means of skin friction measurements in turbulent shear flow generated inside a bespoke Taylor-Couette (TC) apparatus, the design and operational features of which are discussed extensively in §3.I. All measurements were performed using a smooth, no-slip aluminum rotor and at an ambient temperature of (23 ± 1) °C. During a typical experiment, the cell gap was filled with the dilute polymer solution to be evaluated, and the angular speed Ω of the rotor was varied in discrete steps over the range $10\,\mathrm{rad\,s^{-1}} \leqslant \Omega \leqslant 125\,\mathrm{rad\,s^{-1}}$. At each step, the flow inside the gap was allowed to reach steady state, after which the frictional torque $\mathscr{T}$ on the rotor was sampled and averaged over a period of 10 s. The standard deviation in torque values about the mean was less than 2 % at each step.

In accordance with the usual convention for TC flows, we define the Reynolds number $\mathrm{Re} = \rho V d/\eta$ based on the gap width d, the wall speed $V = R_i\Omega$ of the rotor, and the density ρ and the viscosity η of the working fluid. The average wall shear stress $\tau_w = \mathscr{T}/2\pi R_i^2 L$ at the rotor surface (cf. Eq. 3.17), and the friction factor $C_f = 2\tau_w/\rho V^2$ (cf. Eq. 2.3), were then calculated from the experimentally measured torque versus speed curve. When the fluid inside the cell gap is Newtonian, one can use matched asymptotic expansions for the azimuthal angular momentum to derive a logarithmic friction law of the form[203]

$$V^+ = M \log \mathrm{Re}_\tau + N\,, \tag{4.4}$$

as discussed previously in §3.I.B, Eq. 3.18; here $V^+ = V/u_\tau$ is the rotor speed normalized by the friction velocity $u_\tau = \sqrt{\tau_w/\rho}$, $\mathrm{Re}_\tau = \rho u_\tau d/\eta$ is the shear Reynolds number at the rotor wall, and the constants M and N are characteristic of the particular TC geometry and are independent of the flow speed and fluid properties. In Fig. 4.10, experimental friction curves obtained from flow measurements are presented in the form of Prandtl-von Kármán plots, in which V^+ is graphed as a function of Re_τ on semi-logarithmic axes.

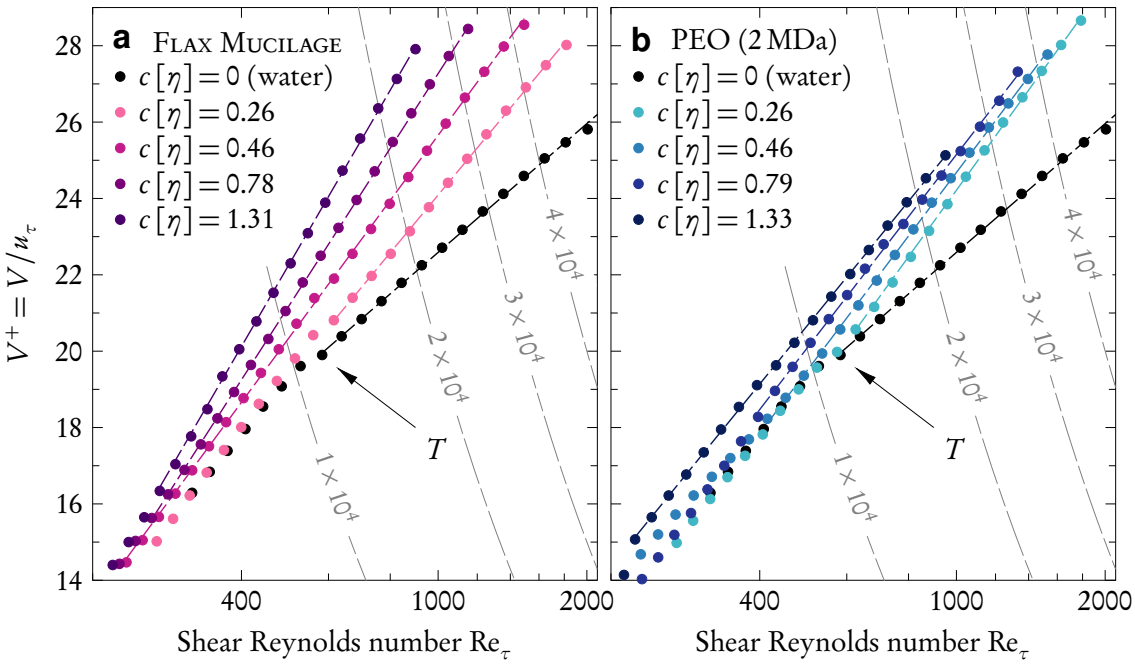

FIGURE 4.10. Experimental friction curves for (a) flax mucilage, and (b) aqueous PEO solutions at identical values of the normalized concentration $c[\eta]$, in Prandtl-von Kármán coordinates. T marks the point of transition to featureless (Newtonian) turbulence in the TC apparatus, as discussed in §3.I.B. The dashed lines in both panels are linear least-squares fits of Eqs. 4.4 and 4.5 to the experimental data in the turbulent regime, and the gray curves denote contours of constant Reynolds number $\mathrm{Re} = \rho V d/\eta_0$.

The black data points denote baseline measurements in pure water, and the sharp change in the slope of this curve marks the transition to featureless Newtonian turbulence, which occurs at a critical Reynolds number of $\mathrm{Re}_{\mathrm{crit}} \simeq 11\,000$ in the bespoke TC apparatus (see discussion in §3.I.B). As evident from the plot, the friction data beyond this point shows good conformance to the functional form predicted by Eq. 4.4, and a linear least-squares fit in this region was used to extract the slope M of the (Newtonian) baseline.

In the case of aqueous PEO and flax mucilage solutions, the transition to polymeric turbulence, in general, was observed to occur at lower wall speeds V in comparison to the pure Newtonian solvent.[66] Given that solutions of long chain polymers, at the large localized strain rates encountered in turbulence, may concurrently undergo both viscous shear-thinning in regions of dominant shear flow, as well as strain hardening in regions of strong extensional flow, there exists some degree of incertitude as to the correct choice of the solution viscosity η to be used in the definition of Re_τ; different

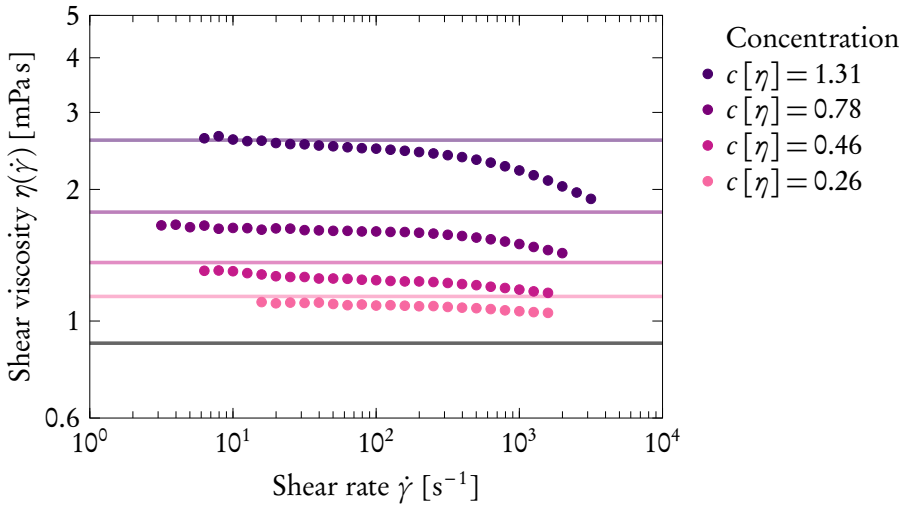

FIGURE 4.11. Shear viscosity of flax mucilage solutions used in the frictional drag measurements shown in Fig. 4.10. The data markers show the viscosity $\eta(\dot{\gamma})$ as a function of the shear rate $\dot{\gamma}$, measured using a standard double-gap concentric cylinder geometry on the AR-G2 rheometer ($T = 25\,°\mathrm{C}$). The horizontal solid lines denote viscosities measured independently using a glass capillary viscometer, which are indeed in good agreement with the rheometry data at low shear rates. The black line at the bottom corresponds to pure deionized water ($\eta_w = 8.9 \times 10^{-4}\,\mathrm{Pa\,s}$), and serves as an absolute lower bound on the viscosity of aqueous polymer solutions.

authors have, in the past, set it equal to the solvent viscosity η_s,[59] the solution viscosity η_0 at zero shear rate,[78] the viscosity η_∞ at infinite shear rate (obtained from a Carreau-Yasuda fit, see Eq. 2.2),[66] or the local shear viscosity $\eta\left(\dot{\gamma}_w\right)$ corresponding to the shear rate $\dot{\gamma}_w$ at the wall.[79] For the data in Fig. 4.10, we have opted to use the zero shear rate viscosity η_0; the dilute solutions used in these experiments had η_0 not too different from the viscosity η_s of the pure solvent, and showed no appreciable shear thinning at shear rates $\dot{\gamma} \leq 10^3\,\mathrm{s}^{-1}$ (see Fig. 4.11). More importantly, however, using the zero shear rate viscosity η_0 seemed to yield a good convergence of the polymeric friction curves with the Newtonian baseline in the region prior to the onset of drag reduction, despite there being no apparent reason to anticipate this collapse a priori: the flow state immediately preceding featureless turbulence in the TC apparatus is one of turbulent Taylor vortices,[193] in contrast to pipe flows for which the preceding state is one of laminar shear flow and is directly responsible for the superposition of the polymeric and the pure solvent curves in the pre-transition regime.[59]

Post transition to fully developed turbulence, the experimental friction curves for the dilute mucilage and PEO solutions diverge sharply away from the Newtonian baseline, as

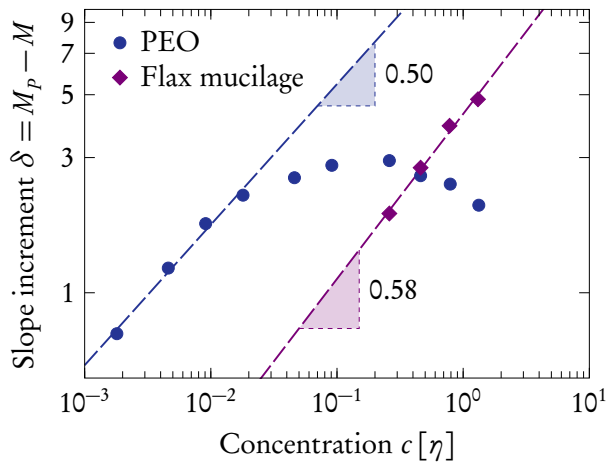

FIGURE 4.12. The slope increment δ derived from Fig. 4.10 for aqueous PEO and mucilage solutions, as a function of the normalized polymer concentration $c[\eta]$. The dashed lines denote linear least-squares fits to the data in log-log coordinates.

seen in Fig. 4.10, panels (a) and (b) respectively; the upward deviation implies a decrease in the friction factor $C_f = 2/(V^+)^2$ in comparison to the pure solvent, and by extension, a reduction in the wall shear stress τ_w at a given rotor speed V. Analogous to the behavior observed in pipe flows, the friction data for polymer solutions are well described by linear fits on the Prandtl-von Kármán plot of the form

$$V^+ = M_P \log \mathrm{Re}_\tau + N_P \,, \tag{4.5}$$

which is similar to the pure solvent baseline, Eq. 4.4, albeit with a higher slope $M_P > M$ that depends on the polymer additive employed, and its concentration c in solution. Following Virk (1970),[244] we define the *slope increment* $\delta = M_P - M$ as the change in slope of the polymeric friction curve with respect to the Newtonian baseline, and utilize this as a measure of the drag reduction efficacy of a given polymer solution. Insofar as the shear viscosity η appears only in the abscissa of the Prandtl-Kármán plot, a different choice for its value will result merely in a horizontal shift of the curves in Fig. 4.10; the slope M_P and the slope increment δ are thus independent of the specific choice of the fluid viscosity η used in defining the shear Reynolds number Re_τ.

Figure 4.12 shows the slope increment δ as a function of the normalized concentration $c[\eta]$ for aqueous PEO and flax mucilage solutions. In the dilute limit, the slope increment for aqueous PEO solutions scales with concentration according to $\delta \sim (c[\eta])^{1/2}$; a similar square-root dependence on polymer concentration has been reported previously for flexible drag-reducing chains in turbulent pipe flows.[59,244] At higher concentrations

of dissolved PEO ($c[\eta] \sim 0.1$), δ reaches a maximum and subsequently decreases with concentration, indicating the onset of maximum drag reduction (MDR). In the case of flax mucilage, a stronger dependence of the slope increment on the concentration, $\delta \sim (c[\eta])^{0.58}$, is observed, presumably on account of the charged semiflexible chains that constitute the acidic fraction of mucilage; it is, however, also possible that the concentrations employed (even at 1:800 seed-to-water ratio) were not sufficiently dilute for the $\delta \sim c^{1/2}$ scaling behavior to be discernible.[244]

B. *Practical Considerations in Engineering Systems*

Percentage Drag Reduction and Polymer Cost

The Prandtl-von Kármán representation and the slope increment δ, as discussed above, serve as valuable tools in a semi-empirical approach to analyzing and quantifying the drag reduction effect of polymer additives. Nevertheless, from a practical standpoint, the quantity that is often of immediate interest in engineering applications is the net decrease in fluid friction—either the wall shear stress in external flows, or the head loss per unit length in internal flows—achieved in comparison to the unmodified (Newtonian) solvent under identical conditions of wall speed or flow rate. Accordingly, it is apposite to define a percentage drag reduction $\mathscr{D}$ given by (cf. Eq. 2.6)

$$\mathscr{D} = \frac{\tau_{w,N} - \tau_w}{\tau_{w,N}} \cdot 100\,\% \tag{4.6}$$

where $\tau_{w,N}$ and τ_w are, respectively, the frictional wall shear stresses measured in the Newtonian solvent (i.e. water) and in the dilute polymer solution at the same rotor speed Ω, or equivalently, at the same Reynolds number $\mathrm{Re}_s = \rho V d / \eta_s$ calculated based on the viscosity η_s ($= \eta_w$) of the pure solvent. Defined this way, the percentage drag reduction $\mathscr{D}$ increases with increasing Reynolds number Re_s for both PEO and mucilage solutions, a direct consequence of the growing separation between the diverging polymer and solvent lines as seen in Figs. 4.10. The presence of dissolved polymer chains, besides acting to suppress near-wall turbulence, also has the concomitant effect of increasing the shear viscosity η of the solution; this in turn enhances viscous dissipation in the flow, which counteracts the drag reduction effected by chain elasticity and thereby offsets the overall decrease in skin friction attained. Inasmuch as the viscoelastic suppression of near-wall turbulence is increasingly effective at larger Reynolds numbers (or greater turbulence intensities), there exists a threshold value of the Reynolds number Re_s above which the macromolecular disruption of turbulent momentum transport outweighs the increase in fluid viscosity, providing a net positive reduction in skin friction (or head loss) vis-á-vis the pure solvent in the absence of additives. This is evident in Fig. 4.13, where the

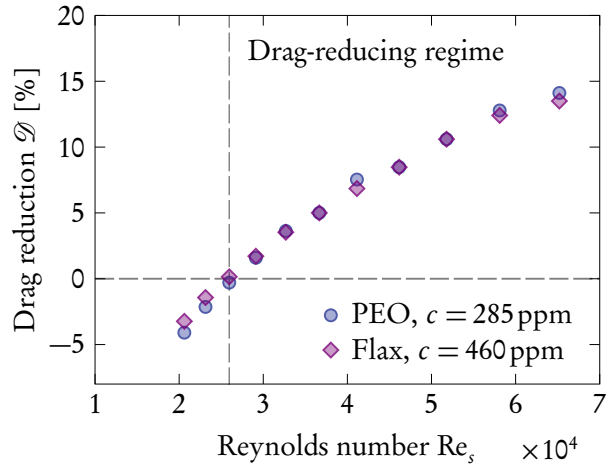

FIGURE 4.13. The percentage drag reduction $\mathscr{D}$ as a function of the Reynolds number Re_s for a 285 ppm aqueous solution of PEO, and a 1:400 extract ($c = 460$ ppm) of flax mucilage. The two solutions show near identical performance in the drag-reducing regime, $\mathrm{Re}_s \geqslant 26\,000$.

percentage drag reduction $\mathscr{D}$ is shown as a function of the Reynolds number Re_s for an aqueous, 285 ppm solution of PEO, and a 1:400 extract ($c = 460$ ppm) of flax mucilage. Both solutions are drag-reducing at Reynolds numbers $\mathrm{Re}_s \geqslant 26\,000$, but exert a greater frictional drag on the rotor at lower speeds than pure water on account of their higher shear viscosity and the inadequate intensity of turbulence in the flow.

Referring again to Fig. 4.13, the flax extract is seen to yield almost identical levels of drag reduction as the PEO solution throughout the drag-reducing regime (at the respective concentrations of each polymer mentioned above); the mucilage solution can thus potentially serve as an equally efficacious bio-sourced substitute for the synthetic PEO solution. The high cost of synthetic long chain polymers, and the logistic hurdles involved in transporting the requisite quantities of additives onboard, are cited as the two principal roadblocks to the cost-effective deployment of polymers in marine and naval applications.[4,44,227] Costing studies in the past have generally concluded that marine drag reduction becomes economical at increasing ship speeds, with rise in fossil fuel prices, or with the availability of lower-cost drag-reducing polymers.[227] Industrial grade PEO marketed for large-scale use (for example, in paper manufacturing) is typically quite polydisperse, and contains a substantial fraction of low molar mass chains that are largely ineffectual in reducing frictional drag. To minimize the total dry volume of additives conveyed, and thereby render its onboard storage and handling practicable, the polymer stock should predominantly comprise high molar mass drag-reducing chains, which in turn entails expensive fractionation and processing steps that can significantly add to

the net cost of production (for example, laboratory grade PEO of high molar mass and low polydispersity costs upwards of \$300/kg). Assuming that bulk quantities of high molar mass PEO can be procured at \$50/kg (a fairly conservative estimate), the 285 ppm aqueous solution in Fig. 4.13 would incur a cost of \$14/m^3 for the polymer used in its preparation. By contrast, the price of unprocessed flax seeds was \$0.37/kg as of January 2018,[245] which translates to a material cost of less than \$1/m^3 for the 1:400 mucilage extract in Fig. 4.13 that shows comparable drag reduction performance. This cost can be reduced even further if spent flax meal (post extraction of linseed oil) is substituted for fresh seeds as the source of mucilage.[33] A concurrent advantage of using seed mucilage as a drag reducing agent is the inherently low polydispersity of its high molar mass constituents (see Fig. 4.3), as is typically the case with many macromolecules of biological origin.

Mechanical Degradation of Mucilage Polysaccharides

A key concern in the selection of viable drag reducing additives, especially for use in closed conduit flow applications such as pipelines, is the longevity of the drag reduction effect under sustained shear flow, which in turn is dictated by the resistance of the dissolved polymer chains to flow-induced degradation.[246–248] At high turbulence intensities, the elongational stresses on individual chains can grow sufficiently intense to cause scission of intrachain covalent bonds, leading to a progressive decline in the average chain length (or equivalently, the molar mass), and an attendant loss of drag reduction efficacy over time.[249] It has been reported that rigid polymers, such as those present in xanthan gum and okra mucilage, are more resistant to chain scission than flexible chains in turbulent flows; nevertheless, a decrease in percentage drag reduction still occurs with time, and has been attributed to the de-aggregation of polymer chains under sustained shear.[66, 109]

To assess the effect of mechanical degradation, the 285 ppm aqueous PEO solution and the 1:400 flaxseed extract were both subjected to identical conditions of sustained shear flow inside the TC apparatus, at a constant Reynolds number of $\mathrm{Re}_s = 62\,000$; the resulting deterioration in the percentage drag reduction $\mathscr{D}(t)$ was continuously monitored as a function of the elapsed time t since the inception of turbulent flow. The experimental data is shown in Fig. 4.14(a). At $t = 0$, both solutions yielded comparable initial levels of drag reduction ($\mathscr{D}_{\mathrm{PEO}}(0) \simeq \mathscr{D}_{\mathrm{FM}}(0) = 13\,\%$) at $\mathrm{Re}_s = 62\,000$. The diminution in drag reduction levels over time for the two solutions is well described using a least-squares regression to the empirical *Brostow equation*, given by[71, 250, 251]

$$\frac{\mathscr{D}(t)}{\mathscr{D}(0)} = \frac{1}{1 + W\,(1 - e^{-r\,t})}\,, \tag{4.7}$$

where W and r are fit parameters that denote, respectively, a representative number

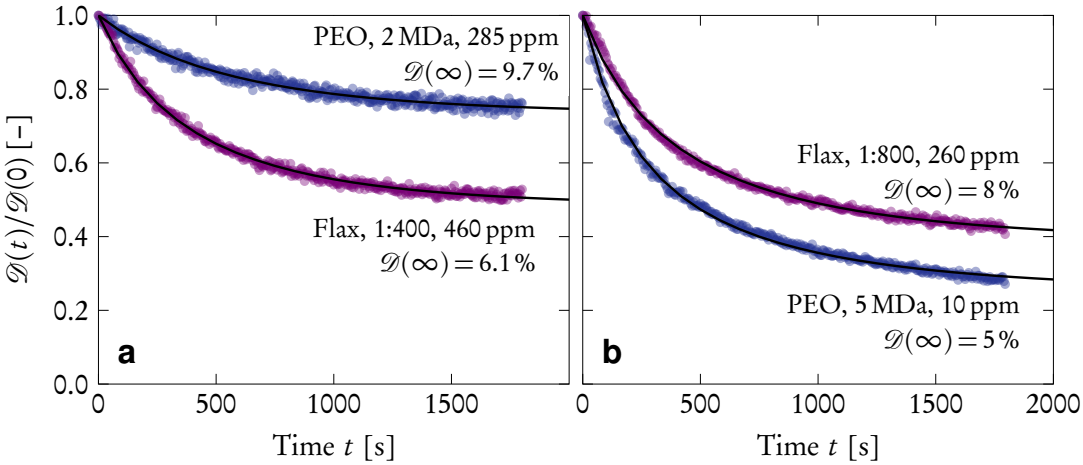

FIGURE 4.14. Diminution in the percentage drag reduction $\mathscr{D}(t)$ with time t for (a) a 285 ppm aqueous solution of 2 MDa PEO, and a 1:400 ($c = 460$ ppm) mucilage extract, under sustained shearing at $\mathrm{Re}_s = 62\,000$; and (b) a 10 ppm solution of 5 MDa PEO, and a 1:800 ($c = 260$ ppm) flax mucilage extract, under sustained shearing at $\mathrm{Re}_s = 59\,400$. The solid curves represent least-squares fits of the Brostow model, Eq. 4.7, to the experimental data.

of breakage points per chain, and a characteristic time rate of degradation. The rates of degradation r (obtained from the fit) for the two solutions were comparable, with $r_{\mathrm{PEO}} \simeq r_{\mathrm{FM}} = 1.4 \times 10^{-3}\,\mathrm{s}^{-1}$, suggesting similar time scales for chain scission. In the limit of $t \to \infty$, Eq. 4.7 gives $\mathscr{D}(\infty) = \mathscr{D}(0)/(1 + W)$, yielding a prediction for the asymptotic value of the percentage drag reduction expected at long times when the length of dissolved chains has been reduced sufficiently to render flow-induced scission processes inoperative.[249] For the two solutions in Fig. 4.14(a), we obtain $\mathscr{D}_{\mathrm{PEO}}(\infty) = 9.7\,\%$ and $\mathscr{D}_{\mathrm{FM}}(\infty) = 6.1\,\%$; the terminal percentage drag reduction for the flax seed extract is thus smaller by about 37 % as compared to the aqueous 2 MDa PEO solution.

Alternatively, Fig. 4.14(b) compares the degradation rate of flax mucilage against aqueous PEO of greater molar mass ($M_w \approx 5$ MDa), which is consequently more susceptible to mechanical degradation than the 2 MDa PEO discussed above. In this test, a 10 ppm solution of PEO, and a 1:800 extract ($c = 260$ ppm) of flax mucilage, were both subjected to prolonged shear flow in the TC apparatus at a constant Reynolds number of $\mathrm{Re}_s = 59\,400$. The concentrations were chosen such that the two solutions yielded comparable levels of initial drag reduction [$\mathscr{D}_{\mathrm{PEO}}(0) = 21\,\%$, and $\mathscr{D}_{\mathrm{FM}}(0) = 20\,\%$] at $t = 0$. The decline in percentage drag reduction over time was again modeled using the Brostow equation, Eq. 4.7; the rates of degradation r for the two solutions were similar, with $r_{\mathrm{PEO}} = 9.3 \times 10^{-4}\,\mathrm{s}^{-1}$ for the PEO solution, and $r_{\mathrm{FM}} = 1.1 \times 10^{-3}\,\mathrm{s}^{-1}$ for the mucilage

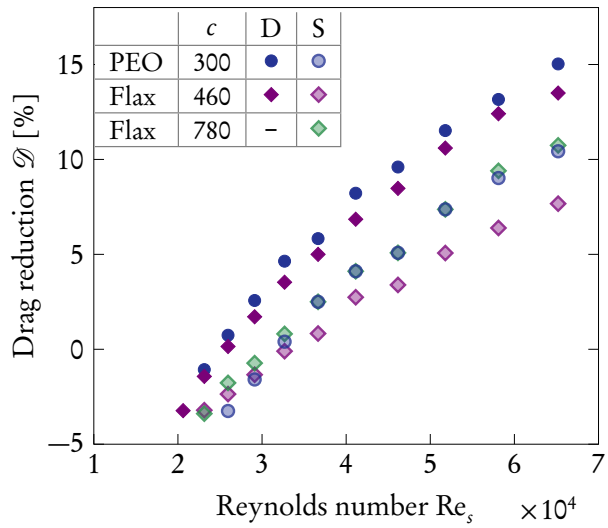

FIGURE 4.15. The percentage drag reduction $\mathscr{D}$, as a function of the Reynolds number Re_s, for PEO and flax mucilage solutions in deionized water (D) and synthetic seawater (S). The polymer concentrations c in the legend are reported in ppm.

extract. As $t \to \infty$, the asymptotic drag reduction $\mathscr{D}(\infty)$ for the two solutions were also comparable, with $\mathscr{D}_{\mathrm{PEO}}(\infty) = 5\,\%$ for the PEO solution, and $\mathscr{D}_{\mathrm{FM}}(\infty) = 8\,\%$ for the mucilage solution. The dilute mucilage extract thus performs equally well as aqueous PEO in this instance, displaying similar longevity and resistance to degradation as the latter under prolonged exposure to turbulent flow conditions.

Drag Reduction In Seawater: Effect of Salinity

A significant point of concern in employing polymer additives for marine drag reduction is the effect of salinity on the drag reduction efficacy of dissolved polymer chains. The addition of salts, and the resulting decrease in the radius of gyration of chains in the solution due to charge screening, have been shown to adversely affect the drag-reducing ability of several water-soluble long chain polymers, including PEO. As expected, the effect is more severe in solutions of polyelectrolytes than in the case of neutral chains.[37,76] To study the effect of salinity on turbulent drag reduction, flow measurements were performed on PEO and flax mucilage solutions prepared using synthetic seawater (Ricca Chemical Company, substitute ocean water without heavy metals conforming to ASTM standard D1141[252]), which has a salinity of approximately $35\,\mathrm{g\,kg^{-1}}$ and an ionic strength equivalent to 0.6 M aqueous NaCl. As seen in Fig. 4.15, a 302 ppm solution of PEO and a 1:400 ($c = 460$ ppm) flax mucilage extract yield comparable drag reduction levels (dark

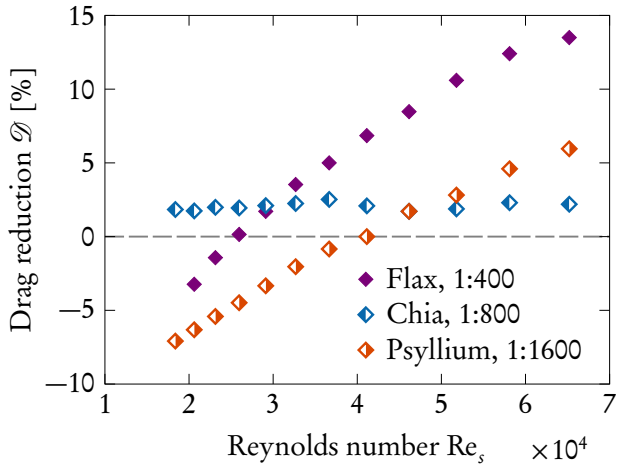

FIGURE 4.16. The percentage drag reduction $\mathscr{D}$ as a function of the Reynolds number Re_s for various seed mucilage solutions. Data are shown for a 1:400 aqueous extract derived from flax seeds, a 1:800 extract from chia seeds, and a 1:1600 extract from psyllium husk.

symbols) in pure water free of dissolved salts. In synthetic seawater, both polymers display a loss of drag reduction efficacy (light symbols), with the mucilage solution experiencing a larger decrement in percentage drag reduction; this is expected on account of the acidic fraction in mucilage,[32] and is consistent with the sensitivity of the intrinsic viscosity $[\eta]$ to the solvent ionic strength discussed in §4.II.B. Furthermore, the drag reduction deficit relative to PEO (in seawater) can be compensated by increasing the seed-to-water weight ratio from 1:400 ($c = 460$ ppm) to 1:200 ($c = 780$ ppm) at the extraction stage (denoted by light green diamonds in Fig. 4.15), which amounts to a roughly 70 % increase in the concentration of dissolved polysaccharides in the final mucilage solution.

IV. Closing Remarks

A. *Exploring Alternate Sources of Mucilage*

Although the focus of this study was primarily on mucilage extracted from flax seeds, a number of other plant sources can also serve as potential sources of inexpensive, high molar mass polysaccharides for turbulent drag reduction. For example, Fig. 4.16 shows preliminary drag reduction measurements using aqueous mucilage extracted from chia seeds, *Salvia hispanica*, and the husk of psyllium seeds, *Plantago ovata*; these seeds are today widely consumed as high-fiber foods and dietary supplements, precisely on account of their indigestible, water-soluble polysaccharide content. The principal drag-reducing

component of chia mucilage is a complex polysaccharide comprising xylose, mannose, glucose, arabinose, and galacturonic acid residues, with molar mass in the range 0.8–2 MDa.[34] The polysaccharide content of psyllium husk comprises highly branched arabinoxylan chains with molar mass of 0.95–1.1 MDa, and displays a marked affinity for spontaneous physical gelation in pure water, mediated by intermolecular hydrogen bonds.[35,36] For the experiments shown in Fig. 4.16, the mucilage from these other seeds was extracted in much the same way as in the case of flax, by soaking the unprocessed seeds (or seed husk) in warm water for 30 min, at a temperature of 80 °C for chia seeds, and 40 °C in the case of psyllium husk. The mucilaginous envelope of chia seeds swells and retains considerably more water than flax seeds, and is more firmly adherent to the seed coat; this makes extraction slightly more difficult without shearing the seeds, reducing the mucilage yield in the supernatant solution. The extraction protocol thus requires further refinement and optimization to maximize the polysaccharide yield, minimize protein and salt contamination, and enhance the solubility of mucilage (i.e. inhibit gelation).

As evident from Fig. 4.16, the polysaccharides in chia mucilage display drag reduction behavior that is qualitatively distinct from that shown by mucilage sourced from flax or psyllium seeds; specifically, the percentage drag reduction remains unchanged with increasing Reynolds number. This is, in fact, a known characteristic feature of relatively rigid and elongated drag-reducing polymers, such as charged polyelectrolyte chains, and is sometimes designated as 'Type B' drag reduction in the literature (in contrast to the 'Type A' drag reduction typical of flexible polymer chains, for which the percentage drag reduction increases with increasing Reynolds number).[59,253]

B. *A Brief Note on Biodegradability*

An essential prerequisite for any polymer-based marine drag reduction strategy is a careful evaluation of possible ecological effects of drag-reducing polymers—synthetic or natural—discharged into oceans and navigable water bodies. Although seed mucilage is certainly biodegradable at small scales, a more extensive study is required to fully preclude any unforeseen impact on the marine ecosystem, before implementing or deploying large-scale drag reduction techniques that would release significant quantities of biopolymers into the ocean. Unfortunately, such a comprehensive investigation of large-scale and long-term effects is beyond the scope of this focused study. Nevertheless, one can find strong suggestive evidence in the literature that any potential impact of these biodegradable polysaccharides in the ocean ecosystem will be minimal. A number of polysaccharides similar to those in flax are known to biodegrade rapidly under bacterial action, fully breaking down in laboratory solutions within a few days.[109,230] The ocean already harbors considerable amounts of dissolved organic matter (DOM),

derived from both terrestrial sources as well as secreted naturally by marine microbes, amounting to an impressive 700 Gt of oceanic carbon content.[232] About 30 % of this DOM is made up of biopolymers greater than 1 kDa in molar mass, including various polysaccharides. These polysaccharides are readily degraded by the enzymatic action of various oceanic microbes;[231,232] they are converted into simple sugars at rapid turnover rates, and eventually consumed and recycled by oceanic bacteria and fungi.

Notes

The results presented in this chapter have been published in the following peer-reviewed article by the author.

A. Rajappan and G. H. McKinley. Epidermal biopolysaccharides from plant seeds enable biodegradable turbulent drag reduction. *Sci. Rep.* **9**:18263 (2019).

5 *Combining Polymers & Plastrons for Enhanced Drag Reduction*

Despite polymer additives and superhydrophobic walls being well known as stand-alone methods for frictional drag reduction in turbulent flows, attempts to deploy them jointly in an additive fashion has remained as yet unsuccessful. Through experimental friction measurements in turbulent Taylor-Couette flow, we demonstrate in this chapter that the two techniques may indeed be successfully combined to achieve enhanced levels of frictional drag reduction in wall-bounded turbulence. An additive law is proposed that yields accurate quantitative predictions of this combined drag reduction effect at low concentrations of the dissolved polymer. The surfactant activity of polymer chains is shown to severely impact the wall slip on randomly textured superhydrophobic surfaces, leading to appreciable diminution in the net drag reduction efficacy of the polymer-surface combination.

I. Introduction

The addition of soluble, high molar mass polymers has long been known to be an effective strategy for reducing frictional drag in turbulent flows.[44,59] Even at dilute concentrations as low as 1–10 ppm, dissolved long-chain polymers interact with the near-wall coherent flow structures, disrupting momentum transport to the wall and yielding concomitant reductions in the frictional wall shear stress of 20–40 %.[44,45,59] As discussed at length in §2.I, the phenomenon of turbulent drag reduction by polymeric solutes has been extensively investigated in numerous experimental[44,59,254] and computational studies[23,24,45] spanning the seven decades since its discovery, and a diverse array of synthetic as well as naturally occurring high polymers have been successfully employed as drag reducing agents in various turbulent flow configurations.[105,114] In Chapter 4 of this thesis, the epidermal polysaccharide content, or mucilage, in flaxseeds was proposed as an attractive substitute for synthetic drag-reducing polymers in large-scale aqueous systems.[67]

Meanwhile, following rapid advances in surface fabrication techniques over the last

two decades, superhydrophobic texturing of wetted solid boundaries has recently emerged as a viable method of drag reduction in wall-bounded aqueous flows.[25,40,119,121,255] As reviewed in §2.II, drag-reducing superhydrophobic surfaces incorporate hydrophobic micro-textural features capable of stabilizing a thin layer of air—called the *plastron*—that remains pinned to the texture asperities in the Cassie-Baxter state, even when submerged underwater.[40,121] This intervening gas layer, in turn, shields the liquid phase from direct contact with the underlying solid substrate over large areal patches of the flow boundary, as has been confirmed experimentally via direct confocal imaging of the plastron interface.[178,256] Even as the usual no-slip condition continues to hold in regions of direct solid-liquid contact, the liquid-air interface atop the plastron layer serves as a nearly shear-free boundary over which the flow slips with minimal friction. The effect of this composite boundary on the outer flow is often modeled by an equivalent homogeneous slip velocity V_S at the wall, given by the Navier slip condition $V_S = b\,\tau_w/\eta$ (cf. Eq. 2.35); here η is the dynamic viscosity of the liquid, τ_w the shear stress at the wall, and b represents an "effective" slip length characterizing the drag-reducing properties of the superhydrophobic texture.[40] Despite early successes in laminar drag reduction dating as far back as 1996,[257] progress towards the use of superhydrophobic surfaces in turbulent flows has been relatively slow, due in part to challenges in fabricating robust textures capable of sustaining an intact plastron layer even under the intense pressure fluctuations typically encountered in turbulence.[20,25] Several such surfaces have nevertheless been developed in recent years, and turbulent drag reductions of up to 50 % on periodically micropatterned surfaces, and up to 30 % on scalable, randomly textured surfaces, have been reported in the current literature.[25,31,169]

As a result of these developments, there now exist two independent routes to realizing practicable levels of drag reduction in turbulent flows: (*i*) dissolved polymer chains, which alter near-wall flow dynamics and disrupt momentum transport across the turbulent boundary layer, and (*ii*) plastron-supporting superhydrophobic surfaces, which enable diminished contact of the liquid phase with the solid boundary, in effect inducing a slip velocity at the wall. Insofar as these physical mechanisms operate via fundamentally distinct pathways, a natural question arises if the two approaches may be employed jointly to achieve enhanced reductions in frictional drag. Despite sustained research interest in both polymers and superhydrophobic surfaces as stand-alone methods for drag mitigation, this possibility of combining the two techniques has, rather surprisingly, remained poorly explored in the extant literature. The only prior instance of polymers being used in conjunction with superhydrophobic textures for drag reduction seems to be an early experimental study by Watanabe and Udagawa (2001),[257] who measured the frictional pressure drop of aqueous polyethylene oxide (PEO) solutions in a circular pipe treated with a water-repellent fluoropolymer coating. Although they separately reported wall slip

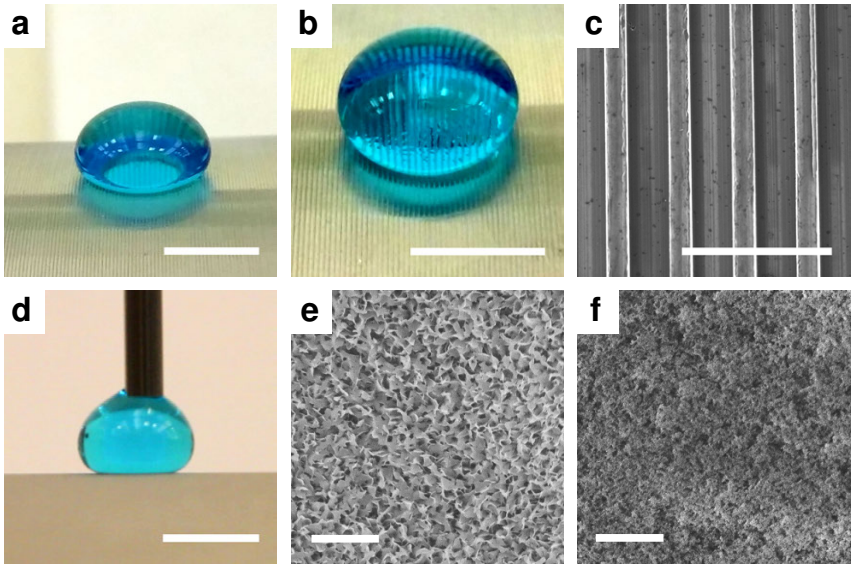

FIGURE 5.1. (a) A water drop, dyed blue, placed on the surface of the grooved superhydrophobic rotor (S_G). A reflective plastron is visible at the circular base of the drop. (b) A closer image of the basal surface of the drop in panel (a); the plastron within the groove troughs appears enlarged due to refraction. (c) SEM image of the grooved rotor surface. (d) A drop of water, colored blue, deposited on the randomly textured superhydrophobic rotor (S_R). (f) SEM image of the random texture before hydrophobization with the Glaco solution; the characteristic crossed leaflet nanostructure of boehmite is clearly visible. (g) The random texture in panel (f) after treatment with Glaco solution, showing the underlying boehmite layer completely covered by hydrophobic silica nanoparticles. SCALE BARS denote 5 mm in panels (a), (b), and (d); 500 µm in (c); and 1 µm in (e) and (f).

in the laminar regime and polymer drag reduction in the turbulent regime, no combined effect arising from the two mechanisms operating in concert was observed, presumably due to the loss of entrapped gas from their superhydrophobic texture leading to plastron collapse in the turbulent regime. Recently, Davis and Park (2019)[258] presented direct numerical simulations of viscoelastic turbulent channel flow in the presence of wall slip; their preliminary results, however, indicated a slip-induced increase (rather than decrease) in the apparent drag.

This chapter presents frictional drag measurements in the bespoke TC apparatus which provide a definite and affirmative answer to the question posed above: dissolved polymer chains can indeed act in parallel with superhydrophobic walls to generate net reduction in turbulent drag far greater than that obtainable from either method employed independently. The cooperative drag reduction effect is studied for various combinations

involving one of two common water-soluble polymers, namely polyacrylamide (PAM) or polyethylene oxide (PEO), paired with one of two prototype drag-reducing superhydrophobic surfaces: either a regular pattern of streamwise microgrooves, or a scalable random texture possessing hierarchical multi-scale roughness. The surface activity of PEO is observed to adversely influence the wall slip on the randomly textured surface, leading to significant diminution in the overall drag reduction efficacy of this polymer-surface combination. In cases where such interfacial effects are absent, an additive friction law is proposed that yields fairly accurate predictions of the combined drag reduction performance expected of a given polymer-surface pair, each possessing known individual drag-reducing characteristics.

II. Preparation of Polymers and Superhydrophobic Surfaces

A. *Fabrication of drag-reducing superhydrophobic textures*

To facilitate a quantitative assessment of the contribution of wall slip in combined drag reduction experiments, robust aerophilic textures were required that yielded repeatable slip length characteristics consistently across multiple test runs. Accordingly, two durable superhydrophobic textures were prepared for use in turbulent flow experiments in the TC apparatus: a 'canonical,' regularly patterned surface consisting of a periodic array of streamwise grooves, and a scalable random texture comprising irregular hierarchical roughness at multiple length scales. The process of fabricating these prototype surfaces is briefly described in this section.

Superhydrophobic Grooves

To fabricate the grooved surface (hereafter denoted by S_G), the cylindrical surface of the rotor was machined on a CNC lathe to generate a periodic array of parallel rectangular microgrooves aligned in the circumferential (streamwise) direction, similar to the grooved rotor profile used in the earlier work by Van Buren and Smits (2017).[171] The grooves were then hydrophobized by dip-coating in a dilute ($\approx 0.1\,\%$) solution of a water-repellent fluoropolymer resin (Teflon AF 2400, Chemours) dissolved in HCFC-225 (Asahiklin AK225, Asahi Glass Company), and subsequently baked at elevated temperature on a hot plate in accordance with manufacturer guidelines: 175 °C for 10 min to evaporate the solvent, followed by 5 min at 245 °C above the glass transition temperature of the resin ($T_g \simeq 240\,°\mathrm{C}$), and finally at 330 °C for 15 min to enhance adhesion. The dip-coating and baking steps were repeated at least five times to yield a mechanically durable hydrophobic layer firmly adherent to the underlying aluminum substrate. Inspection of the final texture under a scanning electron microscope (SEM) revealed a well-formed groove profile

coated uniformly by a conformal layer of hydrophobic resin, with no appreciable levels of secondary nano-scale roughness. Figure 5.1(a) shows a sessile drop of water deposited atop the curved surface of the rotor; a magnified view of the base of the same drop can be seen in Fig. 5.1(b), and the individual plastrons bridging the groove crests are clearly discernible. A representative micrograph of the grooved surface is shown in Fig. 5.1(c). Textural dimensions, inferred from similar SEM images obtained at multiple sampling spots, were used to determine an average spatial periodicity of $l = 204\,\mu\text{m}$ and a solid fraction of $\phi = 0.33$ for the groove pattern.

Superhydrophobic Random Texture

The superhydrophobic random texture (hereafter denoted by S_R) was prepared identically to the 80-grit sandblasted, etched and boehmitized aluminum surface described in Ref. [31], and referred to as 'SEB-80' in that study. The rough texture was generated by first sandblasting the rotor surface with 80 grit media (of average particle size 165 µm), etching in a concentrated 12 M (37 % by volume) solution of hydrochloric acid for 25 s, and finally boehmitizing in boiling deionized water for 30 min. Afterwards, the surface was treated with a commercial water-repellent coating (Glaco Mirror Coat Zero, SOFT99, Japan) comprising 30–50 nm hydrophobic silica particles dispersed in 2-propanol.[259] The textured rotor was dip-coated in the Glaco solution, dried in ambient air for 10 min, and subsequently baked for 30 min at 200 °C on a hot plate; the coating and baking steps were repeated thrice to ensure a robust coating with uniform areal coverage. As reported in Ref. [31], this process yields a superhydrophobic surface possessing multiple tiers of hierarchical roughness, with advancing and receding contact angles of $\theta_A = (152 \pm 1)°$ and $\theta_R = (148 \pm 1)°$ respectively[31] [see Fig. 5.1(d)]. Figure 5.1, panels (e) and (f) respectively show scanning electron micrographs of the superhydrophobic random texture before and after treatment with the Glaco solution; the porous boehmite layer helps support and retain the hydrophobic silica on the aluminum substrate, and is seen to be completely overspread by nanoparticles after three rounds of dip-coating and baking.

B. *Preparation of aqueous drag-reducing polymer solutions*

Dilute solutions of aqueous polyacrylamide (PAM) and polyethylene oxide (PEO) were employed as model drag-reducing polymers in this study, each comprising flexible, linear chains of large molar mass ($\geqslant 10^6\,\text{g}\,\text{mol}^{-1}$). Both polymers were procured in powder form and used as is without further purification, as described in §3.II.A. Briefly, a 0.4 % stock solution of each polymer was prepared by gently dispersing the requisite quantity of powder in deionized water, and allowing it to hydrate and dissolve gradually on a laboratory bench-roller over several days to ensure uniform laminar mixing. Dilute solutions

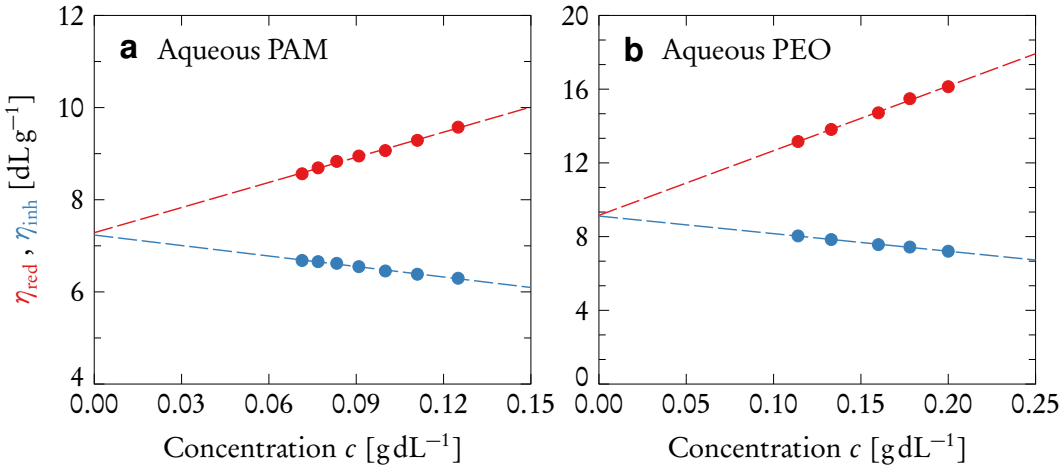

FIGURE 5.2. Huggins-Kraemer extrapolation plots for (a) aqueous PAM, and (b) aqueous PEO samples, employed in frictional drag measurements in this chapter. See §3.II.B for a discussion on the experimental determination of the instrinsic viscosity $[\eta]$.

of desired concentrations, for use in flow tests, were subsequently prepared by diluting this stock solution with an appropriate volume of deionized water.

As a direct characterization of the macromolecular properties of the drag-reducing chains in solution, the intrinsic viscosity $[\eta]$ for each of the two polymers above was determined by successive dilution in an Ubbelöhde glass capillary viscometer, as per the procedure detailed in §3.II.B. The resulting Huggins-Kraemer plots are shown in Fig. 5.2; the conventional extrapolation to zero concentration yielded intrinsic viscosities of $[\eta]_{\mathrm{PAM}} = 7.26\,\mathrm{dL\,g^{-1}}$ and $[\eta]_{\mathrm{PEO}} = 9.13\,\mathrm{dL\,g^{-1}}$ for the aqueous PAM and PEO samples, respectively. The intrinsic viscosity $[\eta]$, in turn, was used to infer the viscosity-averaged molar mass M_v of the dissolved chains, by means of the empirical Mark-Houwink-Sakurada equation $[\eta] = K\,(M_v)^a$ (cf. Eq. 3.44).[84,213] Utilizing empirical values of the constants K and a available in the literature,[214,260] a viscosity-averaged molar mass of approximately $M_{v,\mathrm{PAM}} \simeq 2.54 \times 10^6\,\mathrm{g\,mol^{-1}}$ for the PAM sample, and $M_{v,\mathrm{PEO}} \simeq 1.72 \times 10^6\,\mathrm{g\,mol^{-1}}$ for PEO, were obtained.

Lastly, the critical overlap concentration c^* for flexible chains in good solvents may be estimated from their intrinsic viscosity as $c^* = 0.77/[\eta]$ (cf. Eq. 3.53),[217] yielding $(c^*)_{\mathrm{PAM}} = 1.1\,\mathrm{g\,L^{-1}}$ and $(c^*)_{\mathrm{PEO}} = 0.84\,\mathrm{g\,L^{-1}}$ for aqueous PAM and PEO solutions, respectively. The solutions used in flow tests were considerably more dilute, with concentrations in the range of $10\,\mathrm{ppm} \leqslant c \leqslant 200\,\mathrm{ppm}$, corresponding to normalized concentrations of $0.009 \leqslant c/c^* \leqslant 0.24$. Experimental viscometric data for the various dilute polymer solutions used in turbulent drag reduction experiments are summarized in Table 5.1.

TABLE 5.1. Concentration c and relative viscosity $\eta_r = \eta_0/\eta_w$ of dilute PAM and PEO solutions used in experimental friction measurements. The relative viscosities reported here are averaged values derived from capillary viscometry of each test solution.

Polymer	Concentration c [ppm]	c/c^*	Relative viscosity $\eta_r = \eta_0/\eta_w$
Polyacrylamide (PAM)	10	0.0094	1.01
$([\eta]_{\mathrm{PAM}} = 7.26\,\mathrm{dL\,g^{-1}})$	25	0.024	1.02
	50	0.047	1.04
	100	0.094	1.08
	200	0.19	1.15
Polyethylene oxide (PEO)	50	0.059	1.05
$([\eta]_{\mathrm{PEO}} = 9.13\,\mathrm{dL\,g^{-1}})$	200	0.24	1.19

III. Experimental Results and Discussion

A. *Turbulent Flow Experiments in the Bespoke TC Apparatus*

To assess the drag reduction performance of polymer additives and superhydrophobic surfaces, both individually and in parallel, experimental measurements of the frictional drag were performed in fully developed turbulent shear flow using the bespoke TC apparatus, a full description of which is provided in §3.I. Briefly, the TC device comprises a rotating inner cylinder (rotor) of radius R_i and length L, housed coaxially within a stationary outer cylinder (stator) of radius R_o, creating an annular gap of width $d = R_o - R_i$ to which the flow is confined; the radius ratio of the TC geometry is $R_i/R_o = 0.75$, and the gap aspect ratio is $L/d = 6.0$. The rotor is coupled to a commercial rotational rheometer (AR-G2, TA Instruments), enabling precise measurement of the steady-state frictional torque $\mathcal{T}$ exerted by the fluid as a function of the angular speed Ω.

We define the Reynolds number $\mathrm{Re} = \rho V d/\eta$ for the TC flow in the annular gap based on the gap width d, the azimuthal speed $V = R_i\Omega$ of the rotor wall, and the density ρ and viscosity η of the working fluid. The transition to featureless wall-driven turbulence in the TC apparatus occurs at a critical Reynolds number $\mathrm{Re}_{\mathrm{crit}} \simeq 11\,000$, as determined from the power-law scaling of the baseline torque $\mathcal{T}_N$ with the Reynolds number Re as measured on a smooth no-slip rotor in deionized water (see Fig. 3.4 and the related discussion in §3.I.B). Frictional drag measurements employing polymers or superhydrophobic surfaces were performed at Reynolds numbers $15\,000 \leqslant \mathrm{Re} \leqslant 52\,000$, well into the turbulent flow regime.

All tests were conducted at room temperature, measured to be (21.0 ± 0.5) °C during

tests involving the randomly textured superhydrophobic surface, and (23.0 ± 0.5) °C in all other cases. A typical experiment involved varying the angular velocity Ω of the rotor in discrete steps, and recording the mean steady-state frictional torque $\mathcal{T}$ at constant rotor speed. The average shear stress $\tau_w = \mathcal{T}/2\pi R_i^2 L$ at the rotor wall, and the friction velocity $u_\tau = \sqrt{\tau_w/\rho}$ in the near-wall layer, were then calculated from the experimental torque versus speed data. Finally, the shear Reynolds number was computed based on the gap width as $\mathrm{Re}_\tau = \rho u_\tau d/\eta$. The reference viscosity η here was set equal to either the viscosity of water $\eta_w(T)$, or in tests involving drag-reducing polymers, the zero shear rate viscosity $\eta_0(T)$ of the dilute polymer solution, at the corresponding test temperature T; the viscosity η_0 was determined independently for each polymer solution using a glass capillary viscometer in accordance with the procedure outlined in §3.II.B, and is listed in Table 5.1. In advance of tests employing a superhydrophobic rotor wall, the working fluid was allowed to aerate freely inside a ventilated container for several hours to reach air saturation at ambient temperature, so as to prevent undue depletion of the plastron layer by diffusion of gas into the liquid phase. Each flow curve in this study was derived from multiple replicate experiments, whose data sets were averaged before subsequent analysis.

B. *Individual and Combined Drag Reduction Measurements*

In this section, empirical friction curves are presented from turbulent flow measurements performed in the TC apparatus using water as well as dilute polymer solutions, with and without a superhydrophobic texture applied to the rotor wall. For clarity, results are organized into five sections based on the working fluid inside the cell gap (water or polymer solution) and the flow boundary condition (no-slip, superhydrophobic grooves or random superhydrophobic texture) prevailing at the rotor surface.

Water + No-Slip Rotor

In fully turbulent TC flow of a Newtonian fluid, matched asymptotic expansions for the azimuthal angular momentum in the flow gap yield a logarithmic friction law of the form (cf. Eq. 3.18)[203]

$$V_N^+ = M \log \mathrm{Re}_\tau + N, \tag{5.1}$$

where $V^+ = V/u_\tau$ is the rotor wall speed expressed in inner units, the subscript 'N' denotes Newtonian flow, and the constants M and N are determined by the radius ratio $\zeta = R_i/R_o$ of the TC geometry. In Fig. 5.3, panels (a) and (b), experimental friction data are presented in Prandtl-von Kármán coordinates, wherein V^+ is shown as a function of the shear Reynolds number Re_τ on semi-logarithmic axes. The friction data for the smooth no-slip rotor in deionized water in the fully turbulent regime (black hollow

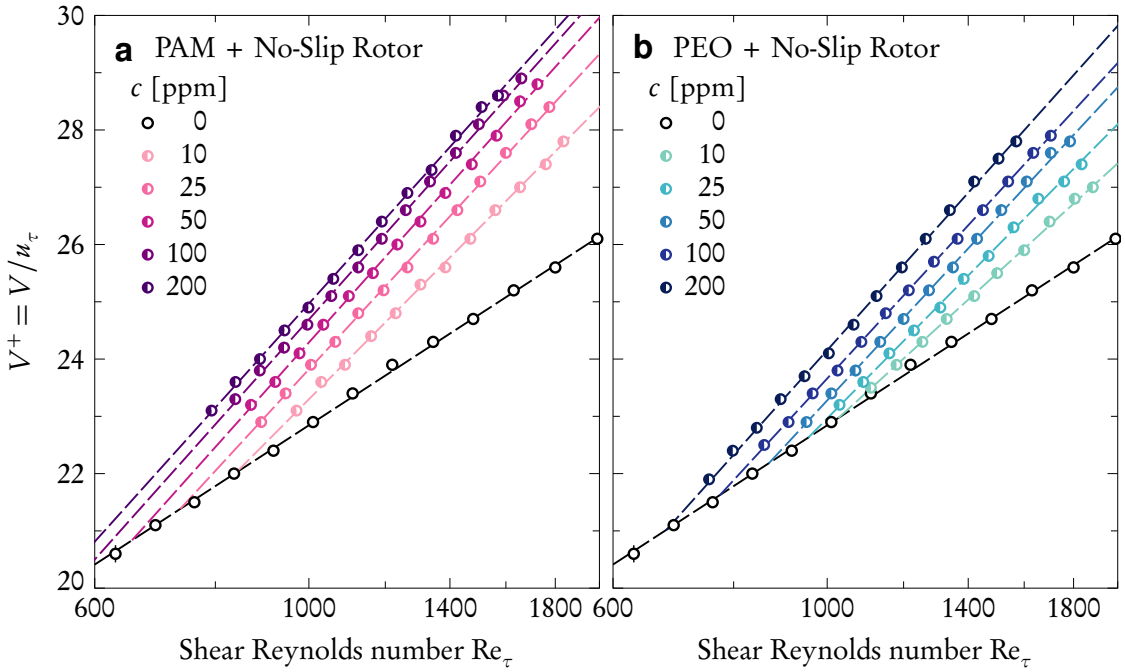

FIGURE 5.3. Experimental friction curves for the smooth no-slip rotor in aqueous solutions of (a) PAM, and (b) PEO, at different polymer concentrations, showing turbulent drag reduction induced by the dissolved polymer chains. The black hollow circles in both panels denote the baseline friction data for the no-slip rotor in pure, deionized water. The dashed lines represent linear least-squares fits of Eqs. 5.1 and 5.2 to the experimental data.

circles in Fig. 5.3) show good conformance to the functional form predicted by Eq. 5.1, and a linear least-squares regression to this baseline data was used to obtain the constants $M = 4.76$ and $N = -10.0$ for the bespoke TC apparatus [cf. Fig. 3.5(a), and Eq. 3.19].

POLYMER SOLUTION + NO-SLIP ROTOR

To characterize the drag reduction efficacy of the aqueous PAM and PEO solutions, frictional drag measurements were performed using the smooth no-slip rotor, employing dilute solutions of each polymer as the working fluid in the cell gap. The resulting data are shown in Fig. 5.3, panels (a) and (b) respectively, for a series of dilute PAM and PEO solutions of various concentrations. Analogous to the case of turbulent drag reduction in pipe flows,[59] the experimental friction curves are well described by straight lines on the Prandtl-von Kármán plot, of the form

$$V_P^+ = M_P \log \mathrm{Re}_\tau + N_P \,, \tag{5.2}$$

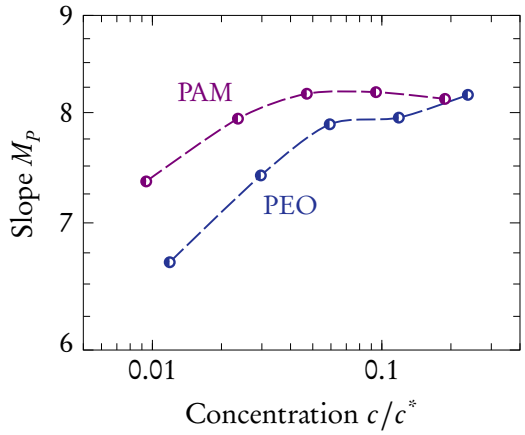

FIGURE 5.4. The slope M_P of the polymeric friction curves in Fig. 5.3, as a function of the normalized concentration c/c^*. The individual slopes were obtained from linear least-squares fits of Eq. 5.2 to the experimental friction data, as shown in Fig. 5.3. The dashed curves are provided solely for visual guidance.

where the subscript 'P' denotes polymeric turbulence, and the constants M_P and N_P, inferred from linear least-squares fits to the data, now depend also on the polymer used and its concentration c in solution. The drag-reducing effect of the dissolved polymer is evinced by the higher slope of the polymeric friction curves, , $M_P > M$, and their upward divergence from the Newtonian baseline in the turbulent regime. This becomes more evident if we consider the non-dimensional friction factor $C_f = 2\tau_w/\rho V^2$ (cf. Eq. 2.3), which may equivalently be expressed as $C_f = 2/(V^+)^2$; a larger V^+ therefore implies a smaller C_f, and by extension, a reduced frictional shear stress τ_w, at the same imposed speed V of the rotor wall. As expected, the drag reduction effect grows with increasing Reynolds number, and at greater concentrations of the dissolved polymer.[59] Figure 5.4 shows the variation of the slope M_P with the normalized polymer concentration c/c^* for aqueous PAM and PEO solutions, determined empirically from linear fits of Eq. 5.2 to the data in Fig. 5.3.

WATER + SUPERHYDROPHOBIC ROTOR

Figure 5.5(a) shows the experimental friction data for the grooved (S_G) and the randomly textured (S_R) superhydrophobic rotors, as measured in deionized, air-saturated water; unlike the polymeric case, the friction curves do not converge to the Newtonian, no-slip baseline for Reynolds numbers approaching $\mathrm{Re}_{\mathrm{crit}}$, reflecting the fact that slip-mediated drag reduction is effective in both the turbulent and the pre-transition flow regimes. The

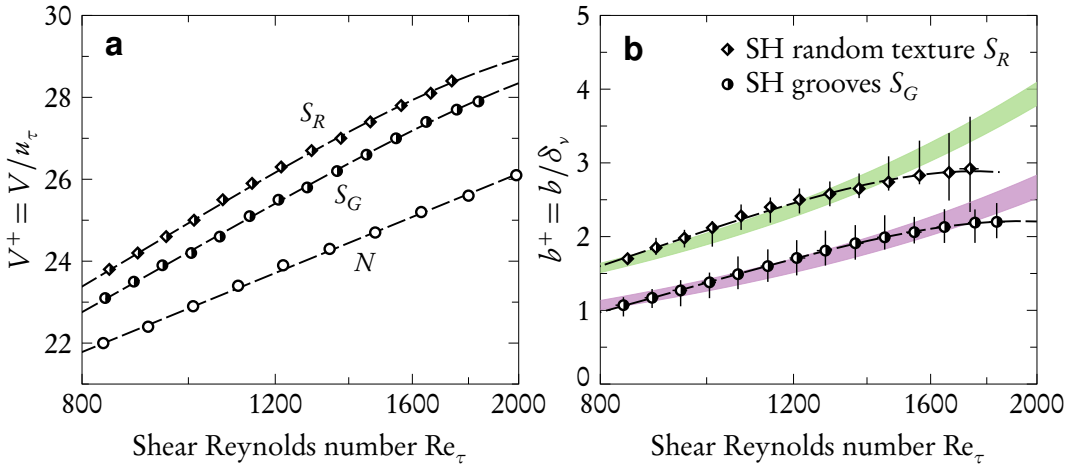

FIGURE 5.5. (a) Experimental friction curves for the grooved rotor (S_G) and the randomly textured rotor (S_R) in air-saturated deionized water, showing drag reduction induced by wall slip. The baseline data for the no-slip rotor (N) is also included for comparison. (b) The slip length b^+ for the two superhydrophobic rotors, derived from the data in panel (a), as a function of the shear Reynolds number Re_τ. The dashed curves represent least-squares quadratic polynomial fits to the data. The two colored bands denote, respectively, the expected linear variation of b^+ for a constant (dimensional) slip length of $b = (17 \pm 1)\,\mu\mathrm{m}$ for the grooved rotor S_G (purple band), and $b = (25 \pm 1)\,\mu\mathrm{m}$ for the randomly textured rotor S_R (green band).

skin friction law for the turbulent TC flow of a Newtonian fluid with an effective slip boundary condition at the inner wall was derived by Srinivasan et al. (2015),[178] and is given by

$$V_S^+ = M \log \mathrm{Re}_\tau + N + b^+, \tag{5.3}$$

where the subscript 'S' denotes a superhydrophobic rotor wall, $b^+ = b/\delta_\nu$ is the effective slip length b expressed in wall units $\delta_\nu = \eta/\rho u_\tau$, and the constants M and N are identical to those in Eq. 5.1, the baseline curve for a no-slip rotor wall. Drag reduction arising from wall slip induced by the plastron layer atop the rotor surface is once again evident as an upward shift of the superhydrophobic friction curves relative to the no-slip baseline. Figure 5.5(b) shows the effective slip length b^+ for both textures, inferred from experimental data using Eq. 5.3, as a function of the shear Reynolds number Re_τ. Notice that for a constant (dimensional) slip length b, the dimensionless slip length $b^+ = b/\delta_\nu = b\,\mathrm{Re}_\tau/d$ increases linearly with the shear Reynolds number Re_τ. As seen in Fig. 5.5(b), the effective wall slip b^+ for both superhydrophobic textures increases at first with increasing Re_τ, but subsequently saturates at high rotor speeds owing to a decrease in the physical slip length b caused by the progressive flow-induced collapse of the plastron layer. To

capture this gradual variation at high Reynolds numbers, the empirical slip curves for the two superhydrophobic rotors were individually fit to simple quadratic polynomials of the form $b^+ = A + B\,\mathrm{Re}_\tau + C\,\mathrm{Re}_\tau^2$, denoted by the dashed curves in Fig. 5.5; the goal was to facilitate a smooth interpolation of the slip length at intermediate values of Re_τ in later analyses.

The effective slip length over an alternating pattern of no-slip and shear-free stripes at the wall was derived analytically by Philip (1972)[153,154] in the limit of creeping flows, and is given by $b_{\|} = (l/\pi)\log\sec[\pi(1-\phi)/2]$ in the direction parallel to the stripe pattern, and $b_{\perp} = (1/2)b_{\|}$ perpendicular to it. The situation is, as expected, more involved in the case of turbulent boundary layers, wherein the effective slip is determined by a complex interplay of both streamwise and spanwise slip lengths on the texture: In essence, spanwise slip strengthens near-wall vortices and enhances momentum transport, partially offsetting the drag reduction produced by streamwise slip through a forward displacement of the mean velocity profile.[167] The effective slip length b^+ thus depends non-trivially on the local tensorial slip pattern at the wall and the viscous length scale of the inner flow, and a quantitative prediction for generic surface textures usually warrants computational methods. Furthermore, the slip length on the grooved rotor at large flow speeds may also be influenced adversely by the curvature of the air-water interface spanning the groove troughs,[261,262] occasional defects in the groove geometry, or the flow-induced collapse of the plastron in a small number of grooves.[171] The above complexities notwithstanding, a rough estimate of the anticipated slip length on the grooved texture[263] may be obtained as $b \approx b_{\|} - b_{\perp} = (l/2\pi)\log\sec[\pi(1-\phi)/2] = 22\,\mu\mathrm{m}$, which is consistent with the average (dimensional) slip length of $b = 17\,\mu\mathrm{m}$ observed in experiments over the finite range of Reynolds numbers investigated. For the superhydrophobic random texture, experimental friction data in Fig. 5.5 yield an average slip length of $b = 25\,\mu\mathrm{m}$, in excellent agreement with $b = 24\,\mu\mathrm{m}$ reported for the identically fabricated 'SEB-80' surface in Ref. [31].

Polymer Solution + Grooved Superhydrophobic Rotor

Having characterized the drag reduction efficacy of the two polymers and the two superhydrophobic textures individually, combined drag reduction measurements were performed on each of the four possible polymer-surface pairs, starting with the superhydrophobic grooved rotor immersed in aqueous PAM and PEO solutions. A representative friction curve for the grooved rotor in 50 ppm aqueous PAM solution is shown in Fig. 5.6(a), labeled as curve C_G; individual friction curves for the no-slip rotor in 50 ppm PAM solution (curve P), and for the grooved rotor in water (curve S_G)—reproduced from Figs. 5.3(a) and 5.5(a) respectively—are also included for comparison.

Over the full range of experimentally accessible Reynolds numbers, the combined drag reduction produced by the polymer-surface pair is larger than that obtained from

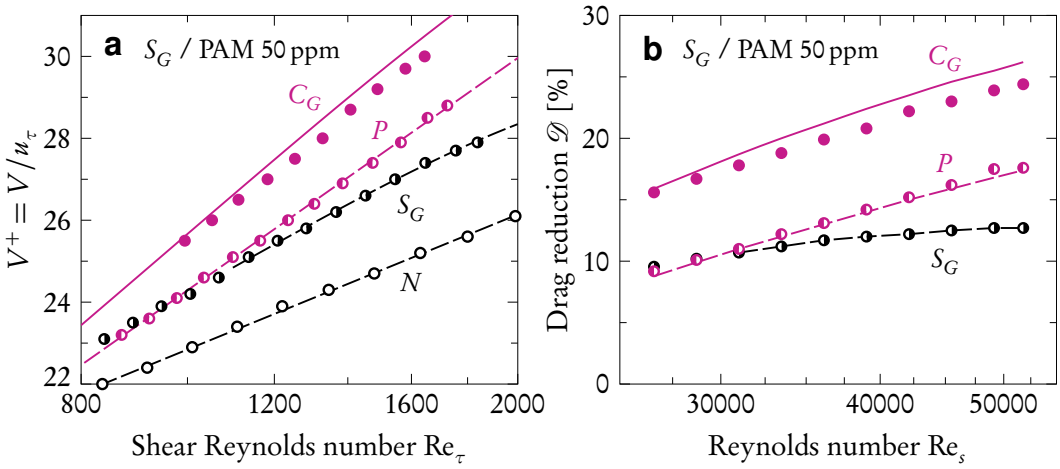

FIGURE 5.6. (a) Combined drag reduction data (C_G) for the grooved superhydrophobic rotor in a 50 ppm solution of aqueous PAM. Also included for comparison are the individual friction curves for the no-slip rotor in water (N) and in 50 ppm aqueous PAM (P), as well as for the grooved superhydrophobic rotor in deionized water (S_G). (b) The percentage drag reduction $\mathscr{D}$ corresponding to the data shown in panel (a). The solid curves in panels (a) and (b) respectively denote the ideal drag reduction estimates $V_C^{+\circ}$ and $\mathscr{D}_C^\circ$ predicted by Eqs. 5.5 and 5.10.

either technique employed independently, signifying that the two mechanisms can indeed operate additively to yield enhanced overall drag reduction in the turbulent regime. From a practical standpoint, the quantity that is often of immediate interest in engineering applications is the net decrease in fluid friction (i.e., the reduction in the wall shear stress in external flows, or the reduction in the pressure drop per unit length in internal flows) that can be achieved in comparison to the flow of the unmodified (Newtonian) liquid over no-slip walls under identical conditions of imposed wall speed or flow rate. Accordingly, the percentage drag reduction is defined as (cf. Eq. 2.6),

$$\mathscr{D} = \frac{\tau_{w,N} - \tau_w}{\tau_{w,N}} \cdot 100\,\% \,, \tag{5.4}$$

where τ_w is the actual shear stress measured at the rotor wall with either one or both drag reduction mechanisms in operation, and $\tau_{w,N}$ is the baseline shear stress on the no-slip rotor in deionized water at the same rotor speed V (or equivalently, at the same solvent-based Reynolds number $\mathrm{Re}_s = \rho V d/\eta_w$ defined using the viscosity η_w of pure water). In Fig. 5.6(b), the data in Fig. 5.6(a) is represented as the percentage drag reduction $\mathscr{D}$ versus the Reynolds number Re_s, and the enhancement in drag reduction gained by combining polymers and plastrons is again apparent.

A Two-Layer Model for Combined Drag Reduction

We attempt to formulate an empirical model for predicting the combined drag reduction effect expected of a given polymer-wall pair, provided their individual drag reduction properties are known beforehand. Insofar as both polymeric and superhydrophobic drag reduction result from complex modifications of the near-wall dynamics, mediated by dissolved macromolecules and wall slip, it is to be expected that their concurrent action will elicit mutual interactions that are amenable to prediction only through numerical methods.[258] Nonetheless, disregarding these complexities for the time being, a simple two-layer model (see Fig. 5.7) for the near-wall boundary layer can be envisioned, wherein it is assumed that: (*i*) viscoelastic effects operating predominantly in the buffer layer and beyond[23,24] are largely oblivious to the influence of wall slip, which is confined mostly to the viscous sublayer;[16–19] and (*ii*) the average flux of streamwise momentum to the wall (i.e. the frictional shear stress) constitutes the principal mode of information exchange between the viscous sublayer and the outer flow. In this simple additive framework, the individual velocity defects from Eqs. 5.2 and 5.3 can be superimposed to derive a composite wall friction law of the form

$$V_C^{+\circ} = V_P^+ + \left(V_S^+ - V_N^+\right) = M_P \log \mathrm{Re}_\tau + N_P + b^+, \tag{5.5}$$

representing a linear addition of velocity increments suitably scaled in wall units; here the subscript 'C' denotes 'combined' drag reduction, and the superscript $^\circ$ indicates an ideal estimate derived from the additive, two-layer model described above. Rearranging Eq. 5.5 into the form

$$\left(V_C^{+\circ} - V_N^+\right) = \left(V_P^+ - V_N^+\right) + \left(V_S^+ - V_N^+\right), \tag{5.6}$$

we see that it simply represents an addition of the individual velocity increments (at a given Re_τ) from the respective polymeric and superhydrophobic friction curves, to construct the combined friction law in Prandtl-von Kármán coordinates. Obtaining the corresponding estimate for the percentage drag reduction $\mathscr{D}_C^\circ$ at a specified Re_s is, however, less straightforward on account of the non-linear relationship between the wall shear stress (or the shear Reynolds number) and the imposed wall speed (or the solvent-based Reynolds number) implied by Eq. 5.5. Denoting the (unknown) value of Re_τ by x, and substituting the relation $V^+ = V/u_\tau = \mathrm{Re}_s/\eta_r \mathrm{Re}_\tau$ (where $\eta_r = \eta_0/\eta_w$ is the relative viscosity of the polymer solution), Eq. 5.5 becomes

$$\mathrm{Re}_s = \eta_r\, x \left[M_P \ln x + N_P + b^+(x)\right], \tag{5.7}$$

which is an implicit non-linear equation to be solved for $x = \mathrm{Re}_\tau$. With the slip length b^+ approximated by a quadratic polynomial of the form $b^+(x) = A + Bx + Cx^2$ (see

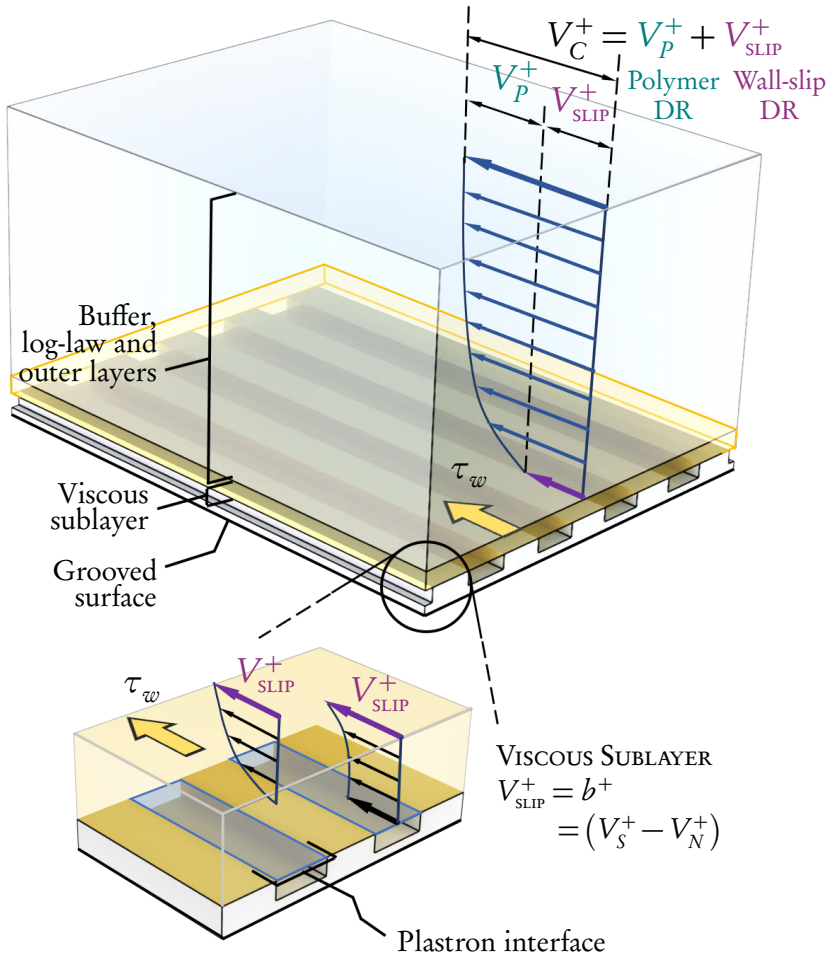

FIGURE 5.7. Schematic depiction of the additive two-layer model for combined drag reduction in wall-bounded turbulence. The inset shows a magnified view of the thin near-wall viscous sublayer within which the composite flow boundary conditions are assumed to homogenize, yielding a uniform effective slip velocity V_{SLIP}^+ perceived by the outer layers. Dimensions are merely intended to be illustrative, and are not to scale.

discussion following Eq. 5.3), Eq. 5.7 does not in general admit a closed-form solution in elementary functions. A suitable fixed-point iteration, such as the cubically convergent Halley's method[264] given by

$$x_{n+1} = x_n - \frac{2f(x_n)f'(x_n)}{2[f'(x_n)]^2 - f(x_n)f''(x_n)}\,, \tag{5.8}$$

is therefore employed to locate the root $\hat{x}$ of the function $f(x) = \mathrm{Re}_s - \eta_r x\,[M_P \ln x + N_P + b^+(x)]$, from which $V_C^{+\circ} = \mathrm{Re}_s/\eta_r\,\hat{x}$ can be computed. Similarly, the baseline friction law, Eq. 5.1, can be inverted to yield (cf. Eq. 3.22)

$$V_N^+ = M \cdot W\big(e^{N/M}\mathrm{Re}_s'\big), \tag{5.9}$$

where $\mathrm{Re}_s' = \mathrm{Re}_s/M$, and $W(x)$ denotes (the principal branch of) the product logarithm function (also known as the Lambert W function, see Eq. 3.23). The additive estimate for the percentage drag reduction can then be obtained simply as

$$\mathscr{D}_C^\circ(\mathrm{Re}_s) = \left[1 - \left(\frac{V_N^+}{V_C^{+\circ}}\right)^2\right] \cdot 100\,\%\,, \tag{5.10}$$

for a specified value of the wall speed V (or equivalently, for a specific value of the solvent-based Reynolds number $\mathrm{Re}_s = \rho V d/\eta_w$).

In Figs. 5.6(a) and 5.6(b), the solid curves represent the wall friction as predicted by Eq. 5.5, and the corresponding estimate for the percentage drag reduction $\mathscr{D}_C^\circ$ computed using Eq. 5.10, for the grooved superhydrophobic rotor in 50 ppm aqueous PAM solution. While there is good agreement with experimental data especially at moderate Reynolds numbers ($\mathrm{Re}_s \leqslant 30\,000$), the actual drag reduction levels (denoted by filled circles) are seen to be consistently smaller than the ideal value predicted by the two-layer model (represented by the solid line). This, in turn, suggests that 'higher order' interactions between the two drag reduction mechanisms serve to counteract rather than reinforce one another, and the additive law given by Eq. 5.5 consequently represents an upper bound for the combined drag reduction levels that are actually realizable in practice.

In Fig. 5.8(a), the percentage drag reduction $\mathscr{D}_C$ measured on the grooved rotor is shown as a function of the Reynolds number Re_s at different concentrations c of aqueous PAM. Drag reduction initially increases with rising polymer concentration, attains a maximum, and subsequently falls off at concentrations exceeding 50 ppm; this latter decline at large concentrations can be ascribed to the increasing shear viscosity $\eta_0(c)$ of the polymer solution, which enhances viscous dissipation in the flow and thereby detracts from the drag reduction arising from the polymeric suppression of turbulence.

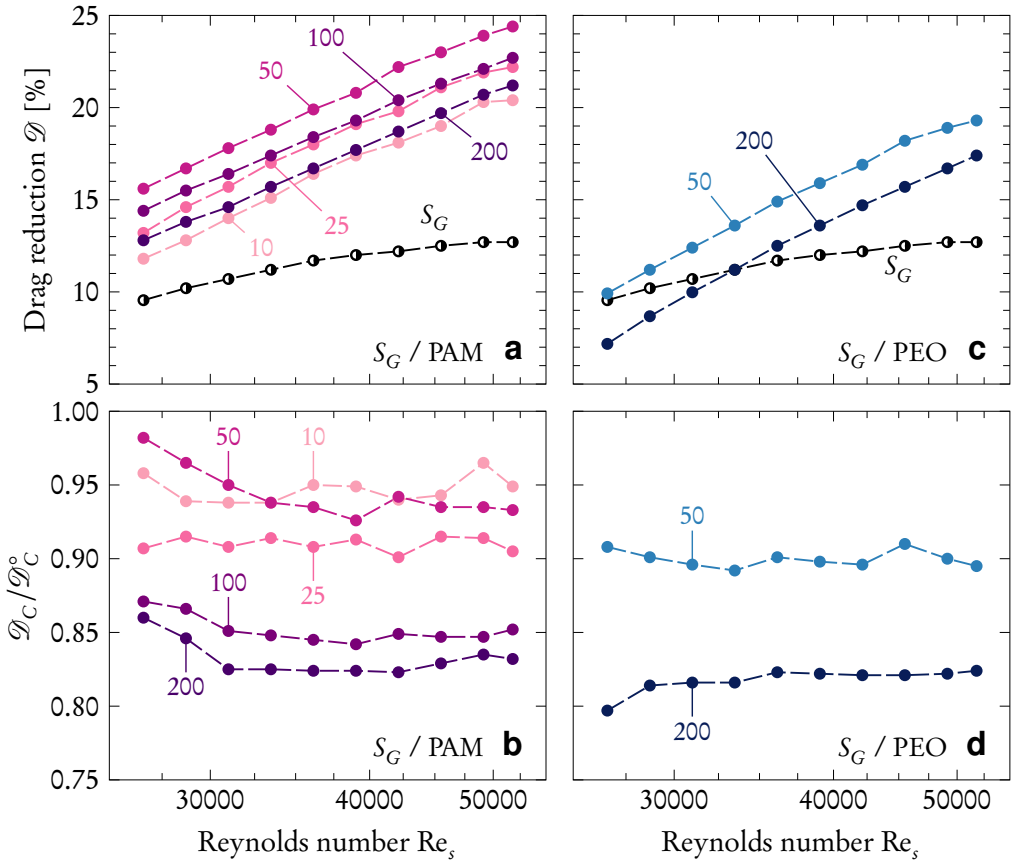

FIGURE 5.8. (a) Percentage drag reduction $\mathscr{D}_C$ for the grooved rotor in aqueous PAM solutions of various concentrations. The annotations denote the polymer concentration c in ppm. (b) The ratio $\mathscr{D}_C/\mathscr{D}_C^\circ$ of the actual drag reduction achieved to the ideal estimate predicted by the two-layer model, for the data shown in panel (a). (c) and (d) Drag reduction data for the grooved rotor in aqueous PEO solutions, analogous to those reported for PAM in panels (a) and (b).

Figure 5.8(b) shows the ratio of the actual drag reduction $\mathscr{D}_C$ to the ideal value $\mathscr{D}_C^\circ$ predicted by Eq. 5.10, and attests to the predictive utility of the simple empirical model derived above; the actual drag reduction $\mathscr{D}_C$ is within 90 % of the model prediction $\mathscr{D}_C^\circ$ for concentrations $c \leqslant 50$ ppm, and is within 80 % of the predicted value for concentrations up to 200 ppm. Thus the additive law, in general, yields a good first estimate of the friction reduction achievable in dilute polymer solutions, but increasingly overpredicts the combined effect as the polymer concentration c is increased. Finally, Figs. 5.8(c) and 5.8(d) show analogous curves for drag measurements on the grooved rotor in PEO solutions at two different concentrations; excepting the smaller overall drag reduction

in comparison to PAM solutions due to a more pronounced viscous effect (which is consistent with the larger value of $[\eta]_{\mathrm{PEO}}$), the results are otherwise seen to be qualitatively similar.

Polymer Solution + Randomly Textured Superhydrophobic Rotor

Although periodically patterned textures—exemplified by the streamwise groove array discussed in the preceding section—serve as useful canonical surfaces with tunable slip properties, their high fabrication cost and limited scalability render them impracticable in large-scale engineering applications. There is thus a practical imperative to explore combined drag reduction strategies that use scalable superhydrophobic textures with irregular surface roughness. As a proof of concept demonstration of the combined drag reduction technique using scalable textures, drag measurements were performed on the randomly textured rotor in 50 ppm aqueous solutions of PAM and PEO; the resulting friction curves are shown in Figs. 5.9(a) and 5.9(c) in Prandtl-von Kármán coordinates, and the percentage drag reduction in Figs. 5.9(b) and 5.9(d). In aqueous PAM solutions, experimental results mirror the case of superhydrophobic grooves discussed above, and the additive law yields an excellent prediction for the drag reduction levels actually observed. In stark contrast, the combined drag reduction measured in the aqueous PEO solution falls well short of the ideal drag reduction levels predicted by Eqs. 5.5 and 5.10. In fact, as seen in Fig. 5.9(d), the combined percentage drag reduction at Reynolds numbers $\mathrm{Re}_s \leqslant 40\,000$ is smaller than the purely superhydrophobic drag reduction obtained if no polymer is added to the working fluid. The marked difference in behavior between PAM and PEO solutions is intriguing, inasmuch as both polymers comprise flexible, linear, non-ionic chains with comparable macromolecular properties. In the next section, the 'anomalous' behavior of PEO is explained as a consequence of the preferential adsorption of its amphiphobic chains at the plastron interface.

C. *Surface-Active Polymers and Interfacial Effects*

A number of commonly employed drag-reducing polymers, both synthetic (e.g., PEO) and natural (e.g., xanthan gum), are known to exhibit surface activity in aqueous solutions.[265,266] At chemical equilibrium, solutions of such polymers exist with a fraction of their dissolved chains preferentially adsorbed at the air-water interface. For example, the $(-CH_2-CH_2-)$ alkyl moeity of the ethylene oxide repeat unit is sufficiently hydrophobic to render PEO chains surface-active, thereby depressing the surface tension of the solution when dissolved in water.[265] The presence of trace contaminants or surfactant impurities, often unavoidable in industrial practice, could suffice to impart significant surface activity in solutions of otherwise surface-inactive polymer samples. Even if the diminution

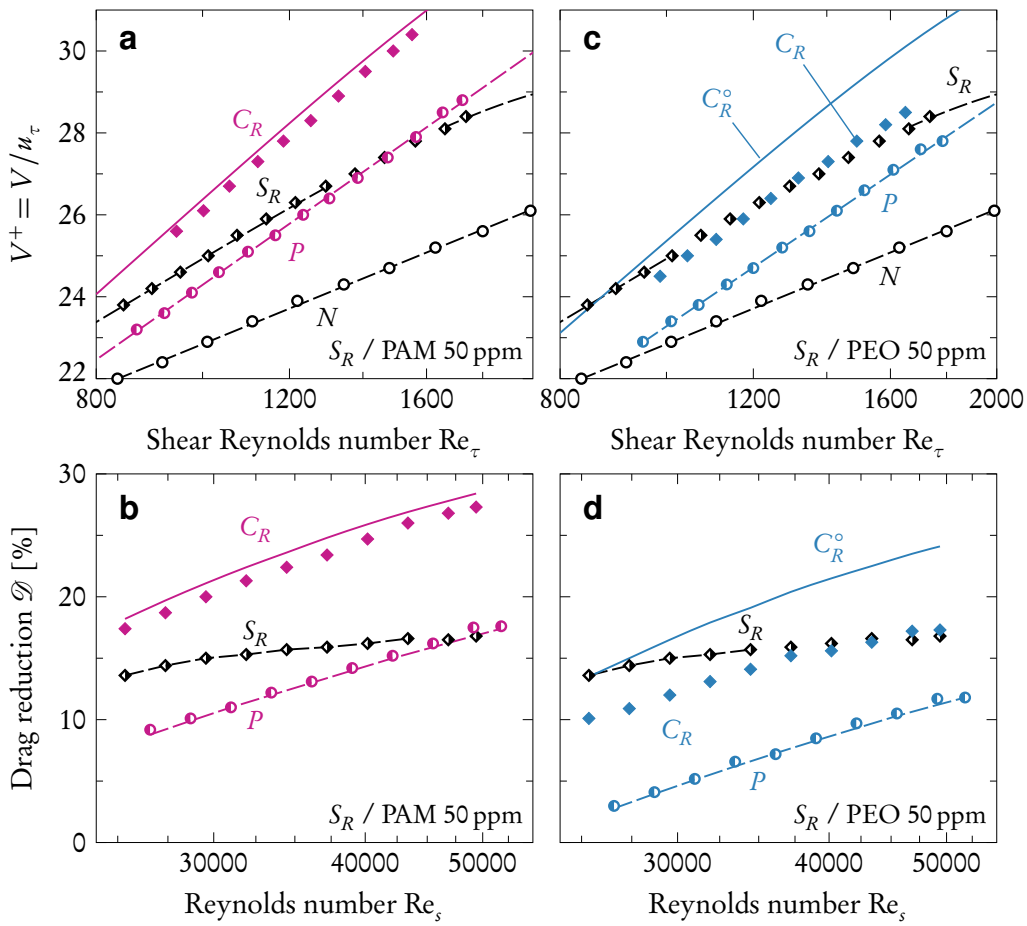

FIGURE 5.9. (a) Combined drag reduction data (labeled C_R) for the randomly textured rotor in a 50 ppm solution of aqueous PAM. The individual friction curves for the no-slip rotor in water (N) and in 50 ppm aqueous PAM (P), and for the randomly textured rotor in deionized water (S_R), are also included for comparison. (b) The percentage drag reduction $\mathscr{D}$ corresponding to the data shown in panel (a). The solid curves in panels (a) and (b) respectively denote the ideal additive estimates $V_C^{+\circ}$ and $\mathscr{D}_C^\circ$ predicted by Eqs. 5.5 and 5.10. (c) and (d) Drag reduction curves for the randomly textured rotor in 50 ppm aqueous PEO, analogous to the data for PAM shown in panels (a) and (b). In the case of PEO, the actual drag reduction observed in experiments (data markers labeled C_R) falls well short of the ideal estimate denoted by the solid curves (separately labeled C_R° for clarity).

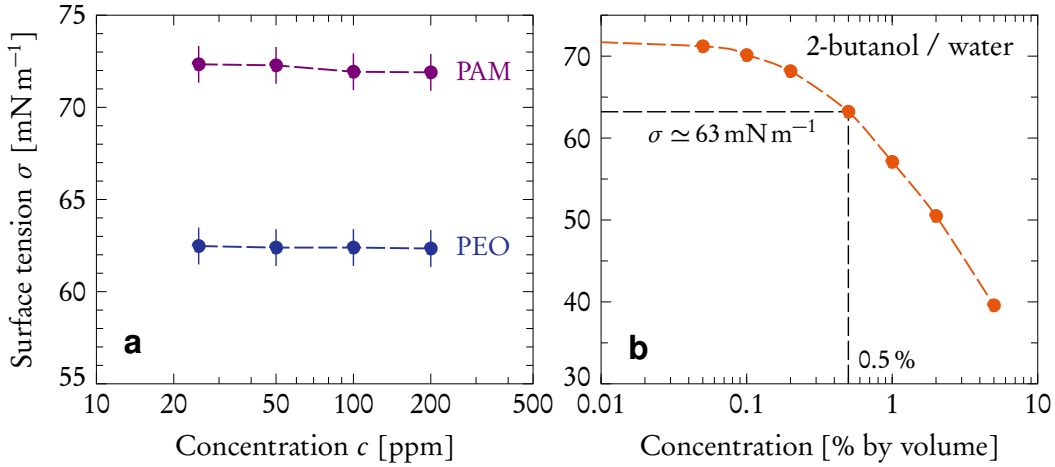

FIGURE 5.10. (a) Surface tension σ of aqueous PAM and PEO solutions as a function of the polymer concentration c. The surface tension of water is unaltered by the addition of PAM, and that of the PEO solution is largely independent of c within the range of concentrations employed in flow tests. (b) Surface tension of a binary solution of 2-butanol in water, as a function of the percentage volume of 2-butanol.

in surface tension is insufficient to precipitate an outright collapse of the plastron layer (followed by transition to the fully-wetted, drag-increasing Wenzel state[25]), the presence of adsorbed surfactant molecules can nevertheless have a significant impact on the slip properties of the air-water interface atop the superhydrophobic texture. For instance, Peaudecerf et al. (2017)[267] showed that even at trace concentrations of dissolved surfactants, the external flow generates surfactant gradients along the plastron layer which, in turn, induces adverse Marangoni stresses that diminish, or even completely eliminate, slip at the wall. The plastron interface then essentially behaves like a rigid, no-slip boundary, and the drag reducing ability of the texture is lost.

To ascertain the possibility of surface-active polymer chains interfering with the slip characteristics of superhydrophobic textures, the surface tension of aqueous PAM and PEO solutions was measured at room temperature ($T = 23\,°\mathrm{C}$) using the Wilhelmy plate method, at concentrations identical to those used in flow experiments. The data are shown in Fig. 5.10(a); barring experimental uncertainties, the surface tension of water remained unaltered (at $\sigma \simeq 72\,\mathrm{mN\,m^{-1}}$) with the addition of PAM, but was reduced to approximately $\sigma \simeq 62\,\mathrm{mN\,m^{-1}}$ in the presence of dissolved PEO. These values are in excellent concordance with the data reported in prior literature,[265,268] and confirm the non-negligible adsorption of PEO chains at the air-water interface, as well as the absence of such interfacial effects in aqueous PAM solutions.

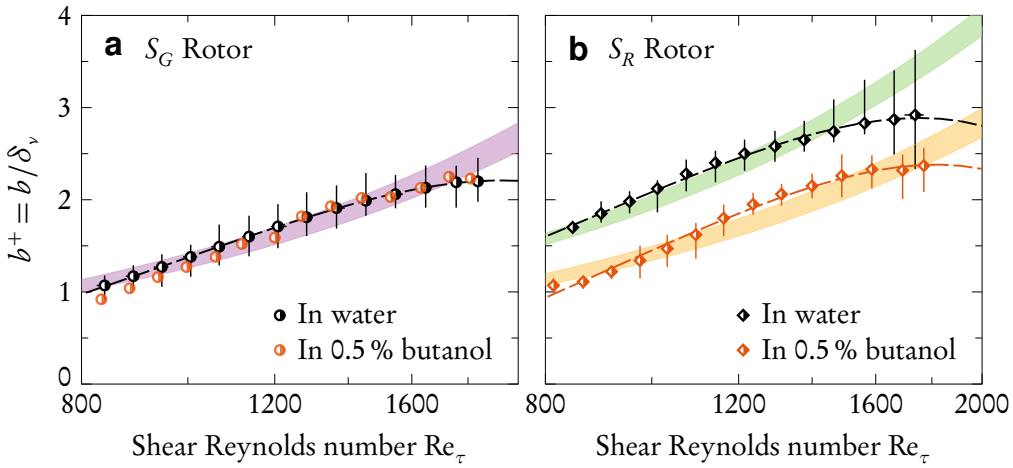

FIGURE 5.11. Experimentally determined slip lengths b^+ on (a) the grooved rotor, and (b) the randomly textured rotor, in a 0.5 % solution of 2-butanol in water. The original slip length curves for the two rotors, as measured in pure water, are also reproduced from Fig. 5.5(b) for comparison. In panel (a), the purple band denotes the expected (linear) variation of b^+ for a constant slip length of $b = (27 \pm 1)\,\mu\mathrm{m}$, identical to that shown in Fig. 5.5(b). In panel (b), the green and yellow bands similarly correspond to $b = (25 \pm 1)\,\mu\mathrm{m}$ [the original slip length as seen in Fig. 5.5(b)], and $b = (18 \pm 1)\,\mu\mathrm{m}$, the diminished slip length in the butanol solution.

In an attempt to simulate the effect of dissolved PEO on wall slip in isolation from its drag reducing properties, frictional drag measurements were performed on the two superhydrophobic rotors in a 0.5 % solution of 2-butanol in water; butanol was chosen on account of its excellent miscibility with water, and its relatively low volatility at room temperature. As seen in Fig. 5.10(b), adding 0.5 % by volume of butanol lowers the surface tension of water to approximately $\sigma \simeq 63\,\mathrm{mN\,m^{-1}}$, which is quite close to that of the dilute PEO solutions used in drag reduction experiments. Figures 5.11(a) and 5.11(b) show the slip length b^+ for the two surfaces as measured in the butanol/water system; the original slip length curve for each surface in deionized water, shown in Fig. 5.5(b), is also reproduced for comparison. As evident from the plot, the effective slip on the grooved rotor is largely unaffected by the presence of adsorbed[269] butanol at the interface, which is consistent with the observations of Peaudecerf et al. (2017);[267] the lack of transverse flow barriers obstructing the groove pattern precludes the development of surfactant gradients and attendant Marangoni stresses, since these require the presence of stagnation lines against which surfactant molecules can accumulate. In contrast, the average slip length on the randomly texture is appreciably diminished (from $b \simeq 25\,\mu\mathrm{m}$ to $b \simeq 18\,\mu\mathrm{m}$) in the butanol solution. This may either be a consequence of adverse Marangoni stresses,

arising from surfactant gradients that form adjacent to flow-obstructing texture asperities, or may also be due to the lowering and further impalement of the air-water interface into the random texture, caused by the reduction in the surface tension of the liquid phase.[270]

Figures 5.12(a) and 5.12(b) show the friction data for the superhydrophobic random texture in 50 ppm aqueous PEO [reproduced from Figs. 5.9(c) and 5.9(d)], alongside the revised model estimates [orange solid curves labeled $(C_R^\circ)'$] re-computed based on the diminished slip length measured in the butanol/water solution [the orange data markers in Fig. 5.11(b)]. While there is now improved agreement between the predicted values and experimental data, it is also evident that this simple correction to the degree of wall slip is still inadequate to completely account for the drag reduction deficit observed on the random texture in the presence of dissolved PEO molecules. Numerical simulations of wall-bounded turbulence that take into account both surfactant kinetics as well as the dynamics of the partially rigidified plastron interface atop the random texture may be required to fully elucidate the complex interactions of near-wall turbulence, interfacial gradients, and wall slip operating in combined drag reduction systems employing surface-active polymers such as PEO.

IV. Closing Remarks

The experimental results presented above demonstrate that significant enhancements in the overall drag reduction at large Reynolds numbers can be achieved using scalable superhydrophobic textures applied to solid boundaries, in conjunction with dissolved polymers added at suitable concentrations to the turbulent liquid phase. For example, at $\mathrm{Re}_s = 50\,000$, dissolved PAM at a concentration of 50 ppm yields a polymer-mediated drag reduction of approximately 18 % [cf. Fig. 5.9(b)], whereas the randomly textured superhydrophobic wall by itself generates a comparable slip-induced drag reduction of about 17 %. By combining the two techniques, an overall drag reduction of 27 % can be achieved, which is well in excess of the stand-alone drag reduction levels attainable from either method employed independently. Furthermore, a concurrent deployment of polymer additives and superhydrophobic walls can be utilized as a 'fail-safe' drag reduction strategy, capable of resilient operation over a wide range of Reynolds numbers and flow conditions: at low Reynolds numbers, the superhydrophobic wall would provide continued friction reduction even in the laminar and transitional flow regimes where polymeric drag reduction is inoperative or ineffective; and at high Reynolds numbers, the dissolved polymer chains would sustain a residual level of turbulent drag reduction even if the trapped air layer over the superhydrophobic wall is lost due to fluctuation-induced plastron collapse.[257]

It was further shown in this chapter that the physical adsorption of PEO chains at

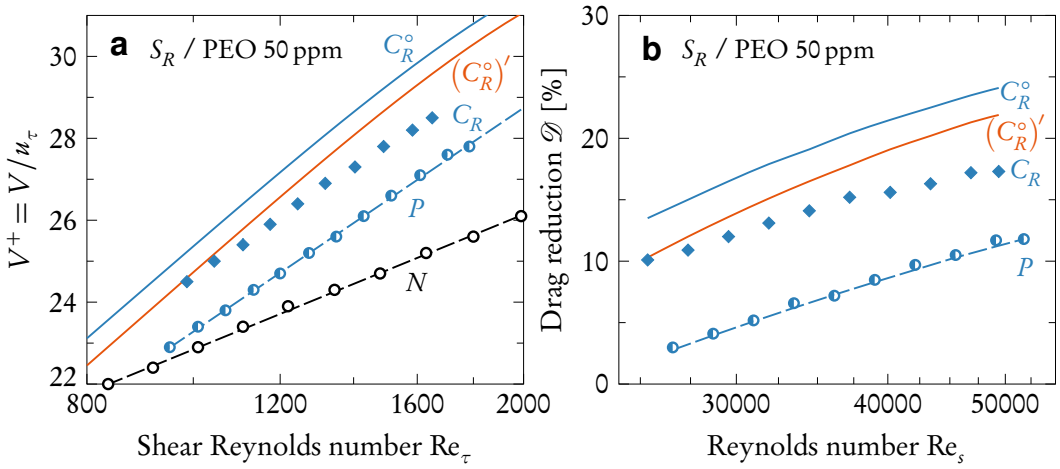

FIGURE 5.12. Combined drag reduction estimates for the randomly textured superhydrophobic rotor in 50 ppm aqueous PEO, re-computed based on the diminished slip length measured in the 0.5 % butanol solution [shown in Fig. 5.11(b)]. The revised predictions are denoted by the orange solid curves labeled $(C_R^\circ)'$; all other curves are identical to those in panels (c) and (d) of Fig. 5.9.

the air-water interface adversely influences the slip properties of the superhydrophobic random texture, severely impacting the overall drag reduction efficacy of the combined polymer-surface system. This strong surfactant effect may partly serve to rationalize the surprising lack of prior reports on combined drag reduction in the literature, given the widespread use of PEO as a model polymer additive in experimental drag reduction investigations. The decisive role of interfacial effects, in turn, suggests that a careful evaluation of the surfactant activity of candidate drag-reducing polymers is a vital prerequisite for ensuring the successful design and implementation of combined drag reduction strategies in potential large-scale applications.

Notes

The results presented in this chapter appear in the following manuscripts by the author, either submitted or undergoing peer review as of August 7, 2020.

A. RAJAPPAN and G. H. MCKINLEY. Polymers and plastrons in parallel yield enhanced turbulent drag reduction. Submitted (2020).

A. RAJAPPAN and G. H. MCKINLEY. Cooperative drag reduction in turbulent flows using polymer additives and superhydrophobic walls. *Phys. Rev. Fluids*, under revision (2020).

The space below is intentionally left blank.

6 *Conclusion*

I. A Brief Summary of Results

This thesis looks at two well-known methods of frictional drag reduction in wall-bounded turbulent flows—polymer additives, and plastron-stabilizing walls—and strives to address some of the current practical challenges impeding their widespread adoption in real-life aqueous flow systems. To identify these challenges and gain a contextual appreciation of their relevance, the extant literature on both drag reduction methods was surveyed briefly in Chapter 2. As a long-standing technique, and arguably the most well-developed of all drag reduction strategies attempted to date, the addition of polymers has been extensively investigated and tested in a variety of flow configurations, as documented in a vast corpus of research literature. Although the emergence of superhydrophobic surfaces is by comparison a more recent development, rapid strides towards the fabrication of scalable and durable textures have been reported in the past ten years, helping to propel aerophilic texturing of the wall from a theoretical possibility into a potentially viable strategy for large-scale drag reduction in the near future. After an appraisal of existing challenges and unexplored topics gleaned from this review of current literature, two questions of practical significance were identified for targeted study in the reminder of the thesis: the search for eco-friendly and cost-effective alternatives to synthetic drag-reducing agents, and the possibility of combining polymer additives with superhydrophobic walls to achieve enhanced reductions in frictional drag. The principal conclusions of the study are briefly summarized in this section.

Biopolymer Alternatives to Synthetic Drag-Reducing Agents

In Chapter 4, the epidermal polysaccharide content, or mucilage, present in the bran of common seeds such as flax, chia and psyllium, was proposed as a biodegradable and low-cost alternative to synthetic drag reducing agents in aqueous flows. Although plant biopolymers have been previously explored in the context of drag reduction, past research in this area has traditionally focused on vegetable gums such as guar; seed mucilage has remained largely neglected as a source of drag-reducing chains.

As a prototypical model for seed-based polysaccharides, mucilage from the commonly available brown flaxseed, *Linum usitatissimum*, was extracted and analyzed in §4.II. The mucilage was eluted from unbroken seeds by simple hot water extraction, and its constituent macromolecules were studied using size exclusion chromatography. The resulting molar mass distribution was bimodal, with peaks centered at $M_1 = 1.71\,\mathrm{MDa}$ and $M_2 = 2.45\,\mathrm{MDa}$ 1; this was consistent with the known presence of high molar mass neutral arabinoxylans in the mucilage, alongside negatively charged rhamnogalacturonan chains of slightly lower molar mass. The aggregate distribution yielded number- and weight-averaged molar masses of $M_n = 2.22\,\mathrm{MDa}$ and $M_w = 2.32\,\mathrm{MDa}$ respectively, with an overall polydispersity index of $\mathrm{PDI} = 1.05$ suggesting a relatively narrow distribution of chain lengths. A Flory exponent of $\nu = 0.69$ was inferred from the SEC data 2, indicating the presence of charged, semiflexible chains. This was further confirmed during measurements of the intrinsic viscosity $[\eta]$, which was found to be highly sensitive to the ionic strength of the solution 3. Desalted mucilage, on dilution, displayed a distinct Fuoss regime typical of polyelectrolyte chains 4, which disappeared in the presence of added salts. The intrinsic viscosity of the as-extracted mucilage solution, obtained by an isoionic dilution procedure, was $[\eta]_{\mathrm{FM}} = 10.03\,\mathrm{dL\,g^{-1}}$, which was quite close to that of 2 MDa PEO in water 5; the latter was therefore adopted as the benchmark against which the drag reduction efficacy of dilute mucilage was assessed during turbulent flow measurements.

1 Fig.4.3, p.112
2 Fig.4.4, p.113
3 Fig.4.7, p.118
4 Fig.4.5, p.115
5 Fig.4.6, p.116

Capillary breakup experiments performed on dilute mucilage solutions with added sucrose yielded chain relaxation times which were up to two orders of magnitude smaller than that obtained for aqueous PEO chains of similar molar mass; furthermore, the relaxation time displayed a much stronger power-law dependence on concentration in the case of mucilage than for PEO 6. Both effects were attributed to the strong charge screening and diminution in solvent quality caused by the dissolved sucrose, which affects the charged polysaccharide chains in mucilage much more strongly than the charge-neutral

6 Fig.4.9, p.121

PEO molecules.

In §4.III, frictional drag measurements were presented for aqueous PEO and flax mucilage solutions of various concentrations 7; the mucilage, in general, displayed drag reduction efficacy comparable to that of PEO in the turbulent regime. Specifically, a 1:400 extract of flax mucilage ($c = 460$ ppm) yielded near identical levels of drag reduction as a 285 ppm solution of 2 MDa PEO, over the full range of Reynolds numbers $2 \times 10^4 \leqslant \mathrm{Re}_s \leqslant 7 \times 10^4$ accessible during experiments; a maximum percentage drag reduction of $\mathscr{D} = 14\,\%$ was recorded for both solutions at $\mathrm{Re}_s = 65\,000$ 8. A simple cost analysis showed that the PEO solution would incur a raw material cost of \$14/m^3 at current estimated market prices for the industrial grade polymer, whereas the mucilage extract would only require flax seeds costing less than \$1/m^3. This represents a 14-fold reduction in cost without loss in drag reduction efficacy, a number than can be further improved if spent flax meal is utilized as the source of mucilage in place of fresh unprocessed seeds.

7 Fig.4.10, p.124

8 Fig.4.13, p.128

The susceptibility of mucilage polysaccharides to mechanical degradation was evaluated under sustained turbulent shear flow inside the TC apparatus, at constant Reynolds number $\mathrm{Re}_s \approx 6 \times 10^4$. The diminution in percentage drag reduction with time was well described by the Brostow equation 9, which was used to infer the asymptotic drag reduction $\mathscr{D}(\infty)$ at long times, as well as a characteristic time rate of degradation b for the polymer chains. For solutions yielding comparable levels of initial drag reduction, both PEO and flax mucilage solutions displayed identical rates of degradation of approximately $b \approx 10^{-3}\,\mathrm{s}^{-1}$, which in turn corresponds to a time scale of $1/b \approx 1000$ s for flow-induced chain scission.

9 Fig.4.14, p.130

To assess the effect of salinity on drag reduction by mucilage in marine environments, flow measurements were performed in the TC apparatus on seed extracts prepared in synthetic seawater. Whereas both PEO and flax mucilage displayed a loss of drag reduction efficacy in the presence of dissolved salts, mucilage was more severely impacted on account of its acidic polysaccharide constituents; for instance, the percentage drag reduction at $\mathrm{Re}_s = 65\,000$ for a 1:400 extract of flax mucilage ($c = 460$ ppm) declined from $\mathscr{D} = 13\,\%$ in deionized water to about $\mathscr{D} = 8\,\%$ in synthetic seawater 10. The drag reduction deficit relative to PEO could be compensated by increasing the weight ratio of seeds to water from 1:400 to 1:200 during extraction; importantly, the mucilage solution remained competitive in terms of raw material cost even after this two-fold increase in the required quantity of seeds.

10 Fig.4.15, p.131

As an extension to the study of flax mucilage, proof of concept experiments

were performed using the water-soluble mucilage extracted from chia seeds, *Salvia hispanica*, and from the hull of psyllium seeds, *Plantago ovata*; both seed extracts yielded net reductions in drag under turbulent flow conditions in the TC apparatus 11. The idea of utilizing plant biopolymers as substitutes for synthetic drag-reducing agents was also explored in the context of oil-based flows, and preliminary results are reported in Appendix A. Tree resins (such as mastic and dammar) and plant latices (such as natural rubber and gutta), known to contain oil-soluble polymeric fractions, were identified as candidate sources of drag-reducing chains for turbulent hydrocarbon flows. To achieve turbulent shear flow conditions in viscous alkane oils, a redesigned version of the TC apparatus was built to enable flow measurements to be performed at elevated temperatures. 12 Initial experiments with rubber latex were positive, with a $50\,\mathrm{g\,mL^{-1}}$ solution in dodecane yielding a percentage drag reduction of $\mathscr{D} = 6\,\%$ at a Reynolds number of $\mathrm{Re}_s = 5.5 \times 10^4$ 13.

11 Fig.4.16, p.132
12 Fig.A.3, p.175
13 Fig.A.10, p.184

Combined Use of Polymers and Plastrons

In Chapter 5, the possibility of combining polymer additives with superhydrophobic walls was investigated as a potential strategy for augmenting the net reduction in frictional drag attainable in turbulent aqueous flows. To this end, two aerophilic surfaces with robust slip length characteristics were fabricated: a periodic texture comprising streamwise rectangular microgrooves (S_G), and a hierarchical random texture (S_R) produced by sandblasting, acid etching, and boehmitizing the aluminum substrate 14. Frictional drag measurements were performed on both surfaces in deionized water, and the repeatability of their individual friction curves was verified over multiple experiments. The grooved rotor (S_G) yielded turbulent drag reduction consistent with an effective slip length of $b = 17\,\mu\mathrm{m}$, and the randomly textured rotor (S_R) similarly gave a slip length of $b = 25\,\mu\mathrm{m}$ 15.

14 Fig.5.1, p.137
15 Fig.5.5, p.145

For the polymer component, aqueous PAM ($M_v = 2.54\,\mathrm{MDa}$) and PEO ($M_v = 1.72\,\mathrm{MDa}$) solutions of various dilute concentrations were employed; the individual drag reduction efficacy of each solution was characterized by means of turbulent drag measurements in the TC apparatus using a smooth, no-slip rotor 16. Combined drag reduction measurements were then performed by pairing each of the two superhydrophobic rotors first with PAM solutions, and later with PEO. In the case of PAM, drag reduction was indeed found to be additive; the overall drag reduction achieved was greater than that obtained from either polymers or superhydrophobic rotors individually, over the full range of Reynolds numbers investigated. For instance, at $\mathrm{Re}_s = 50\,000$, aqueous

16 Fig.5.3, p.143

PAM at a concentration of 50 ppm yielded a polymeric drag reduction of 18 %, whereas the randomly textured superhydrophobic wall by itself produced a slip-induced drag reduction of 17 % 17. On combining the two, an overall drag reduction of 27 % was obtained, well in excess of the stand-alone drag reduction levels achieved from either method operating in isolation. When aqueous PAM was employed as the drag-reducing polymer, no qualitative difference in the combined drag reduction effect was noted between the regular groove pattern and the random superhydrophobic texture.

17 Fig.5.9, p.153

To predict the combined drag reduction levels to be expected from a given polymer-surface pair whose individual drag reduction properties are known beforehand, an empirical friction law was derived based on a simple two-layer model of the boundary layer 18, wherein the individual velocity increments arising from polymeric drag reduction and wall-slip add linearly after suitable scaling by wall units. Excellent agreement with experimental data was observed, especially at moderate Reynolds numbers ($\mathrm{Re}_s \leqslant 30\,000$) and for dilute solutions; the experimentally observed drag reduction levels were within 90 % of the model prediction for polymer concentrations $c \leqslant 50$ ppm, and within 80 % for $c \leqslant 200$ ppm 19. Even so, the actual drag reduction was consistently smaller than the ideal value predicted by the two-layer model, suggesting that nonlinear interactions between the two drag reduction mechanisms serve to counteract rather than reinforce one another; the additive law thus provides an upper bound for the combined drag reduction levels that are actually realizable in practice.

18 Fig.5.7, p.149

19 Fig.5.8, p.151

In flow measurements employing aqueous PEO, a marked difference was observed in drag reduction behavior between the grooved and the randomly textured surfaces: Whereas the grooved rotor yielded drag reduction levels consistent with the additive model, the randomly textured rotor showed a sharp deterioration in efficacy; for $\mathrm{Re}_s \leqslant 40\,000$, in fact, the combined drag reduction fell below even the purely slip-induced drag reduction levels obtained in the absence of any added polymer 20. The loss of additivity in PEO was attributed to the surface activity of its amphiphobic molecules, as confirmed by surface tension measurements. While the addition of PAM had no effect on the surface tension of water, the addition of PEO produced a depression in surface tension of approximately $\Delta\sigma = 10\,\mathrm{mN\,m^{-1}}$ in the range of concentrations employed in drag reduction measurements 21. To simulate the adverse influence of PEO chains on wall slip, frictional drag measurements were repeated on the two rotors in a 0.5 % solution of butanol, which had a surface tension equal to that of dilute PEO solutions. Whereas slip on the grooved rotor was unaffected

20 Fig.5.9, p.153

21 Fig.5.10, p.154

(consistent with its lack of transverse flow barriers), the effective slip length on the random texture was reduced from $b = 25\,\mu\text{m}$ in water to $b = 18\,\mu\text{m}$ in the butanol solution [22], suggesting the development of adverse Marangoni stresses that 'rigidify' the plastron interface. The diminution in slip length was found to partially account for the discrepancy between the actual and anticipated drag reduction levels for the random texture in PEO solutions [23]. This strong interfacial effect, in turn, was suggested as a probable rationalization for the surprising lack of prior reports on combined drag reduction in the literature, given the widespread use of PEO as a model polymer additive in experimental drag reduction investigations.

22 Fig.5.11, p.155

23 Fig.5.12, p.157

Precís

The mucilage extracted from seeds such as flax, chia, and psyllium was shown to be a viable substitute for synthetic polymer additives in large-scale flow systems, offering comparable drag reduction efficacy and flow longevity at a substantially lower raw material cost. Oil-soluble plant biopolymers, such as natural rubber, may analogously be employed as useful drag-reducing agents in hydrocarbon flows. It was further shown that the joint deployment of polymer additives with superhydrophobic walls can serve as an effective technique for enhancing the overall drag reduction attainable in wall-bounded turbulence. A careful evaluation of the surface activity of candidate drag-reducing polymers is vital to ensuring the successful design and implementation of combined drag reduction strategies in large-scale applications.

II. Potential Avenues for Future Research

Exploring Alternate Sources of Mucilage

In Chapter 4, the epidermal polysaccharides in flax mucilage were studied extensively as a prototypical model for high molar mass drag-reducing chains derivable from plant seeds. Later, drag reduction was also demonstrated using chia and psyllium extracts, but these mucilage sources were not explored in any detail beyond this initial proof of concept on account of time and resource constraints. The specific choice of the above three plant species for preliminary investigations was motivated chiefly by their popular use as fiber foods and dietary supplements. However, mucilage production in seeds and fruits (a process termed *myxodiaspory*) is a ubiquitous phenomenon among angiosperms, and a number of flowering plant species, both wild and domesticated, produce seeds with mucilaginous envelopes.[271] Clearly, there exists tremendous scope for exploration and optimization in identifying the best candidates for the extraction of drag-reducing polysaccharides; a systematic quantification of the drag reduction efficacy, longevity, and cost of viable mucilage polymers will help make an informed comparison to determine the most suitable and cost-effective candidates for deployment in real-life applications. Even within a given species, the best plant lines or cultivars for mucilage extraction can be identified, since the mucilage content of seeds can vary considerably between different varieties and artificial breeding lines.[272,273] A comprehensive set of empirical data on the drag reduction potential of common biopolymers, their rates of shear degradation, and the effects of dissolved salts and surfactants, will significantly aid in the downselection of drag reducing additives and their concentrations for various engineering applications in general, and for marine drag reduction in particular.

Furthermore, recent advances in synthetic and systems biology techniques have enabled us to identify and alter plant and bacterial genomes involved in the biosynthesis of mucilage and extracellular polysaccharides;[274–277] these novel methods may in the future enable the selection and engineering of high-yield bacterial strains or plant cultivars that can support large-scale commercial extraction of biopolymers of even greater molar masses that are especially well-suited for turbulent drag reduction. With further advances in this direction, commercially harvested mucilage-based drag reducing agents may hold the key to transforming polymer drag reduction techniques into a practical and cost-effective strategy for energy-efficient propulsion in real-life maritime applications.

Intermolecular Associations and Cross-Linking

The idea of imparting a small degree of temporary associations or cross-links between polymer chains to enhance the "effective" molar mass, and thereby its drag reduction

efficacy, is a well-explored technique in the literature. A classic example is the use of alkaline tetraborate to induce reversible cross-linking between chains of guaran, the principal polysaccharide in guar gum; a mild degree of cross-linking (i.e. below the percolation threshold) has been shown to yield appreciable enhancements in the drag reduction efficacy.[278] The same technique is also used to tune the viscosity of guar-based hydraulic fracturing fluids, whereby the pH of the guar gel is reduced to break the borate cross-links and enable facile "flowback" of the spent fluid. Similarly, monomeric units that spontaneously (and reversibly) self-assemble into supramolecular polymeric aggregates have also been successfully demonstrated to reduce drag in non-polar solvents.[279]

Along the same lines, the identification of suitable co-additives that can initiate inter-chain associations between mucilage polysaccharides could considerably enhance their efficacy and utility as drag reducing agents in aqueous turbulent flows. Indeed, the synthesis of biocomposite materials from flax fibers and mucilage have been reported in the literature using cross-linking agents such as glutaraldehyde and epichlorohydrin;[280,281] however, both chemicals are quite toxic, the latter severely so. Clearly, less harmful alternatives to these reagents would be preferable; in this regard, plant-sourced enzymes such as genipin (obtained from *Gardenia* and *Genipa* fruits) or laccase (produced by many plants and fungi) have known cross-linking activity, and are therefore attractive candidates that merit further investigation in the context of drag reduction.

On a related note, the presence of an ionic surfactant such as sodium dodecyl sulfate (SDS) has been shown to enhance the drag reduction efficacy of dissolved PEO chains, and improve their resistance to mechanical degradation under turbulent flow conditions.[282] The effect is attributed to the expansion of PEO chains, resulting from ionic repulsion between surfactant micelles that form along the polymer backbone.[282] It would be interesting to explore if a similar effect can be elicited in mucilage polysaccharides by a suitable choice of surfactant, either natural or synthetic. Preliminary experiments show that SDS, unfortunately, has no analogous fortifying effect on the drag reduction performance of flax mucilage.

Mechanistic Modeling of Combined Drag Reduction

In Chapter 5, a simple two-layer framework was proposed as a preliminary attempt to model the interaction of dissolved polymers and wall-slip in combined drag reduction experiments. To 'leading order,' the two effects were assumed to operate independently of each other, interacting only via their shared (wall-normal) flux of fluid momentum, resulting in an additive superposition of defect velocities when suitably expressed in wall units. However, as discussed in Chapter 2, it is known that both dissolved polymers and wall-slip induce complex changes in the dynamics of near-wall turbulence,[24,167] and it is to be expected that the two mechanisms will inevitably interact with one another;

indeed, this is to some extent evinced by the systematic overprediction of the actual drag reduction by the additive friction law. The presence of surface active solutes adds a further layer of complexity, since surfactant gradients on the plastron interface could be influenced in non-trivial ways by turbulent mixing in the overlying liquid. Numerical simulations of wall-bounded turbulence, that take into account both surfactant kinetics and the dynamics of the partially rigidified plastron, are thus necessary to fully elucidate the complex interactions of near-wall turbulence, interfacial gradients, and wall slip operating in combined drag reduction systems employing surface-active polymers such as PEO. Such computational studies will hopefully provide further insight into the combined drag reduction mechanism, and lead to a physically motivated *ansatz* for the friction law that is valid for large drag reduction levels in the HDR and MDR regimes. In addition to practical advantages as a predictive engineering tool, such a model may also provide new mechanistic insights, and contribute to ongoing scientific efforts towards understanding the physics of polymeric and slip-mediated drag reduction in wall-bounded turbulence.

The space below is intentionally left blank.

A *Plant-Based Drag Reducers for Hydrocarbon Flows*

This appendix provides a synopsis of exploratory investigations into the utility of oil-soluble natural polymers for drag reduction in turbulent hydrocarbon flows. The design, construction, and baseline flow characterization of an upgraded Taylor-Couette device, capable of performing frictional drag measurements in turbulent hydrocarbon flows at elevated temperatures, are discussed. Preliminary experimental results are presented that explore the use of polyisoprene in natural rubber latex as a drag-reducing polymer for oil-based applications.

I. Introduction

A. *Background and Motivation*

A key objective of this thesis has been to study the use of plant-sourced biopolymers as low-cost, eco-friendly, and biodegradable substitutes for synthetic drag reducing agents in wide-ranging turbulent flow systems. Indeed, a diverse array of natural polysaccharides have been explored over the years as potential drag reducers in aqueous turbulent flows: these include water-soluble derivatives of cellulose, various food gums, amylopectin, alginate, carrageenan, chitosan, aloe vera gel, and the pectin-containing sap of plants such as okra.[68,105,109] In the petroleum industry, biopolymer gums such as guar and xanthan have long been employed on a commercial scale in various water-based well operations—for example, as viscosifying additives in drilling muds, or as proppant suspending agents for conferring yield stress in hydraulic fracturing fluids.[47,111] In Chapter 3, the mucilage extracted from common seeds was studied in detail and shown to be a potential, low-cost drag reducer for large-scale aqueous systems, particularly in marine applications.

Even so, the extant literature on drag-reducing biopolymers has focused almost exclusively on water-soluble polysaccharides derived from various plant, animal and bacterial sources;[105,114] these are, of course, insoluble in hydrocarbons and most organic solvents,

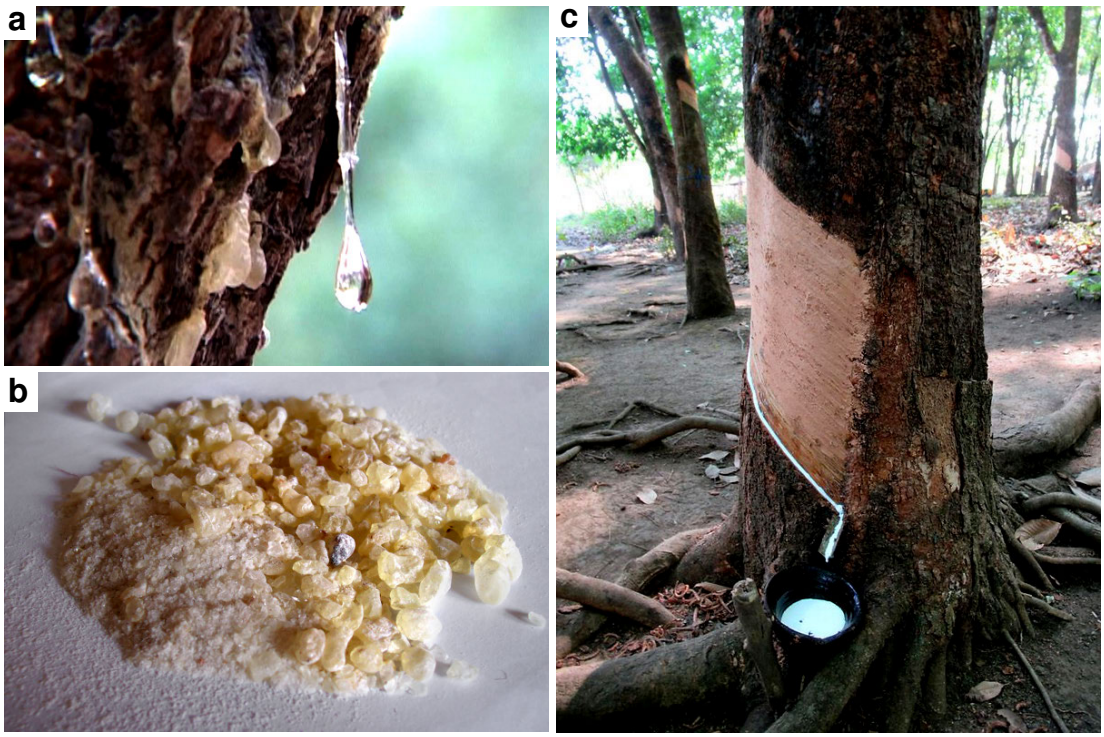

FIGURE A.1. Examples of oil-soluble plant biopolymers. (a) A pendant drop of mastic resin hangs from the branch of the mastic tree, *Pistacia lentiscus*. (b) Pale yellow beads of dammar resin, produced by trees belonging the family *Dipterocarpacea*. (c) Liquid latex drips from a freshly made incision on the bark of the Pará rubber tree *Hevea brasiliensis*. The milky white emulsion drains into and coagulates inside the collection cup, whence it is periodically recovered. For image sources and attribution, see p. 185.

and their utility is consequently limited solely to aqueous systems. However, the mitigation of frictional drag in the pipeline transport of crude oil and petroleum products is a vital area of application with vast potential for cost and energy savings; indeed, synthetic drag reducing agents (DRAs) have been routinely deployed in oil pipelines for the past several decades, including in long-distance networks such as the Trans-Alaska Pipeline System.[38] Given the widespread adoption of DRAs in the petroleum industry, a natural question arises if oil-soluble biopolymers, analogously to their water-soluble counterparts, can serve as useful drag reducing additives in turbulent flows of crude oil or refined products. Certain natural resins and plant exudates, such as rubber latex, are already known to contain polymeric fractions of moderate to large molar mass;[39] these may be explored as candidate sources of oil-soluble and environment-friendly drag-reducing chains which

could supplement (or potentially replace) the expensive and highly engineered synthetic agents used today, for turbulent flows of hydrocarbons or in well operations that involve biphasic water/oil emulsions.

B. *Oil-Soluble Plant Biopolymers*

Tree Resins

Resins are solid or semi-solid exudates secreted by plants (commonly trees) in response to mechanical injury; most resins produced today on a commercial scales are harvested through deliberate injury, or "tapping," of the trunk.[283] Resins consist of a complex mixture of various organic compounds collectively known as terpenes, and can be distinguished from gums (a different category of plant biopolymers) by their insolubility in water. Oil-soluble resins dissolve in hydrocarbons, whereas spirit-soluble resins dissolve in alcohols and like organic solvents.[283] Whereas most resin constituents are small organic molecules, some resins are known to contain a polymeric fraction that could serve as a potential source of oil-soluble chains of moderately large molar mass. An example is the resin *mastic* [see Fig. A.1(a)] exuded by the mastic tree *Pistacia lentiscus*, which has historically been valued as a traditional food flavorant in the eastern Mediterranean. Mastic resin contains a polymeric fraction which is soluble in dichloromethane, and consisting primarily of cis-1,4-poly-β-myrcene chains with molar masses in the range 20–100 kDa.[284] Similarly, the resin *dammar* [Fig. A.1(b)] is produced by trees of the family *Dipterocarpacea*, principally those belonging to the genera *Shorea* and *Hopea*. Dammar is freely soluble in aromatic hydrocarbons such as toluene, and aside from various acidic and neutral terpenoid compounds and polysaccharides, also contains a polymeric fraction composed of polycadinene.[285]

Plant Latices

Latex is the term applied to the milky white colloid exuded by certain species of flowering plants from sites of external injury, and as a deterrent against natural predation.[283] Latex comprises an emulsion of polymer microparticles (usually polyisoprene) dispersed in an aqueous phase, and coagulates on exposure to air. The predominant commercial source of polyisoprene latex today is by far the Pará rubber tree, *Hevea brasiliensis*[286] [see Fig. A.1(c)]; alternative sources of natural rubber that have been explored include the latices of Guayule plant, *Parthenium argentatum*; the Panama rubber tree, *Castilla elastica*; and the rubber fig, *Ficus elastica*. These latices yield the elastomeric polymer *cis*-1,4-polyisoprene, which can be chemically crosslinked (or 'vulcanized') with suitable additives and modifiers to produce hardened, thermoset rubber. On the other hand, lat-

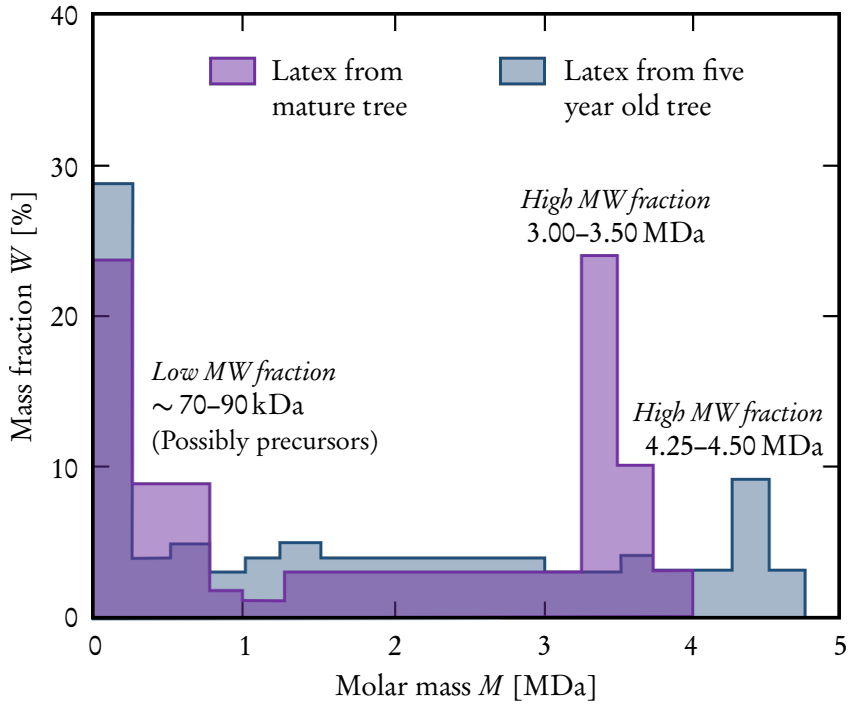

FIGURE A.2. Histogram depicting the molar mass distribution of polymers constituting the oil-soluble fraction of natural rubber latex. Figure adapted from Ref. [39].

ices of the gutta tree, *Palaquium gutta*, and the balatá tree, *Manilkara bidentata*, consist mainly of the isomeric polymer chain *trans*-1,4-polyisoprene which, unlike the amorphous cis form in rubber, crystallizes into a rigid, non-elastic solid called *gutta*.[283] As a natural, non-toxic, and bioinert thermoplastic, gutta-percha derived from *Palaquium* latex is widely used today as an obturation filler in endodontic procedures. Gutta-balatá was employed as a cheaper alternative to gutta-percha before the advent of synthetic substitutes, and was once used in the manufacture of high-quality golf balls.

Aside from cellulose, natural rubber is arguably the most important plant-sourced biopolymer of industrial relevance in modern times, and is utilized in a wide variety of applications and consumer products. The worldwide production of natural rubber stood at 13.6 million tonnes in 2017, accounting for 47 % of the total rubber produced that year; its price in 2017 was approximately \$2/kg.[287] The liquid rubber latex harvested from *Hevea* trees contains over 50 % by weight of solids, mostly in the form of colloidal polymer particles of size 0.08–2 µm.[286] As mentioned above, the polymer content in latex is principally *cis*-1,4-polyisoprene, a neutral flexible chain that is soluble in hydrocarbons including heptane, benzene, toluene, and cyclohexane.[288] Figure A.2 shows the molar

mass distribution of the oil-soluble polymer in unprocessed rubber latex, fractionated and analyzed by means of a differential solvent extraction technique.[39] The distribution is distinctly bimodal, with a low molar mass fraction (70–90 kDa) presumably composed of precursor molecules, alongside a high molar mass fraction comprising 3.0–4.5 MDa polymer chains.[39] Furthermore, the "immature" latex drawn from a five-year-old tree yielded a polymeric fraction of slightly larger molar mass, $4.25\,\mathrm{MDa} \leqslant M \leqslant 4.50\,\mathrm{MDa}$, than the latex tapped from a mature tree, for which the molar masses were in the range $3.00\,\mathrm{MDa} \leqslant M \leqslant 3.50\,\mathrm{MDa}$.[39] Given its low cost, wide availability, and known presence of high molar mass constituents, rubber latex seems to be a promising candidate for future exploration as a source of oil-soluble biopolymers for turbulent drag reduction in hydrocarbon flows.

II. Frictional Drag Measurements in Liquid Alkanes

For evaluating the drag reduction efficacy of oil-soluble polymers under flow and process conditions relevant to real-life service, frictional drag measurements were performed in turbulent shear flow of heavy alkane oils, such as hexadecane or dodecane, that do not solidify at room temperature (i.e. melting point $T_{\mathrm{mp}} \leqslant 20\,°\mathrm{C}$); liquid alkanes lighter than dodecane were either too volatile to permit facile handling, or considered too unrepresentative of the typical solvents and chemical environments encountered in field operations. The physical properties of dodecane at various temperatures are listed in Table A.1; as a liquid, it is both less dense and more viscous than water, resulting in a kinematic viscosity of $\nu = 1.99\,\mathrm{mm^2\,s^{-1}}$ which is twice that of water at room temperature. Given the strict upper bound on rotor angular speed ($\Omega \leqslant 300\,\mathrm{rad\,s^{-1}}$) imposed by the operating limits of the AR-G2 rheometer, this twofold increase in the kinematic viscosity of the working fluid reduces the range of experimentally accessible Reynolds numbers $\mathrm{Re} = R_i \Omega d/\nu$ in the TC apparatus by half, severely curtailing its utility for turbulent drag reduction measurements at room temperature.

To surmount this practical limitation, flow measurements were instead conducted at elevated temperatures, so as to lower the viscosity of alkane solvents to more manageable levels; for example, at a temperature of $T = 50\,°\mathrm{C}$, the kinematic viscosity of dodecane is reduced to $\nu = 1.26\,\mathrm{mm^2\,s^{-1}}$, which is only 26 % greater than that of water at ambient temperature. To this end, a redesigned version of the TC apparatus was constructed, which was capable of performing frictional drag measurements in organic solvents at temperatures of up to $T = 50\,°\mathrm{C}$; the design and flow characterization of this bespoke flow device, hereafter referred to as the high temperature Taylor-Couette (or HTTC) apparatus, are detailed in this section.

TABLE A.1. Thermophysical data for dodecane at a pressure of $P = 1\,\text{atm}$. For comparison, the properties for water at $T = 20\,°\text{C}$ and $P = 1\,\text{atm}$ are: $\rho = 998.2\,\text{kg}\,\text{m}^{-3}$, $\eta = 1.002\,\text{mPa}\,\text{s}$, and $\nu = 1.004\,\text{mm}^2\,\text{s}^{-1}$. Data sourced from Ref. [289].

Temperature T [°C]	Density ρ [kg m^{-3}]	Dynamic viscosity η [mPa s]	Kinematic viscosity ν [mm^2 s^{-1}]
20	749.4	1.489	1.987
25	745.7	1.359	1.822
30	742.0	1.246	1.679
35	738.3	1.148	1.555
40	734.6	1.061	1.444
45	731.0	0.9843	1.347
50	727.3	0.9160	1.259
55	723.6	0.8550	1.182
60	719.9	0.8002	1.112

A. *The High Temperature Taylor-Couette Apparatus*

The basic design and flow geometry of the HTTC device are very similar to that of the bespoke TC apparatus after which it is modeled; Fig A.3 shows a schematic sectional view of the HTTC fixture and its key components. The rotor and stator dimensions in the new design were reworked to utilize the full range of available operating speeds, $0\,\text{rad}\,\text{s}^{-1} \leqslant \Omega \leqslant 300\,\text{rad}\,\text{s}^{-1}$, without exceeding the maximum torque limit of the AR-G2 rheometer. The rotor, as before, was machined from aluminum 6061-T6 alloy, and had a radius $R_i = 25.4\,\text{mm}$ and length $L = 81.7\,\text{mm}$; it was provided with a hollow interior recess that remains air-filled when submerged, which serves to minimize extraneous fluid friction acting on the bottom face. The rotor is enclosed concentrically inside a cylindrical glass stator of radius $R_o = 38.9\,\text{mm}$; this yields a working gap of $d = R_o - R_i = 13.5\,\text{mm}$ for the HTTC geometry, with an attendant radius ratio of $\zeta = R_i/R_o = 0.653$, and a gap aspect ratio of $\xi = L/d = 6.05$. Borosilicate glass was chosen for the stator cylinder on account of its optical transparency, its excellent chemical compatibility with organic solvents, its low thermal expansivity that minimizes dimensional variations during temperature changes, and its greater thermal conductivity than acrylic that results in faster thermal equilibration times for the working fluid within the cell gap. As in the original TC apparatus, two fluidic ports were drilled through the aluminum base to permit filling and draining of the gap between experiments.

The key new feature incorporated in the HTTC design was, of course, the capability for active temperature control of the working fluid. To this end, the glass stator was enclosed in a thermal jacket through which warm water can be circulated at the requisite

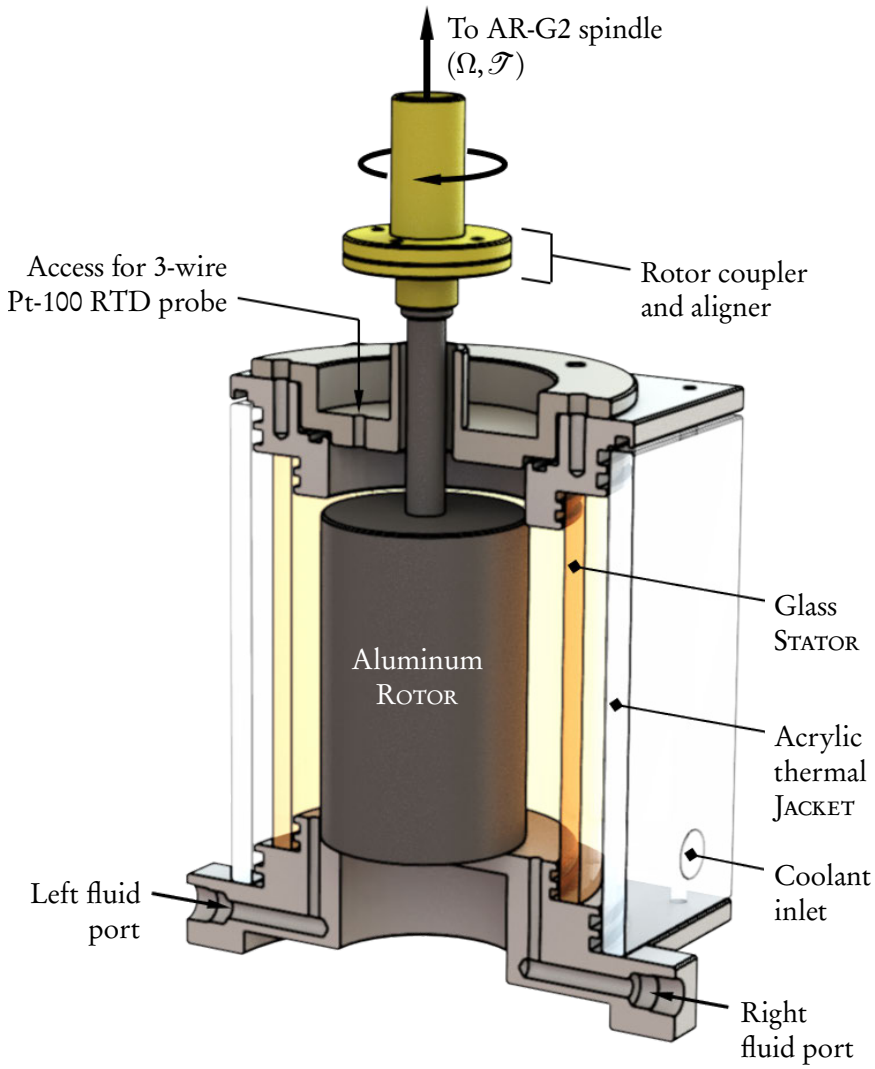

Figure A.3. A schematic sectional view of the high temperature Taylor-Couette (HTTC) apparatus, utilized for frictional drag measurements in alkanes. Also see Fig. A.4

temperature using a laboratory thermal circulator (F12, Julabo). The rectangular water jacket was fabricated out of optically clear acrylic to provide thermal insulation while maintaining visual access to the flow cell; its plane outer faces also help minimize the refractive optical distortion caused by the cylindrical curvature of the stator wall. A 3-wire 100 Ω platinum (Pt-100) RTD probe, affixed to the acrylic cap and projecting into the liquid plenum above the rotor, was used to monitor the temperature of the working fluid in the cell gap via a calibrated digital readout.

Leakproof sealing between different components was achieved by means of Buna-N o-rings and rubber gaskets, with an option to switch to Viton o-rings for more aggressive aromatic solvents. The o-ring seats on the aluminum lid and base were intentionally designed as external, outward-facing grooves, so that robust sealing and adequate o-ring compression was maintained even as the various parts underwent differential thermal expansion at elevated operating temperatures. The fixture was designed to allow complete disassembly for periodic cleaning, decontamination, and seal replacements; during normal operation, the parts were held together securely under longitudinal compression by four threaded tension rods running vertically between the lid and the base. An additional feature in the new design was the inclusion of an adjustable shaft coupling, to correct for misalignments between the rotational axes of the rotor and the rheometer spindle; this greatly simplified the elimination of rotor eccentricity, a process that usually entailed tedious and iterative manual adjustments in the old design.

Table A.2 compares the dimensions, geometric ratios and flow parameters of the HTTC apparatus described above, with those of the TC apparatus described in §3.I.A (and used in flow experiments involving aqueous systems in Chapters 4 and 5). Figure A.4 shows the HTTC device fully assembled and mounted on the AR-G2 rheometer during a typical flow experiment.

B. *Calibration of Baseline Friction*

The baseline flow characterization for the HTTC device was performed along the same lines as for the original TC apparatus, following a procedure analogous to the one described in §3.II.B. As discussed therein, the primary flow inside the TC cell gap is unstable to radial perturbations above a critical rate of rotation, and develops secondary vortical flow patterns as the rotor speed Ω is increased. After transitioning through a series of unsteady, and later turbulent, secondary flow regimes, the flow eventually transitions to featureless (Newtonian) turbulence when a critical Reynolds number, $\mathrm{Re}_{\mathrm{crit}}$, is reached.

To accurately locate the point of transition to this terminal flow regime, baseline friction measurements were performed in pure dodecane at an operating temperature of $T = (40.0 \pm 0.5)\,°\mathrm{C}$; to this end, the steady state frictional torque $\mathscr{T}$ was measured at

TABLE A.2. A comparison of the dimensions, geometry ratios and key flow parameters between the bespoke TC apparatus used earlier in this study for aqueous flow measurements (see §3.I), and the HTTC apparatus described in this appendix and used for turbulent flow measurements in liquid alkanes. Asterisks denote flow quantities estimated approximately.

Parameter		Unit	HTTC device	TC apparatus
WORKING FLUID				
Liquid/Solvent			Dodecane	Water
Temperature	T	°C	40	25
Density	ρ	$\mathrm{kg\,m^{-3}}$	735	997
Dynamic viscosity	η	mPa s	1.06	0.890
Kinematic viscosity	ν	$\mathrm{mm^2\,s^{-1}}$	1.44	0.893
DIMENSIONS				
Rotor radius	R_i	mm	25.4	38.1
Stator radius	R_o	mm	38.9	50.8
Rotor length	L	mm	81.7	76.2
Cell gap	d	mm	13.5	12.7
Bottom end gap		mm	1.00	0.10
GEOMETRY RATIOS				
Radius ratio	ζ	—	0.653	0.750
Aspect ratio	ξ	—	6.052	6.000
FLOW PARAMETERS				
Transition Reynolds number	$\mathrm{Re_{crit}}$	—	9900	11 000
Max. Reynolds number	Re_∞	—	68 700	86 800
Max. angular speed	Ω_∞	$\mathrm{rad\,s^{-1}}$	290	160
Max. wall speed	V_∞	$\mathrm{m\,s^{-1}}$	7.37	6.10
Max. shear Reynolds number*	$\mathrm{Re}_{\tau,\infty}$	—	2700	3000
Max. wall shear stress*	$\tau_{w,\infty}$	Pa	60	50
Transition viscous length scale*	$\delta_{\nu,\mathrm{crit}}$	µm	26	18
Min. viscous length scale	$\delta_{\nu,\infty}$	µm	5	4

FIGURE A.4. The HTTC apparatus fully assembled and mounted on the AR-G2 rheometer during a flow measurement. The 3-wire lead from the Pt-100 RTD probe to the digital readout can be seen emerging from the cap at the top. The orange tubes visible on the right and left sides are, respectively, coolant inlet and outlet lines that convey water between the acrylic jacket and the thermal circulator (not seen in the picture).

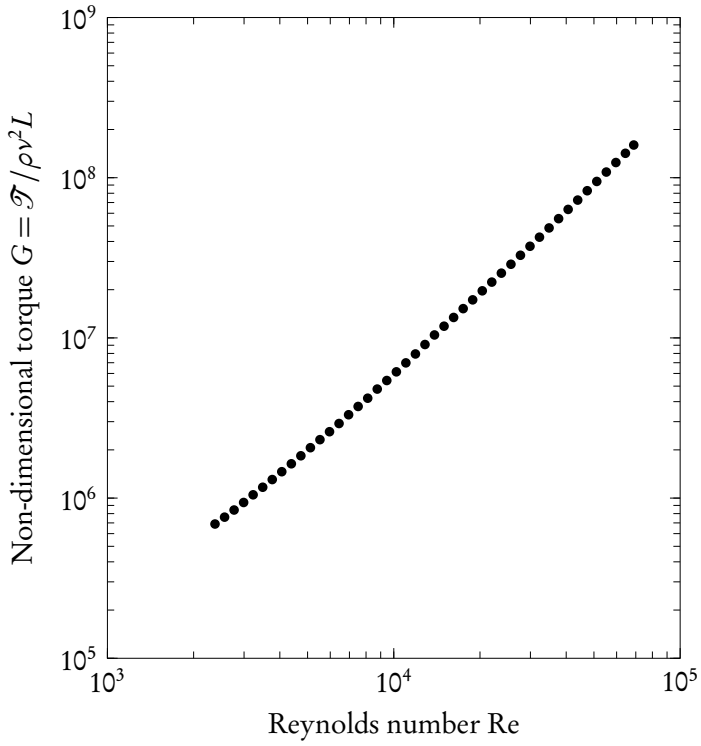

FIGURE A.5. The baseline friction curve for the HTTC apparatus, obtained for a smooth no-slip rotor in dodecane at a working temperature of $T = (40.0 \pm 0.5)\,°\mathrm{C}$. The data is represented as the non-dimensional rotor torque $G = \mathscr{T}/\rho\nu^2 L$ versus the Reynolds number Re.

discrete rotor speeds spanning $10\,\mathrm{rad\,s^{-1}} \leqslant \Omega \leqslant 290\,\mathrm{rad\,s^{-1}}$, corresponding to Reynolds numbers in the range $2 \times 10^3 \leqslant \mathrm{Re} \leqslant 7 \times 10^4$. The results are shown in Fig. A.5, wherein the non-dimensional torque $G = \mathscr{T}/\rho\nu^2 L$ (cf. Eq. 3.12) is shown as a function of the Reynolds number Re. To determine the transition Reynolds number $\mathrm{Re}_{\mathrm{crit}}$ from this curve, we adopt the method proposed by Lathrop, Fineberg and Swinney (1992),[196] and assume a power law scaling for the frictional torque of the form $G \sim \mathrm{Re}^{\alpha}$ valid in the limit of large Reynolds numbers; this then yields the torque exponent α, given by (cf. Eq. 3.13)

$$\alpha = \frac{\mathrm{d}\log G}{\mathrm{d}\log \mathrm{Re}}. \tag{A.1}$$

The baseline friction data in Fig. A.5 comprises discrete torque measurements at uniform log intervals of $\Delta(\log_{10}\mathrm{Re}) = 0.033$; the local exponent α was inferred from this curve by means of a sliding linear least squares fit over 15 adjacent data points (equivalent to a log

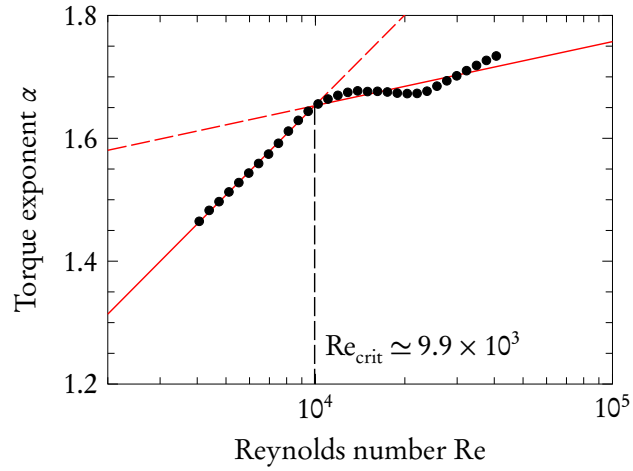

FIGURE A.6. The local torque exponent α as a function of the Reynolds number Re, derived from the baseline curve for the HTTC apparatus shown in Fig. A.5. A change in slope is observed near $\mathrm{Re}_{\mathrm{crit}} \simeq 9.9 \times 10^3$, indicating the point of transition to the featureless turbulent flow regime. The red lines denote piecewise log-linear fits to $\alpha(\mathrm{Re})$ in the vicinity of the transition point, given by Eq. A.2.

interval of $\Delta(\log_{10}\mathrm{Re}) = 0.47$). The exponent α is shown as a function of the Reynolds number Re in Fig. A.6. As evident from the plot, α increases monotonically with Re, indicating the absence of a unique power law scaling that holds uniformly throughout this range of Reynolds numbers. However, a marked discontinuity in the slope of the curve is observed at $\mathrm{Re} = 9.9 \times 10^3$, indicating a change in the dependence of α on Re (and by extension, the scaling of G with Re). Following Lathrop et al.,[196] we identify $\mathrm{Re}_{\mathrm{crit}} 9.9 \times 10^3$ as the critical Reynolds number at which featureless (Newtonian) turbulent flow is attained the HTTC cell gap.

An empirical expression for α may be derived by means of piecewise linear fits to the experimental friction data in the vicinity of the transition point:

$$\alpha = \begin{cases} 1.65 + 0.487 \log_{10}(\mathrm{Re}/\mathrm{Re}_{\mathrm{crit}}) & \mathrm{Re} \leqslant \mathrm{Re}_{\mathrm{crit}} \\ 1.65 + 0.104 \log_{10}(\mathrm{Re}/\mathrm{Re}_{\mathrm{crit}}) & \mathrm{Re} > \mathrm{Re}_{\mathrm{crit}} \end{cases} \tag{A.2}$$

At the point of transition, a critical torque exponent of $\alpha = 1.65$ was observed, which is quite close to the marginal stability exponent[196] of $\alpha = 5/3$.

In the turbulent regime, $\mathrm{Re} \geqslant \mathrm{Re}_{\mathrm{crit}}$, the baseline friction in a Newtonian fluid may be described by a logarithmic friction law of the form[203] (cf. Eq. 3.18)

$$V^+ = M \log \mathrm{Re}_\tau + N\,, \tag{A.3}$$

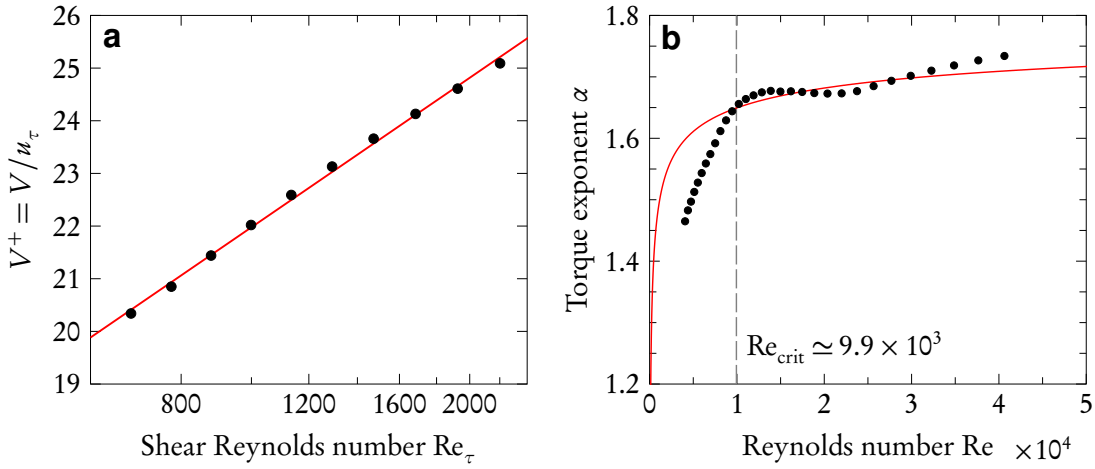

FIGURE A.7. (a) The baseline friction curve for the HTTC apparatus in Prandtl-von Kármán coordinates. The red line denotes the linear least-squares fit used to extract the empirical constants M and N appearing in Eq. A.3. (b) The torque exponent α as a function of the Reynolds number Re, reproduced from Fig. A.6. The solid red curve indicates the theoretical prediction for α, Eq. A.5, computed using the values of M and N (see Eq. A.4) inferred from the fit in panel (a).

where $V^+ = V/u_\tau = R_i\Omega/u_\tau$ is the rotor speed normalized by the friction velocity $u_\tau = \sqrt{\tau_w/\rho}$ at the inner boundary layer (cf. Eq. 2.8), $\mathrm{Re}_\tau = \rho u_\tau d/\eta$ is the shear Reynolds number at the inner wall (cf. Eq. 2.10), and M and N are constants that depend on the radius ratio ζ of the TC geometry. As seen In Fig. A.7(a), the friction curve for pure dodecane in Prandtl-von Kármán coordinates shows good conformance to the functional form predicted by Eq. A.3, and a linear least-squares regression was used to extract the characteristic constants

$$M = 4.10 \quad \text{and} \quad N = -6.32 \tag{A.4}$$

quantifying the baseline friction for the HTTC apparatus in the turbulent flow regime.

As derived in §3.I.B, the friction law given by Eq. A.3 yields an explicit analytic expression for the torque exponent α, namely (cf. Eq. 3.25)

$$\alpha = \frac{\mathrm{d}\log G}{\mathrm{d}\log \mathrm{Re}} = 2\left[1 - \frac{1}{1 + \mathrm{W}\left(e^{N/M}\mathrm{Re}'\right)}\right], \tag{A.5}$$

where $\mathrm{Re}' = \mathrm{Re}/M$, and $\mathrm{W}(x)$ denotes (the principal branch of) the product logarithm function (also known as the Lambert W function). Figure A.7(b) compares Eq. 3.25 with the value of α inferred directly from regression to the experimental data; a good fit is indeed observed for Reynolds numbers exceeding the critical point, $\mathrm{Re} \geqslant \mathrm{Re}_{\mathrm{crit}} = 9.9 \times 10^3$.

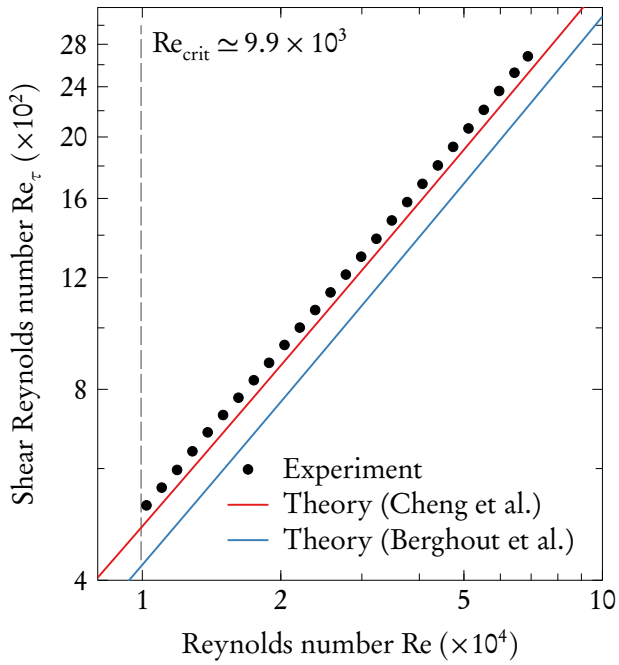

FIGURE A.8. The baseline friction curve for the HTTC apparatus in the featureless turbulent flow regime, compared with the semi-empirical models of Cheng et al. (Eq. 3.26) and Berghout et al. (Eq. 3.29), both evaluated for a radius ratio of $\zeta = 0.653$.

Furthermore, the baseline data was also validated against recent semi-empirical models for terminal Taylor-Couette turbulence, published recently by Cheng et al. (2020)[206] and Berghout et al. (2020),[207] given by Eqs. 3.26 and 3.29 respectively; these models yield predictions for the baseline friction with no adjustable parameters aside from the radius ratio $\zeta = 0.653$, which is fixed by the rotor and stator radii. Figure A.8 compares the experimental baseline for the HTTC apparatus with the friction curves predicted by the two models; as seen from the plot, the data shows good agreement with the three-layer model of Cheng et al., Eq. 3.26, and the slight discrepancy between theory and experiment arises presumably from end effects and the relatively moderate range of operating Reynolds numbers attained in the HTTC device.

C. *Preliminary Studies on Drag-Reducing Polymers*

POLYISOBUTYLENE

As a synthetic benchmark for evaluating the drag reduction efficacy of plant biopolymers, turbulent friction measurements were performed in the HTTC apparatus using dilute

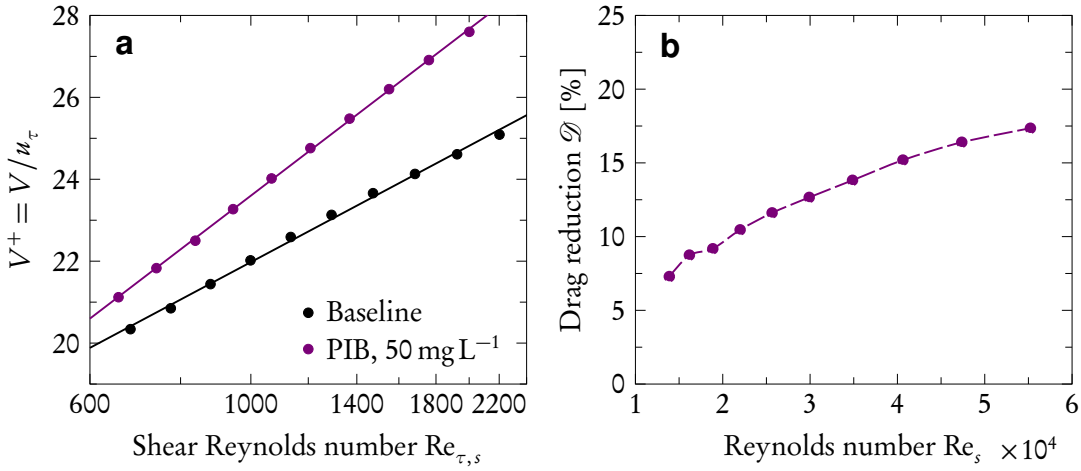

FIGURE A.9. Experimental friction data for a 50 mg L^{-1} solution of PIB (molar mass 4.7 MDa) in dodecane, measured at $T = (40.0 \pm 0.5)$ °C. (a) Friction curve in Prandtl-von Kármán coordinates, showing polymeric drag reduction. The solid line is a linear least-squares fit to the data. (b) The percentage drag reduction $\mathscr{D}$ (relative to pure dodecane at 40 °C) as a function of the Reynolds number Re_s. The dashed curve is solely for visual guidance.

solutions of polyisobutylene (PIB), which has previously been employed in the literature as a drag reducing additive in turbulent hydrocarbon flows. A high molar mass sample of PIB (Alfa Chemistry, $M_w \simeq 4.7 \times 10^6\,\mathrm{g\,mol^{-1}}$) was procured in the form of a rubbery solid mass, which was then dissolved in toluene to prepare a concentrated stock solution ($c = 5.1\,\mathrm{g\,L^{-1}}$) as per the procedure outlined in §3.II.A. Afterwards, 3.9 mL of the PIB stock was diluted in dodecane to a final volume of 400 mL, yielding a dilute solution of polymer concentration $c = 50\,\mathrm{mg\,L^{-1}}$. Frictional drag measurements were performed on this solution in the HTTC apparatus, at an operating temperature of $T = (40.0 \pm 0.5)$ °C; the resulting data are shown in Fig. A.9. The dissolved polymer yielded a slope increment of $\delta = M_P - M = 1.78$ in Prandtl-von Kármán coordinates, with an attendant percentage drag reduction of $\mathscr{D} = 17\,\%$ at a Reynolds number of $\mathrm{Re}_s = 5.5 \times 10^4$.

NATURAL RUBBER

Natural rubber latex was procured as a white liquid emulsion (Centrifuged Natural Latex Liquid Rubber, Holden's Latex), unprocessed except for centrifugation to increase the solid content to $\sim 62\,\%$. A 6 mL aliquot of liquid latex was spread on a polystyrene petri dish, and allowed to dry in ambient air over a warm hot plate at 50 °C for 1 h. After all water content had evaporated, 3.5 g of residual dry solid content was recovered in

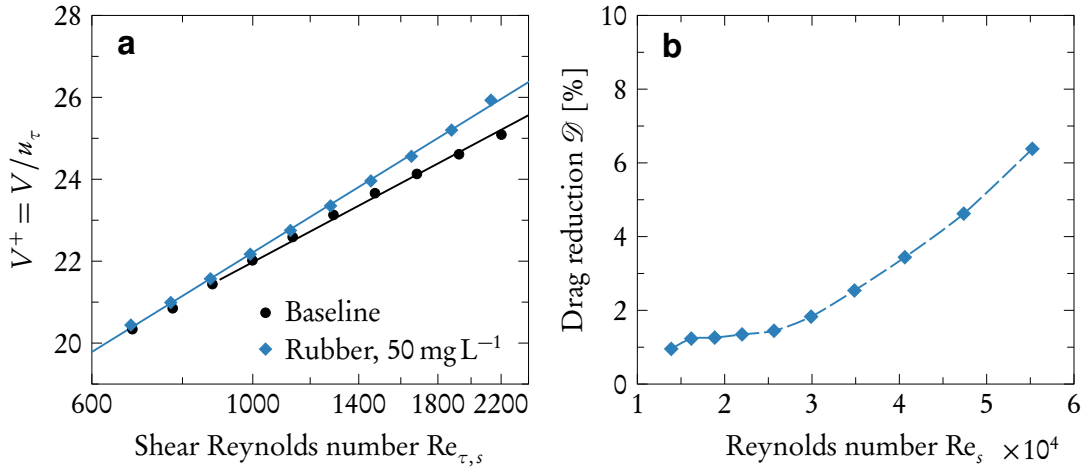

FIGURE A.10. Experimental friction data for a 50 mg L^{-1} solution of natural rubber in dodecane, measured at $T = (40.0 \pm 0.5)$ °C. (a) Friction curve in Prandtl-von Kármán coordinates, showing polymeric drag reduction. The solid line is a linear least-squares fit to the data. (b) The percentage drag reduction $\mathscr{D}$ (relative to pure dodecane at 40 °C) as a function of the Reynolds number Re_s. The dashed curve is solely for visual guidance.

the form of a thin translucent sheet or crêpe. The thin membrane of dried latex was mixed with 300 mL of toluene in a sealed container and allowed to dissolve gradually on a laboratory bench roller for several weeks, yielding a stock solution of approximately 11.7 g L^{-1} polyisoprene rubber in toluene (with small amounts of other naturally occurring contaminants). As in the case of PIB, a 50 mg L^{-1} rubber solution was prepared by further diluting 1.7 mL of the stock solution in dodecane to a final volume of 400 mL. This solution was then utilized for flow measurements in the HTTC apparatus, at a temperature of $T = (40.0 \pm 0.5)$ °C; the resulting friction curves are shown in Fig. A.10. The dissolved rubber produced a slope increment of $\delta = M_P - M = 0.66$ in Prandtl-von Kármán coordinates, resulting in a percentage drag reduction of $\mathscr{D} = 6\,\%$ at a Reynolds number of $\mathrm{Re}_s = 5.5 \times 10^4$.

Image Credits and Attribution

Page	Figure	Image source and attribution
34	2.1	Photographs (a) and (b) sourced from *Celebrating 40 Years of Drag Reduction Leadership—The Evolution of LSPI's Technology*, LiquidPower Specialty Products Inc. `www.liquidpower.com/newsletter/celebrating-40-years`
35	2.2	New York Fire Department photo. Reproduced from Ref. [1].
36	2.3	(a) Photo from Grace's Guide to British Industrial History. `www.gracesguide.co.uk/HMS_Highburton` (b) Reproduced from Ref. [48]. (c) Still frame from *Barracuda and olive sea snake* (video), Britannica Academic, Encyclopædia Britannica. `academic.eb.com/levels/collegiate/assembly/view/195568` (accessed June 1, 2020).
55	2.6	(a) Free use photo from `pixabay.com` (c) Photo by Musa from `www.flickr.com`, licensed under CC BY 2.0. Images (b) and (d) reproduced from Ref. [118].
93	3.9	(a) Author's own work. (b) Photo of Ubbelöhde glass capillary viscometer sourced from Cannon Instrument Company online product catalog. `www.cannoninstrument.com`
170	A.1	(a) Photo by Tobias Rütten from `commons.wikimedia.org`, licensed under CC BY-SA 2.5. (b) Photo © Manolis Kazamias (2002); fair use. Sourced from *Know-how of cultivating mastic on the island of Chios,* Intangible Cultural Heritage of Humanity, UNESCO, `ich.unesco.org/en/RL/know-how-of-cultivating-mastic-on-the-island-of-chios-00993` (c) Photo by David Stanley from `www.flickr.com`, licensed under CC BY 2.0.

The space below is intentionally left blank.

References

[1] Anon. Slippery water cuts friction loss. *Fire Eng.* **122**:48–49 (September 1969).

[2] H. Tennekes and J. L. Lumley. *A First Course in Turbulence*. The MIT Press (1972).

[3] S. B. Pope. *Turbulent Flows*. Cambridge University Press (2000).

[4] M. Perlin and S. Ceccio. *Mitigation of Hydrodynamic Resistance*. World Scientific (2015).

[5] S. A. Mäkiharju, M. Perlin, and S. L. Ceccio. On the energy economics of air lubrication drag reduction. *Int. J. Nav. Arch. Ocean* **4**:412–422 (2012).

[6] International Maritime Organization. Third IMO greenhouse gas study 2014. International Maritime Organization, London, UK (2015).

[7] P. A. Stone, F. Waleffe, and M. D. Graham. Toward a structural understanding of turbulent drag reduction: nonlinear coherent states in viscoelastic shear flows. *Phys. Rev. Lett.* **89**:208301 (2002).

[8] P. A. Stone, A. Roy, R. G. Larson, F. Waleffe, and M. D. Graham. Polymer drag reduction in exact coherent structures of plane shear flow. *Phys. Fluids* **16**:3470–3482 (2004).

[9] W. Li, L. Xi, and M. D. Graham. Nonlinear travelling waves as a framework for understanding turbulent drag reduction. *J. Fluid Mech.* **565**:353–362 (2006).

[10] A. Roy, A. Morozov, W. van Saarloos, and R. G. Larson. Mechanism of polymer drag reduction using a low-dimensional model. *Phys. Rev. Lett.* **97**:234501 (2006).

[11] W. Li and M. D. Graham. Polymer induced drag reduction in exact coherent structures of plane poiseuille flow. *Phys. Fluids* **19**:083101 (2007).

[12] K. Kim, R. J. Adrian, S. Balachandar, and R. Sureshkumar. Dynamics of hairpin vortices and polymer-induced turbulent drag reduction. *Phys. Rev. Lett.* **100**:134504 (2008).

[13] L. Xi and M. D. Graham. Active and hibernating turbulence in minimal channel flow of Newtonian and polymeric fluids. *Phys. Rev. Lett.* **104**:218301 (2010).

[14] L. Xi and M. D. Graham. Dynamics on the laminar-turbulent boundary and the origin of the maximum drag reduction asymptote. *Phys. Rev. Lett.* **108**:028301 (2012).

[15] L. Xi and M. D. Graham. Intermittent dynamics of turbulence hibernation in Newtonian and viscoelastic minimal channel flows. *J. Fluid Mech.* **693**:433–472 (2012).

[16] M. B. Martell, J. B. Perot, and J. P. Rothstein. Direct numerical simulations of turbulent flows over superhydrophobic surfaces. *J. Fluid Mech.* **620**:31–41 (2009).

[17] M. B. Martell, J. P. Rothstein, and J. B. Perot. An analysis of superhydrophobic turbulent drag reduction mechanisms using direct numerical simulation. *Phys. Fluids* **22**:065102 (2010).

[18] H. Park, H. Park, and J. Kim. A numerical study of the effects of superhydrophobic surface on skin-friction drag in turbulent channel flow. *Phys. Fluids* **25**:110815 (2013).

[19] A. Rastegari and R. Akhavan. On the mechanism of turbulent drag reduction with super-hydrophobic surfaces. *J. Fluid Mech.* **773**:R4 (2015).

[20] J. Seo, R. García-Mayoral, and A. Mani. Pressure fluctuations and interfacial robustness in turbulent flows over superhydrophobic surfaces. *J. Fluid Mech.* **783**:448–473 (2015).

[21] J. Seo and A. Mani. On the scaling of the slip velocity in turbulent flows over superhydrophobic surfaces. *Phys. Fluids* **28**:025110 (2016).

[22] M. Perlin, D. R. Dowling, and S. L. Ceccio. Freeman scholar review: passive and active skin-friction drag reduction in turbulent boundary layers. *J. Fluids Eng.* **138**:091104 (2016).

[23] M. D. Graham. Drag reduction and the dynamics of turbulence in simple and complex fluids. *Phys. Fluids* **26**:101301 (2014).

[24] L. Xi. Turbulent drag reduction by polymer additives: fundamentals and recent advances. *Phys. Fluids* **31**:121302 (2019).

[25] K. B. Golovin, J. W. Gose, M. Perlin, S. L. Ceccio, and A. Tuteja. Bioinspired surfaces for turbulent drag reduction. *Phil. Trans. R. Soc. A.* **374**:20160189 (2016).

[26] S. L. Ceccio. Friction drag reduction of external flows with bubble and gas injection. *Annu. Rev. Fluid Mech.* **42**:183–203 (2010).

[27] E. S. Winkel, G. F. Oweis, S. A. Vanapalli, D. R. Dowling, M. Perlin, M. J. Solomon, and S. L. Ceccio. High-Reynolds-number turbulent boundary layer friction drag reduction from wall-injected polymer solutions. *J. Fluid Mech.* **621**:259–288 (2009).

[28] K. A. Lay, R. Yakushiji, S. Mäkiharju, M. Perlin, and S. L. Ceccio. Partial cavity drag reduction at high Reynolds numbers. *J. Ship Res.* **54**:109–119 (2010).

[29] B. Dean and B. Bhushan. Shark-skin surfaces for fluid-drag reduction in turbulent flow: a review. *Phil. Trans. R. Soc. A* **368**:4775–4806 (2010).

[30] J. W. Gose, K. Golovin, M. Boban, J. M. Mabry, A. Tuteja, M. Perlin, and S. L. Ceccio. Characterization of superhydrophobic surfaces for drag reduction in turbulent flow. *J. Fluid Mech.* **845**:560–580 (2018).

[31] A. Rajappan, K. Golovin, B. Tobelmann, V. Pillutla, Abhijeet, W. Choi, A. Tuteja, and G. H. McKinley. Influence of textural statistics on drag reduction by scalable, randomly rough superhydrophobic surfaces in turbulent flow. *Phys. Fluids* **31**:042107 (2019).

[32] J. Warrand, P. Michaud, L. Picton, G. Muller, B. Courtois, R. Ralainirina, and J. Courtois. Large scale purification of water-soluble polysaccharides from flaxseed mucilage, and isolation of a new anionic polymer. *Chromatographia* **58**:331–335 (2003).

[33] J. Warrand, P. Michaud, L. Picton, G. Muller, B. Courtois, R. Ralainirina, and J. Courtois. Flax (Linum usitatissimum) seed cake: A potential source of high molecular weight arabinoxylans? *J. Agric. Food Chem.* **53**:1449–1452 (2005).

[34] M. I. Capitani, L. J. Corzo-Rios, L. A. Chel-Guerrero, D. A. Betancur-Ancona, S. M. Nolasco, and M. C. Tomás. Rheological properties of aqueous dispersions of chia (*Salvia hispanica L.*) mucilage. *J. Food Eng.* **149**:70–77 (2009).

[35] L. Yu, G. E. Yakubov, W. Zeng, X. Xing, J. Stenson, V. Bulone, and J. R. Stokes. Multi-layer mucilage of *Plantago ovata* seeds: Rheological differences arise from variations in arabinoxylan side chains. *Carbohydr. Polym.* **165**:132–141 (2017).

[36] L. Yu, G. E. Yakubov, M. Martínez-Sanz, E. P. Gilbert, and J. R. Stokes. Rheological and structural properties of complex arabinoxylans from *Plantago ovata* seed mucilage under non-gelled conditions. *Carbohydr. Polym.* **193**:179–188 (2018).

[37] R. M. Andrade, A. S. Pereira, and E. J. Soares. Drag reduction in synthetic seawater by flexible and rigid polymer addition into a rotating cylindrical double gap device. *J. Fluids Eng.* **138**:021101 (2016).

[38] E. D. Burger, W. R. Munk, and H. A. Wahl. Flow increase in the Trans Alaska Pipeline through use of a polymeric drag-reducing additive. *J. Petrol. Tech.* **34**:377–386 (1982).

[39] B. Westall. The molecular weight distribution of natural rubber latex. *Polymer* **9**:243–248 (1968).

[40] J. P. Rothstein. Slip on superhydrophobic surfaces. *Annu. Rev. Fluid Mech.* **42**:89–109 (2010).

[41] B. A. Toms. Some observations on the flow of linear polymer solutions through straight tubes at large Reynolds numbers. In *Proceedings of the International Congress on Rheology* volume II pages 135–141 Amsterdam (1949). North Holland Publishing Co.

[42] K. J. Mysels. Flow of thickened fluids. U. S. Patent 2,492,173 (December 1949).

[43] G. A. Agoston, W. H. Harte, H. C. Hottel, W. A. Klemm, K. J. Mysels, H. H. Pomeroy, and J. M. Thompson. Flow of gasoline thickened by napalm. *Ind. Eng. Chem.* **46**:1017–1019 (1954).

[44] J. W. Hoyt. The effect of additives on fluid friction. *J. Basic Eng.* **94**:258–285 (1972).

[45] C. M. White and M. G. Mungal. Mechanics and prediction of turbulent drag reduction with polymer additives. *Annu. Rev. Fluid Mech.* **40**:235–256 (2008).

[46] R. H. J. Sellin, J. W. Hoyt, J. Poliert, and O. Scrivener. The effect of drag reducing additives on fluid flows and their industrial applications Part 2: Present applications and future proposals. *J. Hydraul. Res.* **20**:235–292 (1982).

[47] R. Barati and J. T. Liang. A review of fracturing fluid systems used for hydraulic fracturing of oil and gas wells. *J. Appl. Polym. Sci.* **131**:40735 (2014).

[48] H. J. S. Canham, J. P. Catchpole, and R. F. Long. Boundary layer additives to reduce ship resistance. *The Naval Architect* **2**:187–213 (1971).

[49] R. A. Mostardi, L. C. Thomas, H. L. Greene, F. Vanessen, and R. F. Nokes. Suppression of atherosclerosis in rabbits using drag reducing polymers. *Biorheology* **15**:1–14 (1978).

[50] H. L. Greene, R. F. Mostardi, and R. F. Nokes. Effects of drag reducing polymers on initiation of atherosclerosis. *Polym. Eng. Sci.* **20**:499–504 (1980).

[51] A. P. Sawchuck, J. L. Unthank, and M. C. Dalsing. Drag reducing polymers may decrease atherosclerosis by increasing shear in areas normally exposed to low shear stress. *J. Vasc. Surg.* **20**:761–764 (1999).

[52] M. V. Kameneva, Z. J. Wu, A. Uraysh, B. Repko, K. N. Litwak, T. R. Billiar, M. P. Fink, R. L. Simmons, B. P. Griffith, and H. S. Borovetz. Blood soluble drag-reducing polymers prevent lethality from hemorrhagic shock in acute animal experiments. *Biorheology* **41**:53–64 (2004).

[53] D. Scott. Slippery water in fire hoses. *Science* **164**:1466 (1969).

[54] A. Emerson. Model experiments using dilute polymer solutions instead of water. *Trans. North East Coast Inst. Eng. Shipbuild.* **81**:201–204 (1965).

[55] S. Thurston and R. D. Jones. Experimental model studies of non-Newtonian soluble coatings for drag reduction. *J. Aircraft* **2**:122–126 (1965).

[56] M. W. M. Rosen and N. E. Cornford. Fluid friction of fish slimes. *Nature* **234**:49–51 (1971).

[57] J. W. Hoyt. Hydrodynamic drag reduction due to fish slimes. In T. Y. T. Yu, C. J. Brokaw, and C. Brennen, editors, *Swimming and Flying in Nature* pages 653–672. Springer Boston (1975).

[58] R. Sureshkumar, A. N. Beris, and R. A. Handler. Direct numerical simulation of the turbulent channel flow of a polymer solution. *Phys. Fluids* **9**:743–755 (1997).

[59] P. S. Virk. Drag reduction fundamentals. *AIChE J.* **21**:625–656 (1975).

[60] J. Page and T. A. Zaki. Streak evolution in viscoelastic Couette flow. *J. Fluid Mech.* **742**:520–551 (2014).

[61] A. S. Pereira, G. Mompean, R. L. Thompson, and E. J. Soares. Elliptical, parabolic, and hyperbolic exchanges of energy in drag reducing plane Couette flows. *Phys. Fluids* **29**:115106 (2017).

[62] A. S. Pereira, G. Mompean, L. Thais, E. J. Soares, and R. L. Thompson. Active and hibernating turbulence in drag-reducing plane Couette flows. *Phys. Rev. Fluids* **2**:084605 (2017).

[63] A. S. Pereira, G. Mompean, L. Thais, and E. J. Soares. Transient aspects of drag reducing plane Couette flows. *J. Non-Newton. Fluid Mech.* **241**:60–69 (2017).

[64] A. Keller, G. Kiss, and M. R. Mackley. Polymer drag reduction in Taylor vortices. *Nature* **257**:304–305 (1975).

[65] O. Crumeyrolle, I. Mutabazi, and M. Grisel. Experimental study of inertioelastic Couette-Taylor instability modes in dilute and semidilute polymer solutions. *Phys. Fluids* **14**:1681–1688 (2002).

[66] A. S. Pereira, R. M. Andrade, and E. J. Soares. Drag reduction induced by flexible and rigid molecules in a turbulent flow into a rotating cylindrical double gap device: Comparison between poly (ethylene oxide), polyacrylamide, and xanthan gum. *J. Non-Newton. Fluid Mech.* **202**:72–87 (2013).

[67] A. Rajappan and G. H. McKinley. Epidermal biopolysaccharides from plant seeds enable biodegradable turbulent drag reduction. *Sci. Rep.* **9**:18263 (2019).

[68] J. S. Paschkewitz, C. D. Dimitropoulos, Y. X. Hou, V. S. R. Somandepalli, M. G. Mungal, E. S. G. Shaqfeh, and P. Moin. An experimental and numerical investigation of drag reduction in a turbulent boundary layer using a rigid rodlike polymer. *Phys. Fluids* **17**:085101 (2005).

[69] S. Tamano, M. D. Graham, and Y. Morinishi. Streamwise variation of turbulent dynamics in boundary layer flow of drag-reducing fluid. *J. Fluid Mech.* **686**:352–377 (2011).

[70] H. J. Choi and M. S. Jhon. Polymer-induced turbulent drag reduction. *Ind. Eng. Chem. Res.* **35**:2993–2998 (1996).

[71] C. A. Kim, J. T. Kim, K. Lee, H. J. Choi, and M. S. Jhon. Mechanical degradation of dilute polymer solutions under turbulent flow. *Polymer* **41**:7611–7615 (2000).

[72] J.-I. Sohn, C. A. Kim, H. J. Choi, and M. S. Jhon. Drag-reduction effectiveness of xanthan gum in a rotating disk apparatus. *Carbohydr. Polym.* **45**:61–68 (2001).

[73] C. A. Kim, S. T. Lim, H. J. Choi, J.-I. Sohn, and M. S. Jhon. Characterization of drag reducing guar gum in a rotating disk flow. *J. Appl. Polym. Sci.* **83**:2938–2944 (2002).

[74] S. T. Lim, H. J. Choi, D. Biswal, and R. P. Singh. Turbulent drag reduction characteristics of amylopectin and its derivative. *e-Polymers* **4**:066 (2004).

[75] C. H. Hong, K. Zhang, H. J. Choi, and S. M. Yoon. Mechanical degradation of polysaccharide guar gum under turbulent flow. *J. Ind. Eng. Chem.* **16**:178–180 (2010).

[76] C. H. Hong, H. J. Choi, K. Zhang, F. Renou, and M. Grisel. Effect of salt on turbulent drag reduction of xanthan gum. *Carbohydr. Polym.* **121**:342–347 (2015).

[77] R. B. Bird, R. C. Armstrong, and O. Hassager. *Dynamics of Polymeric Liquids. Volume 1. Fluid Mechanics*. John Wiley and Sons, Inc. second edition (1987).

[78] P. S. Virk, H. S. Mickley, and K. A. Smith. The ultimate asymptote and mean flow structure in Toms' phenomenon. *J. Appl. Mech.* **37**:488–493 (1970).

[79] H.-W. Bewersdorff and N. S. Berman. The influence of flow-induced non-Newtonian fluid properties on turbulent drag reduction. *Rheol. Acta* **27**:130–136 (1988).

[80] M. D. Warholic, H. Massah, and T. J. Hanratty. Influence of drag-reducing polymers on turbulence: effects of Reynolds number, concentration and mixing. *Exp. Fluids* **27**:461–472 (1999).

[81] P. K. Ptasinski, B. J. Boersma, F. T. M. Nieuwstadt, M. A. Hulsen, B. H. A. A. Van Den Brule, and J. C. R. Hunt. Turbulent channel flow near maximum drag reduction: simulations, experiments and mechanisms. *J. Fluid Mech.* **490**:251–291 (2003).

[82] J. L. Lumley. Drag reduction by additives. *Annu. Rev. Fluid Mech.* **1**:367–384 (1969).

[83] P. K. Kundu, I. M. Cohen, and D. R. Dowling. *Fluid Mechanics*. Academic Press sixth edition (2016).

[84] M. Rubinstein and R. H. Colby. *Polymer Physics*. Oxford University Press (2003).

[85] R. G. Larson. Instabilities in viscoelastic flows. *Rheol. Acta* **31**:213–263 (1992).

[86] E. Balkovsky, A. Fouxon, and V. Lebedev. Turbulent dynamics of polymer solutions. *Phys. Rev. Lett.* **84**:4765–4768 (2000).

[87] M. Chertkov, I. Kolokolov, V. Lebedev, and K. Turitsyn. Polymer statistics in a random flow with mean shear. *J. Fluid Mech.* **531**:251–260 (2005).

[88] V. Steinberg. Elastic stresses in random flow of a dilute polymer solution and the turbulent drag reduction problem. *C. R. Phys.* **10**:728–739 (2009).

[89] L. Zhu, H. Schrobsdorff, T. M. Schneider, and L. Xi. Distinct transition in flow statistics and vortex dynamics between low- and high-extent turbulent drag reduction in polymer fluids. *J. Non-Newton. Fluid Mech.* **262**:115–130 (2018).

[90] L. Zhu and L. Xi. Vortex axis tracking by iterative propagation (VATIP): A method for analyzing three-dimensional turbulent structures. *J. Fluid Mech.* **866**:169–215 (2019).

[91] L. Zhu and L. Xi. Vortex dynamics in low- and high-extent polymer drag reduction regimes revealed by vortex tracking and conformation analysis. *Phys. Fluids* **31**:095103 (2019).

[92] D. Samanta, Y. Dubief, M. Holzner, C. Schäfer, A. N. Morozov, C. Wagner, and B. Hof. Elasto-inertial turbulence. *Proc. Natl. Acad. Sci. U. S. A.* **110**:10557–100562 (2013).

[93] G. H. Choueiri, J. M. Lopez, and B. Hof. Exceeding the asymptotic limit of polymer drag reduction. *Phys. Rev. Lett.* **120**:124501 (2018).

[94] J. M. Lopez, G. H. Choueiri, and B. Hof. Dynamics of viscoelastic pipe flow in the maximum drag reduction limit. *J. Fluid Mech.* **874**:699–719 (2019).

[95] J. L. Lumley. Drag reduction in turbulent flow by polymer additives. *J. Polym. Sci. Macromol. Rev.* **7**:263–290 (1973).

[96] C. W. Macosko. *Rheology: Principles, Measurements, and Applications*. Wiley-VCH, Inc. (1994).

[97] A. B. Metzner and A. P. Metzner. Stress levels in rapid extensional flows of polymeric fluids. *Rheol. Acta* **9**:174–181 (1970).

[98] H. Usui and Y. Sano. Elongational flow of dilute drag reducing fluids in a falling jet. *Phys. Fluids* **24**:214–219 (1981).

[99] M. Tabor and P. G. de Gennes. A cascade theory of drag reduction. *Europhys. Lett.* **2**:519–522 (1986).

[100] K. R. Sreenivasan and C. M. White. The onset of drag reduction by dilute polymer additives, and the maximum drag reduction asymptote. *J. Fluid Mech.* **409**:149–164 (2000).

[101] P. Pincus. Excluded volume effects and strected polymer chains. *Macromolecules* **9**:386–388 (1976).

[102] R. B. Bird, P. J. Dotson, and N. L. Johnson. Polymer solution rheology based on a finitely extensible bead-spring chain model. *J. Non-Newton. Fluid Mech.* **7**:213–235 (1980).

[103] M. D. Chilcott and J. M. Rallison. Creeping flow of dilute polymer solutions past cylinders and spheres. *J. Non-Newton. Fluid Mech.* **29**:381–432 (1988).

[104] R. Sureshkumar and A. N. Beris. Effect of artificial stress diffusivity on the stability of numerical calculations and the flow dynamics of time-dependent viscoelastic flows. *J. Non-Newton. Fluid Mech.* **60**:53–80 (1995).

[105] W. J. Han and H. J. Choi. Role of bio-based polymers on improving turbulent flow characteristics: materials and applications. *Polymers* **9**:209 (2017).

[106] S. R. Deshmukh, K. Sudhakar, and R. P. Singh. Drag-reduction efficiency, shear stability, and biodegradation resistance of carboxymethyl cellulose-based and starch-based graft copolymers. *J. Appl. Polym. Sci.* **43**:1091–1101 (1991).

[107] J. W. Hoyt. Drag reduction in polysaccharide solutions. *Trends Biotechnol.* **3**:17–21 (1985).

[108] W. Interthal and H. Wilski. Drag reduction experiments with very large pipes. *Colloid Polym. Sci.* **263**:217–229 (1985).

[109] E. C. Coelho, K. C. O. Barbosa, E. J. Soares, R. N. Siqueira, and J. C. C. Freitas. Okra as a drag reducer for high Reynolds number water flows. *Rheol. Acta* **55**:983–991 (2016).

[110] H. Maier, M. Anderson, C. Karl, K. Magnuson, and R. L. Whistler. Guar, locust bean, tara and fenugreek gums. In R. L. Whistler and J. N. Bemiller, editors, *Industrial Gums* pages 181–226. Academic Press London (1993).

[111] F. García-Ochoa, V. E. Santos, J. A. Casas, and E. Gómez. Xanthan gum: production, recovery, and properties. *Biotechnol. Adv.* **18**:549–579 (2000).

[112] A. Ziolkovska. Laws of flaxseed mucilage extraction. *Food hydrocoll.* **26**:197–204 (2012).

[113] V. Kontogiorgos, I. Margelou, N. Georgiadis, and C. Ritzoulis. Rheological characterization of okra pectins. *Food hydrocoll.* **29**:356–362 (2012).

[114] W. J. Han, Y. Z. Dong, and H. J. Choi. Applications of water-soluble polymers in turbulent drag reduction. *Processes* **5**:24 (2017).

[115] H.-W. Bewersdorff and R. P. Singh. Rheological and drag reduction characteristics of xanthan gum solutions. *Rheol. Acta* **27**:617–627 (1988).

[116] S. R. Deshmukh, P. N. Chaturvedi, and R. P. Singh. The turbulent drag reduction by graft copolymers of guargum and polyacrylamide. *J. Appl. Polym. Sci.* **30**:4013–4018 (1985).

[117] S. R. Deshmukh and R. P. Singh. Drag reduction characteristics of graft copolymers of xanthangum and polyacrylamide. *J. Appl. Polym. Sci.* **32**:6163–6176 (1986).

[118] W. Barthlott and C. Neinhuis. Purity of the sacred lotus, or escape from contamination in biological surfaces. *Planta* **202**:1–8 (1997).

[119] B. Bhushan and Y. C. Jung. Natural and biomimetic artificial surfaces for superhydrophobicity, self-cleaning, low adhesion, and drag reduction. *Prog. Mater. Sci.* **56**:1–108 (2011).

[120] D. Quéré. Wetting and roughness. *Annu. Rev. Mater. Res.* **38**:71–99 (2008).

[121] G. McHale, M. I. Newton, and N. J. Shirtcliffe. Immersed superhydrophobic surfaces: gas exchange, slip and drag reduction properties. *Soft Matter* **6**:714–719 (2010).

[122] B. Mockenhaupt, H.-J. Ensikat, M. Spaeth, and W. Barthlott. Superhydrophobicity of biological and technical surfaces under moisture condensation: stability in relation to surface structure. *Langmuir* **24**:13591–13597 (2008).

[123] T. Wagner, C. Neinhuis, and W. Barthlott. Wettability and contaminability of insect wings as a function of their surface sculptures. *Acta Zool.* **77**:213–225 (1996).

[124] J. W. M. Bush, D. Hu, and M. Prakash. The integument of waterwalking arthropods: form and function. *Adv. Insect Physiol.* **34**:117–192 (2008).

[125] X. F. Gao, X. Yan, X. Yao, L. Xu, K. Zhang, J. Zhang, B. Yang, and L. Jiang. The dry-style antifogging properties of mosquito compound eyes and artificial analogues prepared by soft lithography. *Adv. Mater.* **19**:2213–2215 (2007).

[126] E. Bormashenko, Y. Bormashenko, T. Stein, G. Whyman, and E. Bormashenko. Why do pigeon feathers repel water? Hydrophobicity of pennae, Cassie-Baxter wetting hypothesis and Cassie-Wenzel capillarity-induced wetting transition. *J. Colloid Interface Sci.* **311**:212–216 (2007).

[127] S. Srinivasan, S. S. Chhatre, J. O. Guardado, K.-C. Park, A. R. Parker, M. F. Rubner, G. H. McKinley, and R. E. Cohen. Quantification of feather structure, wettability and resistance to liquid penetration. *J. R. Soc. Interface* **11**:20140287 (2014).

[128] J. Davenport, R. N. Hughes, M. Shorten, and P. S. Larsen. Drag reduction by air release promotes fast ascent in jumping emperor penguins—a novel hypothesis. *Mar. Ecol. Prog. Ser.* **430**:171–182 (2011).

[129] T. Young. An essay on the cohesion of fluids. *Phil. Trans. R. Soc. London* **95**:65–87 (1805).

[130] A. Marmur, C. Della Volpe, S. Siboni, A. Amirfazli, and J. W. Drelich. Contact angles and wettability: towards common and accurate terminology. *Surf. Innov.* **5**:3–8 (2017).

[131] E. G. Shafrin and W. A. Zisman. Upper limits to the contact angles of liquids on solids. In F. M. Fowkes, editor, *Contact Angles, Wettability and Adhesion* volume 43 of *Advances in Chemistry* chapter 9, pages 145–157. American Chemical Society Washington, DC (1964).

[132] R. N. Wenzel. Resistance of solid surfaces to wetting by water. *Ind. Eng. Chem.* **28**:988–994 (1936).

[133] P. G. de Gennes, F. Brochard-Wyart, and D. Quéré. *Capillarity and Wetting Phenomena: Drops, Bubbles, Pearls, Waves*. Springer (2004).

[134] M. Callies and D. Quéré. On water repellency. *Soft Matter* **1**:55–61 (2005).

[135] A. Marmur. The lotus effect: superhydrophobicity and metastability. *Langmuir* **20**:3517–3519 (2004).

[136] C. Ishino, K. Okamura, and D. Quéré. Wetting transitions on rough surfaces. *Europhys. Lett.* **68**:419–425 (2004).

[137] N. A. Patankar. Transition between superhydrophobic states on rough surfaces. *Langmuir* **20**:7097–7102 (2004).

[138] G. Carbone and L. Mangialardi. Hydrophobic properties of a wavy rough substrate. *Eur. Phys. J. E* **16**:67–76 (2005).

[139] A. Tuteja, W. Choi, M. Ma, J. M. Mabry, G. H. McKinley, and R. E. Cohen. Robust omniphobic surfaces. *Proc. Natl. Acad. Sci. U. S. A.* **105**:18200–18205 (2008).

[140] P. Fosberg, F. Nikolajeff, and M. Karlsson. Cassie-Wenzel and Wenzel-Cassie transitions on immersed superhydrophobic surfaces under hydrostatic pressure. *Soft Matter* **7**:104–109 (2011).

[141] E. Bormashenko, R. Pogreb, G. Whyman, Y. Bormashenko, and M. Erlich. Vibration-induced Cassie-Wenzel wetting transition on rough surfaces. *Appl. Phys. Lett.* **90**:201917 (2007).

[142] M. S. Bobji, S. V. Kumar, A. Asthana, and R. N. Govardhan. Underwater sustainability of the "Cassie" state of wetting. *Langmuir* **25**:12120–12126 (2009).

[143] A. Nakajima, K. Hashimoto, and T. Watanabe. Recent studies on superhydrophobic films. *Monatsh. Chem.* **132**:31–41 (2001).

[144] K. K. S. Lau, J. Bico, K. B. K. Teo, M. Chhowalla, G. A. J. Amaratunga, W. I. Milne, G. H. McKinley, and K. K. Gleason. Superhydrophobic carbon nanotube forests. *Nano Lett.* **3**:1701–1705 (2003).

[145] X. Feng and L. Jiang. Design and creation of superwetting/antiwetting surfaces. *Adv. Mater.* **18**:3063–3078 (2006).

[146] S. Srinivasan, S. S. Chhatre, J. M. Mabry, R. E. Cohen, and G. H. McKinley. Solution spraying of poly(methyl methacrylate) blends to fabricate microtextured, superoleophobic surfaces. *Polymer* **52**:3209–3218 (2011).

[147] J. Yang, Z. Zhang, X. Xu, X. Men, X. Zhu, and X. Zhou. Superoleophobic textured aluminum surfaces. *New J. Chem.* **35**:2422–2426 (2011).

[148] K. Golovin, D. H. Lee, J. M. Mabry, and A. Tuteja. Transparent, flexible, superomniphobic surfaces with ultra-low contact angle hysteresis. *Angew. Chem.* **125**:13245–13249 (2013).

[149] P. Kim, M. J. Kreder, J. Alvarenga, and J. Aizenberg. Hierarchical or not? Effect of the length scale and hierarchy of the surface roughness on omniphobicity of lubricant-infused substrates. *Nano Lett.* **13**:1793–1799 (2013).

[150] R. A. Bidkar, L. Leblanc, A. J. Kulkarni, V. Bahadur, S. L. Ceccio, and M. Perlin. Skin friction drag reduction in the turbulent regime using random-textured hydrophobic surfaces. *Phys. Fluids* **26**:085108 (2014).

[151] S. M. R. Razavi, J. Oh, S. Sett, L. Feng, X. Yan, M. J. Hoque, A. Liu, R. T. Haasch, M. Masoomi, R. Bagheri, and N. Milijkovic. Superhydrophobic surfaces made from naturally derived hydrophobic materials. *ACS Sustainable Chem. Eng.* **5**:11362–11370 (2017).

[152] C.-L.-M.-H. Navier. Mémoire sur les lois du mouvement des fluides. *Mem. Acad. Sci. Inst. France* **6**:389–440 (1823).

[153] J. R. Philip. Flows satisfying mixed no-slip and no-shear conditions. *Z. Angew. Math. Phys.* **23**:353–372 (1972).

[154] J. R. Philip. Integral properties of flows satisfying mixed no-slip and no-shear conditions. *Z. Angew. Math. Phys.* **23**:960–968 (1972).

[155] E. Lauga and H. A. Stone. Effective slip in pressure driven Stokes flow. *J. Fluid Mech.* **489**:55–77 (2003).

[156] C. Cottin-Bizonne, C. Barentin, E. Charlaix, L. Bocquet, and J.-L. Barrat. Dynamics of simple liquids at heterogeneous surfaces: molecular dynamics simulations and hydrodynamic description. *Eur. J. Phys. E* **15**:427–438 (2004).

[157] C. Schönecker, T. Baier, and S. Hardt. Influence of the enclosed fluid on the flow over a microstructured surface in the Cassie state. *J. Fluid Mech.* **740**:168–195 (2014).

[158] C. Ybert, C. Barentin, C. Cottin-Bizonne, P. Joseph, and L. Bocquet. Achieving large slip with superhydrophobic surfaces: scaling laws for generic geometries. *Phys. Fluids* **19**:123601 (2007).

[159] K. Watanabe, Yanuar, K. Okido, and H. Mizunuma. Drag reduction in flow through square and rectangular ducts with highly water-repellent walls. *JSME Int. J. Ser. B* **62**:3330–3334 (1996).

[160] K. Watanabe and S. Ogata. Drag reduction for a rotating disk with highly water-repellent wall. *JSME Int. J. Ser. B* **41**:556–560 (1998).

[161] K. Watanabe, Yanuar, and H. Mizunuma. Slip of Newtonian fluids at solid boundary. *JSME Int. J. Ser. B* **41**:525–529 (1998).

[162] K. Watanabe and T. Akino. Drag reduction in laminar flow between two vertical coaxial cylinders. *J. Fluids Eng.* **121**:541–547 (1999).

[163] K. Watanabe, Yanuar, and H. Udagawa. Drag reduction of Newtonian fluid in a circular pipe with a highly water-repellent wall. *J. Fluid Mech.* **381**:225–238 (1999).

[164] J. Ou, J. B. Perot, and J. P. Rothstein. Laminar drag reduction in microchannels using ultrahydrophobic surfaces. *Phys. Fluids* **16**:4635–4660 (2004).

[165] J. Ou and J. P. Rothstein. Direct velocity measurements of the flow past drag-reducing ultrahydrophobic surfaces. *Phys. Fluids* **17**:103606 (2005).

[166] C. Lee and C.-J. Kim. Maximizing the giant liquid slip on superhydrophobic microstructures by nanostructuring their sidewalls. *Langmuir* **25**:12812–12818 (2009).

[167] T. Min and J. Kim. Effects of hydrophobic surface on skin-friction drag. *Phys. Fluids* **16**:L55–58 (2004).

[168] R. Daniello, N. E. Waterhouse, and J. P. Rothstein. Turbulent drag reduction using superhydrophobic surfaces. *Phys. Fluids* **21**:085103 (2009).

[169] H. Park, G. Sun, and C.-J. Kim. Superhydrophobic turbulent drag reduction as a function of surface grating parameters. *J. Fluid Mech.* **747**:722–734 (2014).

[170] B. J. Rosenberg, T. Van Buren, M. K. Fu, and A. J. Smits. Turbulent drag reduction over air- and liquid- impregnated surfaces. *Phys. Fluids* **28**:015103 (2016).

[171] T. Van Buren and A. J. Smits. Substantial drag reduction in turbulent flow using liquid-infused surfaces. *J. Fluid Mech.* **827**:448–456 (2017).

[172] M. A. Samaha, H. V. Tafreshi, and M. Gad el Hak. Effects of hydrostatic pressure on the drag reduction of submerged aerogel-particle coatings. *Colloids Surf. A Physicochem. Eng. Asp.* **399**:62–70 (2012).

[173] K. Moaven, M. Rad, and M. Taeibi-Rahni. Experimental investigation of viscous drag reduction of superhydrophobic nano-coating in laminar and turbulent flows. *Exp. Therm. Fluid Sci.* **51**:239–243 (2013).

[174] S. Gogte, P. Vorobieff, R. Truesdell, A. Mammoli, F. van Swol, P. Shah, and C. J. Brinker. Effective slip on textured superhydrophobic surfaces. *Phys. Fluids* **17**:051701 (2005).

[175] J.-P. Zhao, X.-D. Du, and X.-H. Shi. Experimental research on friction-reduction with superhydrophobic surfaces. *J. Mar. Sci. Appl.* **6**:58–61 (2007).

[176] C. Peguero and K. Breuer. On drag reduction in turbulent channel flow over superhydrophobic surfaces. In B. Eckhardt, editor, *Advances in Turbulence XII* volume 132 pages 233–236 Berlin (2009). Springer.

[177] E. Aljallis, M. A. Sarshar, R. Datla, V. Sikka, A. Jones, and C.-H. Choi. Experimental study of skin friction drag reduction on superhydrophobic flat plates in high reynolds number boundary layer flow. *Phys. Fluids* **25**:025103 (2013).

[178] S. Srinivasan, J. A. Kleingartner, J. B. Gilbert, R. E. Cohen, A. J. B. Milne, and G. H. McKinley. Sustainable drag reduction in turbulent Taylor-Couette flows by depositing scalable superhydrophobic surfaces. *Phys. Rev. Lett.* **114**:014501 (2015).

[179] J. Zhang, H. Tian, Z. Yao, P. Hao, and N. Jiang. Mechanisms of drag reduction of superhydrophobic surfaces in turbulent boundary layer flow. *Exp. Fluids* **56**:1–13 (2015).

[180] H. Ling, S. Srinivasan, K. Golovin, G. H. McKinley, A. Tuteja, and J. Katz. High-resolution velocity measurements in the inner part of turbulent boundary layers over super-hydrophobic surfaces. *J. Fluid Mech.* **801**:670–703 (2016).

[181] M. Nosonovsky and B. Bhushan. Superhydrophobic surfaces and emerging applications: non-adhesion, energy, green engineering. *Curr. Opin. Colloid Interface Sci.* **14**:270–280 (2009).

[182] B. V. Hokmabad and S. Ghaemi. Turbulent flow over wetted and non-wetted superhydrophobic counterparts with random structure. *Phys. Fluids* **28**:015112 (2016).

[183] I. U. Vakarelski, N. A. Patankar, J. O. Marston, D. Y. C. Chan, and S. T. Thoroddsen. Stabilization of Leidenfrost vapour layer by textured superhydrophobic surfaces. *Nature* **489**:274–277 (2012).

[184] I. U. Vakarelski, D. Y. C. Chan, and S. T. Thoroddsen. Leidenfrost vapour layer moderation of the drag crisis and trajectories of superhydrophobic and hydrophilic spheres falling in water. *Soft Matter* **10**:5662–5668 (2014).

[185] D. Saranadhi, D. Chen, J. A. Kleingartner, S. Srinivasan, R. E. Cohen, and G. H. McKinley. Sustained drag reduction in a turbulent flow using a low-temperature Leidenfrost surface. *Sci. Adv.* **2**:e1600686 (2016).

[186] C. Lee and C.-J. Kim. Underwater restoration and retention of gases on superhydrophobic surfaces for drag reduction. *Phys. Rev. Lett.* **106**:014502 (2011).

[187] M. Xu, C. T. Liu, , and C.-J. Kim. Self-powered plastron preservation and one-step molding of semiactive superhydrophobic surfaces. *Langmuir* **36**:8193–8198 (2020).

[188] D. Panchanathan, A. Rajappan, K. K. Varanasi, and G. H. McKinley. Plastron regeneration on submerged superhydrophobic surfaces using in situ gas generation by chemical reaction. *ACS Appl. Mater. Interfaces* **10**:33684–33692 (2018).

[189] P. Du, J. Wen, Z. Zhang, D. Song, A. Ouahsine, and H. Hu. Maintenance of air layer and drag reduction on superhydrophobic surface. *Ocean Eng.* **130**:328–335 (2017).

[190] J. W. Strutt. On the dynamics of revolving fluids. *Proc. R. Soc. Lond. A* **93**:148–154 (1917).

[191] G. I. Taylor. Stability of a viscous liquid contained between two rotating cylinders. *Phil. Trans. R. Soc. A* **223**:289–343 (1923).

[192] R. C. Di Prima and H. L. Swinney. Instabilities and transition in flow between concentric rotating cylinders. In H. L. Swinney and J. P. Gollub, editors, *Hydrodynamic Instabilities and the Transition to Turbulence* volume 45 of *Topics in Applied Physics* chapter 6, pages 139–180. Springer Berlin (1981).

[193] C. D. Andereck, S. S. Liu, and H. L. Swinney. Flow regimes in a circular Couette system with independently rotating cylinders. *J. Fluid Mech.* **164**:155–183 (1986).

[194] S. Grossmann, D. Lohse, and C. Sun. High-Reynolds number Taylor-Couette turbulence. *Annu. Rev. Fluid Mech.* **48**:53–80 (2016).

[195] G. P. Smith and A. A. Townsend. Turbulent Couette flow between concentric cylinders at large Taylor numbers. *J. Fluid Mech.* **123**:187–217 (1982).

[196] D. P. Lathrop, J. Fineberg, and H. L. Swinney. Transition to shear-driven turbulence in Couette-Taylor flow. *Phys. Rev. A* **46**:6390–6405 (1992).

[197] B. Eckhardt, S. Grossmann, and D. Lohse. Torque scaling in turbulent Taylor-Couette flow between independently rotating cylinders. *J. Fluid Mech.* **581**:221–250 (2007).

[198] J. L. Synge. The stability of heterogeneous liquids. *Trans. R. Soc. Can.* **27**:1–18 (1933).

[199] J. L. Synge. On the stability of a viscous liquid between rotating coaxial cylinders. *Proc. R. Soc. Lon. A* **167**:250–256 (1938).

[200] G. S. Lewis and H. L. Swinney. Velocity structure functions, scaling and transitions in high Reynolds number Couette-Taylor flow. *Phys. Rev. E* **59**:5457–5467 (1999).

[201] M. H. Sharqawy, J. H. Lienhard, and S. M. Zubair. Thermophysical properties of seawater: a review of existing correlations and data. *Desalination Water Treat.* **16**:354–380 (2010).

[202] K. G. Nayar, M. H. Sharqawy, L. D. Banchik, and J. H. Lienhard. Thermophysical properties of seawater: A review and new correlations that include pressure dependence. *Desalination* **390**:1–24 (2016).

[203] R. L. Panton. Scaling laws for the angular momentum of a completely turbulent Couette flow. *C. R. Acad. Sci. Paris Ser. II* **315**:1467–1473 (1992).

[204] C. R. Doering and P. Constantin. Energy dissipation in shear driven turbulence. *Phys. Rev. Lett.* **69**:1648–1651 (1992).

[205] S. G. Huisman, D. P. M. van Gils, S. Grossmann, C. Sun, and D. Lohse. Ultimate turbulent Taylor-Couette flow. *Phys. Rev. Lett.* **108**:024501 (2011).

[206] W. Cheng, D. I. Pullin, and R. Samtaney. Large-eddy simulation and modelling of Taylor-Couette flow. *J. Fluid Mech.* **890**:A17 (2020).

[207] P. Berghout, R. Verzicco, R. J. A. M. Stevens, D. Lohse, and D. Chung. Calculation of the mean velocity profile for strongly turbulent Taylor-Couette flow and arbitrary radius ratios. arXiv:2003.03294 (2020).

[208] J. A. Odell, A. J. Muller, K. A. Narh, and A. Keller. Degradation of polymer solutions in extensional flows. *Macromolecules* **23**:3092–3103 (1990).

[209] ASTM International. D1193-06(2018) Standard specification for reagent water. ASTM International, West Conshohocken, PA (2018).

[210] ASTM International. D445-19a Standard test method for kinematic viscosity of transparent and opaque liquids (and calculation of dynamic viscosity). ASTM International, West Conshohocken, PA (2019).

[211] ASTM International. D446-12(2017) Standard specifications and operating instructions for glass capillary kinematic viscometers. ASTM International, West Conshohocken, PA (2017).

[212] R. Pamies, J. G. Hernández Cifre, M. del Carmen López Martínez, and J. G. de la Torre. Determination of intrinsic viscosities of macromolecules and nanoparticles. Comparison of single-point and dilution procedures. *Colloid Polym. Sci.* **286**:1223–1231 (2008).

[213] P. C. Hiemenz and T. P. Lodge. *Polymer Chemistry*. CRC Press second edition (2017).

[214] F. E. Bailey, J. L. Kucera, and L. G. Imhof. Molecular weight relations of poly(ethylene oxide). *J. Polym. Sci.* **32**:517–518 (1958).

[215] K. Devanand and J. C. Selser. Asymptotic behavior and long-range interactions in aqueous solutions of poly(ethylene oxide). *Macromolecules* **24**:5943–5947 (1991).

[216] C. Clasen, J. P. Plog, W. M. Kulicke, M. Owens, C. Macosko, L. E. Scriven, M. Verani, and G. H. McKinley. How dilute are dilute solutions in extensional flows? *J. Rheol.* **50**:849–881 (2006).

[217] W. W. Graessley. Polymer chain dimensions and the dependence of viscoelastic properties on concentration, molecular weight and solvent power. *Polymer* **21**:258–262 (1980).

[218] H. Yamakawa and M. Fujii. Intrinsic viscosity of wormlike chains. Determination of the shift factor. *Macromolecules* **7**:128–135 (1974).

[219] J. Dinic and V. Sharma. Macromolecular relaxation, strain, and extensibility determine elastocapillary thinning and extensional viscosity of polymer solutions. *Proc. Natl. Acad. Sci. U. S. A.* **116**:8766–8774 (2019).

[220] G. H. McKinley. Visco-elasto-capillary thinning and break-up of complex fluids. *Rheol. Rev.* pages 1–48 (2005).

[221] J. Du. Rheological characterization of lubricants in automotive industries through development of a novel capillary breakup extensional rheometer. Master's thesis Massachusetts Institute of Technology (2018).

[222] S. L. Anna and G. H. McKinley. Elasto-capillary thinning and breakup of model elastic liquids. *J. Rheol.* **45**:115–138 (2001).

[223] J. Dinic, Y. Zhang, N. Jimenez, and V. Sharma. Extensional relaxation times of dilute, aqueous polymer solutions. *ACS Macro Lett.* **4**:804–808 (2015).

[224] M. Stelter, G. Brenn, A. L. Yarin, R. P. Singh, and F. Durst. Validation and application of a novel elongational device for polymer solutions. *J. Rheol.* **44**:595–616 (2000).

[225] M. Stelter, G. Brenn, A. L. Yarin, R. P. Singh, and F. Durst. Investigation of the elongational behavior of polymer solutions by means of an elongational rheometer. *J. Rheol.* **46**:507–527 (2002).

[226] M. S. N. Oliveira and G. H. McKinley. Iterated stretching and multiple beads-on-a-string phenomena in dilute solutions of highly extensible flexible polymers. *Phys. Fluids* **17**:071704 (2005).

[227] B. N. Semenov. The pulseless injection of polymeric additives into near-wall flow and perspectives of drag reduction. In K.-S. Choi, editor, *Recent Developments in Turbulence Management* pages 293–308. Springer Dordrecht (1991).

[228] Q. Guo, S. W. Cui, Q. Wang, and J. C. Young. Fractionation and physicochemical characterization of psyllium gum. *Carbohydr. Polym.* **73**:35–43 (2008).

[229] C. E. Wagner, A. C. Barbati, J. Engmann, A. S. Burbidge, and G. H. McKinley. Quantifying the consistency and rheology of liquid foods using fractional calculus. *Food Hydrocoll.* **69**:242–254 (2017).

[230] R. P. Singh, G. P. Karmakar, S. K. Rath, N. C. Karmakar, S. R. Pandey, T. Tripathy, J. Panda, K. Kanan, S. K. Jain, and N. T. Lan. Biodegradable drag reducing agents and flocculants based on polysaccharides: materials and applications. *Polym. Eng. Sci.* **40**:46–60 (2000).

[231] M. Imran, P. B. Poduval, and S. C. Ghadi. *Bacterial degradation of algal polysaccharides in marine ecosystem* pages 189–203. Springer Singapore (2017).

[232] A. W. Decho and T. Gutierrez. Microbial extracellular polymeric substances (EPSs) in ocean systems. *Front. Microbiol.* **8**:922 (2017).

[233] R. M. Fuoss. Viscosity function for polyelectrolytes. *J. Polym. Sci.* **3**:603–604 (1948).

[234] C. Tanford. *Physical Chemistry of Macromolecules*. John Wiley and Sons, Inc. (1961).

[235] K. Zheng, K. Chen, W. Ren, J. Yang, and J. Zhao. Counterion cloud expansion of a polyelectrolyte by dilution. *Macromolecules* **51**:4444–4450 (2018).

[236] R. M. Fuoss and U. P. Strauss. Electrostatic interaction of polyelectrolytes and simple electrolytes. *J. Polym. Sci.* **3**:602–603 (1948).

[237] K. K. T. Goh, D. N. Pinder, C. E. Hall, and Y. Hemar. Rheological and light scattering properties of flaxseed polysaccharide aqueous solutions. *Biomacromolecules* **7**:3098–3103 (2006).

[238] M. Muthukumar. 50th anniversary perspective: A perspective on polyelectrolyte solutions. *Macromolecules* **50**:9528–9560 (2017).

[239] L. E. Rodd, T. P. Scott, J. J. Cooper-White, and G. H. McKinley. Capillary break-up rheometry of low-viscosity elastic fluids. *Appl. Rheol.* **15**:12–27 (2005).

[240] C. G. Malmberg and A. A. Maryott. Dielectric constants of aqueous solutions of dextrose and sucrose. *J. Res. Natl. Inst. Stand.* **45**:299–303 (1950).

[241] A. M. Elfak, G. Pass, G. O. Phillips, and R. G. Morley. The viscosity of dilute solutions of guar gum and locust bean gum with and without added sugars. *J. Sci. Food Agric.* **28**:895–899 (1977).

[242] P. H. Richardson, J. Willmer, and T. J. Foster. Dilute solution properties of guar and locust bean gum in sucrose solutions. *Food Hydrocoll.* **12**:339–348 (1998).

[243] Y. Mo, T. Takaya, K. Nishinari, K. Kubota, and A. Okamoto. Effects of sodium chloride, guanidine hydrochloride, and sucrose on the viscoelastic properties of sodium hyaluronate solutions. *Biopolymers* **50**:23–34 (1999).

[244] P. S. Virk and H. Baher. The effect of polymer concentration on drag reduction. *Chem. Eng. Sci.* **25**:1183–1189 (1970).

[245] National Agricultural Statistics Service. Agricultural prices. Technical report Agricultural Statistics Board, United States Department of Agriculture (February 2018).

[246] T. Rho, J. Park, C. Kim, H. K. Yoon, and H. S. Suh. Degradation of poly(acrylamide) in dilute solution. *Polym. Degrad. Stab.* **51**:287–293 (1996).

[247] V. N. Kalashnikov. Degradation accompanying turbulent drag reduction by polymer additives. *J. Non-Newton. Fluid Mech.* **103**:105–121 (2002).

[248] A. S. Pereira and E. J. Soares. Polymer degradation of dilute solutions in turbulent drag reducing flows in a cylindrical double gap rheometer device. *J. Non-Newton. Fluid Mech.* **179–180**:9–22 (2012).

[249] S. A. Vanapalli, M. T. Islam, and M. J. Solomon. Scission-induced bounds on maximum polymer drag reduction in turbulent flow. *Phys. Fluids* **17**:095108 (2005).

[250] W. Brostow. Drag reduction and mechanical degradation in polymer solutions in flow. *Polymer* **24**:631–638 (1983).

[251] W. Brostow, H. Ertepinar, and R. P. Singh. Flow of dilute polymer solutions: Chain conformations and degradation of drag reducers. *Macromolecules* **23**:5109–5118 (1990).

[252] ASTM International. D1141-98(2013) Standard practice for the preparation of substitute ocean water. ASTM International, West Conshohocken, PA (2013).

[253] P. S. Virk. Drag reduction by collapsed and extended polyelectrolytes. *Nature* **253**:109–110 (1975).

[254] N. S. Berman. Drag reduction by polymers. *Annu. Rev. Fluid Mech.* **10**:47–64 (1978).

[255] C. Lee, C.-H. Choi, and C.-J. Kim. Superhydrophobic drag reduction in laminar flows: a critical review. *Exp. Fluids* **57**:176 (2016).

[256] F. Schellenberger, N. Encinas, D. Vollmer, and H.-J. Butt. How water advances on superhydrophobic surfaces. *Phys. Rev. Lett.* **116**:096101 (2016).

[257] K. Watanabe and H. Udagawa. Drag reduction of Non-Newtonian fluids in a circular pipe with a highly water-repellent wall. *AIChE J.* **47**:256–262 (2001).

[258] E. A. Davis and J. S. Park. Turbulence dynamics of dilute polymer solutions: Apparent slip and the effect of slip-inducing surfaces. In *The 91st Annual Meeting of The Society of Rheology, October 20–24, Raleigh, North Carolina* (2019).

[259] C. Lv, P. Hao, Z. Yao, and F. Niu. Departure of condensation droplets on superhydrophobic surfaces. *Langmuir* **31**:2414–2420 (2015).

[260] K. J. McCarthy, C. W. Burkhardt, and D. P. Parazak. Mark-Houwink-Sakurada constants and dilute solution behavior of heterodisperse poly(acrylamide-co-sodium acrylate) in 0.5 M and 1 M NaCl. *J. Appl. Polym. Sci.* **33**:1699–1714 (1987).

[261] M. Sbragaglia and A. Prosperetti. A note on the effective slip properties for microchannel flows with ultrahydrophobic surfaces. *Phys. Fluids* **19**:043603 (2007).

[262] A. Steinberger, C. Cottin-Bizonne, P. Kleimann, and E. Charlaix. High friction on a bubble mattress. *Nat. Mater.* **6**:665–668 (2007).

[263] C. T. Fairhall and R. García-Mayoral. Spectral analysis of the slip-length model for turbulence over textured superhydrophobic surfaces. *Flow Turbul. Combust.* **100**:961–978 (2018).

[264] T. R. Scavo and J. B. Thoo. On the geometry of Halley's method. *Am. Math. Mon.* **102**:417–426 (1995).

[265] M. W. Kim and B. H. Cao. Additional reduction of surface tension of aqueous polyethylene oxide (PEO) solution at high polymer concentration. *Europhys. Lett.* **24**:229–234 (1993).

[266] C.-E. Brunchi, M. Bercea, S. Morariu, and M. Dascalu. Some properties of xanthan gum in aqueous solutions: effect of temperature and pH. *J. Polym. Res.* **23**:123 (2016).

[267] F. J. Peaudecerf, J. R. Landel, R. E. Goldstein, and P. Luzzatto-Fegiz. Traces of surfactants can severely limit the drag reduction of superhydrophobic surfaces. *Proc. Natl. Acad. Sci. U. S. A.* **114**:7254–7259 (2017).

[268] R. Y. Z. Hu, A. T. A. Wang, and J. P. Hartnett. Surface tension measurement of aqueous polymer solutions. *Exp. Therm. Fluid Sci.* **4**:723–729 (1991).

[269] Y. F. Yano. Correlation between surface and bulk structures of alcohol-water mixtures. *J. Colloid Interface Sci.* **284**:255–259 (2005).

[270] K. Alamé, S. Anantharamu, and K. Mahesh. A variational level set methodology without reinitialization for the prediction of equilibrium interfaces over arbitrary solid surfaces. *J. Comput. Phys.* **406**:109184 (2020).

[271] A. Kreitschitz and S. N. Gorb. The micro- and nanoscale spatial architecture of the seed mucilage—Comparative study of selected plant species. *PLoS One* **13**:e0200522 (2018).

[272] K. Wannerberger, T. Nylander, and M. Nyman. Rheological and chemical properties of mucilage in different varieties from linseed (*Linum usitatissimum*). *Acta Agric. Scand.* **41**:311–319 (1991).

[273] H. A. Gajardo, R. Quian, and B. Soto-Cerda. Agronomic and quality assessment of linseed advanced breeding lines varying in seed mucilage content and their use for food and feed. *Crop Sci.* **57**:2979–2990 (2017).

[274] T. Jenkins, A. Bovi, and R. Edwards. Plants: biofactories for a sustainable future? *Phil. Trans. R. Soc. A* **369**:1826–1839 (2011).

[275] B. H. A. Rehm. Synthetic biology towards the synthesis of custom-made polysaccharides. *Microb. Biotechnol.* **8**:19–20 (2015).

[276] A. Becker. Challenges and perspectives in combinatorial assembly of novel exopolysaccharide biosynthesis pathways. *Front. Microbiol.* **6**:687 (2015).

[277] L. A. Anderson, M. A. Islam, and K. L. J. Prather. Synthetic biology strategies for improving microbial synthesis of "green" biopolymers. *J. Biol. Chem.* **293**:5053–5061 (2018).

[278] J. B. Bello, A. J. Müller, and A. E. Sáez. Effect of intermolecular cross links on drag reduction by polymer solutions. *Polym. Bull.* **36**:111–118 (1996).

[279] E. Sabadini, K. R. Francisco, and L. Bouteiller. Bis-urea-based supramolecular polymer: the first self-assembled drag reducer for hydrocarbon solvents. *Langmuir* **26**:1482–1486 (2010).

[280] S. Alix, S. Marais, C. Morvan, and L. Lebrun. Biocomposite materials from flax plants: Preparation and properties. *Compos. Part A Appl. Sci. Manuf.* **39**:1793–1801 (2008).

[281] F. Paynel, C. Morvan, S. Marais, and L. Lebrun. Improvement of the hydrolytic stability of new flax-based biocomposite materials. *Polym. Degrad. Stab.* **98**:190–197 (2013).

[282] A. A. Mohsenipour and R. Pal. The role of surfactants in mechanical degradation of drag-reducing polymers. *Ind. Eng. Chem. Res.* **52**:1291–1302 (2013).

[283] J. J. W. Coppen. *Gums, Resins and Latexes of Plant Origin*. Food and Agricultural Organization of the United Nations (1995).

[284] K. J. van den Berg, J. van der Horst, J. J. Boon, and O. O. Sudmeijer. Cis-1,4-poly-β-myrcene; the structure of the polymeric fraction of mastic resin (*Pistacia lentiscus* L.) elucidated. *Tetrahedron Lett.* **39**:2645–2648 (1998).

[285] B. G. K. van Aarssen, J. W. de Leeuw, M. Collinson, J. J. Boon, and K. Goth. Occurrence of polycadinene in fossil and recent resins. *Geochim. Cosmochim. Acta* **58**:223–229 (1994).

[286] T. Schmidt, M. Lenders, A. Hillebrand, N. van Deenen, O. Munt, R. Reichelt, W. Eisenreich, R. Fischer, D. Prüfer, and C. S. Gronover. Characterization of rubber particles and rubber chain elongation in *Taraxacum koksaghyz*. *BMC Biochem.* **11**:11 (2010).

[287] International Rubber Study Group. Rubber statistical bulletin. International Rubber Study Group, Singapore (October–December 2018).

[288] L. F. King. Solvents for synthetic rubbers. *J. Chem. Eng. Data* **11**:243–248 (1966).

[289] E. W. Lemmon, M. O. McLinden, and D. G. Friend. Thermophysical properties of fluid systems. In P. J. Linstrom and W. G. Mallard, editors, *NIST Chemistry WebBook, NIST Standard Reference Database Number 69*. National Institute of Standards and Technology Gaithersburg (2020). (retrieved July 20, 2020).